NASA CR-72113
LMSC-A839783

LIQUID PROPELLANT THERMAL CONDITIONING SYSTEM

by

W. H. Sterbentz

prepared for

NATIONAL AERONAUTICS AND SPACE ADMINISTRATION

CONTRACT NAS 3-7942

FACILITY FORM 602
N67-25068
(ACCESSION NUMBER)
268
(PAGES)
CR-72113
(NASA CR OR TMX OR AD NUMBER)
(THRU)
1
(CODE)
28
(CATEGORY)

LOCKHEED MISSILES & SPACE COMPANY
A GROUP DIVISION OF LOCKHEED AIRCRAFT CORPORATION

NOTICE

This report was prepared as an account of Government sponsored work. Neither the United States, nor the National Aeronautics and Space Administration (NASA), nor any person acting on behalf of the NASA:

A) Makes any warranty or representation, expressed or implied, with respect to the accuracy, completeness, or usefulness of the information contained in this report, or that the use of any information, apparatus, method, or process disclosed in this report may not infringe privately owned rights; or

B) Assumes any liaibilities with respect to the use of, or for damages resulting from the use of any information, apparatus, method or process disclosed in this report.

As used above, "person acting on behalf of NASA" includes any employee or contractor of NASA, or employee of such contractor, to the extent that such employee or contractor of NASA, or employee of such contractor prepares, disseminates, or provides access to, any information pursuant to his employment or contract with NASA, or his employment with such contractor.

Requests for copies of this report should be referred to

National Aeronautics and Space Administration
Office of Scientific and Technical Information
Attention: AFSS-A
Washington, D.C. 20546

NASA CR-72113
LMSC-A839783

INTERIM REPORT

LIQUID PROPELLANT THERMAL CONDITIONING SYSTEM

by

W. H. Sterbentz

prepared for

NATIONAL AERONAUTICS AND SPACE ADMINISTRATION

20 April 1967

CONTRACT NAS 3-7942

Technical Management
NASA Lewis Research Center
Cleveland, Ohio
Liquid Rocket Technology Branch
Gordon T. Smith

LOCKHEED MISSILES & SPACE COMPANY
P. O. Box 504
Sunnyvale, California

FOREWORD

The Lockheed Missiles & Space Company, as prime contractor, and AiResearch Manufacturing Company, as subcontractor, are submitting this interim report as partial fulfillment of the requirements of Contract NAS 3-7942, Liquid Propellant Thermal Conditioning System, dated 26 January 1966. This work is being conducted for the National Aeronautics and Space Administration through the NASA Lewis Research Center, Cleveland, Ohio.

This program is guided by W. H. Sturbentz as Program Manager and B. R. Bullard as Assistant Program Manager. Recognition must be given to the dedicated efforts of personnel at both Lockheed and AiResearch, whose service has been invaluable in contributing to the accomplishments presented in this report. In this regard, special mention is given to Mssrs. J. Kimball and J. Ruder of AiResearch for their contributions and dedicated efforts in solving a very challenging problem.

Recognition is also given to the timely and valuable guidance, consultation, and direction provided by Mr. Gordon T. Smith as NASA, LeRC, Program Manager.

The Lockheed & Missiles Space Company and the AiResearch Manufacturing Company are indeed pleased to be conducting this program for the NASA Lewis Research Center. The technical data, results, analyses, and conclusions developed to date on this program are presented in this report.

CONTENTS

Section		Page
	FOREWORD	iii
	ILLUSTRATIONS	vii
	TABLES	xv
	SUMMARY	1
	INTRODUCTION	3
I	SYSTEMS CONCEPTS AND PARAMETRIC ANALYSES	I-1
	Systems Concepts	I-1
	Component Parametric Analyses	I-7
	Fluid Removal Unit	I-7
	Expansion Unit	I-20
	Heat Exchanger Unit	I-34
	Flow Regulator Unit	I-72
	Mixer Unit	I-74
	Symbols and Abbreviations	I-112
II	PROPELLANT MIXING REQUIREMENTS	II-1
	Symbols and Abbreviations	II-46
III	SYSTEM DESIGN METHOD	III-1
	Axial-Impulse, Turbine Driven, Compact Heat Exchanger System	III-1
	Electric Motor Driven Compact Heat Exchanger Systems	III-18
	Symbols and Abbreviations	III-27
IV	APPLICATION OF DESIGN METHOD	IV-1
	Turbine-Driven Fan, Compact Heat Exchanger System	IV-4
	Electric Motor-Driven Fan, Compact Heat Exchanger System	IV-4
	Comparison of Drive Systems	IV-15

Section		Page
V	SYSTEMS OPTIMIZATION	V-1
	Flow and Pressure Control	V-1
	Heat Exchanger and Fan Analysis	V-5
VI	SELECTED SYSTEM DESIGN AND PERFORMANCE	VI-1
	System Performance	VI-1
	Performance of the Selected System	VI-4
	Reliability	VI-8
	Method 1 – 220-Day Mission (Missions 2 and 3)	VI-8
	Method 1 – 8-Day Mission (Mission 1)	VI-17
	Method 2	VI-20
	Vehicle Integration	VI-23
	Mission Environment Considerations	VI-28
	Ground Hold Environment	VI-28
	Vent Gas Utilization	VI-32
	Cooling Supports	VI-32
	Insulation Cooling	VI-34
	Para-Ortho Conversion	VI-35
	Nonvented Oxidizer Tanks	VI-38
	Slush Hydrogen	VI-38
	Symbols and Abbreviations	VI-41
VII	REFERENCES	VII-1
Appendix		
A	VAPOR BUBBLE DETACHMENT	A-1
B	VAPOR BUBBLE CONDENSATION	B-1
C	TANK PRESSURE DECAY RATE	C-1
D	TANK PRESSURE RISE IN STRATIFIED PROPELLANT	D-1
E	SINGLE WALL-BOUND JET	E-1
F	CENTRAL OR AXIAL JET	F-1
G	TWO-DIMENSIONAL JET	G-1
H	SUBSCALE TEST PROGRAM	H-1
Distribution List		DL-1

ILLUSTRATIONS

Figure		Page
I-1	Liquid Propellant Thermal Conditioning Schematic	I-1
I-2	Thermal Conditioning Concepts	I-4
I-3	Wick-Type Liquid Removal Unit	I-9
I-4	Principle of Operation of Wick Device	I-9
I-5	Capillary-Standpipe Liquid Removal Unit Weight	I-11
I-6	Electrode Configurations – Dielectrophoretic Device	I-13
I-7	Dynamic Separator Impeller	I-15
I-8	Centrifugal Separator Rotor Diameter	I-17
I-9	Separation Efficiency as a Function of Fluid Quality	I-19
I-10	Separator Power Requirements	I-21
I-11	Schematic of Continuous-Operating Expansion Valve	I-22
I-12	Expansion Valve Weight	I-24
I-13	Expansion Valve Size	I-24
I-14	Schematic of Intermittent-Operating Expansion Valve	I-26
I-15	Operation of Belleville Spring	I-27
I-16	Pressure Regulator	I-30
I-17	Influence of Tank Pressure and Throttling Valve Pressure Drop on Temperature Drop	I-32
I-18	Influence of Tank Pressure and Throttling Valve Pressure Drop on Fluid Quality at Heat Exchanger Inlet	I-33
I-19	Heat Transfer Coefficients for Annular Flow	I-35
I-20	Heat Transfer Coefficients for Mist Flow	I-36
I-21	Thermodynamic Path Through Expansion Valve and Heat Exchanger	I-38
I-22	Effect of Valve Pressure Ratio on Heat Exchanger Size	I-39
I-23	General Configuration of Counterflow Heat Exchanger	I-40
I-24	Heat Transfer Coefficient for Gaseous Helium	I-42
I-25	Heat Transfer Coefficient for Gaseous Hydrogen	I-43

Figure		Page
I-26	Heat Transfer Coefficient for Liquid Hydrogen	I-44
I-27	Heat Exchanger Weight	I-46
I-28	Heat Exchanger Size	I-47
I-29	Heat Exchanger Hot-Side Pressure Drop (With Helium)	I-48
I-30	Heat Exchanger Weight (With Liquid Hydrogen)	I-49
I-31	Heat Exchanger Size (With Liquid Hydrogen)	I-50
I-32	Heat Exchanger Warm Side Pressure Drop (With Liquid Hydrogen)	I-51
I-33	Typical Tank-Wall Heat Exchanger Design – Mission (2) Vehicle	I-53
I-34	Dimensionless Heat Transfer Rates in a Tank-Wall Heat Exchanger	I-57
I-35	Comparison of Experimental and Predicted Convection Coefficient for Forced Convection Saturated Nucleate Boiling of Hydrogen (Using Chen's Correlation)	I-58
I-36	Influence of Vent Fluid Rate and Tube Diameter on Cold-Side Heat Transfer Coefficients (Hydrogen Gas Flow)	I-59
I-37	Dimensionless Tank-Wall Heat Exchanger Tube Length	I-61
I-38	Integrated Two-Phase Pressure Drop Parameter	I-65
I-39	Effect of Tank Pressure and Valve Discharge Pressure on Tank-Wall Heat Exchanger Weight (Tank Area = 5600 Sq Ft)	I-66
I-40	Effect of Tank Pressure and Valve Discharge Pressure on Tank-Wall Heat Exchanger Weight (Tank Area = 600 Sq Ft)	I-66
I-41	Effect of Tank Pressure and Valve Discharge Pressure on Tank-Wall Heat Exchanger Weight (Tank Area = 200 Sq Ft)	I-67
I-42	Effect of Heat Transfer Coefficients on Tank-Wall Heat Exchanger Weight (Tank Area = 200 Sq Ft)	I-67
I-43	Internal Shroud Weight – Mission (1) Vehicle	I-69
I-44	Internal Shroud Weight – Mission (2) Vehicle	I-70
I-45	Internal Shroud Weight – Mission (3) Vehicle	I-71
I-46	Solenoid Valve	I-73
I-47	Mixer Specific to Rotational Speed Ratio	I-75
I-48	Efficiency Characteristics of Various Mixer Types	I-76
I-49	Rotational and Specific Speed Chart	I-78
I-50	Mixer Tip Speed and Rotor Diameter	I-80
I-51	Mixer Unit Power Requirements	I-81

Figure		Page
I-52	Weight of Electric Motors	I-83
I-53	Volume of Electric Motors	I-84
I-54	Efficiency of Electric Motors	I-85
I-55	Heat Input to Tank Fluid	I-87
I-56	Performance of Production Model Brushless DC Motor	I-88
I-57	Various Types of AiResearch Turbines	I-90
I-58	Conical Overlapping Foil Bearing	I-94
I-59	Estimated Performance Characteristics of Small High-Speed Turbines	I-97
I-60	Estimated Performance of Impulse Turbine	I-98
I-61	Thermodynamic Characteristics of Saturated Hydrogen	I-101
I-62	Estimated Turbine-Drive Characteristics	I-103
I-63	Estimated Turbine-Drive Characteristics	I-104
I-64	Estimated Turbine-Drive Characteristics	I-105
I-65	Estimated Turbine-Drive Characteristics	I-106
I-66	Estimated Turbine-Drive Characteristics	I-107
I-67	Estimated Turbine-Drive Characteristics	I-108
I-68	Typical Impulse Turbine Off Design Torque-Speed-Power Characteristics	I-109
I-69	Typical Off Design Turbine-Drive Characteristics	I-110
II-1	Forced Convection Requirements to Suppress Liquid Hydrogen Boiling on a Tank Wall	II-3
II-2	Experimental Pool Boiling of Hydrogen	II-4
II-3	Local Velocity Required to Detach Hydrogen Vapor Bubbles in a Zero-Gravity Field	II-6
II-4	Mission (2) Vehicle Slosh Baffle Requirements	II-6
II-5	Comparison of Nusselt Correlation with Experimental Steam Data	II-8
II-6	Vapor Condensation Correlations, 0 g and 1 g	II-10
II-7	Tank Pressure Response – Mission (1) Vehicle	II-13
II-8	Tank Pressure Response – Mission (2) Vehicle	II-14
II-9	Tank Pressure Response – Mission (3) Vehicle	II-15
II-10	Tank Pressure Rise Rate With Only Ullage Heating (Ratio of Ullage Volume to Tank Volume Equals 0.05)	II-17
II-11	Valve-Closed-Position Duration for 0- and 220-Day Times After Launch	II-19

Figure		Page
II-12	Amount of Hydrogen Expelled During Valve Opening for 0- and 220-Day Times After Launch	II-20
II-13	Valve-Open-Position Duration of 0 Days After Launch	II-21
II-14	Valve-Open-Position Duration at 220 Days After Launch	II-22
II-15	Velocity and Heat Transfer Coefficients in a Wall-Bound Axisymmetric Jet	II-26
II-16	Single Wall-Bound Jet Degradation, Reynolds Number = 10,000	II-27
II-17	Single Wall-Bound Jet Degradation, Reynolds Number = 1,000	II-28
II-18	Single Wall-Bound Jet Degradation, Reynolds Number = 100	II-29
II-19	Effect of Jet Reynolds Number on Wall-Bound Jet Degradation (Radius Ratio, $R/\delta_{m_o} = 300$)	II-30
II-20	Effect of Jet Reynolds Number of Wall-Bound Jet Degradation (Radius Ratio $R/\delta_{m_o} = 200$)	II-31
II-21	Wall Jet Velocity Loci in Spherical LH_2 Tank	II-32
II-22	Magnitude of Velocities Along Loci of Maximum Velocity Profile in Spherical LH_2 Tank With a Wall Jet	II-33
II-23	Theoretical Mixer Jet Velocity Requirements in Zero Gravity for Complete Circulation	II-36
II-24	Two-Dimensional Flow Test Apparatus	II-37
II-25	Comparison of Theory With Experimental Data for Mixing by an Axial Jet (Two-Dimensional Apparatus	II-39
II-26	Typical Liquid-Ullage Patterns With an Axial Jet	II-41
II-27	Two-Dimensional Flow Test Apparatus With A Single-Wall Bound Jet	II-42
II-28	Jet Velocities Required to Break Through a Gas Bubble Located Behind a Given Baffle in the Two-Dimensional Test Apparatus	II-43
II-29	Typical Liquid-Ullage Patterns With a Single Wall-Bound Jet	II-44
III-1	Typical System Weight Curve, Turbine Drive System	III-2
III-2	Dynamic Separator Power Requirement	III-3
III-3	Fan Power Requirement	III-4
III-4	Axial-Impulse Turbine Output Power	III-5
III-5	Typical Turbine Output and Fan Input Power Matching Characteristic	III-6
III-6	Dynamic Separator Weight (Inlet Quality = 0.9)	III-7
III-7	Expansion Valve Weight	III-8

Figure		Page
III-8	Heat Exchanger Weight	III-9
III-9	Heat Exchanger Flow Ratio	III-10
III-10	Heat Exchanger Fan Weight	III-11
III-11	Turbine Weight – High Inlet Pressures	III-12
III-12	Turbine Weight – Low Inlet Pressures	III-13
III-13	Normalized Fan – Work Weight Penalty	III-14
III-14	Mission (2) Fan Work Weight Penalty	III-17
III-15	Typical System Weight Curves, Motor Drive	III-18
III-16	Electrical Motor Input and Output Power	III-20
III-17	Electrical Power System Weight Penalty	III-21
III-18	Mission (2) Electrical Power System Weight	III-22
III-19	Brushless DC Motor Weight	III-23
III-20	Normalized Motor Energy Weight	III-25
III-21	Mission (2) Motor Energy Weight	III-26
IV-1	Effect of Liquid or Gas Removal on Helium System and Boiloff Weights (Mission 2)	IV-3
IV-2	Mission (1) System Weight Comparison, Turbine Drive	IV-5
IV-3	Mission (2) System Weight Comparison, Turbine Drive	IV-6
IV-4	Mission (3) System Weight Comparison, Turbine Drive	IV-7
IV-5	Mission (2) System Weight, Turbine Drive (P_2 = 2 psia)	IV-8
IV-6	Mission (2) System Weight, Turbine Drive (P_2 = 4 psia)	IV-9
IV-7	Mission (2) System Weight, Turbine Drive (P_2 = 8 psia)	IV-10
IV-8	Mission (2) System Weight, Turbine Drive (P_2 = 10 psia)	IV-11
IV-9	Mission (1) System Weight Comparison, Motor Drive	IV-12
IV-10	Mission (2) System Weight Comparison, Motor Drive	IV-13
IV-11	Mission (3) System Weight Comparison, Motor Drive	IV-14
IV-12	Mission (2) System Weight, Motor Drive (P_2 = 2 psia)	IV-16
IV-13	Mission (2) System Weight, Motor Drive (P_2 = 4 psia)	IV-17
IV-14	Mission (2) System Weight, Motor Drive (P_2 = 8 psia)	IV-18
IV-15	Mission (2) System Weight, Motor Drive (P_2 = 10 psia)	IV-19
IV-16	Mission (2) Weight Comparison of Turbine- and Motor-Driven Systems	IV-20

Figure		Page
IV-17	Typical Speed Torque Characteristics for Drive Systems	IV-23
V-1	Pressure and Flow Control Methods	V-3
V-2	Optimum Thermal Conditioning System Vent Flow Rate for Three Missions (Battery Power Source)	V-12
V-3	Optimum Thermal Conditioning System Vent Flow Rate for Three Missions (Fuel Cell Power Supply)	V-13
VI-1	Thermal Conditioning System	VI-2
VI-2	Absolute Pressure Regulating Valve	VI-3
VI-3	Solenoid Shutoff Valve	VI-3
VI-4	Pressure Switch	VI-5
VI-5	Fan and Motor	VI-5
VI-6	System Performance	VI-6
VI-7	Heat Exchanger Characteristics	VI-7
VI-8	System Reliability Improvement With Redundant Units	VI-10
VI-9	Probable Frequency of Operation	VI-12
VI-10	Quadredundant Arrangement of Solenoid Valves	VI-15
VI-11 a	Recommended Redundant System for Missions (2) and (3)	VI-21
VI-11 b	Totally Redundant System (8-Day Lunar Missions)	VI-22
VI-12	Tank Assembly With Thermal Conditioning System	VI-24
VI-13	Maximum Pressure Spike at Engine Cutoff	VI-25
VI-14a	Tank Pressure History for Mission (2) Vehicle (Stratified Model)	VI-29
VI-14b	Tank Pressure History for Mission (2) Vehicle (Mixed Model)	VI-29
VI-15	Thermal Conditioning System Vent and Checkout Schematic	VI-31
VI-16	Flight Vent Electrical Schematic	VI-33
VI-17	Calculated Heat Leak Through Tank Support System, Mission (2) Vehicle	VI-34
VI-18	Effect of Heat Exchanger Position Within Insulation	VI-35
VI-19	Heat Resulting From Conversion of Parahydrogen to Equilibrium Hydrogen	VI-36
VI-20	Temperature-Enthalpy Relationship for Hydrogen at 1 Atmosphere	VI-37
VI-21	Percent Usable Hydrogen vs Mission Duration (50 Percent Slush)	VI-39
E-1	Glauert's Figure 3 – Turbulent Wall Jet Parameters	E-7
E-2	Curve Fit to Glauert's Results for Turbulent Wall Jet	E-8

Figure		Page
H-1	Two-Dimensional Flow Test Apparatus	H-2
H-2	Modified 2-D Flow Test Apparatus	H-12
H-3	Jet Velocities Required to Break Through a Gas Bubble Located Behind a Given Baffle in the Two-Dimensional Test Apparatus	H-14
H-4	Typical Liquid-Ullage Patterns With a Single Wall-Bound Jet	H-15

TABLES

Table		Page
I-1	Parameters for Analysis	I-5
I-2	Weights of Dielectrophoretic Liquid-Removal Units (Complete Propellant Orientation)	I-14
V-1	Heat Exchanger Design and Performance Data	V-6
V-2	Fan-Motor Performance	V-8
V-3	Reference Mission Flow Rates	V-9
V-4	System Characteristics (Flow-Matched Systems)	V-11
V-5	System Characteristics (Comparison of Flow-Matched and Minimum-Effective-Weight Systems)	V-14
H-1	Experimental Circulation Data	H-4

SUMMARY

For cryogenic propellants to be used efficiently in long-duration missions, the propellant tanks must be vented during zero-gravity coast periods. A venting system concept has been defined that will efficiently control the tank pressures during these periods, in spite of the uncertain location of the ullage or liquid propellant, by venting vapor overboard. In this concept, referred to as a liquid propellant thermal conditioning system, tank fluid is extracted, expanded to a lower temperature and pressure, and passed through a heat exchanger where it absorbs heat from the bulk propellant and the ullage in the tank. This cooling of the tank contents and gas venting results in a desired tank pressure reduction. This program was formulated to investigate the effectiveness of the thermal conditioning system concept for cryogenics tank pressure control.

During this investigation, potential component candidates were defined for use as fluid removal units, expansion units, heat exchanger units, and propellant mixer units. Parametric performance data were developed for these components and are presented in this report. Also, criteria for establishing propellant mixing requirements were derived and are included.

These parametric data and mixing criteria were applied to three reference missions and an optimum thermal conditioning system was defined for the liquid hydrogen tank on each. This flight system consists of:

- Fluid removal unit
- Pressure regulator (expansion unit)
- Compact heat exchanger
- Mixer with dc brushless motor drive
- Solenoid shutoff valve
- Pressure switch

The three missions involved a wide spectrum of vehicle sizes and propellant heating rates, but the same thermal conditioning system was optimum for each. It weighs approximately 15 pounds and can be preassembled onto a 14-inch diameter plate. The motor power consumption is only 2.3 watts when operating, resulting in less than 14 pounds of boiloff for the longest missions (220 days). The brushless dc motor was selected for the mixer drive because of the predicted low power consumption, although brushless dc motors suitable for use in liquid hydrogen are not currently available.

The selected system, with the exception of the motor drive, is being fabricated and will be demonstrated in ground-based tests in a full-scale, 9-foot diameter liquid hydrogen tank. For the test hardware, an ac induction motor is being substituted for the dc brushless motor. This unit was available at low cost and was designed for and has been qualified in liquid hydrogen. It will have a power consumption of 14 watts at the design conditions for the liquid propellant thermal conditioning system.

INTRODUCTION

In the past, cryogenic propellants and their inherently superior performance capability were considered and discarded for long-duration space propulsion systems, such as the Saturn V Apollo Service Module and the Lunar Module, due to uncertainties with respect to the space storability and usability of liquid hydrogen. Liquid hydrogen and liquid oxygen propellants and their high-performance potential were, however, accepted for the Saturn V launch vehicle stages since the special means to store cryogenic propellants in these booster stages were required only to withstand ground hold, launch, ascent environments, and related short flight time. Relatively simple foam-type insulations and ullage volume venting systems have proved effective in containing and venting the volatile cryogens during these short flight times.

In the application of cryogens to long-duration space flight missions, a problem requiring solution involves the venting of propellant vapor during zero or low-gravity coast periods. In a zero- or low-gravity flight environment, the location and movement of the liquid propellant in the tank is uncertain. As a result, venting of the tank through the ground hold vent system is unreliable and at best very inefficient because of the very likely ingestion of large amounts of liquid hydrogen which would be vented directly overboard. Prolonged venting of propellant in such a manner will cause a loss of the mission because of dissipation of propellant and consumption of attitude control propellants to correct for large variations and unbalances in vehicle motions induced by the vent system.

A venting system concept has been defined that will avoid these difficulties. This concept, a liquid propellant thermal conditioning system, maintains tank pressure control through the extraction of either liquid or gaseous hydrogen (and helium gas if present) and utilization of the heat transport properties of this extracted fluid. By passing this

extracted fluid through a high-pressure drop valve, the resulting refrigerated vapor when passed through a heat exchanger can be used to efficiently absorb heat from the bulk propellant and ullage in the propellant tank. This chilling of the fluid contents causes some condensation of ullage gases with a concomitant drop in tank pressure. The refrigerated vapor upon passing through the heat exchanger is converted into a saturated or supersaturated gas and is vented from the propellant tank. The system, in principle, may be operated either intermittently or continuously.

Many configurations of the basic concept are possible. The program described and the results presented in this interim report are addressed to creating a design based upon this concept of a light-weight, reliable, and efficient vent system for the liquid hydrogen tank of long-duration flight space propulsion systems. Three missions and vehicles were selected to which candidate vent systems were applied and analyzed. The data developed are also presented in parametric form to permit their application to other vehicles and missions.

The program is divided into five tasks:

Task I — System Design Concepts and Analysis
Task II — Optimization of System Designs
Task III — Mixing Requirements Evaluation and Test of the Mixer Unit
Task IV — Design, Fabrication, and Testing the Thermal Conditioning Unit
Task V — Evaluation of System Fabrication and Test Data

This interim report presents the design, data, results, evaluations, and conclusions from the completed activities of Task I, II, and III. The report is divided into six sections. The first section contains a description of the system concepts and the parametric results of the component analyses. The second section presents criteria for establishing propellant mixing requirements. The third section describes a method for using the parametric component data in evaluating a system design for a particular mission. This method is then applied to missions (1), (2), and (3) in the fourth section; leading to the selection of a particular system. This system is then optimized in the fifth section and its performance is presented in the sixth.

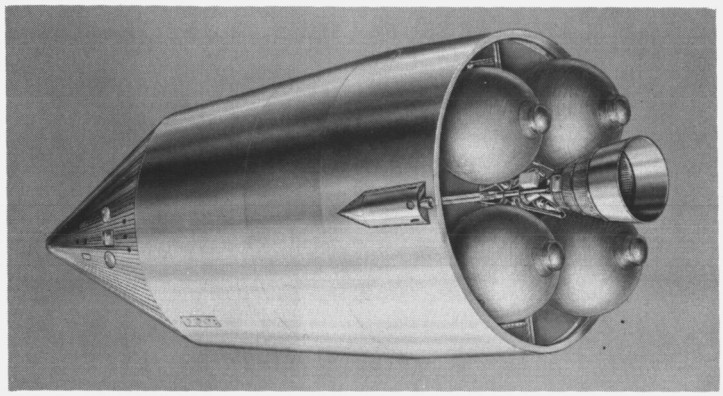

Mission (1) — Earth-Lunar Logistics Mission

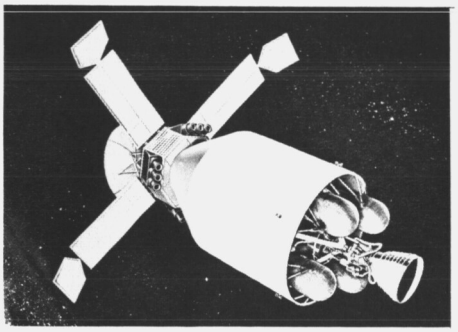

Mission (2) — Earth-Mars Kickstage Mission

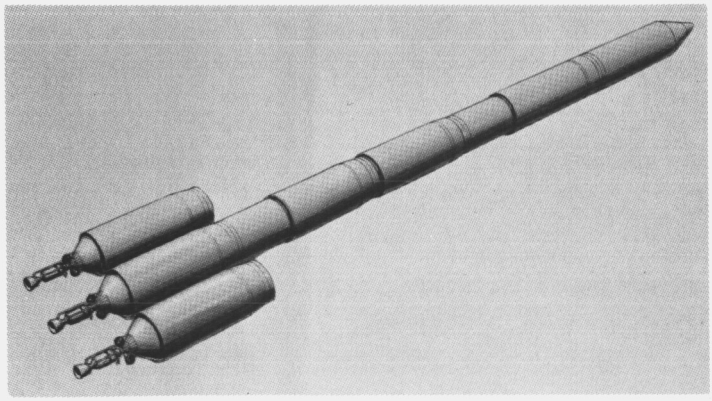

Mission (3) — Earth-Mars Manned Mission

Reference Mission Vehicles

Section I

SYSTEMS CONCEPTS AND PARAMETRIC ANALYSES

SYSTEMS CONCEPTS

The basic function of the liquid propellant thermal conditioning system is to maintain pressure control if the liquid hydrogen tank during zero- and low-gravity coast periods in space flight when location of the gas ullage region is somewhat uncertain. Control of the tank pressure is accomplished through the combined use of the five basic units listed below and shown in Fig. I-1. Figure I-1 also shows the basic thermodynamic process as applied to the vent fluid.

- Fluid removal unit
- Expansion unit
- Heat exchanger unit
- Flow control unit
- Mixer unit

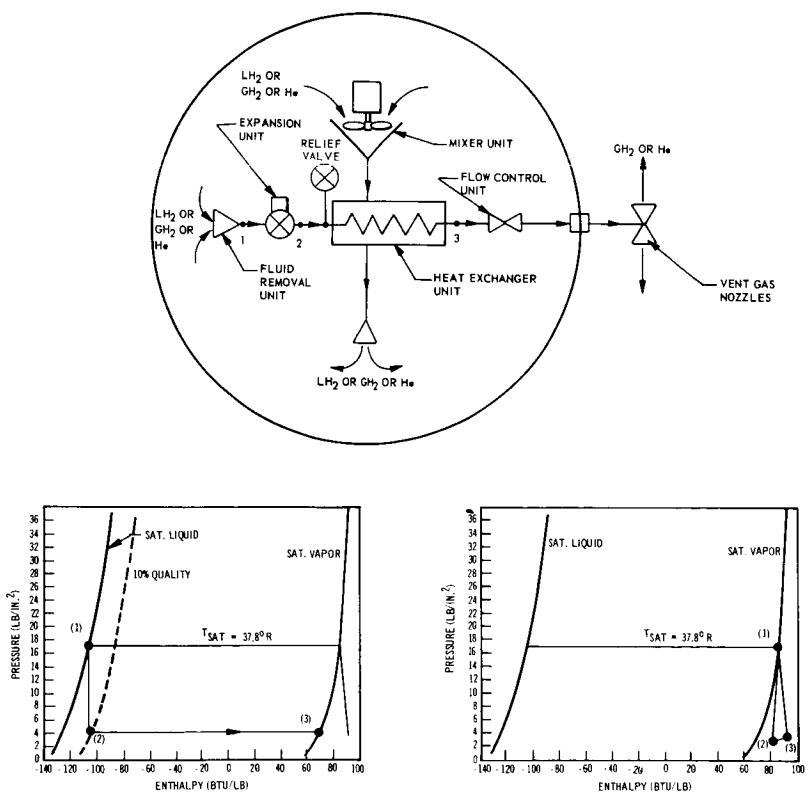

Fig. I-1 Liquid Propellant Thermal Conditioning System Schematic

The fluid removal unit provides gaseous or liquid hydrogen (State (1) on Fig. I-1) to the expansion unit and heat exchanger so that the total enthalpy change is adequate to remove heat deposited in the propellant from heat leaks through insulation, plumbing, and tank support structure.

The expansion unit lowers the pressure and temperature of the incoming fluid (State (2) on Fig. I-1). When flowing liquid hydrogen, this temperature drop provides the necessary thermal driving potential for operation of the heat exchanger. When flowing gaseous hydrogen and/or helium pressurant gas, tank pressure control is accomplished by direct venting of hydrogen boiloff and pressurant gas.

The heat exchanger unit, which may be located inside the tank or on the tank wall, allows the low pressure refrigerated vapor to remove heat from the propellant in the tank. In the process, the refrigerated vapor is converted to a saturated or superheated vapor which is then discharged from the propellant tank (State (3) on Fig. I-1).

A mixer unit may be required, and specifically will be required if the thermal conditioning system employs a compact heat exchanger located in the propellant tank. Since gravity-forced convection is absent in a zero-gravity environment, heat transfer would be limited to the conduction mode only. Consequently, fluid currents should be made to flow over the heat exchanger to increase the heat transfer rates by forced convection and maintain positive pressure control throughout the tank. It is also possible that cooled propellant drawn throughout the heat exchanger and discharged along the tank walls may effect suppression of vapor bubble formation by ensuring a sufficiently large heat transfer coefficient to remove, by forced convection, all heat entering through the tank wall. In the event that bubbles are generated on the tank wall at points of high local heating the mixer will serve to aid in the removal or detachment of vapor bubbles from the wall and ultimate vapor bubble condensation and collapse.

The flow control unit provides the system vent flow shutoff function as well as a fixed orifice flow-area. Because only gaseous hydrogen and/or helium will be present downstream on the heat exchanger cold side, a relatively constant vent flow rate will be attained during periods of tank venting.

On the basis of these system functional requirements, a large number of liquid propellant thermal conditioning system concepts may been defined. To provide a basis for component parametric data development and component matching requirements, a few possible concepts are shown in Fig. I-2.

The conceptual systems serve to identify the components that are to be analyzed parametrically. A list of the important parameters is shown in Table I-1. These parametric data can be used to arrive at optimized systems with matched components for many missions of interest. The independent parameters were studied over the range indicated by the data in the right-hand column.

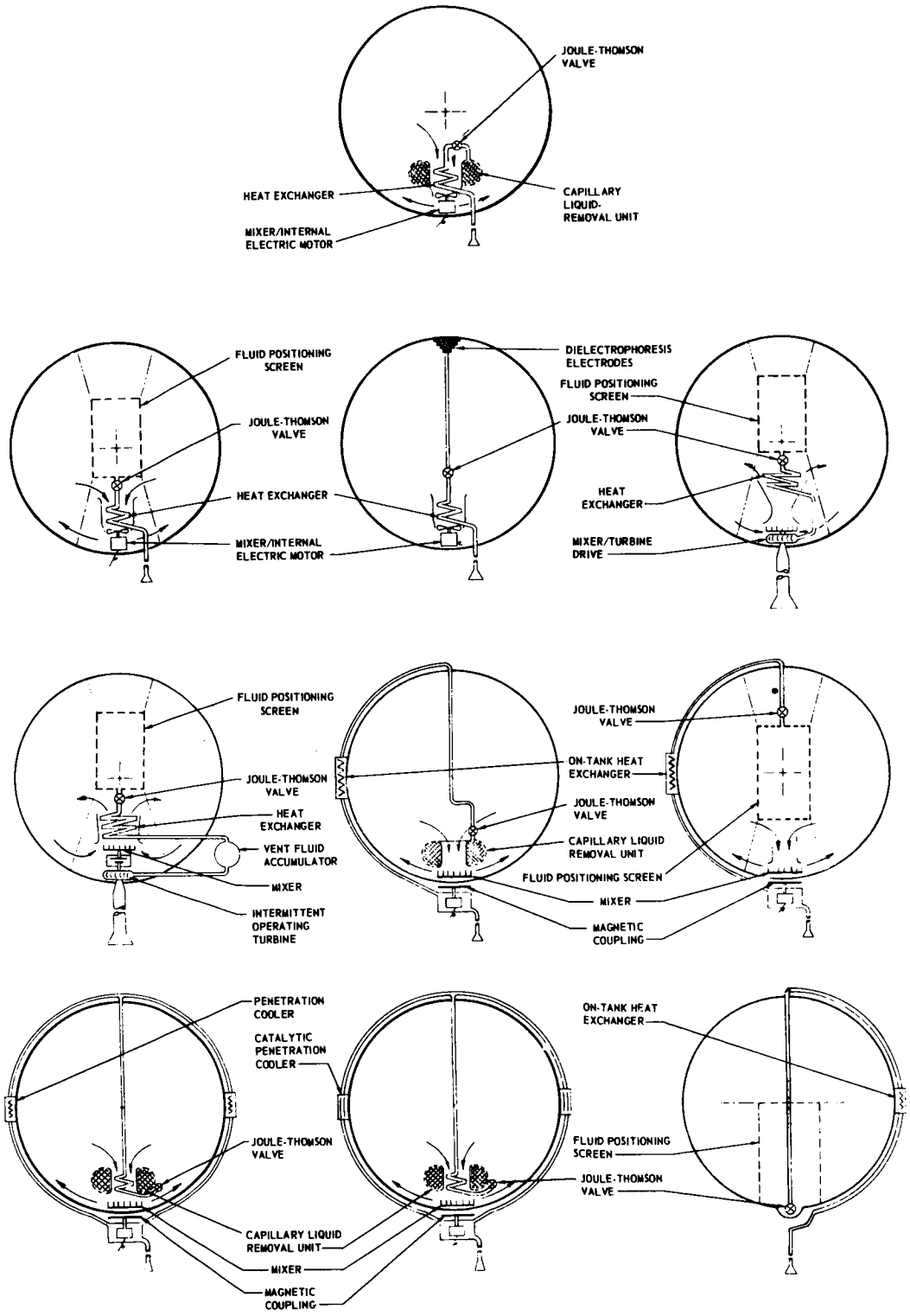

Fig. I-2 Thermal Conditioning Concepts

Table I-1

PARAMETERS FOR ANALYSIS

Component	Dependent Parameter	Independent Parameter	Range of Independent Parameter
Fluid Removal Units			
• Capillary standpipe	Pike dimensions	Minimum ullage volume	> 5%
		Tank diameter	0-30 ft
	Weight	Tank diameter	0-30 ft
		Tank height	0-60 ft
		Minimum ullage	5%
• Wicking device	Weight	Tank height	0-60 ft
		Gravity level	10^{-3}-10^{-15} g/g_o
• Dynamic separator	Weight	Inlet fluid quality	0-90%
	Dimensions	Vent flow rate	0-60 lb/hr
	Power	Separation efficiency	0-100%
• Dielectrophoretic device	Number of electrodes	Voltage	50-200 kv
		Electrode spacing	0-2 in.
		Ullage volume	5-60%
	Weight	Tank height	0-60 ft
		Electrode spacing	0-2 in.
		Voltage	50-200 kv
• Fluid filter	Weight	Flow rate	0-60 lb/hr
Expansion Units			
• Valves	Maximum temperature differential	Valve pressure drop	0-160 psi
	Vent fluid quality into heat exchanger		0-100%
	Weight	Pressure drop	0-160 psi
	Size	Vent fluid flow rate	0-60 lb/hr
		Tank pressure	0-188 psi
Heat Exchanger Units			
• Tank-wall heat exchanger	Cold-side heat transfer coefficients	Vent fluid flow rate	0-60 lb/hr
		Tube size	1/16-1 in.
	Vent fluid pressure drop	Fluid quality	0-100%
		Fluid pressure	4-150 psi

Table I-1 (Cont.)

Component	Dependent Parameter	Independent Parameter	Range of Independent Parameter
	Tube attachment spacing	Tank thickness	0.03-0.2 in.
		Maximum heat flux	10 Btu/hr-ft^2
	Weight	Tube size	1/16-1 in.
		Tank radius	0-15 ft
		Maximum heat flux	10 Btu/hr-ft^2
		Expansion fluid temperature drop	0-30°R
		Tank pressure	0-150
• Compact heat exchanger	Warm-side coefficients	Circulation velocity	0-25 ft/sec
	Weight	Vent fluid flow rate	0-60 lb/hr
	Dimensions	Total heating rate	0-5000 Btu/hr
		Inlet quality	0-100%
		Circulation velocity	0-25 ft/sec
	Vent fluid pressure drop	Vent fluid flow rate	0-60 lb/hr
		Inlet quality	0-100%
		Heat exchanger volume	0-300 in.^{3}
Flow Control Unit			
• Valve	Weight	Flow rate	0-60 lb/hr
Mixer Unit			
• Impeller	Weight	Bulk fluid circulation rate	0-1500 lb/hr
	Diameter	Bulk fluid quality	0-100%
	Power input		
• Electric motors	Diameter	Power output	0-100 w
	Weight	Motor type	
• Turbine	Weight	Vent flow rate	0-60 lb/hr
	Diameter	Inlet pressure	10-50 psia
	Power output	Pressure ratio	5-100
		Efficiency	0-80%

COMPONENT PARAMETRIC ANALYSES

Fluid Removal Unit

A liquid propellant thermal conditioning system design may be based upon one of two premises: (1) that the system will effectively control the liquid hydrogen tank pressure only by withdrawing liquid hydrogen from the tank, or (2) that the system will effectively control tank pressure by withdrawal of either liquid hydrogen or gas mixtures of hydrogen and helium. Under the first premise, the fluid-removal unit must be designed to always withdraw liquid hydrogen during the vent cycle or over-pressurization of the tank and even catastrophic rupture may occur. Under the second premise, the fluid-removal unit is a small and simple fluid filter placed ahead of the intake port of the expansion unit. The only function of this filter is to remove foreign particles such as crystals or dirt which, if allowed to enter the expansion unit port, might cause clogging and flow restriction with its obvious undesired consequences.

A system based upon withdrawal of only liquid hydrogen has one possible advantage over systems operable upon any mixture of liquid or gas. This advantage is manifested in the retention of helium pressurant gas during tank venting. As will be fully discussed in later sections of this report, a smaller total helium pressurant gas supply is required for a given mission, if such gas retention combined with a pressurization system control based upon bulk fluid temperature is possible.

A liquid removal unit to be useful must be a lightweight device that will reliably provide liquid hydrogen to the expansion unit. Therefore, to determine the feasibility of a liquid removal unit, further attention was given to the design of liquid removal devices that will always provide liquid hydrogen to the thermal conditioning system during venting. An obvious technique is the use of propellant settling rockets, but this technique is prohibitively costly of propellant consumption for any of the three missions under consideration.

The basic function of a liquid removal unit is to guarantee a sufficient rate of liquid hydrogen through the expansion unit that the total enthalpy change is equal to, or greater than, the rate at which heat is deposited in the propellant. Four concepts were evaluated:

- Wick device
- Capillary standpipe
- Dielectrophoretic unit
- Dynamic separator

Wick Device. A wick device is shown in Fig. I-3. It consists of a central perforated tube closed at both ends, a liquid absorption or wicking material, and an outer mechanical support shell which also protects against liquid sloshing or circulation loads. The central tube is the reservoir to which the expansion valve is connected. The central tube is replenished from the wicking material which extracts liquid from the main body of liquid by capillary action. This wick device must extend from one wall of the tank to the opposite wall to provide some assurance of being in contact with the liquid propellant, particularly for firing sequences as in Mission (1), where the tank is less than 5 percent full for the last firing. If the wick is dry, the device will selectively feed gas from the tank to the expansion unit.

The process of drawing only liquid hydrogen from the wicking material is based upon designing the device so that the pressure differential due to fluid dynamics across the central tube perforations is less then the equivalent restraining capillary pressure of a gas bubble attached to the central tube perforation. The desired operation of this device is illustrated in the one-dimensional sketch shown in Fig. I-4. Vapor bubbles will not pass through the screen, provided the following equation is satisfied.

$$\Delta P_f + \Delta P_L < \Delta P_B$$

Symbols used throughout this report are listed in the Table of Symbols at the end of the section in which they occur.

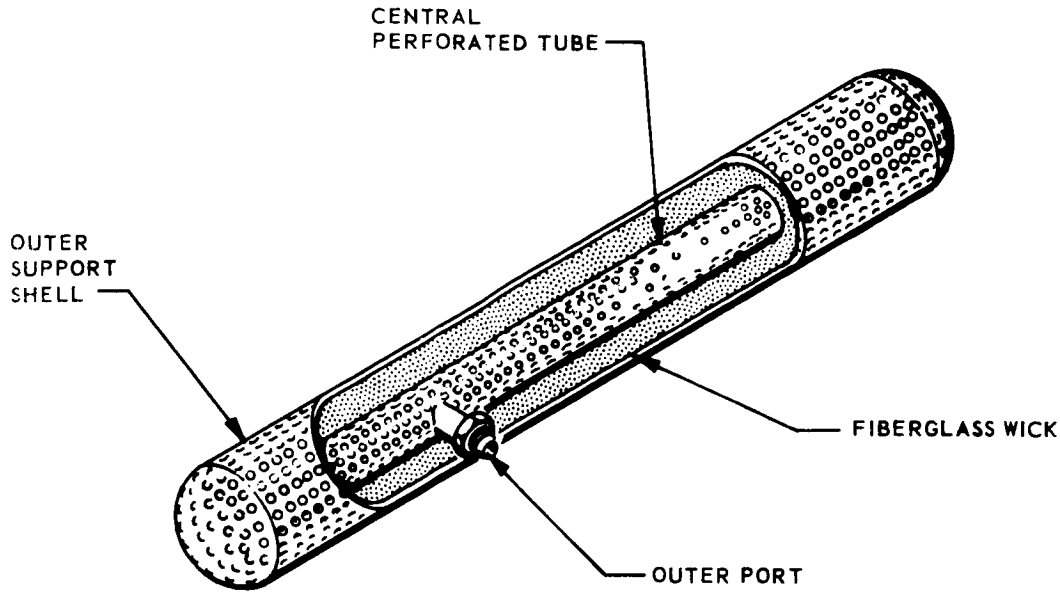

Fig. I-3 Wick-Type Liquid Removal Unit

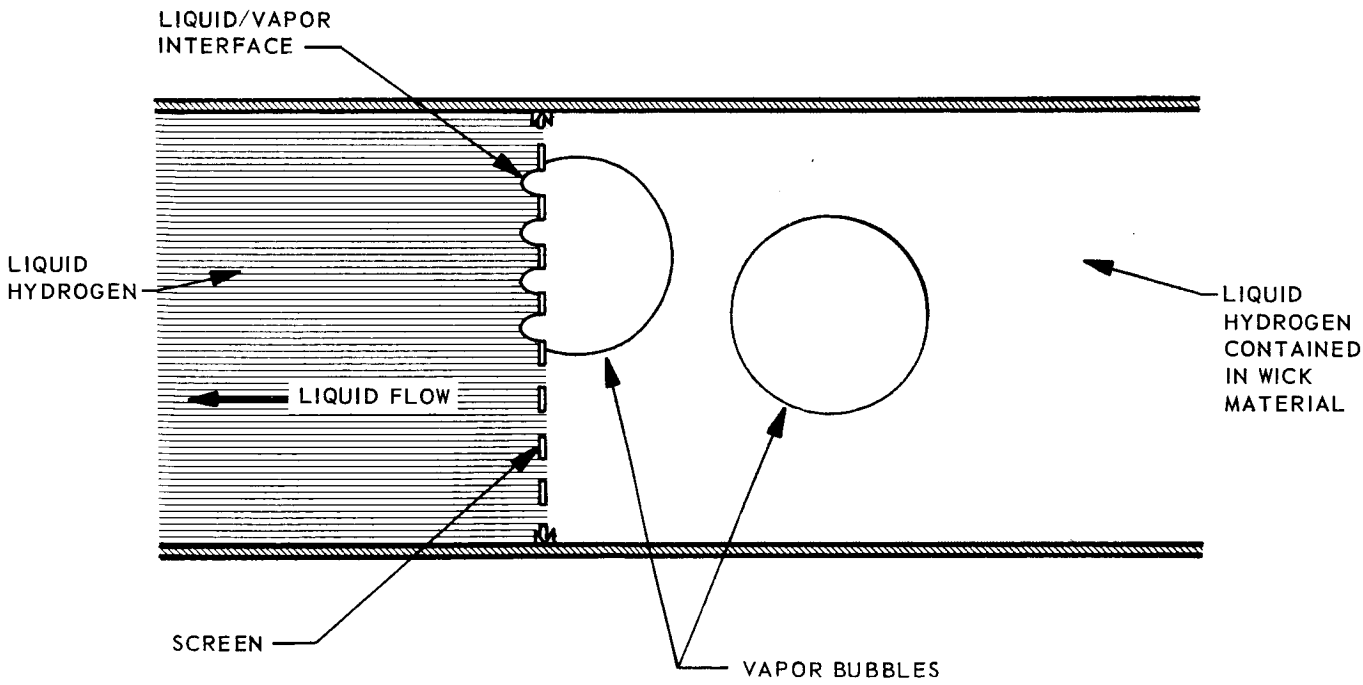

Fig. I-4 Principle of Operation of Wick Device

These quantities are expressed as:

Fluid drag through the screen,

$$\Delta P_f = \frac{\rho_L U^2}{2g_c} C_D$$

Static pressure across the wick,

$$\Delta P_L = \rho_L \left(\frac{g}{g_c}\right) L$$

Capillary pressure across vapor-liquid interface,

$$\Delta P_B = \frac{\sigma \Phi}{g_c R_s}$$

If, however, vapor is present inside the central tube and dries the inside surface, vapor will preferentially pass through the central tube. It is essential, therefore, that the volume enclosed by the central tube be completely void of vapor at all times. Such a condition cannot always be expected, and the unit would then fail to provide liquid hydrogen to the thermal conditioning system. This failure situation is likely to occur during venting when liquid hydrogen saturated at tank pressures higher than the vent cycle shutoff pressure may be present in the reservoir tube. The drop in tank pressure during venting and even the pressure drop across the perforations would cause boiling of the saturated liquid in the reservoir tube. The drying action of the boiling process may result in the selective feeding of gas from the tank to the expansion unit. For these reasons, this device is not recommended for use in a thermal conditioning system.

Capillary Standpipe. The equilibrium configuration of liquid hydrogen in a tank with a capillary standpipe in a zero-gravity environment can be predicted analytically. These predictions have been verified by liquid-liquid tests, drop tower tests, zero-gravity aircraft tests, and Aerobee ballistic rocket tests.

Surface tension in the liquid hydrogen forming the curved meniscus will cause a capillary pressure drop across the liquid/vapor interface. It is this capillary pressure drop that draws the liquid hydrogen into the standpipe. This column of liquid in the standpipe will remain stably positioned unless a sufficiently adverse acceleration is applied. Stability analyses indicate that liquid in the tank will probably remain stable unless the Bond number, based upon tank radius, is greater than approximately 0.1. From experiments conducted to date, the most stable condition occurs if the standpipe diameter is about 25 percent of the tank diameter and extends about 80 percent across the tank. For these conditions, the weight of the capillary standpipe is given by

$$W = 1.256\ R\ L\ (\rho\ \delta)$$

For the vehicles of interest in this program, an aluminum standpipe with 0.013-in. walls will suffice when supported at both ends with tie rods. The weight of a capillary standpipe is shown in Fig. I-5.

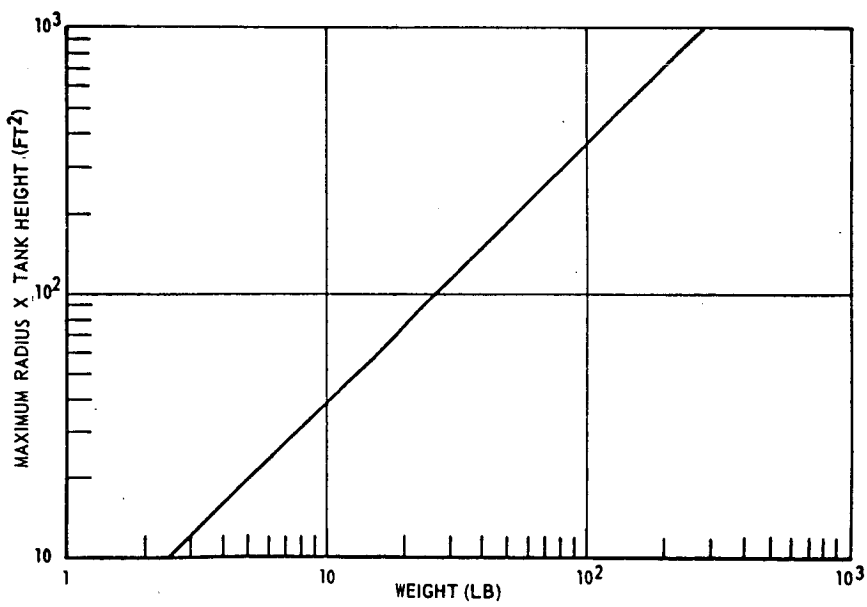

Fig. I-5 Capillary-Standpipe Liquid Removal Unit Weight

This type of liquid-removal unit will not provide stable orientation of the liuquid during accelerations greater than 10^{-7} g for the three vehicles of interest. Another limitation is that the standpipe will not provide stable orientation with a thermal conditioning system that employs a mixer. Therefore, the standpipe can be considered only for a thermal conditioning system operating continuously with a tank-wall heat exchanger without a mixer.

Dielectrophoretic Device. Another liquid removal technique is the dielectrophoretic containment device. The unit consists basically of a series of electrodes, mounted in the tank, to which a high-voltage alternating current is applied. The stability and rate at which liquid is drawn into the space between the electrodes depends on the voltage applied, electrode spacing, dielectric characteristics of the liquid and acceleration environment experienced by the vehicle.

Liquid contained within this device may be extracted by means of a drain tube between appropriate electrodes. Any vapor formed within the electrodes will be forced from the space between the electrodes by dielectrophoretic forces. However, even a dielectrophoretic device cannot be depended upon to provide liquid hydrogen at the expansion unit intake, unless the electrodes span the tank. Such a system, however, may be expected to be quite heavy relative to the weight of the other components of a thermal conditioning system and to the possible weight savings expected from reduced helium pressurant gas requirements. Calculations have been performed to provide a measure of weight of such a system. Three different electrode configurations are shown in Fig. I-6 as applied to the Mission(2) vehicle. Table I-2 presents the weights of dielectrophoretic liquid-removal units for a Mission (2) vehicle.

Obviously, complete orientation results in a large weight penalty to the venting system. Also, the reliability of the vent system is reduced, since failure of the dielectrophoretic unit may interrupt the supply of liquid hydrogen to the intake port of the expansion unit. As with a capillary standpipe, a dielectrophoretic device cannot retain liquid hydrogen when a propellant mixer is in operation. However, a dielectrophoretic device provides some degree of propellant mixing through expulsion of vapor bubbles from the electrodes.

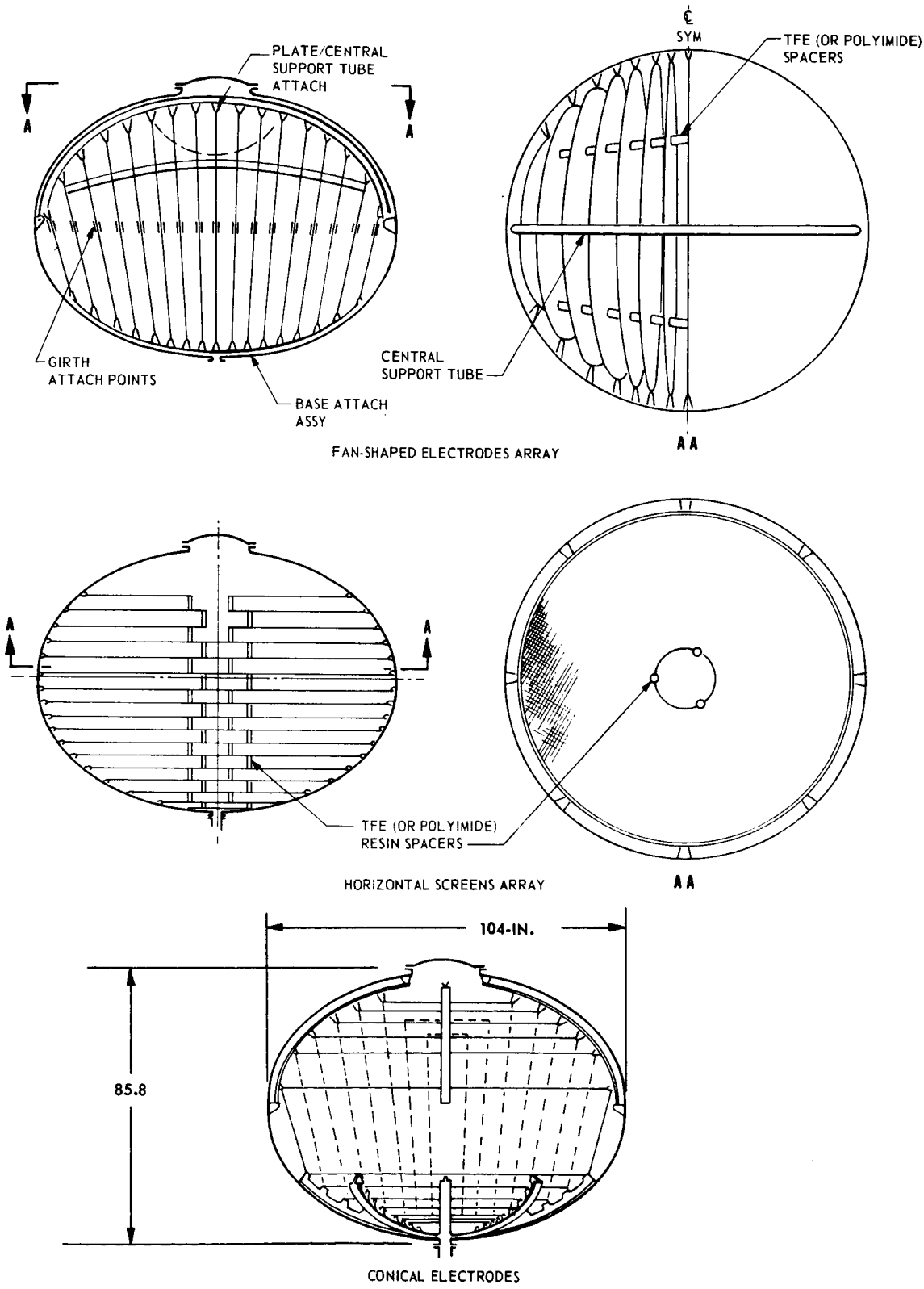

Fig. I-6 Electrode Configurations – Dielectrophoretic Device

Table I-2

WEIGHTS OF DIELECTROPHORETIC LIQUID-REMOVAL UNITS
(COMPLETE PROPELLANT ORIENTATION)

Geometry	Electrode Area (ft^2)	Weight (lb)	Estimated Power Supply (lb)	System Weight (lb)
Horizontal	787	69.5	12.0	81.5
Vertical fan	633	66.3	12.0	78.3
Cone frustum	503	51.0	12.0	63.0

It is significant to note here that a dielectrophoretic device providing for full propellant orientation permits the use of conventional ullage gas vent systems. It should also be noted that operation of a dielectrophoretic device has not been demonstrated in liquid hydrogen. Until extensive experimental evaluation of such devices in liquid hydrogen has been conducted, all conclusions concerning the effectiveness of the device are theoretical. Based upon these factors, a dielectrophoretic device is not recommended for the thermal conditioning system; although, it theoretically offers a means for continuously supplying liquid hydrogen to the expansion unit.

Dynamic Separators. The liquid removal unit considered here is a dynamic separator. The fluid entering the separator will be in a saturated state; any energy imparted to the fluid will tend to vaporize the liquid. To ensure bubble-free liquid delivery from the unit, the use of a centrifugal separator which causes the vapor bubbles to collapse (condense) was considered. The bubble collapse is caused by increasing the static pressure in the centrifugal field above the vapor pressure inside the bubble. Any uncollapsed hydrogen bubbles or any helium gas will be forced toward the center of the unit for removal. The bubble-free liquid can be collected at the periphery of the unit by pitot tubes and then directed to the expansion unit. Figure I-7 shows the dynamic separator impeller.

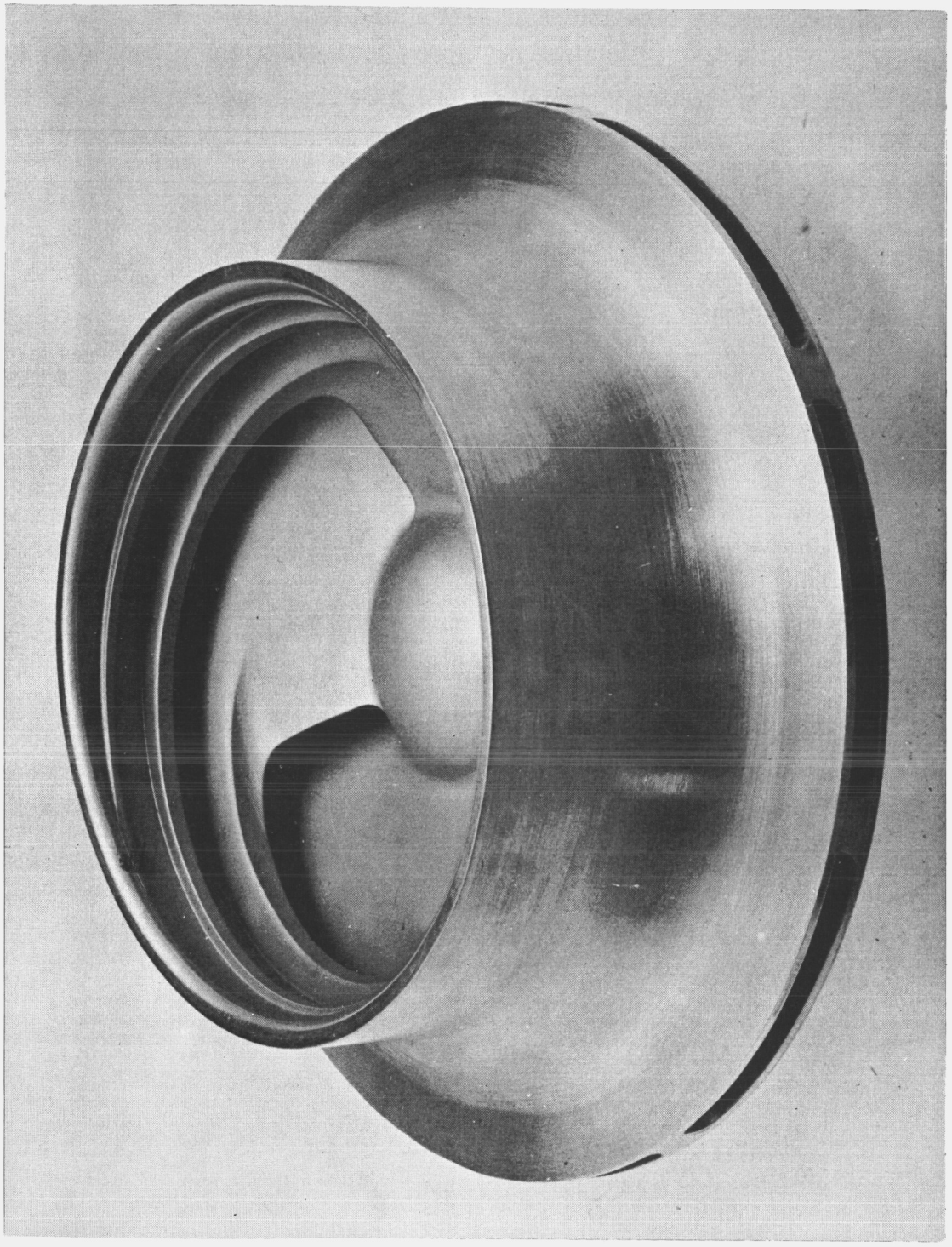

Fig. I-7 Dynamic Separator Impeller

The variables investigated were a bubble-free liquid hydrogen delivery rate of 0.02 to 60 lb/hr, tank pressures of 17 to 150 psia, and an inlet fluid quality of 0.1 to 0.9. It was estimated that the pressure required to collapse all bubbles was twice the vapor pressure by using the theoretical principles presented in references 1 and 2. The minimum rotor tip speed required to obtain the pressure that will ensure that all bubbles are collapsed is:

$$U = \sqrt{\frac{4\,g\,P_V}{\rho}}$$

The rotor size and rotational speed required to achieve the desired tip speed are shown in Fig. I-8. It can be seen that the rotor requirements are more severe for the higher pressures.

In bringing the liquid phase to the tangential velocity u, the energy per unit mass is u^2/g.

Accounting for a possible source of heating due to frictional losses imparted by the rotating device, we take as energy input

$$k\frac{u^2}{g}$$

This increase in energy is usually encountered in rotating equipment such as pumps and compressors. Commonly, k has the value of 1.10. If η_p is the hydraulic efficiency of the separator, i.e., the portion of energy

$$\eta_p\, k\frac{u^2}{g}$$

that goes into compressing the liquid, then the energy loss is

$$(1 - \eta_p)\, k\frac{u^2}{g}$$

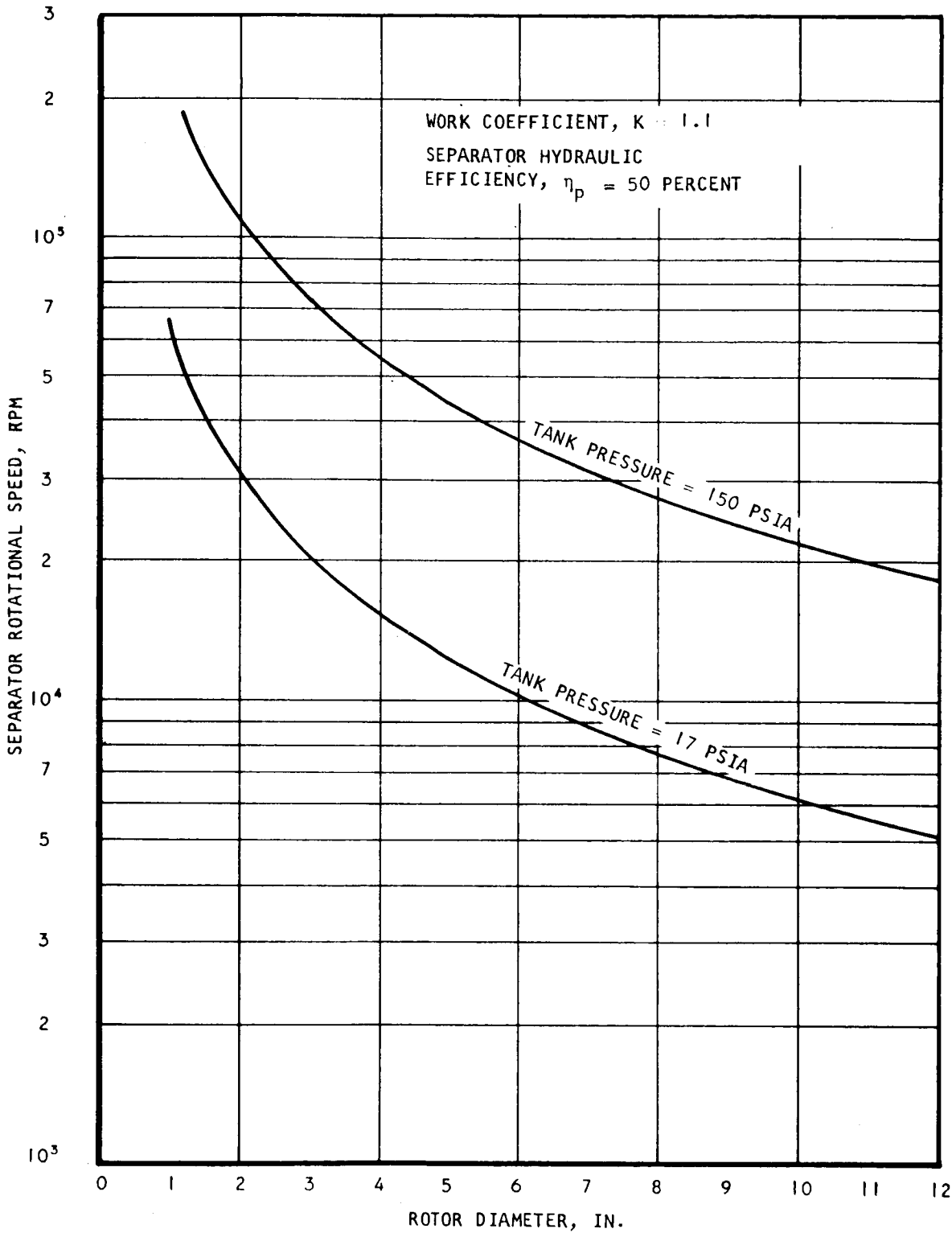

Fig. I-8 Centrifugal Separator Rotor Diameter

This energy loss goes into vaporizing a fraction of the liquid, and also to heat the vapor. For a conservative approach, the assumption is made that all the energy loss goes into vaporization of the liquid.

The amount of unvaporized liquid, free from bubble,is given in terms of the separation efficiency defined as

$$\eta_{separation} = \frac{\text{amount of liquid free from bubble per unit mass of processed liquid}}{x}$$

An energy balance yields then

$$(1 - \eta_{sep})(X)\,L = (1 - \eta_p)\,k\,\frac{u^2}{g}$$

$$\eta_{sep} = 1 - \frac{ku^2}{XLg}(1 - \eta_p)$$

or

$$\eta_{sep} = 1 - \frac{ku^2}{J(1 - X)\,Lg}(1 - \eta_p) \text{ for vapor}$$

Typical values for the work coefficiency and the hydraulic efficiency are 1.1 and 50 percent, respectively. Figure I-9 shows the separation efficiency for various inlet fluid qualities. It can be seen that the separation efficiency drops considerably as the tank pressure and fluid quality is increased. The relative amount of vapor discharged through the center of the unit, therefore, increases. This fluid could be used on the warm side of the heat exchanger. It should be noted that, at a tank pressure of 150 psia, no bubble-free liquid would be obtained at fluid qualities above 0.82. In order for the bubbles to be collapsed under this condition, heat must be removed from the processed liquid during the separation process.

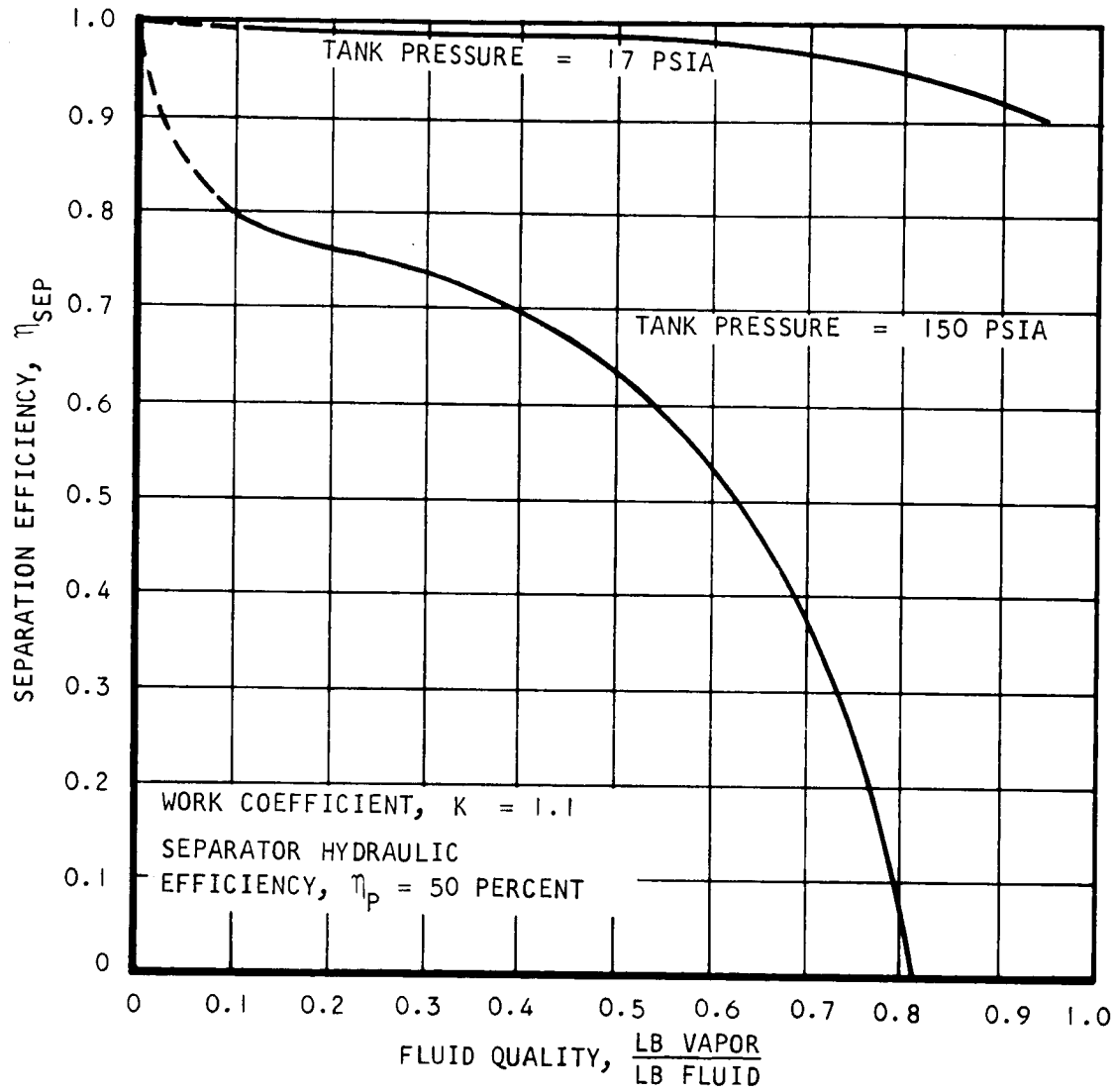

Fig. I-9 Separation Efficiency as a Function of Fluid Quality

Figure I-10 shows the minimum shaft power required to collapse the bubbles as a function of fluid quality and tank pressure. The power requirements at 150 psia are ten to a thousand times higher than at 17 psia. The power requirements at 17 psia could be met with reasonable power supply weights and the dynamic separator may be applicable if the fluid entering the unit contains some liquid. It can be seen from Fig. I-8 that the required tip speed for bubble collapse can be obtained by choosing either rotor size or speed. In any specific case, the design point will probably be chosen to obtain the highest hydraulic efficiency. This will probably result in a rotor less than 3 in. in diameter with resultant separator weights of up to 10 lb. For rotors of this diameter, a rotational speed of 20,000 to 30,000 rpm is required for the unit, which presents some difficulty in providing a suitable drive unit. However, the device may be considered for applications to liquid propellant thermal conditioning systems.

Expansion Unit

The function of the expansion unit is to reduce the pressure and temperature of the vented propellant. This low-temperature fluid can then absorb heat from the bulk of the propellant as it passes through the heat exchanger. Two concepts are considered:

- Expansion valve
- Expansion turbine

Expansion Valve. To make a realistic parametric evaluation of expansion valve weight and size requirements, three valve concepts were evaluated: one for continuous flow with mass and pressure regulation, one for intermittent flow with mass and pressure regulation, and one for continuous or intermittent flow with pressure regulation only. For all concepts, the valve size was extremely small, dictated by hardware limitations rather than by flow rates or control pressure ratio requirements.

For the continuous venting concept with mass and pressure regulation, the required expansion valve is basically a very sensitive modulating relief valve. The unit considered is based primarily on an evaluation of details that incorporate features necessary to produce a trouble-free, minimum weight unit of high reliability. The valve concept evaluated parametrically is shown in Fig. I-11. The unit is a normally closed,

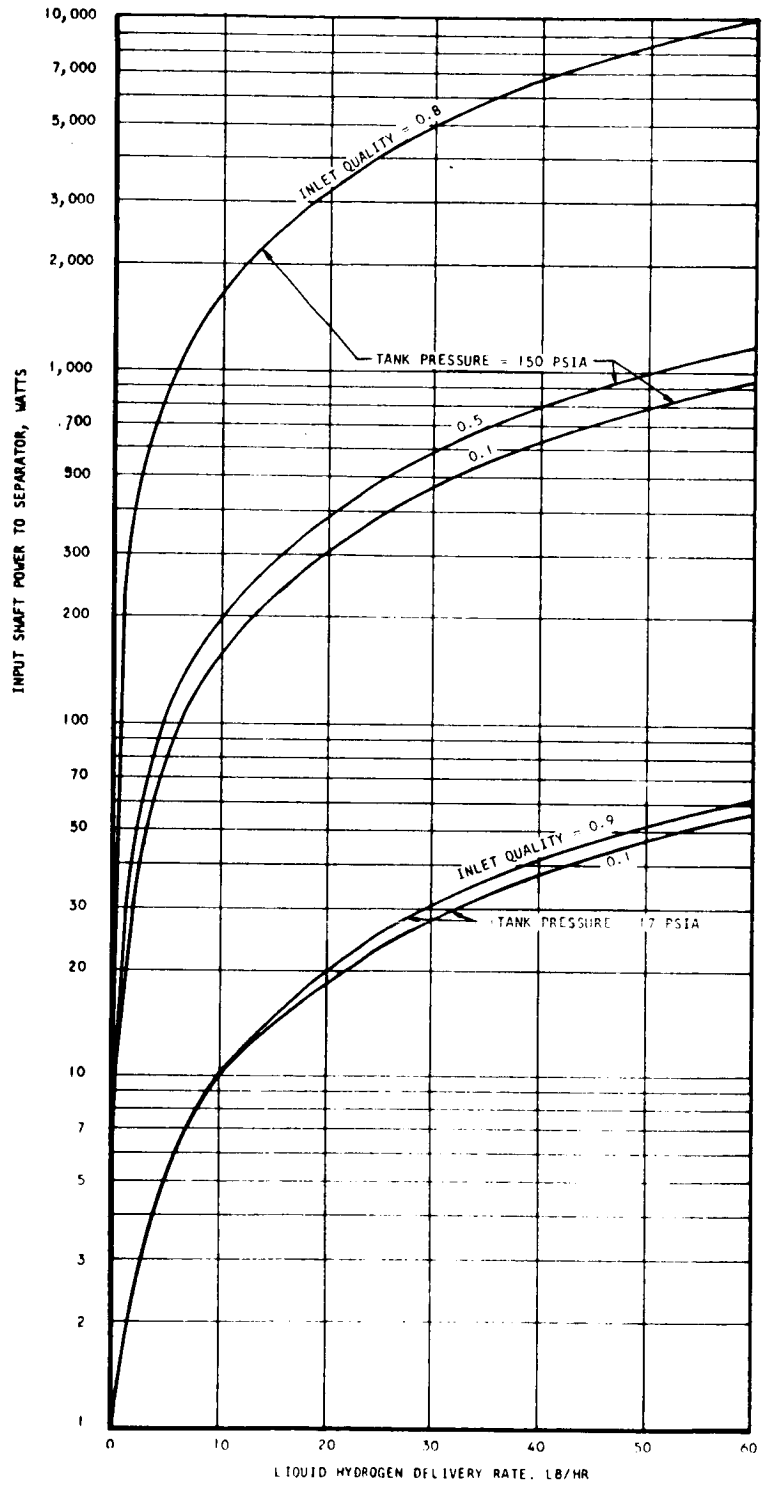

Fig. I-10 Separator Power Requirements

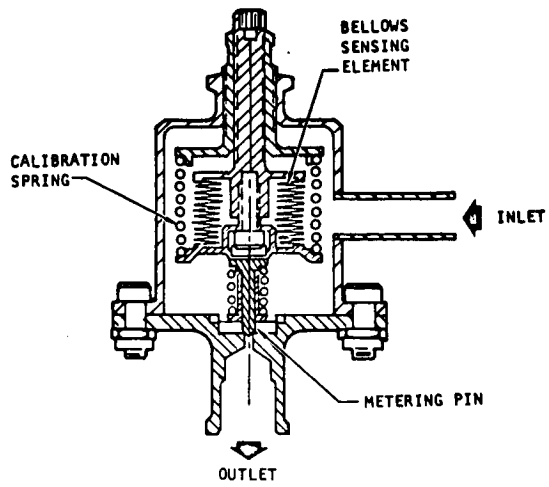

Fig. I-11 Schematic of Continuous-Operating Expansion Valve

upstream, absolute pressure regulating valve. Liquid hydrogen under tank pressure enters the valve body and acts against an evacuated bellows sensing element. This element is initially positioned by the calibration spring to a slightly extended position required to hold the metering pin against the valve seat. When the sensed pressure reaches a predetermined level, the calibration spring force is balanced by the opposing force developed by the pressure acting on the bellows. A slight increase in pressure above this predetermined set value causes the metering valve to modulate open and maintain the desired inlet pressure level.

Preliminary sizing of the unit is based on an assumed tolerance band of ±10 percent in the pressure range from 17 to 50 psia and of ±5 percent for the pressure range from 51 to 150 psia. The required sensitivity and minimum hysteresis is obtained in this configuration by designing for the least possible number of friction points and by maintaining high actuation to friction force ratios.

The expansion unit will be located in a pressurized area, and the design is such that no flange or calibration adjustment screw static seals are required. The valve seat can be machined as an integral part of the outlet body, thus eliminating an insert arrangement requiring static sealing.

This expansion unit is not capable of continuous operation over a wide flow rate range of, for example, 0.02 to 6.0 lb per hour. Preliminary seat sizing calculations indicate that the seat diameters and valve strokes become impractically small (under 0.01 and 0.004 in., respectively) at liquid hydrogen flow rates below approximately 1 lb/hr. Valve seat sizes and strokes required for flow rates below this value are impractical from the standpoint of contamination, manufacturing, and seat loading.

The design approach shown in Fig. I-11 is based on an all stainless steel construction due to the following considerations:

- The introduction of aluminum housing would result in a potential leak path introduced by the necessity of incorporating a hard-seat insert.
- The reliability of stainless steel bellows capsules is substantially greater than aluminum capsules, due to the greater uniformity of the material and the more advanced manufacturing techniques associated with welding stainless steel bellows elements.
- The use of more than one material could introduce potential problems associated with differential thermal expansion and galvanic corrosion.

Figures I-12 and I-13 show the predicted weight and size of the unit. It was found that the weight increase was not a function of flow rate but rather of pressure. The effect of pressure on the overall weight of the unit is also very small, as can be seen in Fig. I-12. The wall thickness of the housing does not increase significantly with pressure because the thickness at low pressure is established by manufacturing and durability standards, rather than operational stress levels. The unit is approximately 2-1/2 in. in diameter. The overall increase in length is a result of an increase in upper housing length to accommodate a longer calibration spring for the higher pressures. In summary, it can be seen that, over the flow rate and pressures considered, the valve weight and size are nearly constant. Further, the weight and size are the smallest practicable for the rates considered here with respect to hardware construction limitations.

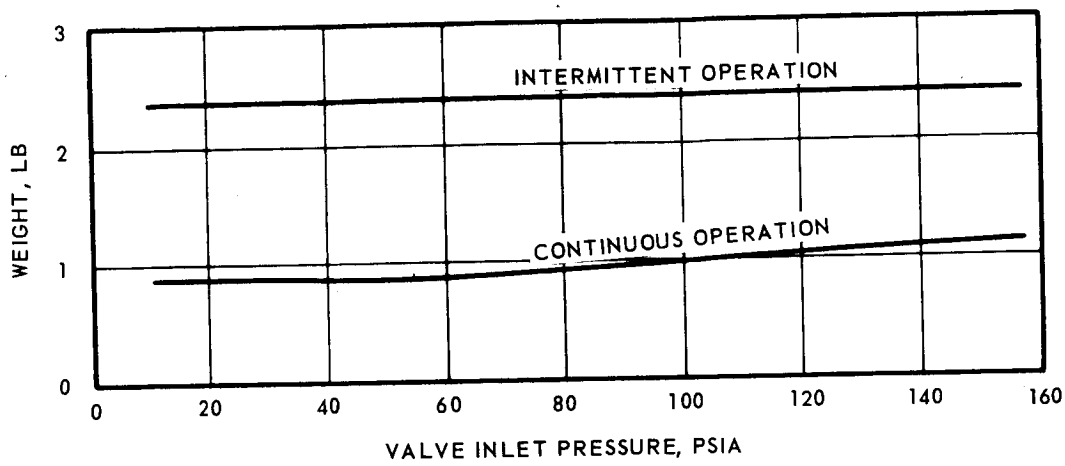

Fig. I-12 Expansion Valve Weight

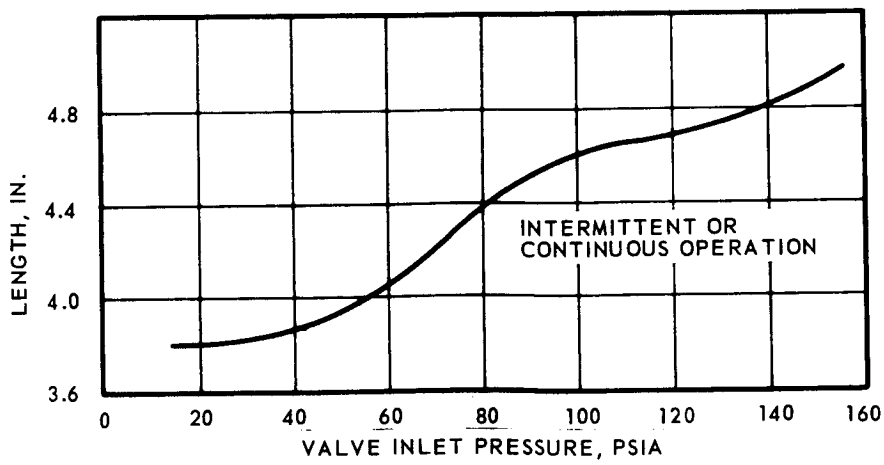

Fig. I-13 Expansion Valve Size

Utilization of an intermittent-operating valve with both mass and pressure regulation capabilities was considered for liquid hydrogen flow rates up to approximately 200 lb/hr. The valve concept developed for the intermittent venting case is shown in Fig. I-14. The unit has a dual function which is performed by independent but physically joined valve sections. The shutoff valve portion of the unit has a snap-acting or dead-band type of operation that utilizes a Belleville spring. The unit is a snap-acting-shutoff valve, integral with a downstream absolute pressure regulating valve. Liquid hydrogen at tank pressure enters the valve body and acts against an evacuated bellows sensing element. This element is initially positioned by the Belleville and calibration spring to a slightly extended position as required to hold the poppet against the valve seat. When the sensed pressure reaches a predetermined level, the Belleville and calibration spring forces are balanced by the opposing pressure force acting on the bellows. A slight increase in pressure above this predetermined value causes the valve to snap fully open. This snap action is obtained by utilizing a combination of spring rates so that the total rate (Belleville, bellows, and coil spring rate) is slightly negative. Thus, the sensed pressure must drop to a value below the actuation pressure in order for deactuation or reseat to occur.

Fluid discharged from the shutoff valve portion of the unit flows through the metering section of the regulating valve portion and thence to the discharge port. Subsequent increase in downstream pressure is sensed by the regulator bellows element. The increased pressure modulates the metering valve to maintain the discharge pressure at the predetermined value. Controlling the discharge pressure in this way ensures control over the downstream portions of the thermal conditioning system, such as the heat exchanger, and results in improved overall system performance.

The operation of the snap-acting shutoff valve portion of the unit can best be understood by referring to Fig. I-15. The Belleville spring, which assists in preloading the valve poppet against its seat, is deflected to Point B on the negative spring-rate side of its load curve. Added to the load (L_{BV}) of the Belleville spring at this point is the net load (L_{CB}) of the bellows, poppet return spring, and calibration spring as well as the load (L_P) produced by the differential pressure across the poppet. For the valve to open, the inlet pressure must increase to a point where the force (P_1A) produced by

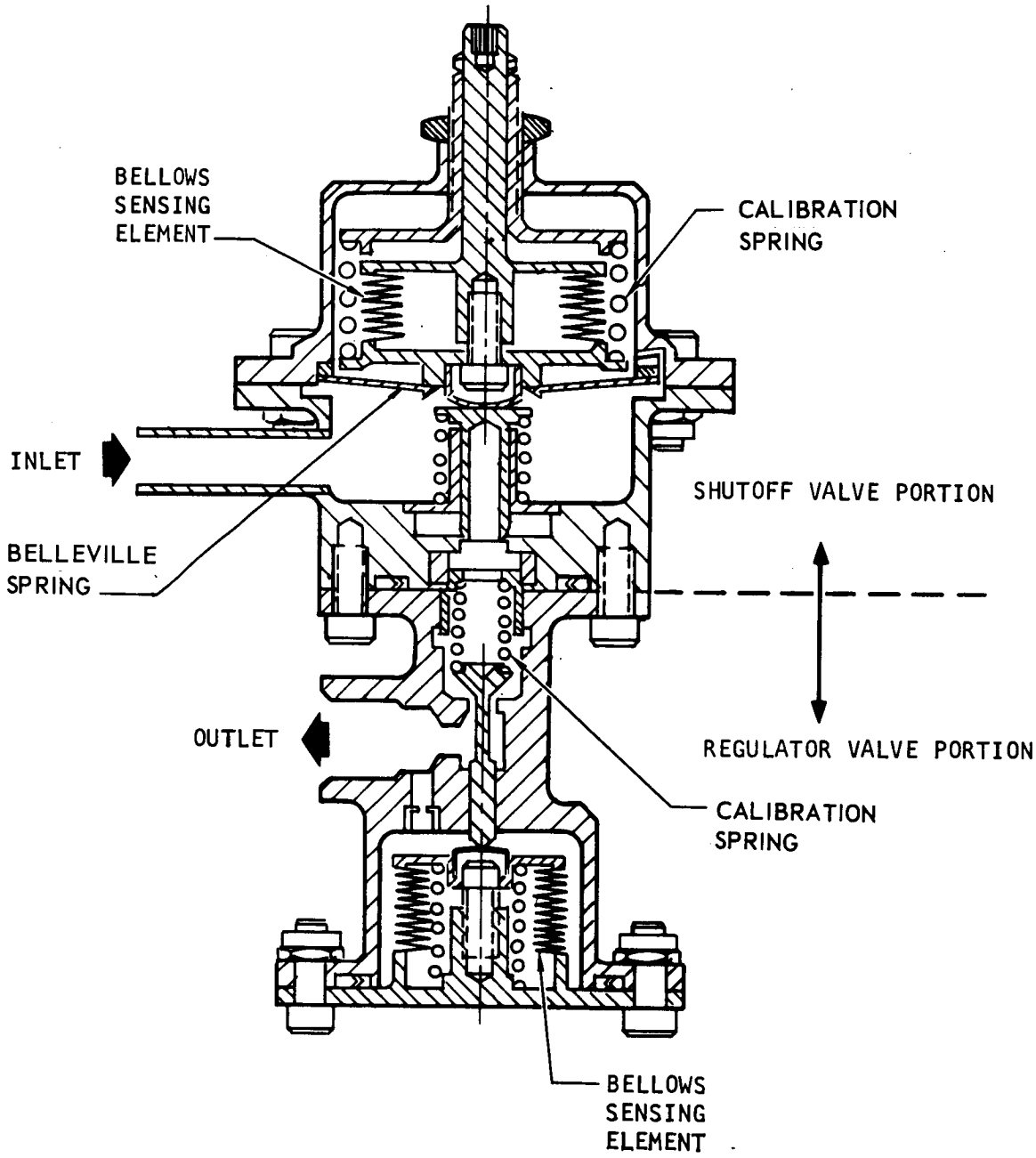

Fig. I-14 Schematic of Intermittent-Operating Expansion Valve

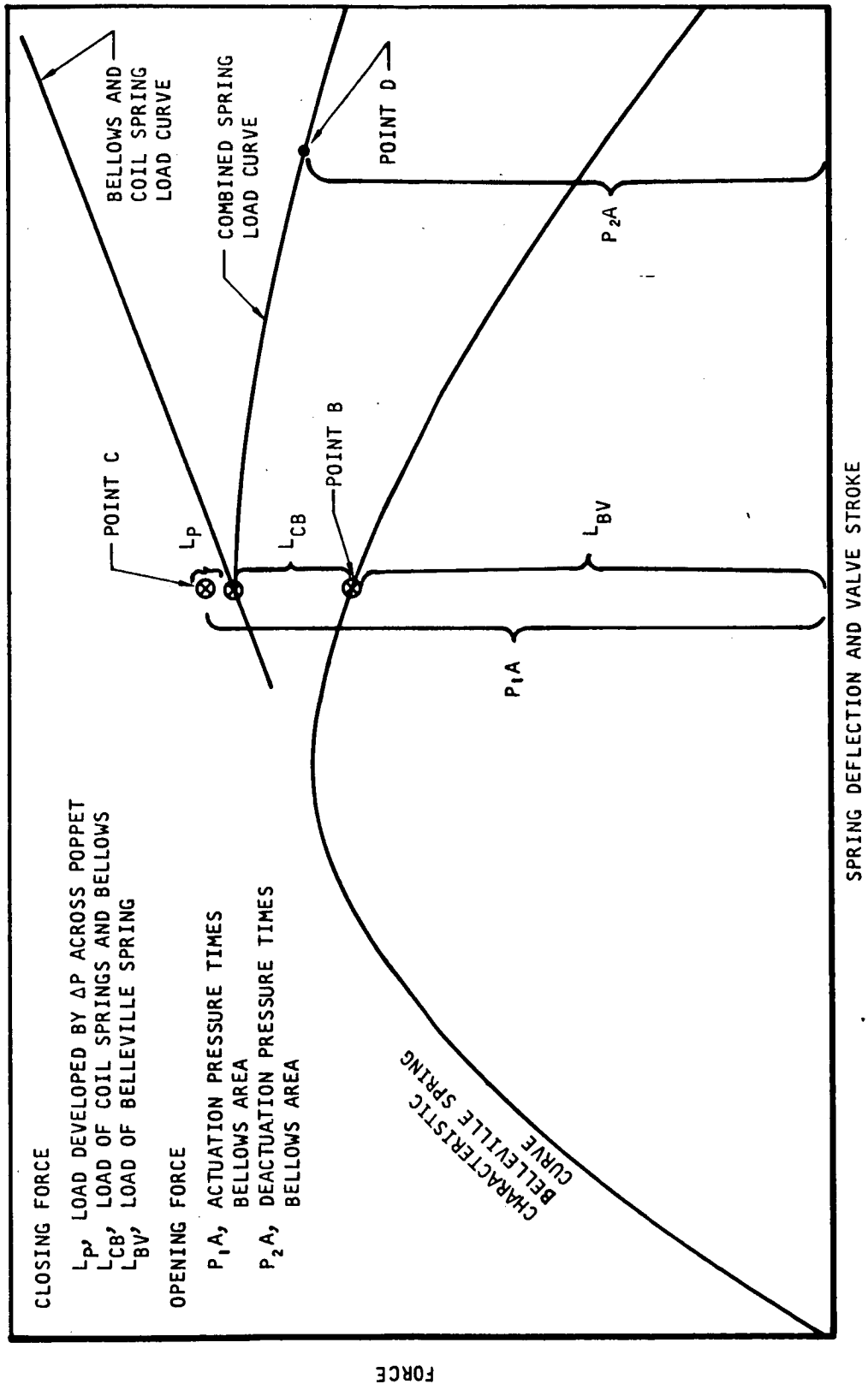

Fig. I-15 Operation of Belleville Spring

the sensed pressure acting on the bellows effective area just exceeds the sum of L_{BV}, L_{CB}, and L_P (P_1A is actually negative with respect to L_{BV}, L_{CB}, and L_P). Once the spring-bellows-poppet assembly begins to move toward the open position the closing force decays along some undefined but nearly straight line between Points C and D. The valve stroke from Point C to any predetermined point (Point D) on the combined spring load curve is controlled by mechanical stops within the bellows. During this stroking action, the P_1A force remains constant so that when Point D is reached there is an excess of force tending to hold the valve open. To effect closure of the valve, the sensed pressure must drop to a reduced level, P_2. At this point, the combined spring force just exceeds the P_2A value and the valve closes because of increasing closing forces.

The regulator valve portion of the unit functions to maintain an outlet pressure at a predetermined absolute value. Fluid admitted to the inlet from the shutoff valve portion flows around the metering valve and into the outlet passage. Outlet pressure is routed through a damping orifice to the evacuated bellows sensing element. When the sensed pressure reaches a value sufficient to overcome the bellows and coil spring preload, the bellows moves downward allowing the metering valve to modulate toward the seat and thus limit the outlet pressure.

Preliminary sizing of the intermittent expansion unit was based on the same tolerance bands assumed for the continuous unit, a ±10 percent band in the pressure range from 17 to 50 psia and a ±5 percent band for the pressure range from 51 to 150 psia. This unit will be located in the pressurized tank area and, therefore, the shutoff valve portion does not contain static seals at the cover flange or at the calibration adjustment screws. A static seal is required at the interface between the two valve portions and at the regulator cover. Both valve seats can be machined as an integral part of their respective valve bodies, thereby reducing the sources of leakage.

This configuration is capable of being scaled to the most favorable size for any specific design requirement within the flow range of approximately 10 to 200 lb/hr of hydrogen. The design is based on the same considerations as outlined in the previous discussion for the continuous-operating valve. Figure I-12 shows the predicted weight of the

intermittent operating unit. The overall package size, which is 3 in. in diameter by 6.2 in. in length, remains basically constant over the entire pressure and flow range. The use of a Belleville spring in the shutoff valve portion of this unit permits considerable latitude in the loads that can be produced without a change in the external package size. The weight increases that result from heavier internal components required at the higher pressures are largely compensated for by the slightly decreased diameters that can be used at these pressures. Thus, the weight increase with tank pressure is negligible. The basic criterion for establishing the size and weight of the regulator-valve portion is the minimum bellows size into which the internal stops and springs can be fitted. Thus, for the intermittent valve, the size and weight are not determined by the required flow rates but by manufacturing limitations which will provide adequate performance.

It is necessary to control both the flow rate and the pressure in the cold side of the heat exchanger so that the heat loads and the available temperature difference are known. The expansion valves just discussed perform both of these functions. However, the practical lower limit of 1 lb/hr is in excess of the continuous flow rates required for the three reference missions which are less than 1 lb/hr. By separating these functions, the system may be designed for a lower flow rate with resulting lower heat exchanger weight. Figure I-16 illustrates a pressure regulator wherein the mass flow regulation function has been removed. Mass flow regulation is provided by a solenoid actuated valve placed downstream from the heat exchanger where volume flows are large as a result of gasifying the hydrogen in the heat exchanger and the low discharge pressures (Fig. I-1).

An expansion valve discharge pressure of about 4 psia was selected for the following reasons: It is sufficiently above the triple point (1 psia) to prevent solid hydrogen from forming in the heat exchanger core and, as will be shown later, yields a low system weight penalty. It also provides sufficient pressure for actuation of the expansion valve by the bellows and allows a choked orifice for flow control to be placed downstream from the heat exchanger.

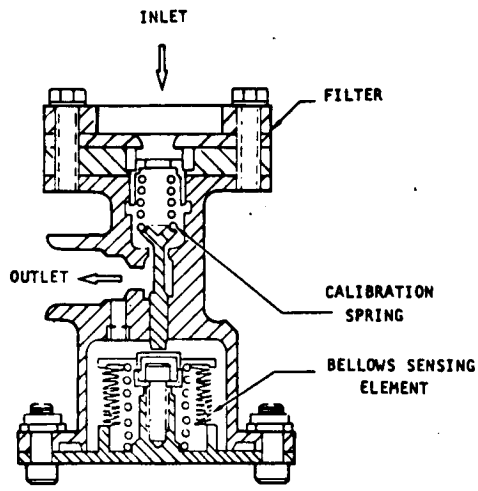

Fig. I-16 Pressure Regulator

It is necessary to place a shutoff valve downstream from the heat exchanger to prevent an expansion below the triple point. This would occur if the exhaust line from the heat exchanger was ducted directly to the vacuum environment of space. The valve can also be a flow limiting device which will improve system operation. The fluid state downstream from the heat exchanger will always be gas, whether gas or liquid enters the expansion valve. The pressure at the flow limiting orifice will be maintained at a constant value of approximately 4 psia. For all conditions, the vapor will be within a few degrees of tank temperature. Thus, the orifice will ensure that the flow through the system will be essentially constant, whether gas or liquid enters the expansion valve. This, then, allows the heat exchanger cold-side flow rate to be closely matched to system requirements.

The pressure regulator which will control the pressure to 4 psia is shown schematically in Fig. I-16. The regulator contains a large integral filter to protect the poppet and seat from particulate contamination. The flow through the valve is modulated by

the bellows which is exposed to regulated downstream pressure. Weights and sizes of the valve as a function of valve inlet pressure are illustrated in Figs. I-12 and I-13.

Thermodynamic performance of any of these valve concepts is shown in Figs. I-17 and I-18 where the temperature drop and vapor quality for liquid hydrogen are presented as a function of propellant tank pressure and valve pressure drop. For Missions (1), (2), and (3), the expected temperature drop across the valve will be about $8^{o}R$. The vapor quality will be about 10 percent.

Expansion Turbine. The use of a turbine to expand the saturated liquid offers no advantages over the use of a valve. It may be noted that since the inlet condition to the expansion unit is saturated liquid and the outlet condition is two-phase, the outlet temperature will be the same for both units operating over the same pressure range. From a thermodynamic viewpoint, the outlet quality may be slightly lower for the turbine. This will have a negligible effect on the heat exchanger and on the flow rate through the thermal conditioning system. Although there are no real advantages in using a turbine, there are many disadvantages, such as:

- There is no simple way to control the system to ensure maintenance of a given outlet pressure.
- For the maximum intermittent flow rates considered (60 lb/hr), the volumetric flow is more than an order of magnitude below that for the smallest turbines built (0.4 in. diameter).
- Liquid turbines are usually designed to ensure that no vapor flashing occurs in the turbine. Here, the design point is a unit to ensure that flashing does occur. This results in a unit that cavitates, tends to erode, and has extremely low efficiency.
- The net work output from the unit is negligible, and in a speed range not directly usable for driving a mixer unit.

In summary, when compared to an expansion valve the disadvantages of using a turbine device as an expansion unit are sufficient to exclude it from further consideration.

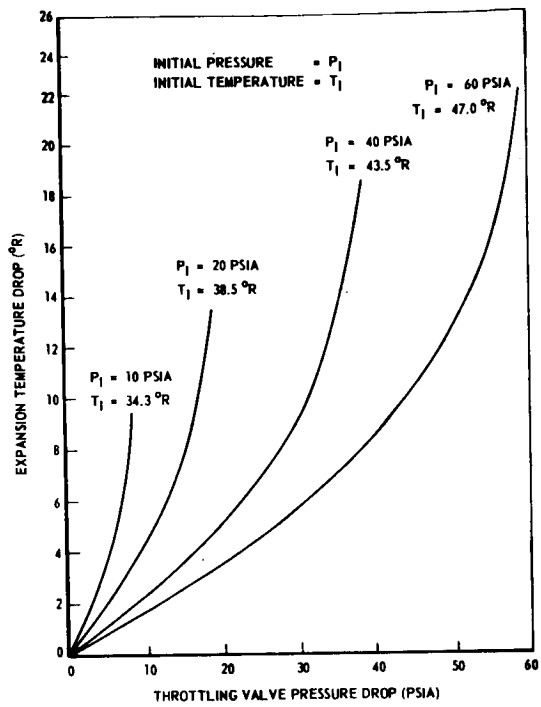

a. $(10 \leq P_{initial} \leq 60)$

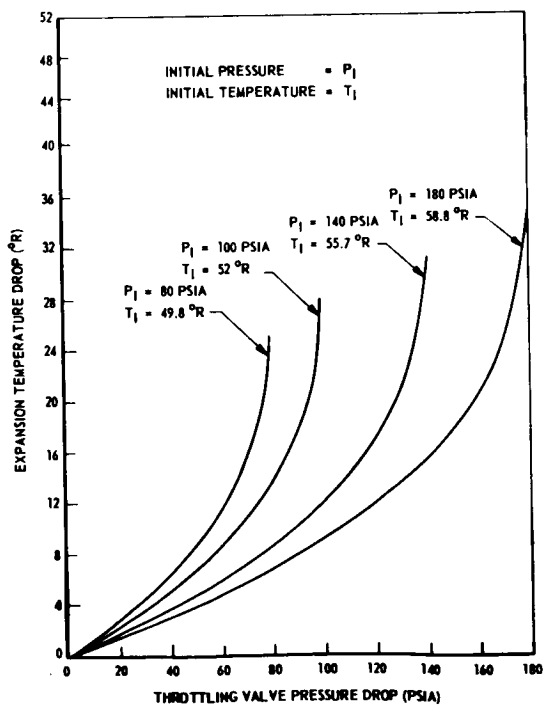

b. $(80 \leq P_{initial} \leq 180)$

Fig. I-17 Influence of Tank Pressure and Throttling Valve Pressure Drop on Temperature Drop

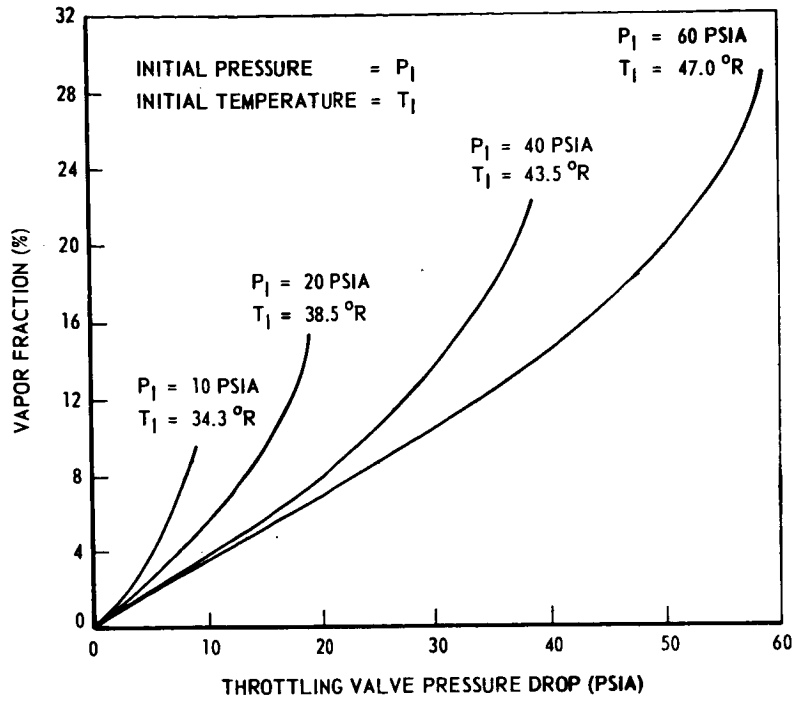

a. $10 \leq P_{initial} \leq 60$

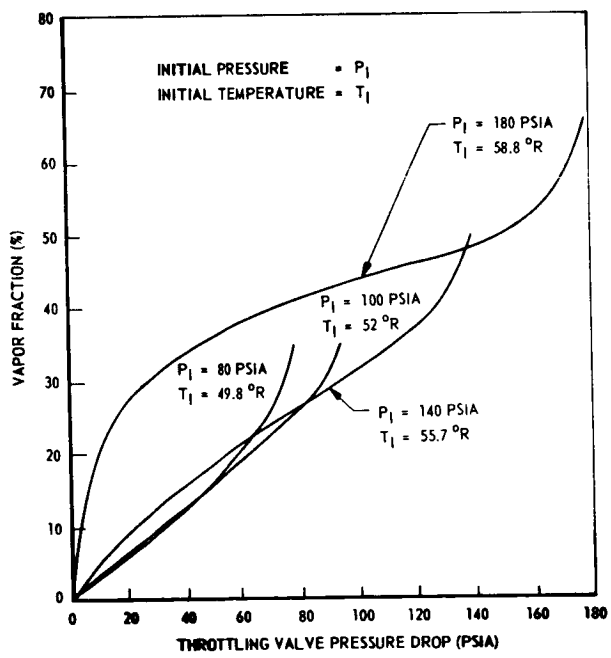

b. $80 \leq P_{initial} \leq 180$

Fig. I-18 Influence of Tank Pressure and Throttling Valve Pressure Drop on Fluid Quality at Heat Exchanger Inlet

Heat Exchanger Unit

The heat exchanger must be capable of transferring to the vented propellant the energy conducted into the propellant tank from the exterior through insulation, plumbing, and support structure, as well as any heat put into the tank to drive the rotating parts of the system. The refrigeration produced by the expansion unit provides the temperature difference for heat transfer. The necessary heat transfer may be accomplished with a compact heat exchanger or with a tank-wall heat exchanger. Each method is treated separately in the following.

Compact Exchanger. The flow phenomena in boiling and condensing hydrogen within a compact heat exchanger is usually envisioned as annular flow at low fluid quality and mist flow at high fluid quality. For annular flow, a layer of liquid hydrogen is attached to the walls of the flow passages and high heat transfer coefficients are obtained. For mist flow, the liquid phase exists as small droplets in the central region of the flow passage. Here, the heat transfer path is from the wall through a hydrogen vapor layer and then to the liquid, resulting in lower heat transfer coefficients.

Two computer programs were developed to predict boiling heat transfer coefficients, and another program was written to evaluate the two-phase pressure drop. The heat transfer coefficients in the annular flow regime were developed using Chen's correlation (Ref. 3), and typical results are shown in Fig. I-19. Hendrick's correlation (Ref. 4) was used in the mist flow regime, and typical results are shown in Fig. I-20. A review of the literature indicated that the correlation of Hendrick was the best available for calculating the heat transfer coefficients in the mist regime. In this study the transition from annular to mist flow was assumed to occur at 50-percent quality. The location of the transition point is conservative based on experience and tests of various investigators. For example, Ref. 5 reported a design and successful test of a remote storage evaporative oil cooling system for aircraft assuming an 80-percent transition point. The computer program for calculating the two-phase regime pressure drop was based on Martinell's correlation (Refs. 6 and 7). The correlation is independent of flow mechanism and is applicable to both boiling and condensing fluids. Since the correlation is for local pressure gradients, an integration must be performed to

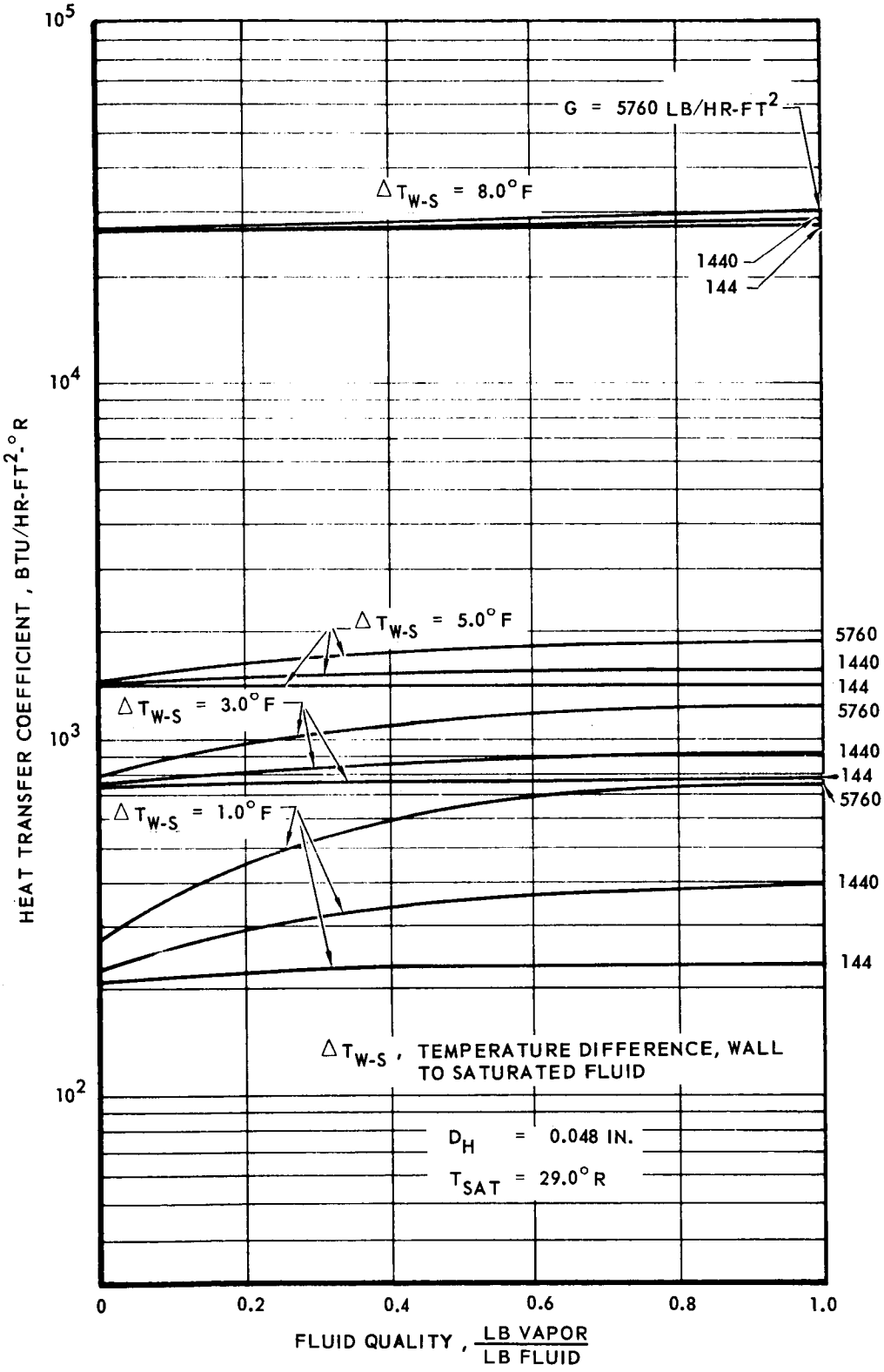

Fig. I-19 Heat Transfer Coefficients for Annular Flow

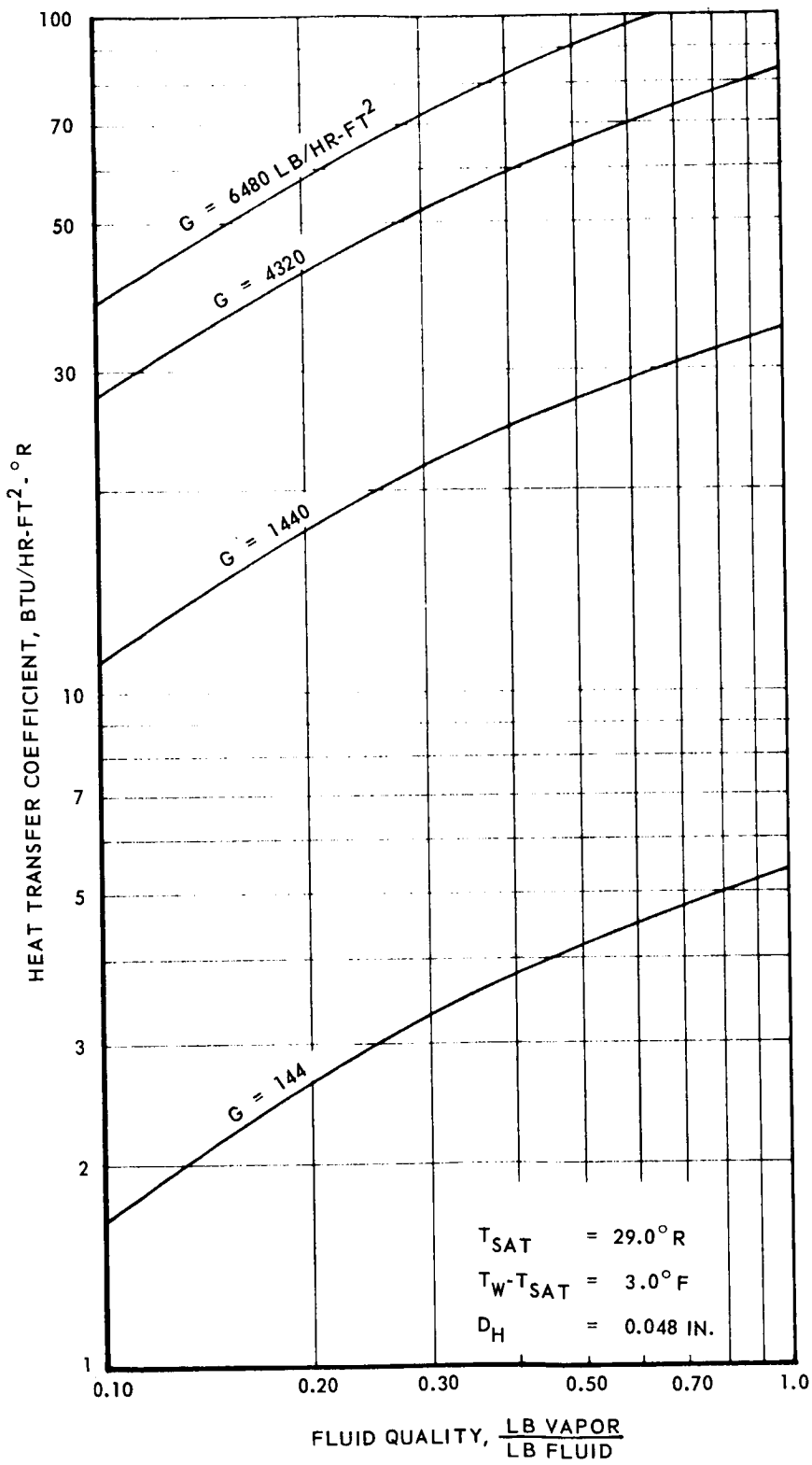

Fig. I-20 Heat Transfer Coefficients for Mist Flow

obtain the overall pressure drop along the two-phase flow passage. The computer program uses a numerical integration method and includes momentum changes to determine the overall pressure drop.

Before evaluating heat exchanger performance characteristics, a short analysis was made of the interactions between the expansion and heat exchange units and their effects on heat exchanger requirements. Figure I-21 is a pressure-enthalpy plot which shows two possible thermodynamic paths for the process. Starting with saturated liquid at a pressure of P_1, various paths can be used to reach the final saturated vapor pressure P_3 by controlling the expansion valve outlet pressure P_2. With large values of P_2/P_1, the temperature difference between the fluids is small while the allowable pressure drop is large. As the value of P_2/P_1 decreases. Thus, at some ratio of P_2/P_1, a minimum size heat exchanger can theoretically be obtained with a given value of P_3/P_1. The effect of the expansion valve pressure ratio on the heat exchanger size over the wide pressure range from 17 to 135 psia is shown in Fig. I-22. The value of the ordinate is an indication of the size of the heat exchanger. It can be seen that the ratio of P_2/P_1 should approach P_3/P_1 to obtain small heat exchangers. Thus, the major pressure change should take place in the expansion valve, not in the heat exchanger.

A counterflow plate-fin heat exchanger was used as the basis for comparison. The general configuration of this type of heat exchanger is shown in Fig. I-23. This configuration has better flow distribution than a crossflow heat exchanger. The evaluated units are made of stainless steel using 20 rectangular fins per in. The fins are offset and are 0.004-in. thick. The hot side fins are 0.075-in. high with an uninterrupted length of 0.15 in. The cold side fins are 0.050-in. high with an uninterrupted length of 0.10 in.

The number of transfer units (NTU), which indicates heat exchanger size, is given by:

$$NTU = \ln\left(\frac{1}{1 - E}\right)$$

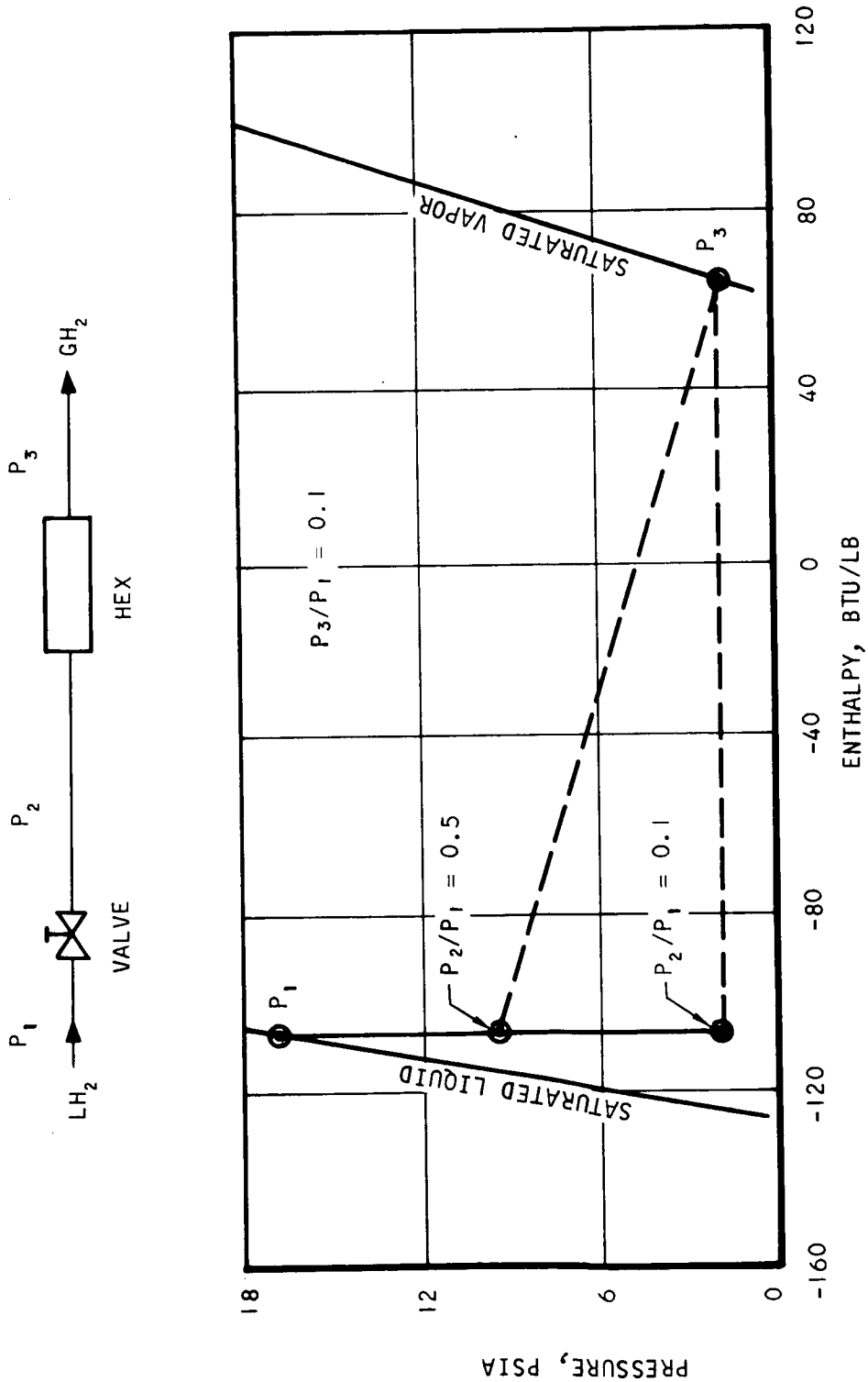

Fig. I-21 Thermodynamic Path Through Expansion Valve and Heat Exchanger

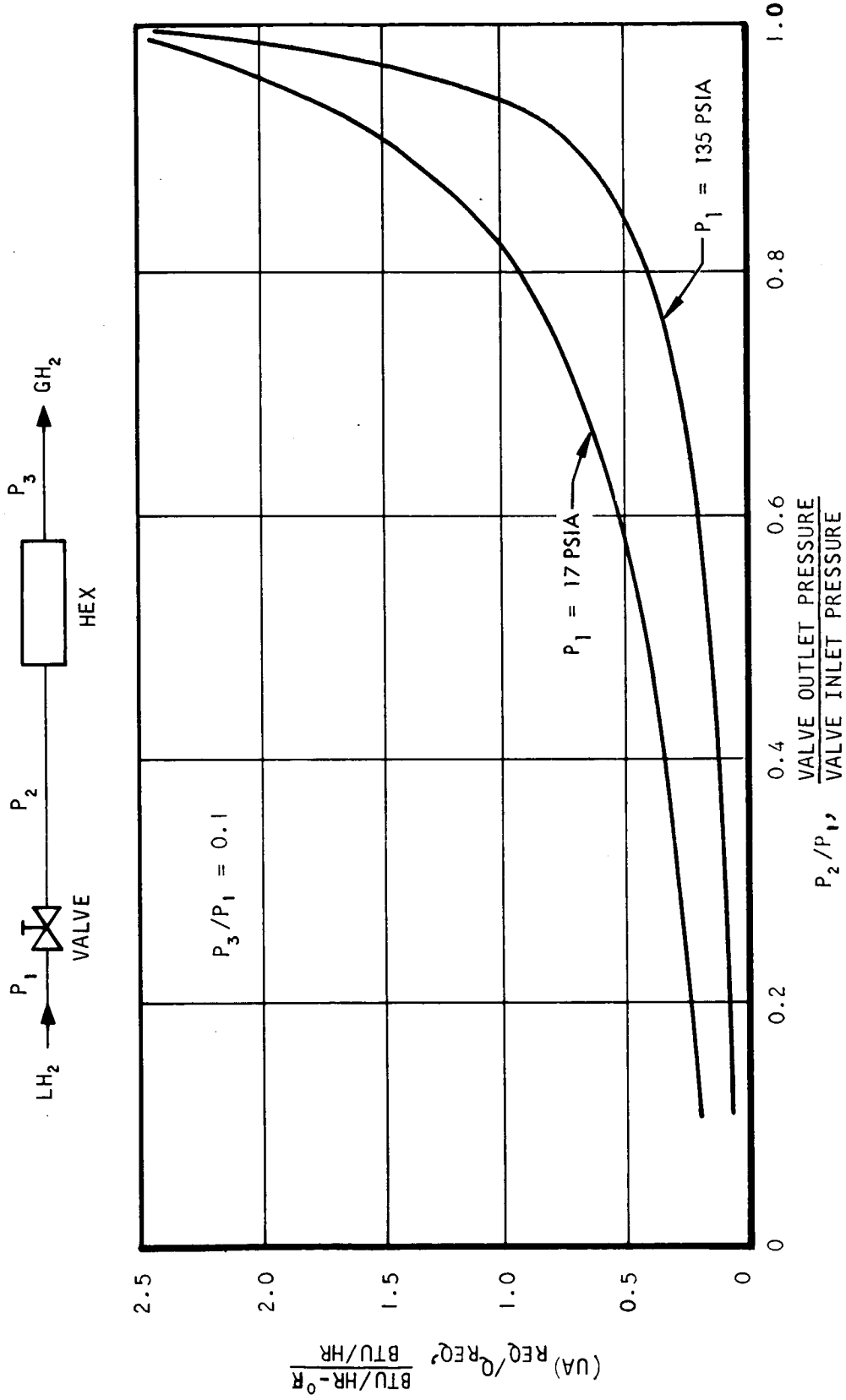

Fig. I-22 Effect of Valve Pressure Ratio on Heat Exchanger Size

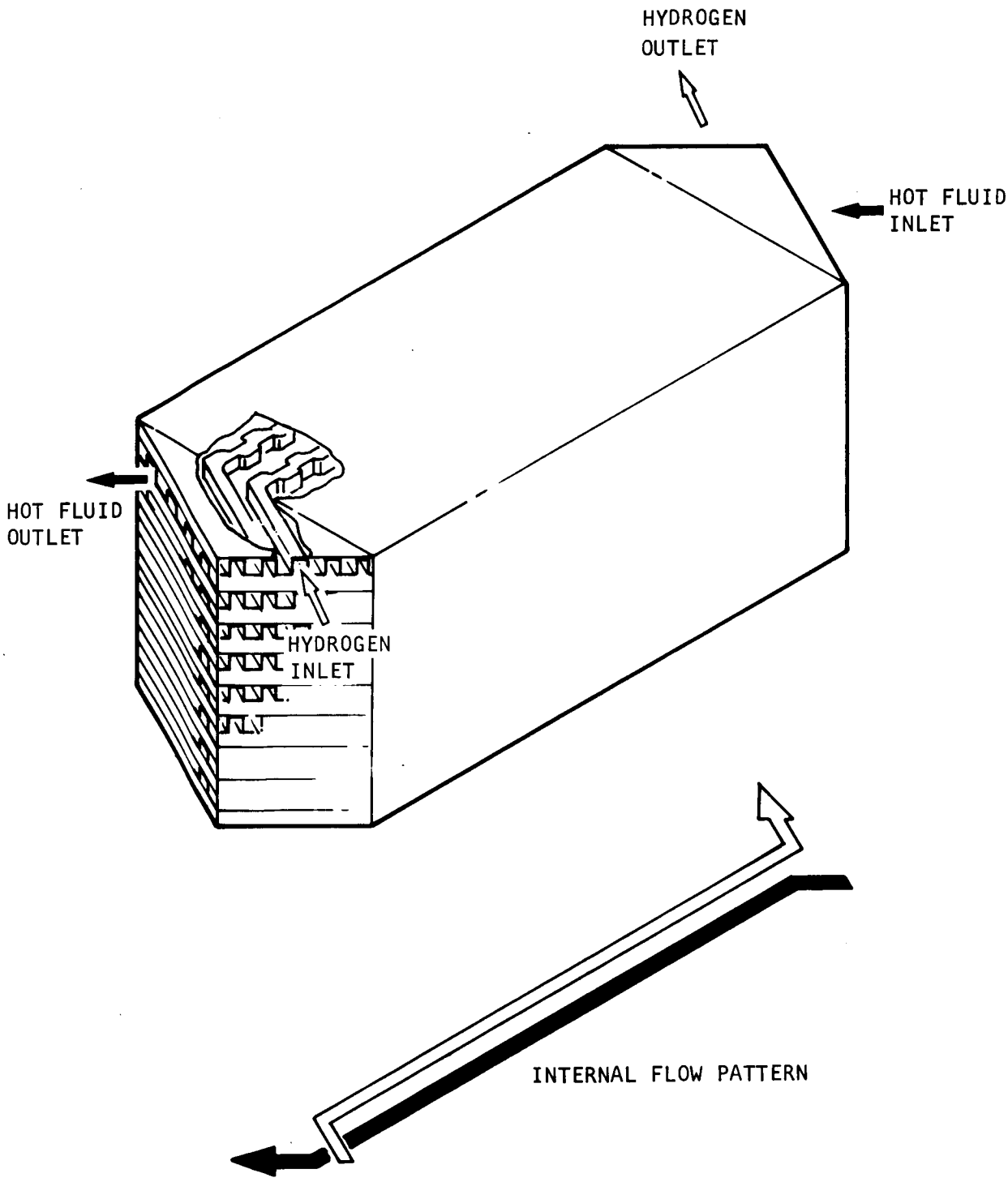

Fig. I-23 General Configuration of Counterflow Heat Exchanger

where E is the heat exchanger effectiveness. An effectiveness of 0.9 was selected for the parametric study. This value of effectiveness gives a good balance between heat exchanger weight and hot side pumping power. A lower effectiveness value such as 0.8 could have been used which would result in a lower heat exchanger weight at the cost of increased pumping power. The best compromise of heat exchanger weight and pumping power is generally evaluated for the conditions and requirements of a specific application. Such an evaluation and optimization has been applied in this study to the thermal conditioning system selected for the reference missions, and is presented and discussed in later sections of this report. For an effectiveness other than 0.9, the change in NTU (and size) can be approximated by:

$$\frac{\Delta NTU}{NTU} = \frac{\Delta E}{(1 - E) \ln \left(\frac{1}{1 - E}\right)}$$

Heat transfer coefficients are compared in Figs. I-24, I-25, and I-26 for helium, gaseous hydrogen, and liquid hydrogen. These are determined from dimensionless experimental heat transfer data that are available on the fins depicted in Fig. I-23. Using helium vapor as the warm side fluid generally results in the largest heat exchanger and largest pressure drop because helium will not condense at the pressures and temperatures under consideration. In addition, for a given warm side mass flow rate, the helium coefficients are lower than the gaseous hydrogen coefficients. Thus, a heat exchanger designed for helium gas only will yield a conservative design.

The parametric study considered three tank pressures (17, 50, and 150 psia) and three expansion ratios between the expansion valve inlet and heat exchanger outlet (approximately 0.1, 0.5, and 0.9). Thus, for a given heat load and warm side fluid, nine different cases were evaluated. The boiling hydrogen undergoes no substantial change in temperature or pressure but a substantial change in quality (outlet quality = 1.0) in the heat exchanger. Helium had a nearly linear temperature decrease along the flow passage.

As can be seen in Figs. I-19 and I-20, the two-phase heat transfer coefficients are, in general, a function of temperature, mass flow, temperature difference, and local

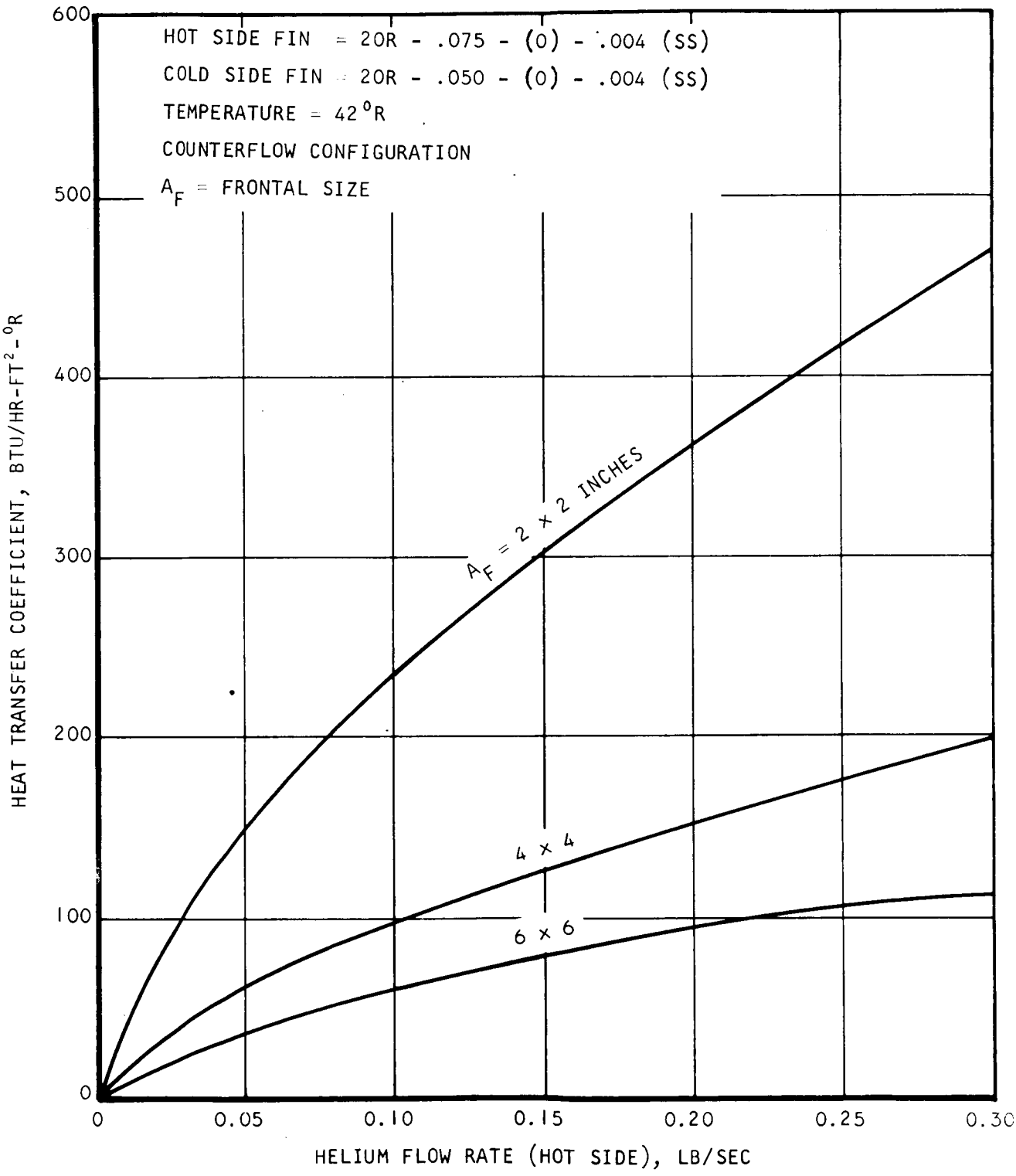

Fig. I-24 Heat Transfer Coefficient for Gaseous Helium

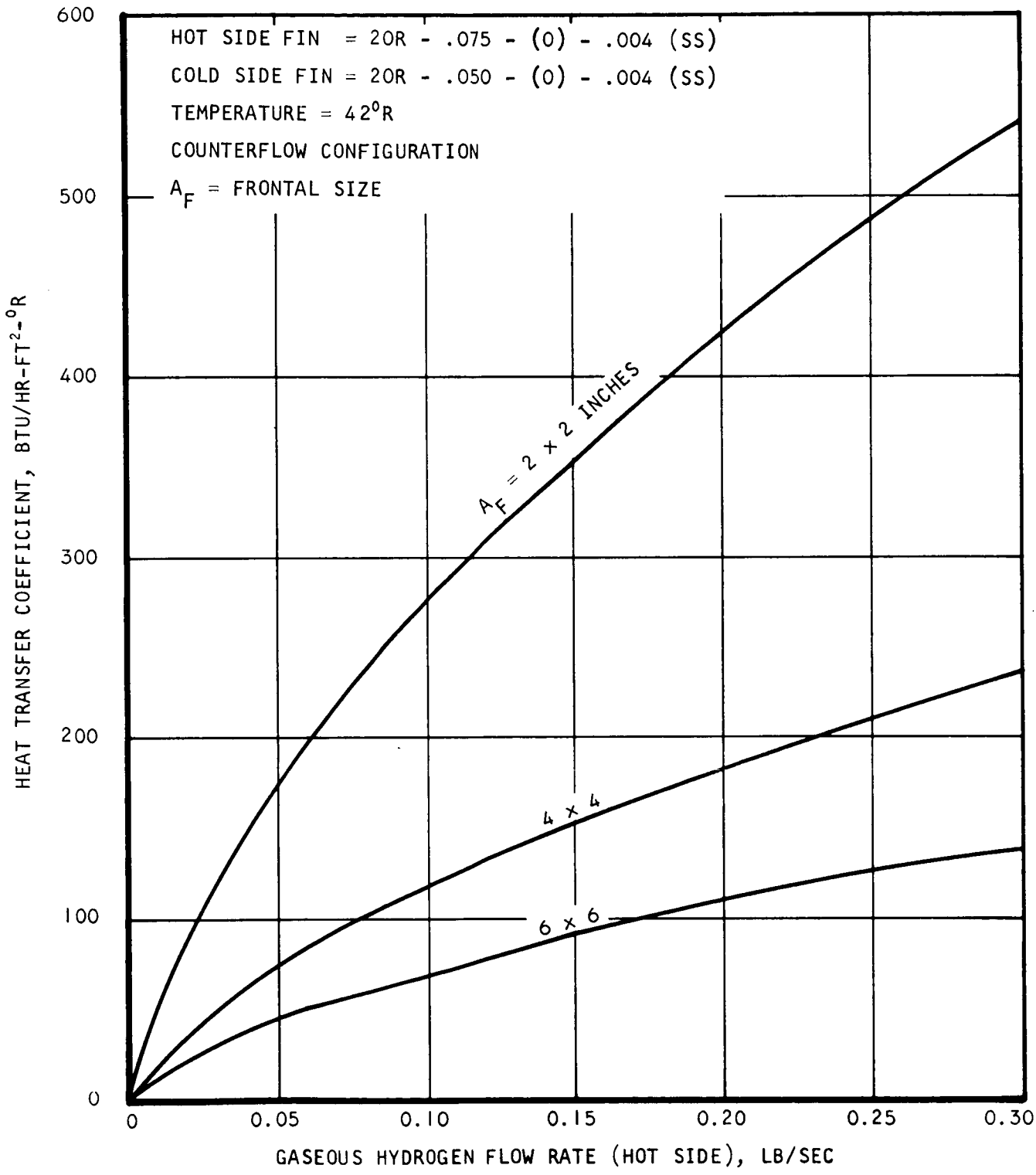

Fig. I-25 Heat Transfer Coefficient for Gaseous Hydrogen

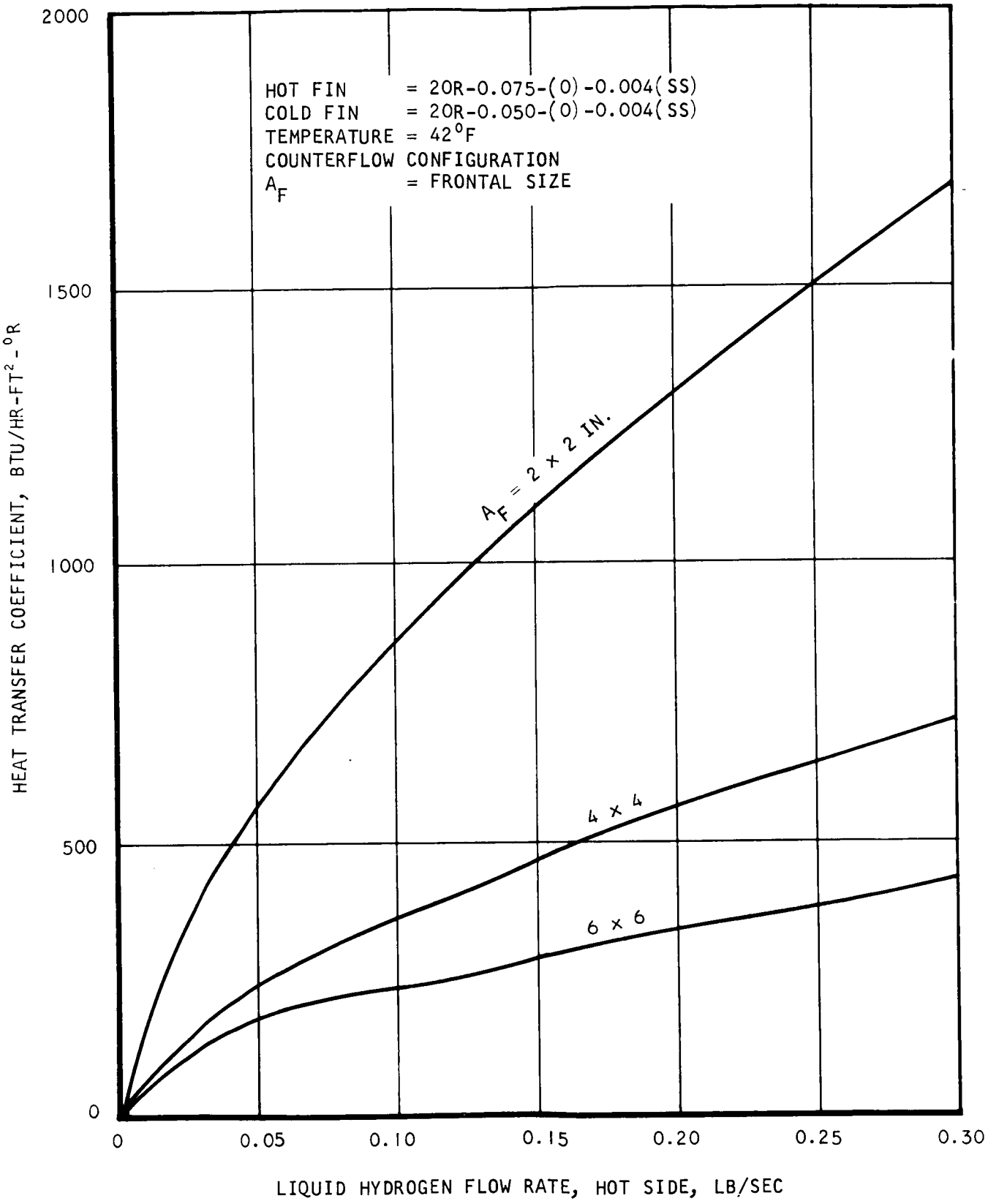

Fig. I-26 Heat Transfer Coefficient for Liquid Hydrogen

quality. As a result, determination of the heat exchanger size required step-by-step integration as well as iteration. The analysis proceeded by first dividing the heat exchanger into several sections. A wall temperature was assumed and the boiling side heat transfer coefficients were calculated (Figs. I-19 and I-20), the warm side heat transfer coefficient was determined (Figs. I-24 and I-26), and the fin effectiveness on the warm and cold sides was calculated. The assumed wall temperature was varied until the following equation was satisfied:

$$h_c = h_h \frac{(\eta A)_h \, (T_h - T_w)}{(\eta A)_c \, (T_w - T_c)}$$

The product of the required overall heat transfer coefficient and the area for a given heat exchange section is:

$$UA = (NTU)\, C_h = C_h \ln \left(\frac{1}{1 - E} \right)$$

The size of the heat exchanger area for a particular section is

$$A_h = (UA) \left[\frac{\frac{A_h}{A_c}}{(\eta h)_c} + \frac{1}{(\eta h)_h} \right]$$

The above procedure is repeated for each section of the heat exchanger to determine the size of the unit. The results are shown in Figs. I-27, I-28, and I-29 with helium as the warm side fluid and in Figs. I-30, I-31, and I-32 with liquid hydrogen as the warm side fluid.

The results were obtained by designing a heat exchanger for a given condition (P_1, P_2/P_1, and heat load) as described above. The frontal area was then varied for various heat loads to hold the mass flux (lb/hr-ft^2) constant. This approach resulted in a series of heat exchangers which have the same length and pressure drop for a

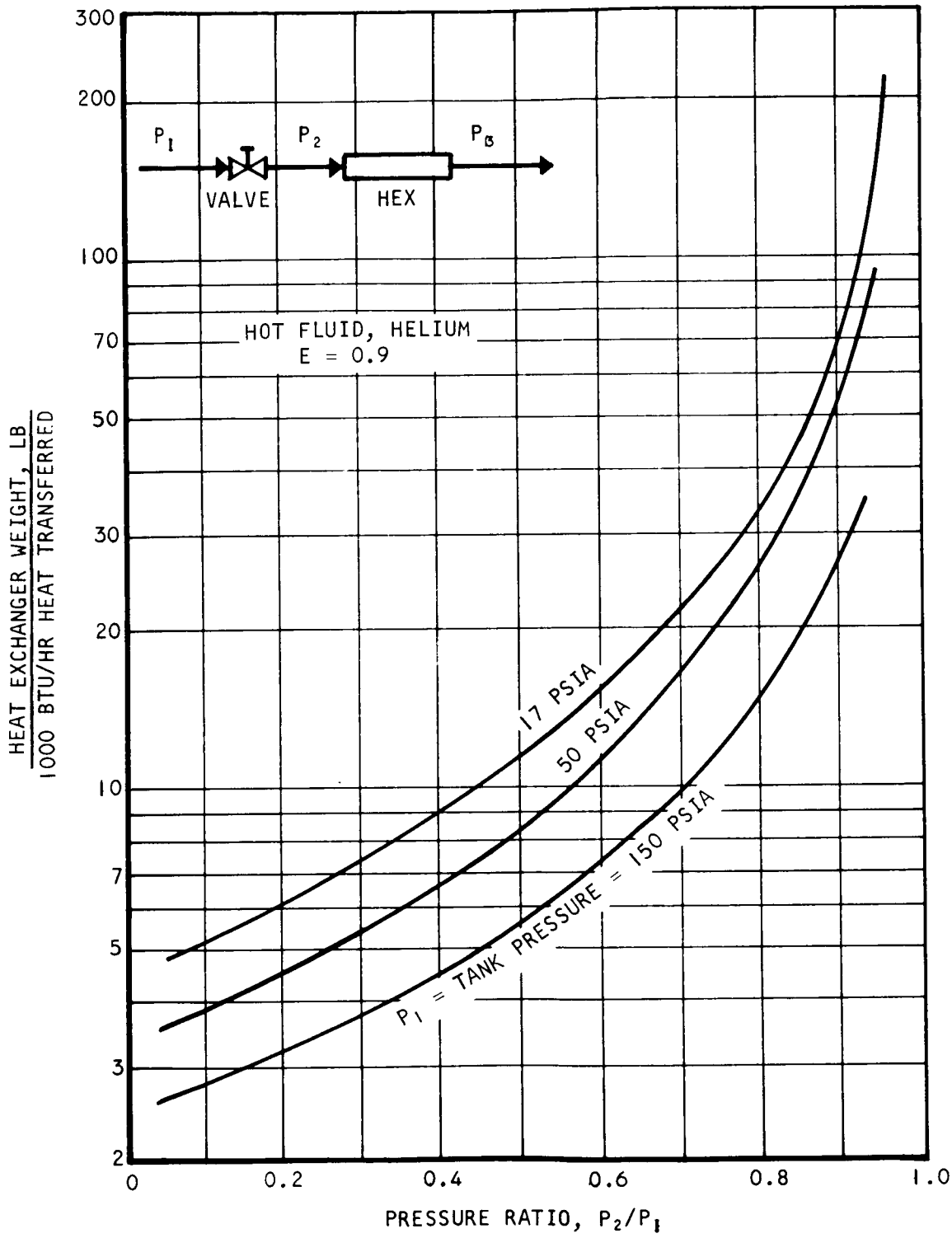

Fig. I-27 Heat Exchanger Weight

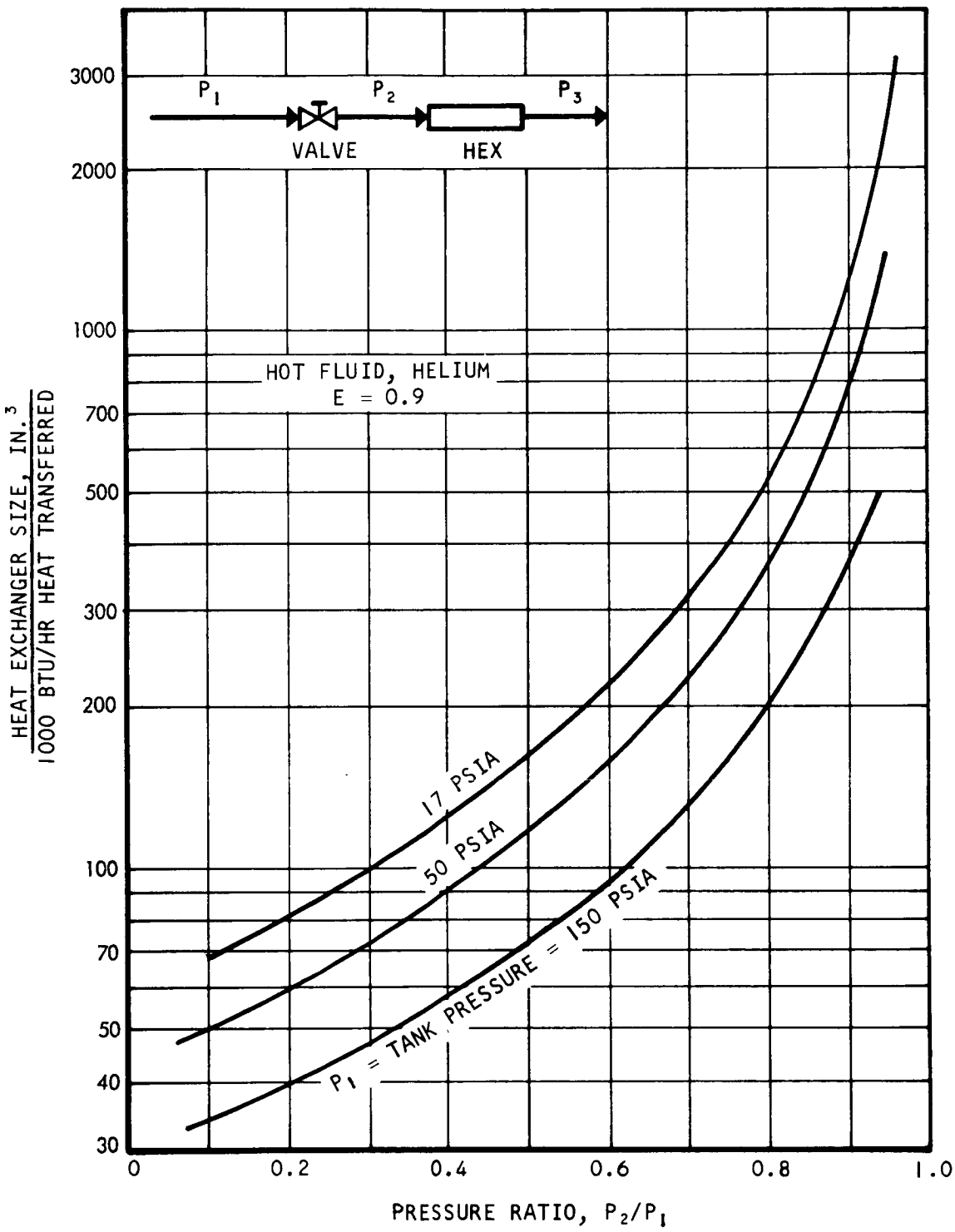

Fig. I-28 Heat Exchanger Size

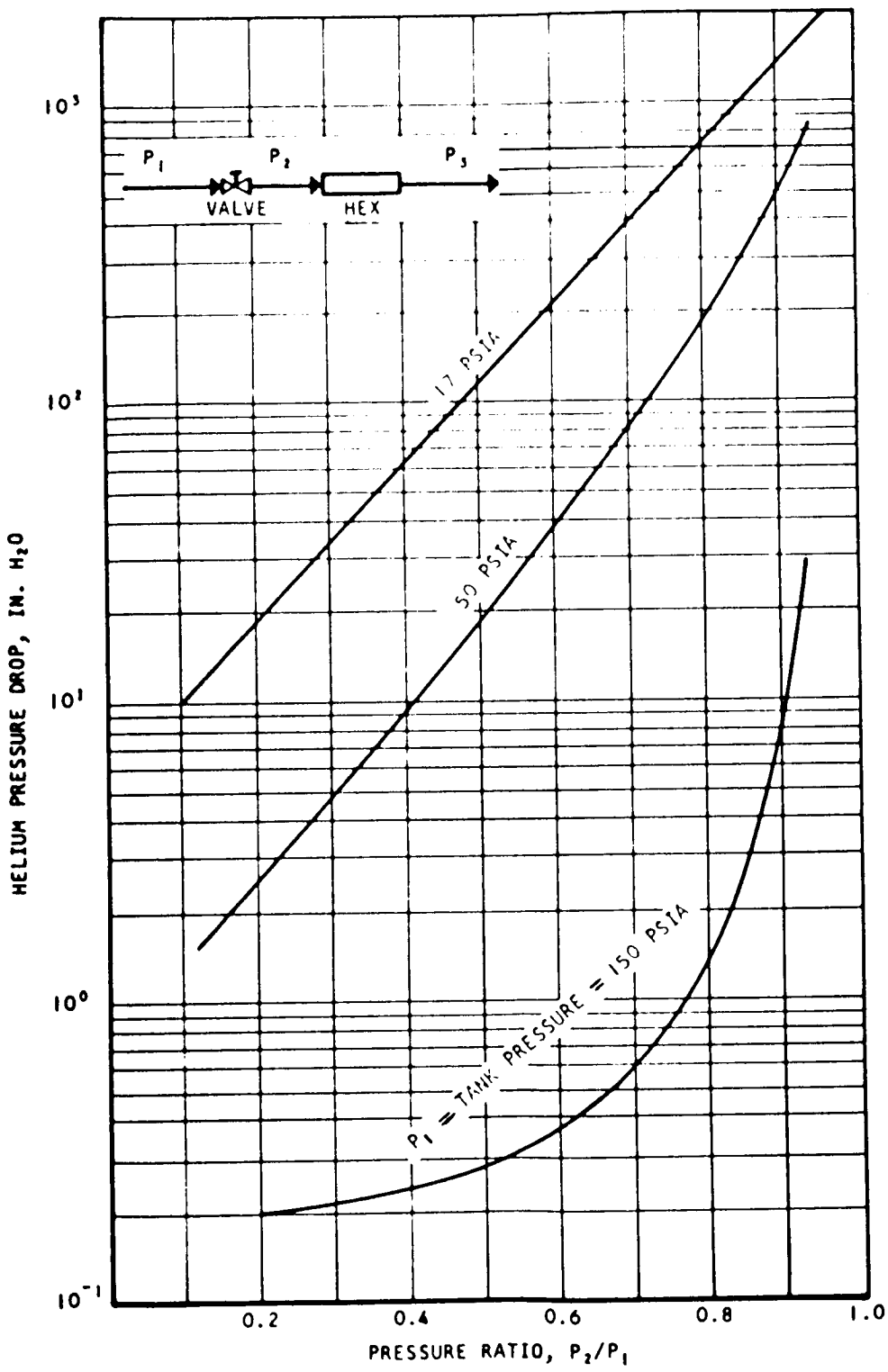

Fig. I-29 Heat Exchanger Hot-Side Pressure Drop (With Helium)

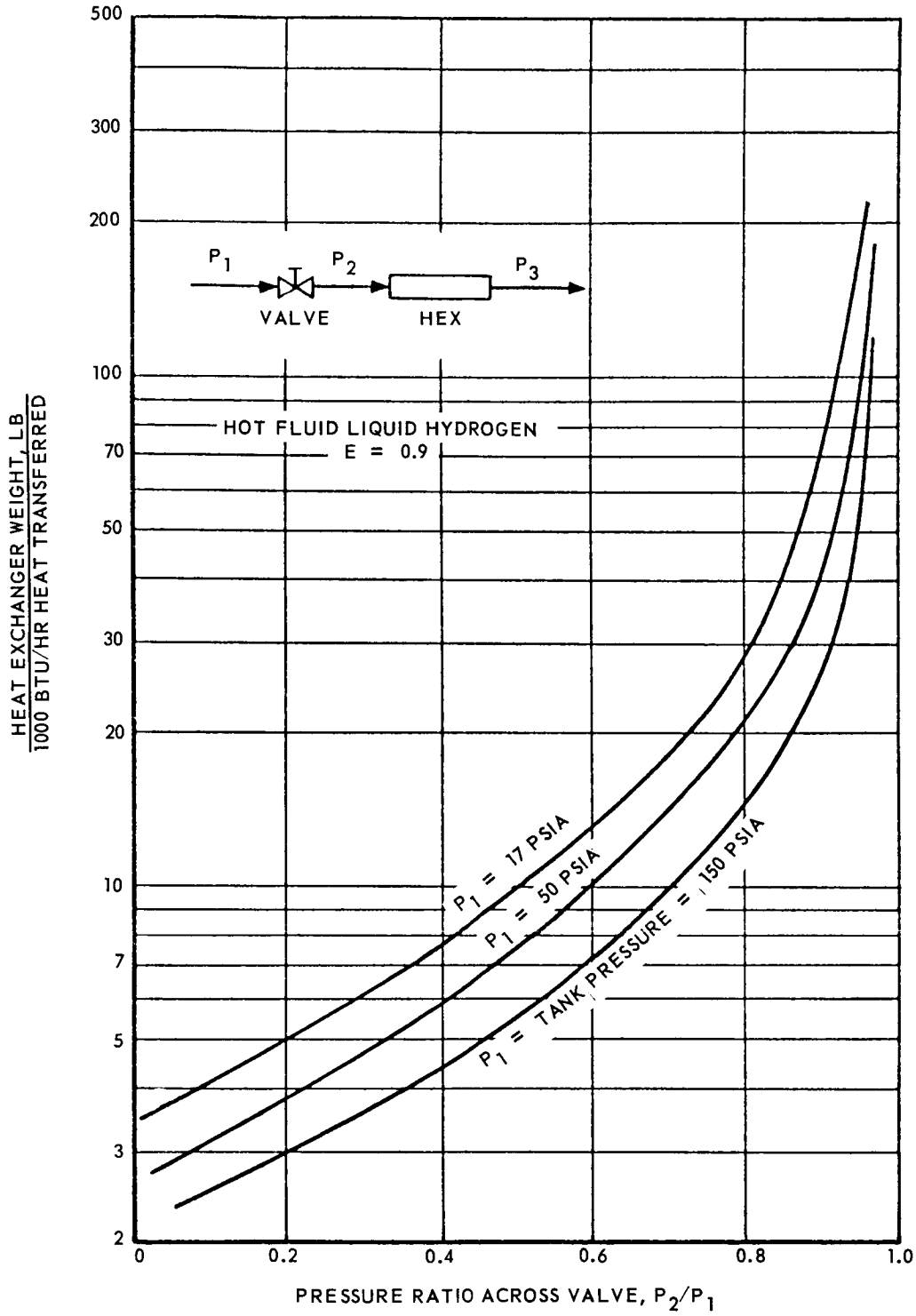

Fig. I-30 Heat Exchanger Weight (With Liquid Hydrogen)

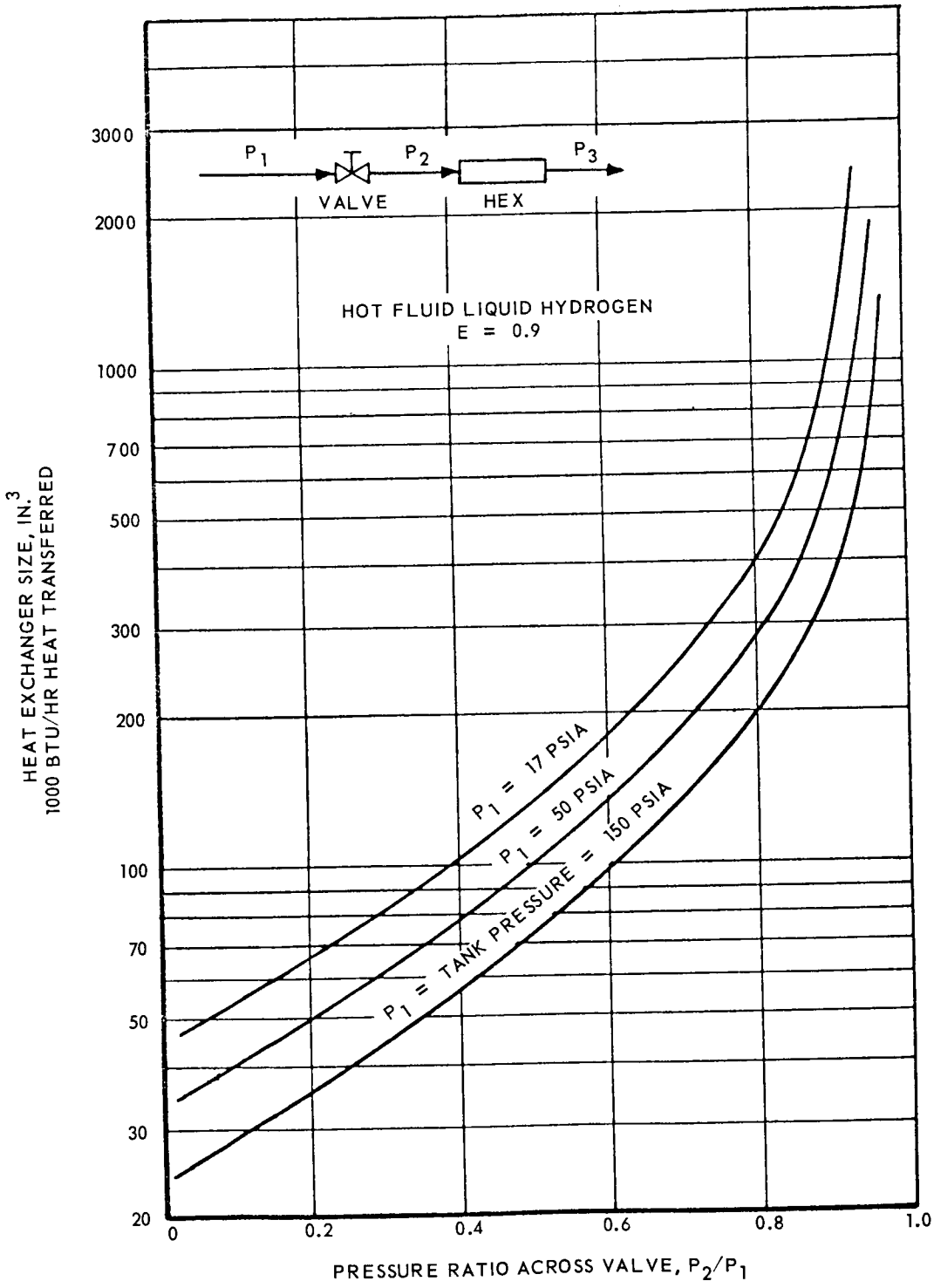

Fig. I-31 Heat Exchanger Size (With Liquid Hydrogen)

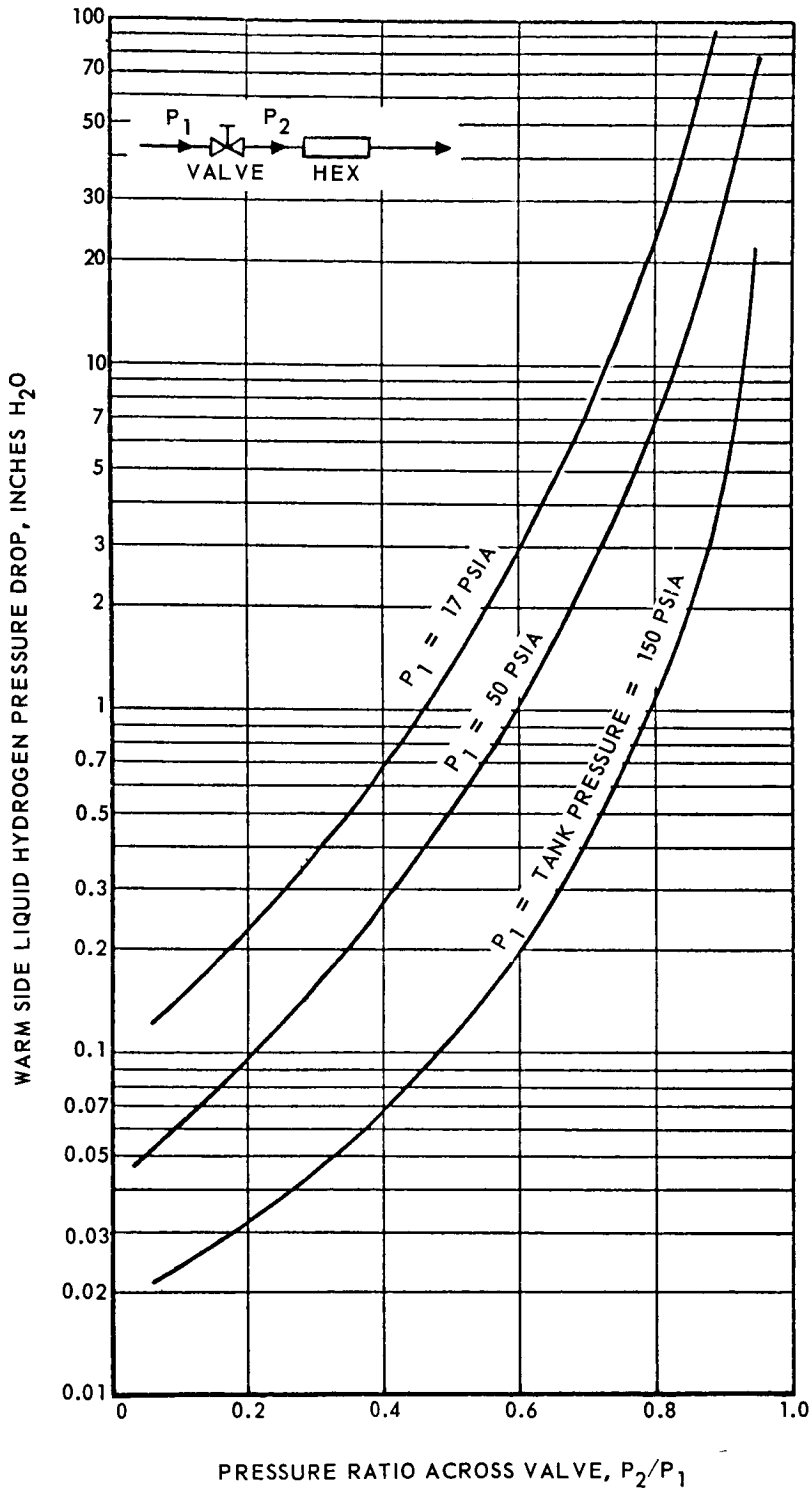

Fig. I-32 Heat Exchanger Warm Side Pressure Drop (With Liquid Hydrogen)

given P_2/P_1 and P_1. It can be seen that the heat exchanger weight and size increase tremendously as the temperature drop across the expansion valve decreases, i.e., as P_2/P_1 increases. The heat exchanger weight and size increase sharply as the expansion ratio exceeds 0.6, and approaches infinity asymptotically as the pressure ratio approaches unity. It should be noted that the heat exchanger weights shown are core weights and do not include manifolding or special packaging requirements. These considerations may result in a 25 percent increase in the weight of the unit.

The weight and size are larger for a given pressure ratio at lower pressures. The same general results were found for the helium pressure drop on the hot side (Fig. I-29). The pressure drop on the cold side (boiling hydrogen) was negligible. The maximum pressure drop at the highest expansion ratio)0.96) and lowest pressure (17 psia) was only 9 in. of water.

It can be seen that relatively light-weight, small size heat exchanger cores are required for any of the reference missions (Table I-1) which have heating rates less than 1000 Btu/hr. For a heat transfer rate of 1000 Btu/hr, heat exchanger cores of about 5 to 6 lb and 70 to 80 cu in. are needed. The compact heat exchanger therefore is a very effective unit for a liquid propellant thermal conditioning system.

Tank Wall Heat Exchanger. The tank-wall heat exchanger is basically a finned tube, with the tank skin as the fin. Figure I-33 shows a typical tank-wall heat exchanger applied to a Mission (2) vehicle. Theoretically, the tank-wall heat exchanger is applicable to either continuous or intermittent operation. Thus, tank pressure control, whether continuous or intermittent, must consider the requirements of or condensation of hydrogen vapor within the propellant tank.

A tank wall heat exchanger can be a tube continuously attached to the tank wall throughout its length, or attached to pins at discrete points on the tank surface. When the tube is attached continuously, and the heat transfer coefficient between the propellant and tank wall is high, most of the vaporization can occur in a relatively small portion of the tube. Consequently, nonuniform cooling of the propellant would result. If a high thermal resistance, which is not affected by the propellant conditions, is inserted,

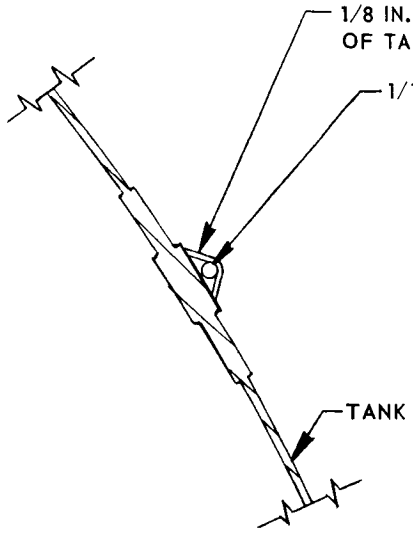

SECTION A

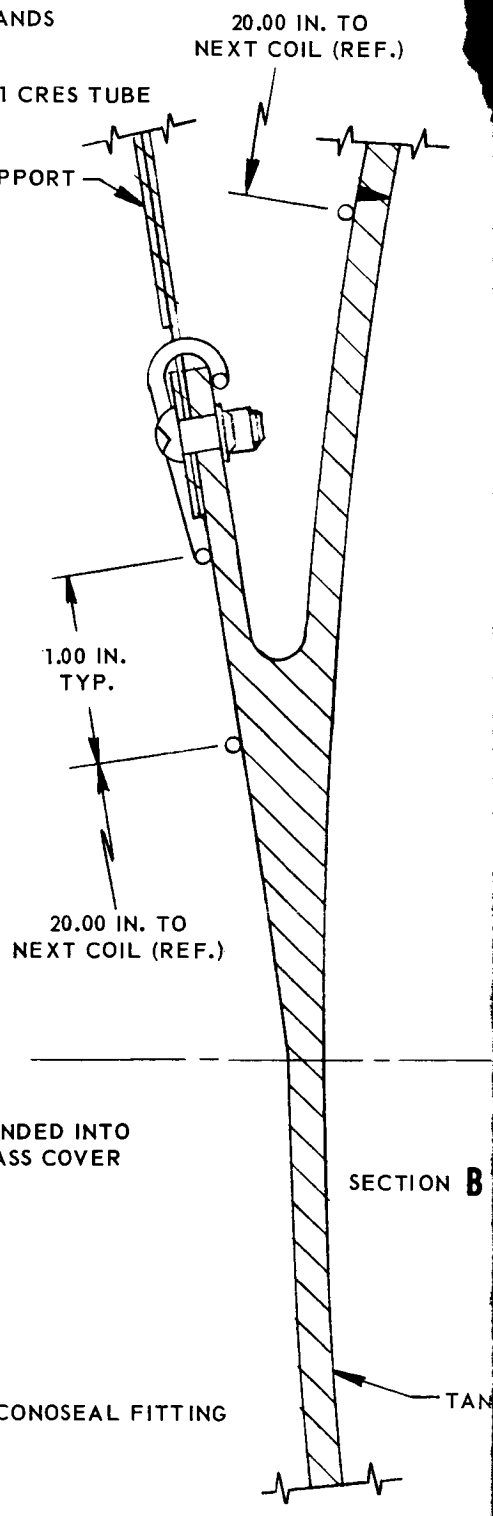

SECTION B

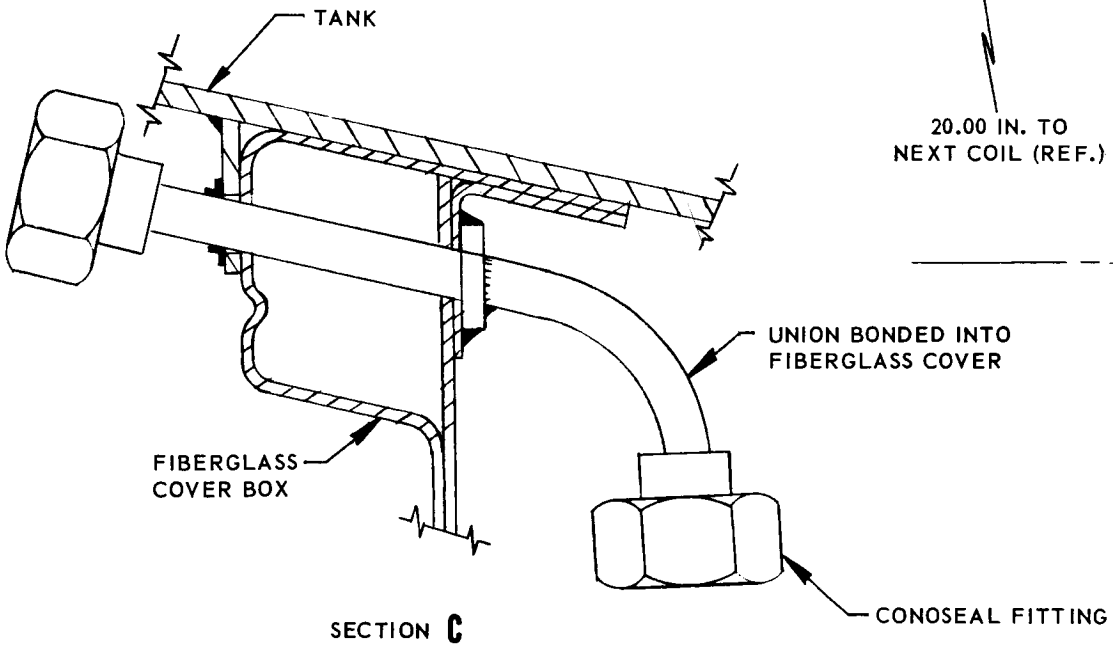

SECTION C

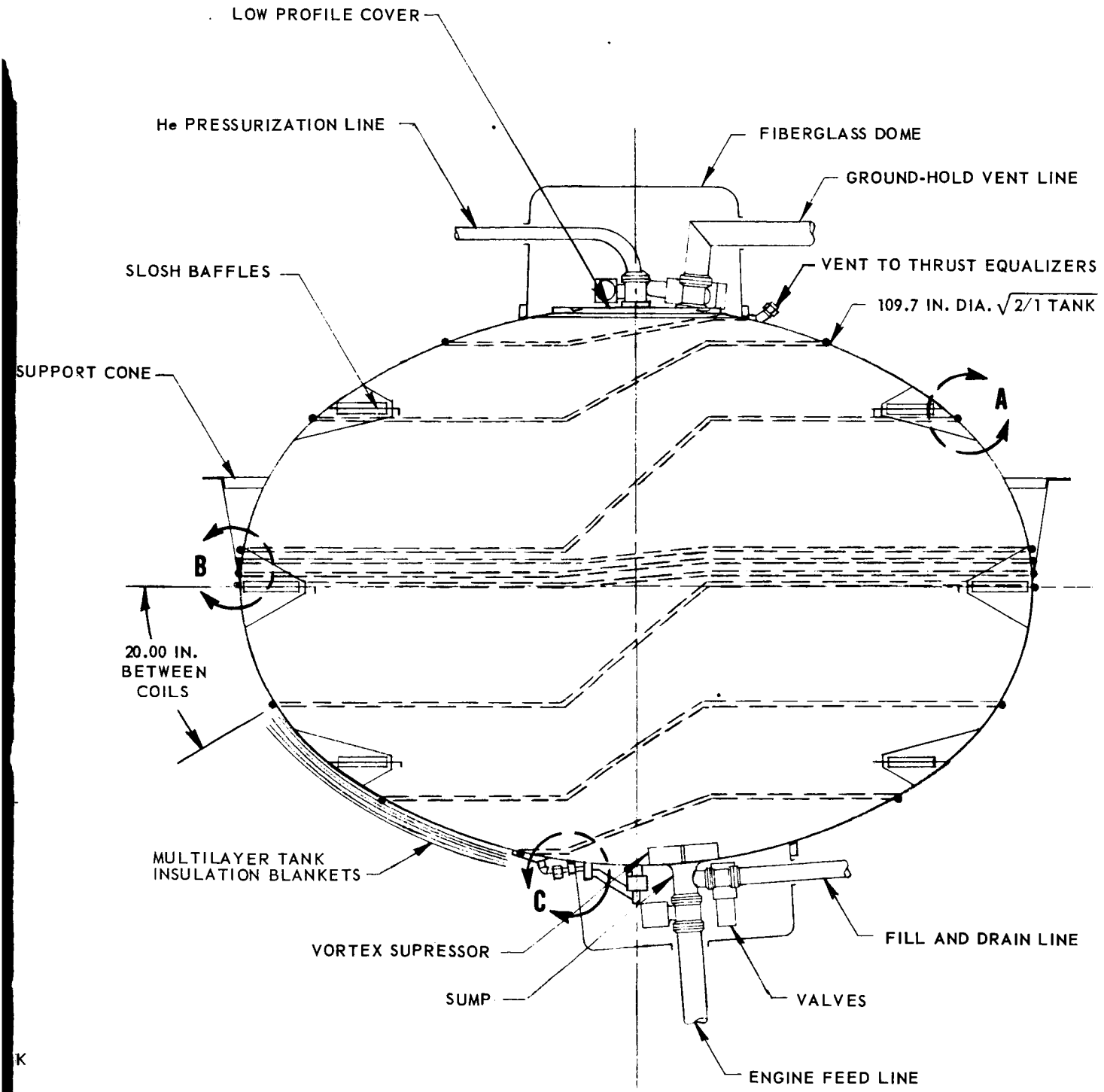

Fig. I-33 Typical Tank-Wall Heat Exchanger Design – Mission (2) Vehicle

it can control the heat flow into a segment of the tube; thus, spacing these point resistances uniformly over the tank tends to ensure more uniform heat transfer and vaporization and should result in more effective pressure control. Therefore, the point attachment method is preferred over the continuous attachment method.

For the discrete point contact, all of the heat is conducted into the pin, of radius a, as shown in this sketch.

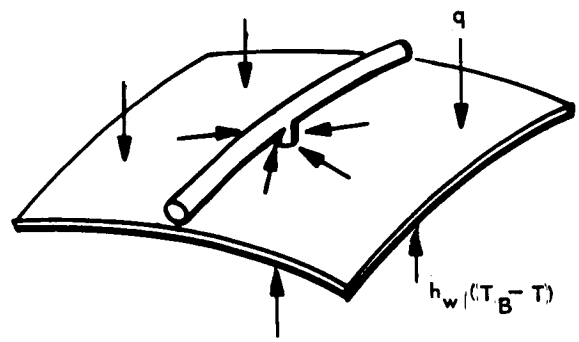

The differential equation describing the temperature distribution in the tank wall is:

$$\frac{d^2T}{dr^2} + \frac{1}{r}\frac{dT}{dr} + \frac{h}{kt}(T - T_B) + q = 0 \qquad (1)$$

To get a closed form solution of this equation, it must be assumed that the heat transfer coefficient between liquid and tank wall and other heat flux is constant over the tank surface. Also, the following two boundary conditions are necessary:

$$\frac{dT}{dr} = 0 \text{ at } r = \infty$$

$$T = T_n \text{ at } r = a$$

The first condition is obvious. The second merely defines, arbitrarily, other temperature at the base of the pin as some constant, T_n. Its relationship to known temperatures is shown later. The assumption of constant h, and the above boundary conditions give the following solution to the differential equation:

$$(T - T^*) = (T_n - T^*) \frac{K_o(r\sqrt{\beta})}{K_o(a\sqrt{\beta})} \tag{2}$$

where $T^* = \left(T_B + \frac{q}{Ah}\right)$

However, it is conservative to assume $q/Ah << T_B$, in which case the heat conducted to the base of the pin is given by

$$Q = 2\pi K_w t_w a\sqrt{\beta} (T_n - T_B) \frac{K_1(a\sqrt{\beta})}{K_o(a\sqrt{\beta})} \tag{3}$$

This equation is plotted in Fig. I-34. The heat conducted into the base of the pin must be transferred into the vented propellant flowing in the tube. This fact can be used to evaluate T_n. If the resistance in the pin is negligible, then

$$Q = h_i A_t (T_n - T_o) \tag{4}$$

Equating these two gives

$$\frac{T_n - T_o}{T_n - T_B} = \frac{K_t t_w}{h_i A} \times \left[2\pi a\sqrt{\beta} \frac{K_1(a\sqrt{\beta})}{K_o(a\sqrt{\beta})}\right] \tag{5}$$

A tank-wall heat exchanger can be divided into evaporator section an a superheater section. In an evaporator where the boiling heat transfer coefficients are very high (Fig. I-35) relative to the conductance in the tank wall, this ratio is much less than 1. Therefore, by making the approximation $T_n \approx T_o$, Eq. (3) becomes:

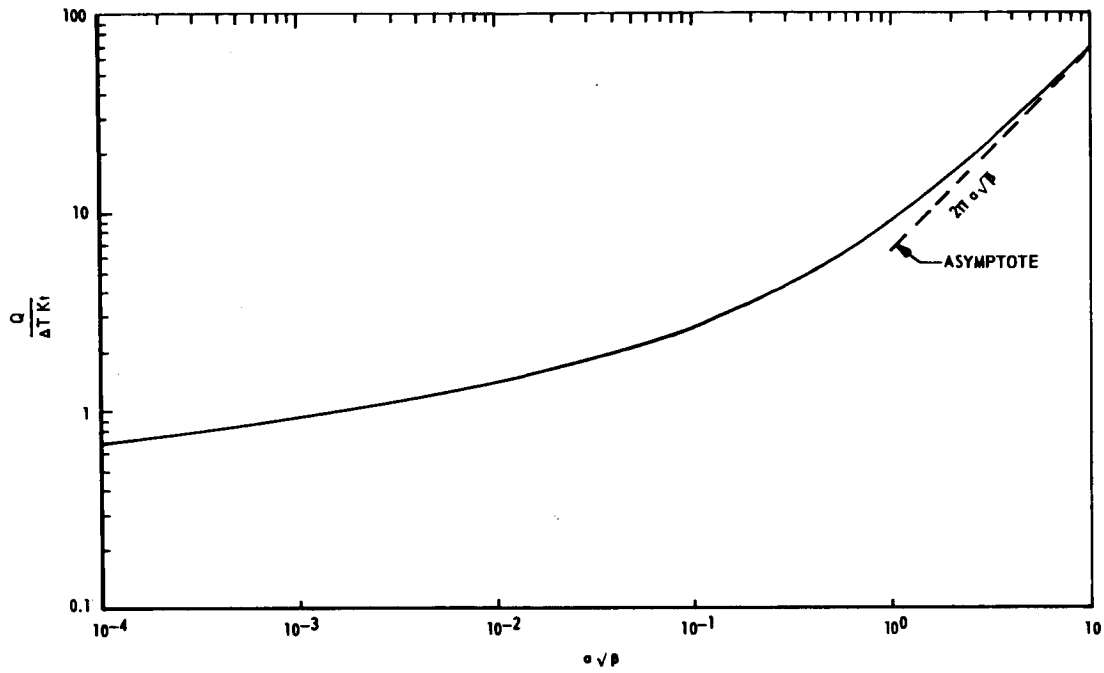

Fig. I-34 Dimensionless Heat Transfer Rates in a Tank-Wall Heat Exchanger

$$Q = 2\pi K_w t_w (T_o - T_B)\, a\sqrt{\beta}\, \frac{K_1(a\sqrt{\beta})}{K_o(a\sqrt{\beta})} \tag{6}$$

In the superheater section, the heat transfer coefficients in the tube are one to two orders of magnitude smaller than the boiling coefficients (Fig. I-36) and $T_n \neq T_o$. Therefore, the general Eqs. (3) and (5) combine to give a more complex expression for the heat transferred at a pin; this is

$$Q = 2\pi K_w t_w (T_o - T_B)\, a\sqrt{\beta}\, \frac{K_1(a\sqrt{\beta})}{K_o(a\sqrt{\beta})} \left[\frac{1}{1 + \frac{K_w t_w}{h_i A_i} \left[2\pi a\sqrt{\beta}\, \frac{K_1(a\sqrt{\beta})}{K_o(a\sqrt{\beta})} \right]} \right] \tag{7}$$

In the superheater, the temperature of the vented propellant is different at each pin, giving a nonsymmetric temperature distribution around each pin. Simultaneously

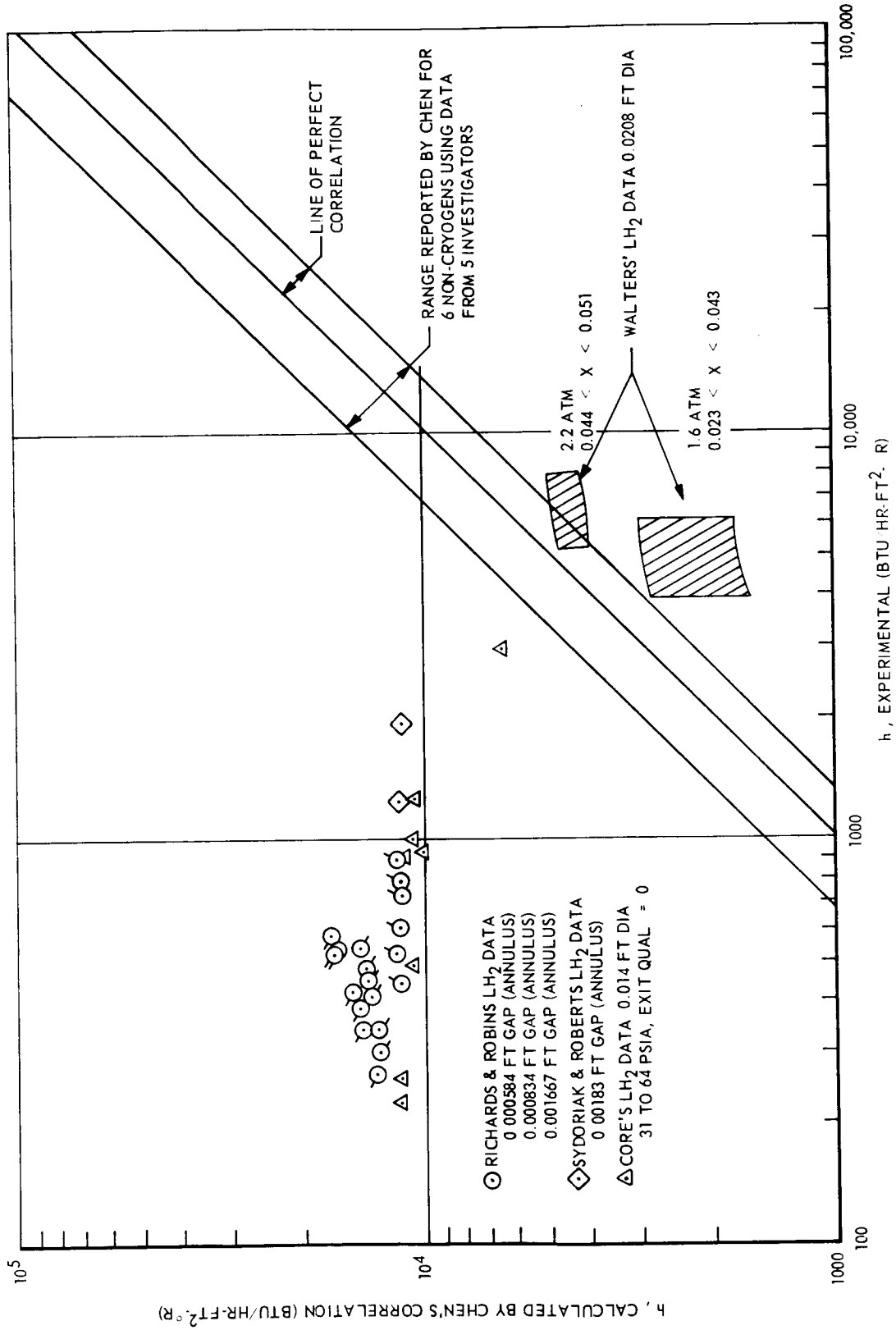

Fig. I-35 Comparison of Experimental and Predicted Convection Coefficient for Forced Convection Saturated Nucleate Boiling of Hydrogen (Using Chen's Correlation)

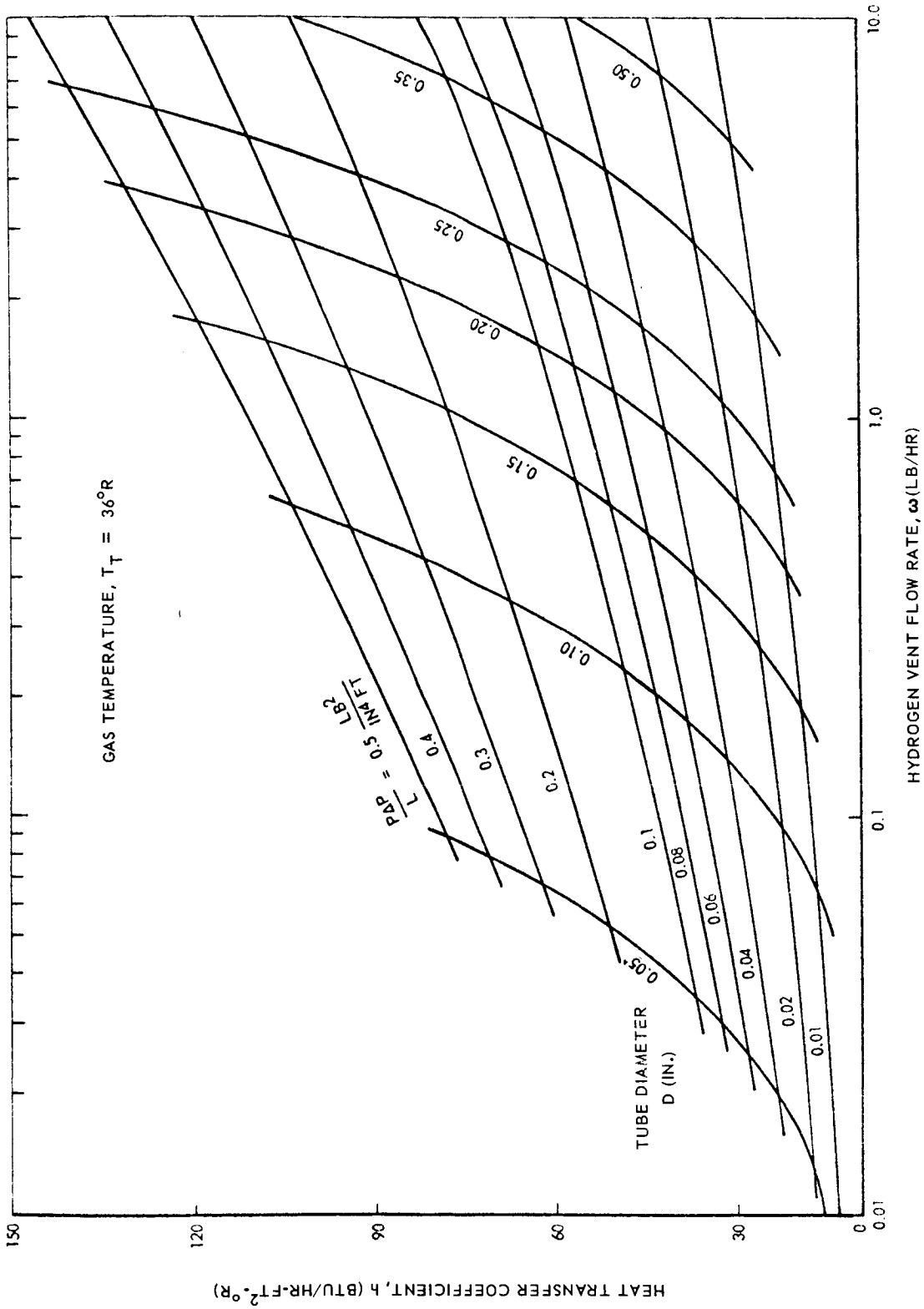

Fig. I-36 Influence of Vent Fluid Rate and Tube Diameter on Cold-Side Heat Transfer Coefficients (Hydrogen Gas Flow)

accounting for nonuniform gradients in the tank wall and a varying sink temperature is an intricate situation requiring that both the wall and the fluid be broken into a nodal network and solved by iteration. This complexity was not pursued.

When only evaporation is being considered, the vent fluid temperature is constant at every point, and the heat transferred at each attach point is the same. Therefore, the total number of pins required for complete vaporization of the vented propellant is given by

$$N = \frac{\omega \lambda}{2\pi K_w t_w (T_o - T_B) a\sqrt{\beta} \dfrac{K_1(a\sqrt{\beta})}{K_o(a\sqrt{\beta})}} \tag{8}$$

These pins must be uniformly spaced over the tank surface and connected by the heat exchanger tubing, in which case the total length of tube is given by

$$L = \left[\frac{\omega \lambda A_s}{2\pi K_w t_w a\sqrt{\beta} (T_o - T_B) \dfrac{K_1(a\sqrt{\beta}}{K_o(a\sqrt{\beta}}} \right]^{1/2} \tag{9}$$

Equation (9) is shown in dimensionless form on Fig. I-37. Using this relationship, one can determine the tube length for a given vent flow rate and tank if the heat transfer coefficient between the propellant and the tank wall is known. If a mixer is used, then the coefficient is a function of the velocity created by this device along the tank wall.

Note that these heat transfer analyses determine only the tube length, with no apparent dependency on the diameter. This is a direct consequence of the assumption that the thermal resistance inside the tube is small compared to that in the tank wall. However, even for such conditions the pressure drop considerations determine the tube diameter, after which the tube weights can be found.

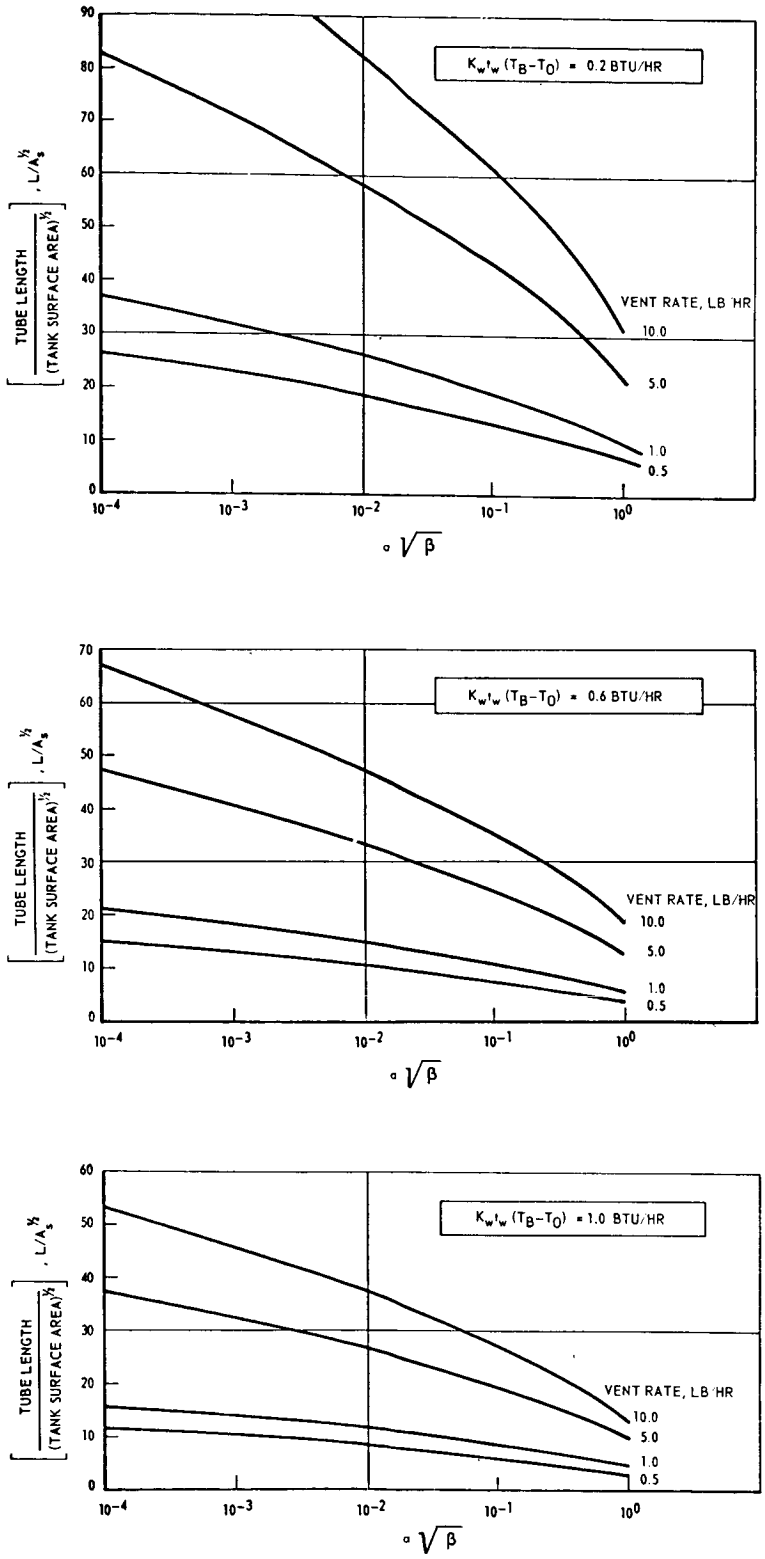

Fig. I-37 Dimensionless Tank-Wall Heat Exchanger Tube Length

The method of calculating pressure drop in the tank wall heat exchanger tube with two-phase flow uses a modification to the Lockhart-Martinelli correlation which accounts for the continuously changing quality of the fluid. Lockhart and Martinelli defined the modulus

$$\Phi_g = \left[\frac{(dP/d\ell)_{TP}}{(dP/d\ell)_g}\right]^{1/2} \tag{10}$$

and they assumed that Φ_g could be correlated by the modulus

$$\chi = \left[\frac{(dP/d\ell)_\ell}{(dP/d\ell)_g}\right]^{1/2} \tag{11}$$

which reduces to

$$\chi = \left(\frac{1 - x}{x}\right)\left(\rho_g/\rho_\ell\right)^{1/2}\left(\frac{\mu_\ell}{\mu_g}\right)^{0.1} \tag{12}$$

The total two-phase pressure gradient can be related to the pressure gradient of saturated vapor.

$$\frac{\Delta P_{TP}}{\Delta P_{100}} = \frac{\Delta P_{TP}}{\Delta P_g}\,\frac{\rho \Delta P_g}{\Delta P_{100}} = \Phi_g^2\, x^{1.8} \tag{13}$$

Using the conventional Fanning equation for pressure drop when all saturated vapor is flowing gives

$$\left(\frac{\Delta P}{\Delta \ell}\right)_{100} = \frac{32 f\, \omega^2}{D^5\, g_c\, \pi^2\, \rho_g} \tag{14}$$

Therefore,

$$\left(\frac{\Delta P}{\Delta \ell}\right)_{TP} = \frac{32 f \omega^2}{\pi^2 g_c \rho_g D^5} \left\{ \Phi_{g_1}^2 \; x^{1.8} \right\} \tag{15}$$

Since this is the local gradient, based on local quality, integration between entrance and exit qualities is necessary to get the total pressure drop. The resulting equation for hydrogen is

$$P \left(\frac{\Delta P}{\Delta L}\right)_{TP} = 2.5 \times 10^{-7} \frac{T \omega^{1.8}}{D^{4.8}} \int_{x_1}^{x_2} \Phi_g^2 \; x^{1.8} \tag{16}$$

The integral is plotted in Fig. I-38 as a function of pressure. From this expression and that for the required tube length, the tube diameter, and thus the weight of the tank-wall heat exchanger, can be found.

The weight of the tube is given by

$$W_t = \pi \rho_t t_t DL \tag{17}$$

Rearranging Eq. (16) to solve for D , and then combining with Eq. (9), the final expression for tube weight becomes

$$\frac{W_t}{\omega} = \pi \rho_t t_t \left\{ \left[\frac{A_s \lambda}{2\pi K_w t_w (T_o - T_B a\sqrt{\beta} \frac{K_1 a\sqrt{\beta}}{K_o a\sqrt{\beta}}} \right]^{0.6} \left[\frac{2.57 \quad (10^{-7}) T_o \int_{x_1}^{x_2} 1.8 \, \Phi_g^2 \, x^{1.8}}{P \Delta P} \right]^{0.21} \right\} \tag{18}$$

If the entrance and exit pressures are selected, the temperatures and quality integral are fixed. The tank wall, tube wall, and fluid properties are fixed, then Eq. (18) reduces to the functional relation

$$\frac{W_t}{\omega} = f\,(P\,,\ \Delta P\,,\ A_s\,,\ a\sqrt{\beta}) \tag{19}$$

These tube weights are shown parametrically in Figs. I-39 through I-42, wherein a stainless steel tube of 0.006-in. wall thickness is assumed.

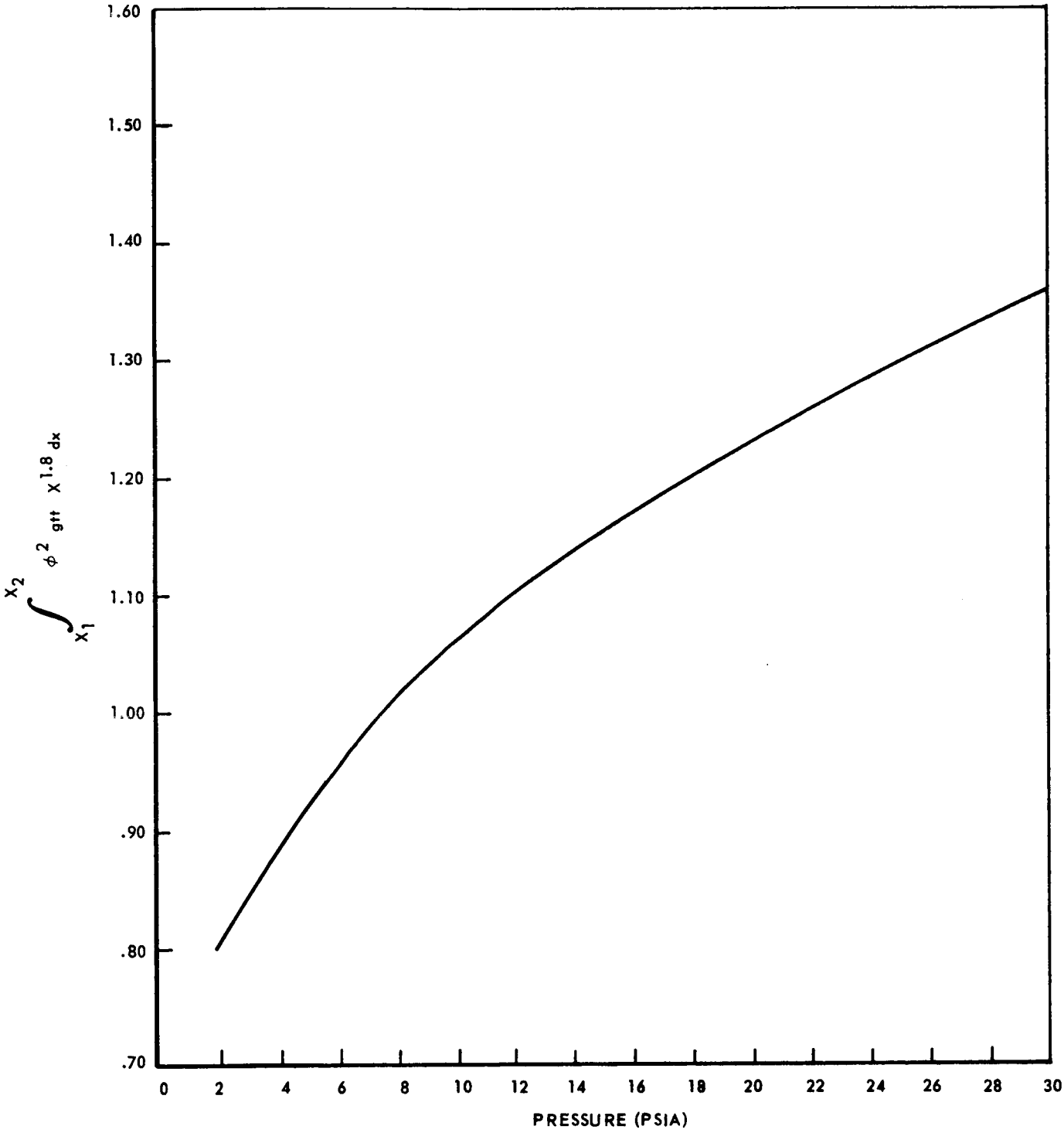

Fig. I-38 Integrated Two-Phase Pressure Drop Parameter

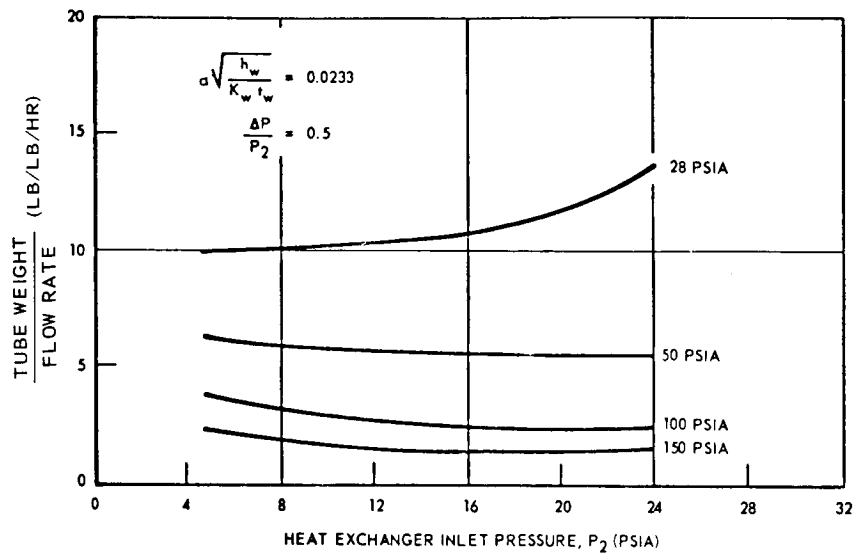

Fig. I-39 Effect of Tank Pressure and Valve Discharge Pressure on Tank-Wall Heat Exchanger Weight (Tank Area = 5600 Sq Ft)

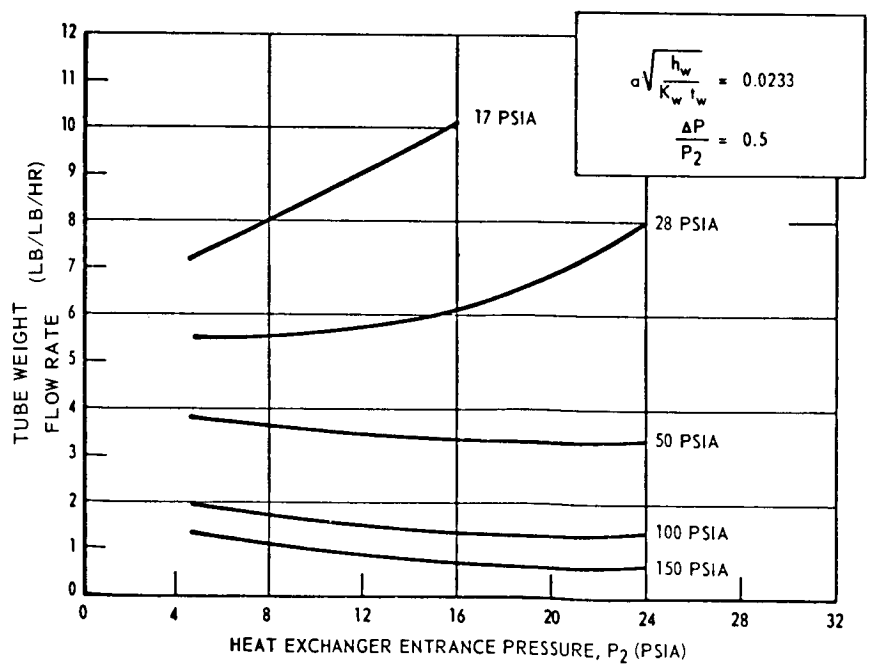

Fig. I-40 Effect of Tank Pressure and Valve Discharge Pressure on Tank-Wall Heat Exchanger Weight (Tank Area = 600 Sq Ft)

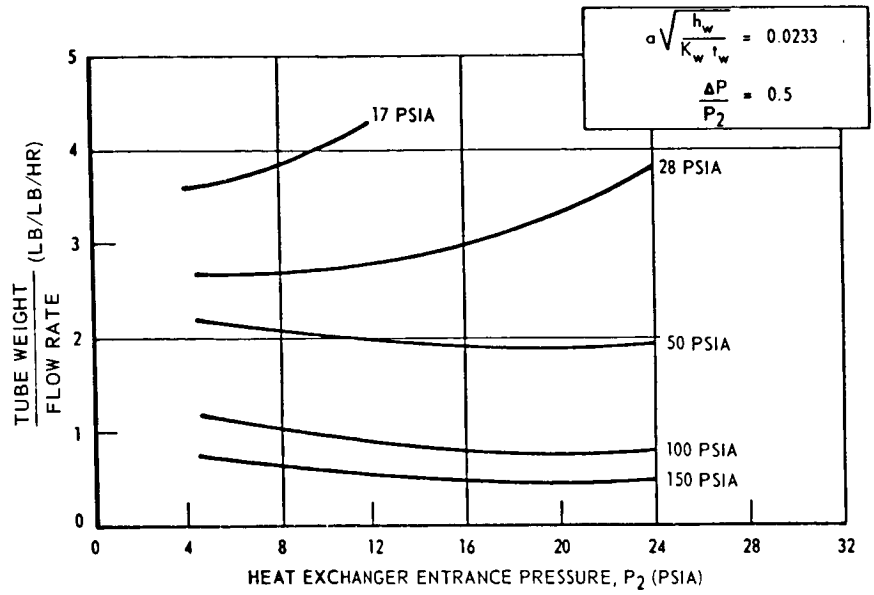

Fig. I-41 Effect of Tank Pressure and Valve Discharge Pressure on Tank-Wall Heat Exchanger Weight (Tank Area = 200 Sq Ft)

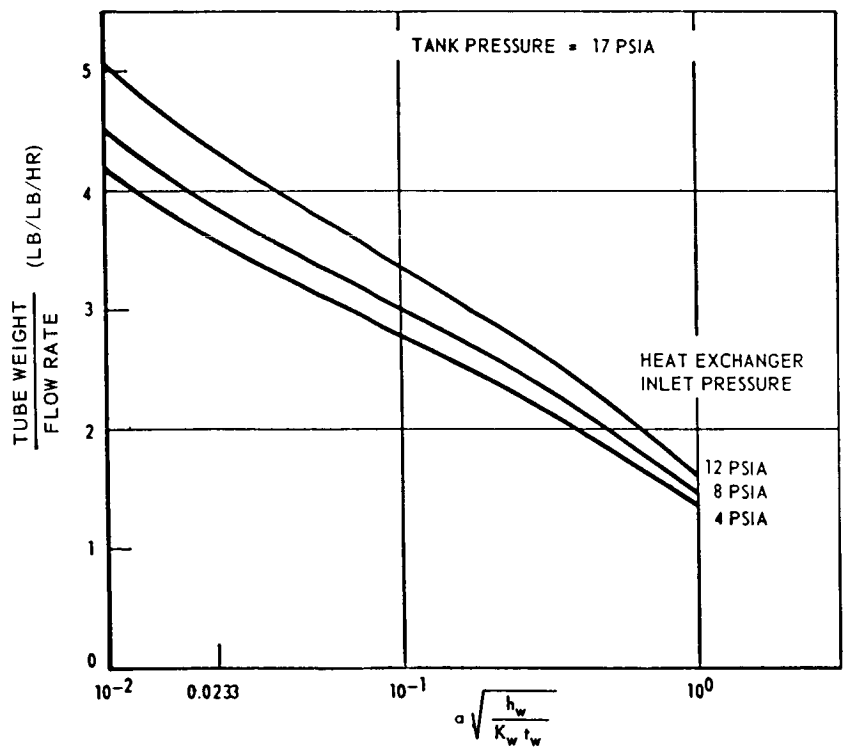

Fig. I-42 Effect of Heat Transfer Coefficients on Tank-Wall Heat Exchanger Weight (Tank Area = 200 Sq Ft)

In the development of this analysis, it was assumed that the heat transfer coefficient was uniform. If the mixer discharge is not contained, the velocity and heat transfer coefficient decay with increased distance from the discharge point. For conservatism the lowest value on the wall should be used. One can achieve a constant heat transfer coefficient by channeling the mixer discharge flow along the wall with an internal shroud. The weight of such a shroud is shown in Figs. I-43 through I-45 for Missions (1) through (3), respectively. It can be seen that the weight of the shroud overshadows tube weight if it extends a significant way up the tank. However, the tank-wall heat exchanger, like the compact heat exchanger, can be concentrated locally, since successful operation depends upon mixing of the propellant. For example, the necessary tubing might be concentrated over the lower 10 percent of the Mission (2) vehicle, and this requires only 4.7 lb of shroud.

A preliminary design study was conducted to establish the additional weight involved for proper attachment of the heat-exchanger tubing to the tank wall. Direct bonding with an adhesive appears to be the lightest installation. However, repeated experience indicates that such adhesive bonding directly to aluminum liquid hydrogen tanks is unreliable with currently available adhesives. Consequently, it was decided to weld aluminum clamps to the tank at properly located attach points. These clamps then secure the tube in place. This attachment technique requires small circular weld lands, uniformly spaced over the tank. The results of this preliminary design effort indicate that the combined weight of weld lands, clamps, and tube fittings is twice that of the tube found from Figs. I-39, I-40, and I-41. Therefore, the heat-exchanger weight is approximately three times that obtained from these figures.

A comparison of the weights of a tank-wall heat exchanger and a compact heat exchanger show that there is no significant weight advantage of one over the other. For example, from Fig. I-27, a compact heat exchanger designed for a vent rate of 1 lb/hr (190 Btu/hr) at a tank pressure of 17 psia will weigh approximately 1.1 lb. From Fig. I-41, a tank wall heat exchanger will weigh approximately 3.5 lb for the Mission (2) vehicle. Selection of the appropriate heat exchanger unit for the thermal conditioning system therefore must be made on other bases. The heat exchanger must be integrated into the insulation or thermal protection system of the liquid hydrogen tank (Fig. I-33).

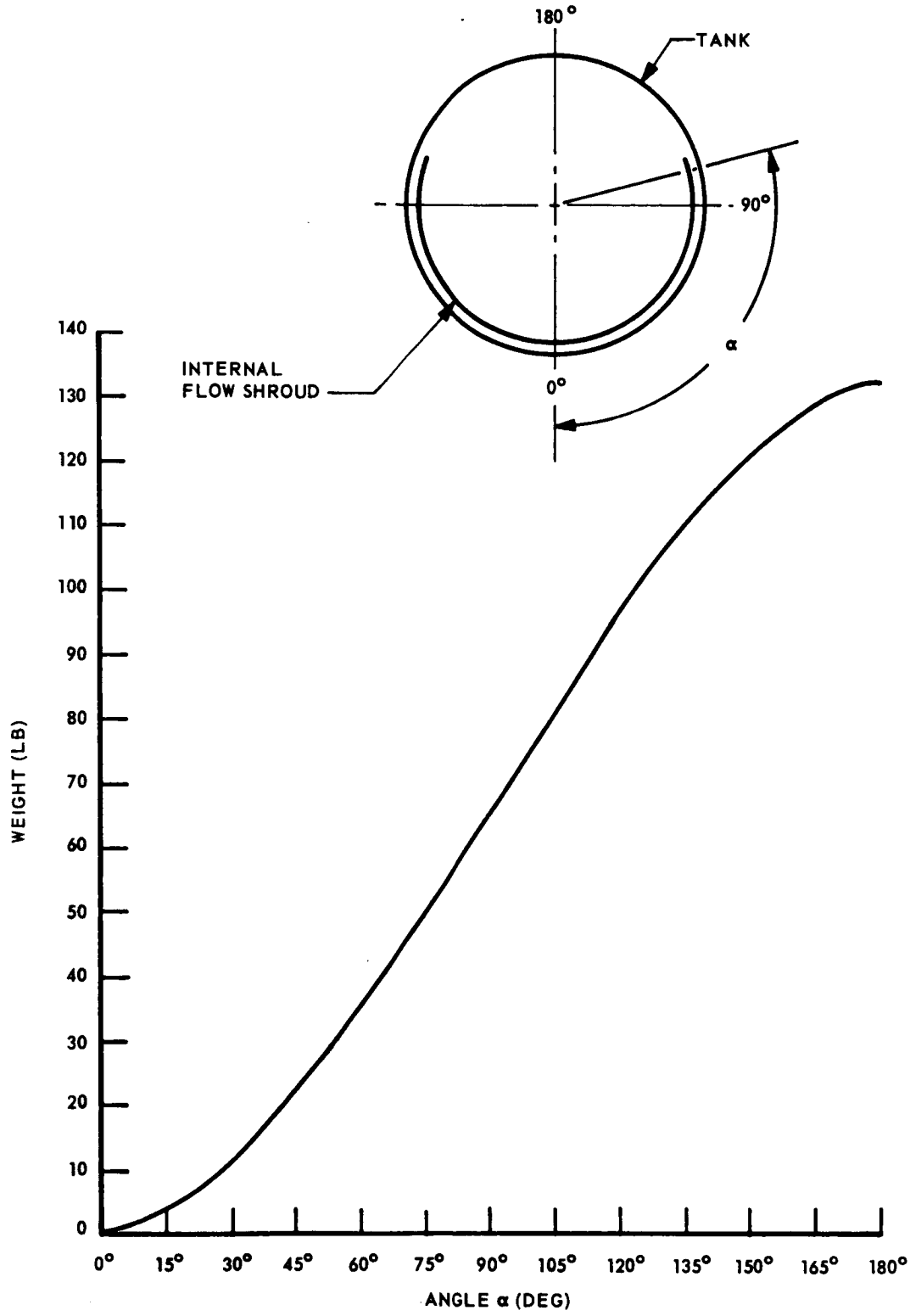

Fig. I-43 Internal Shroud Weight – Mission (1) Vehicle

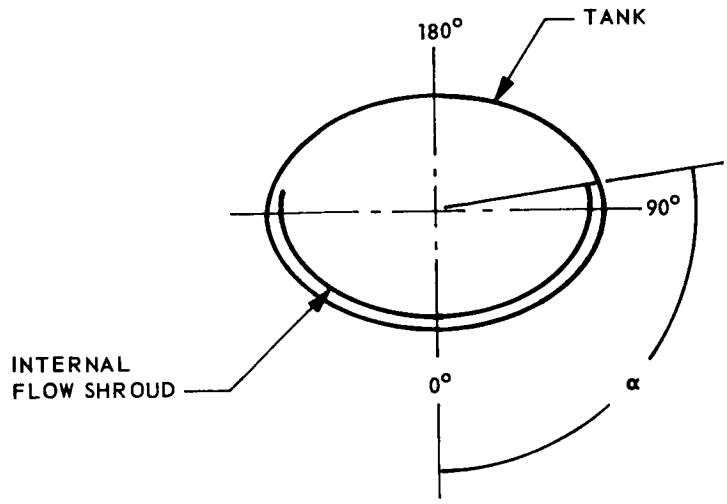

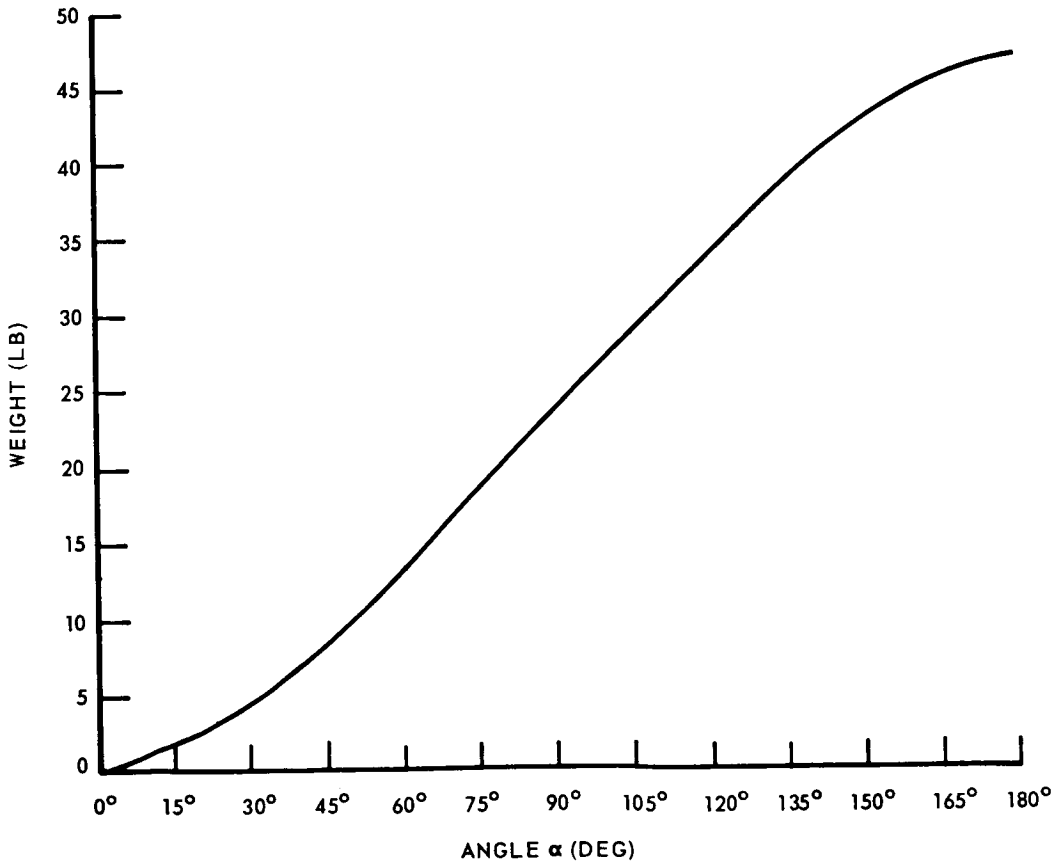

Fig. I-44 Internal Shroud Weight – Mission (2) Vehicle

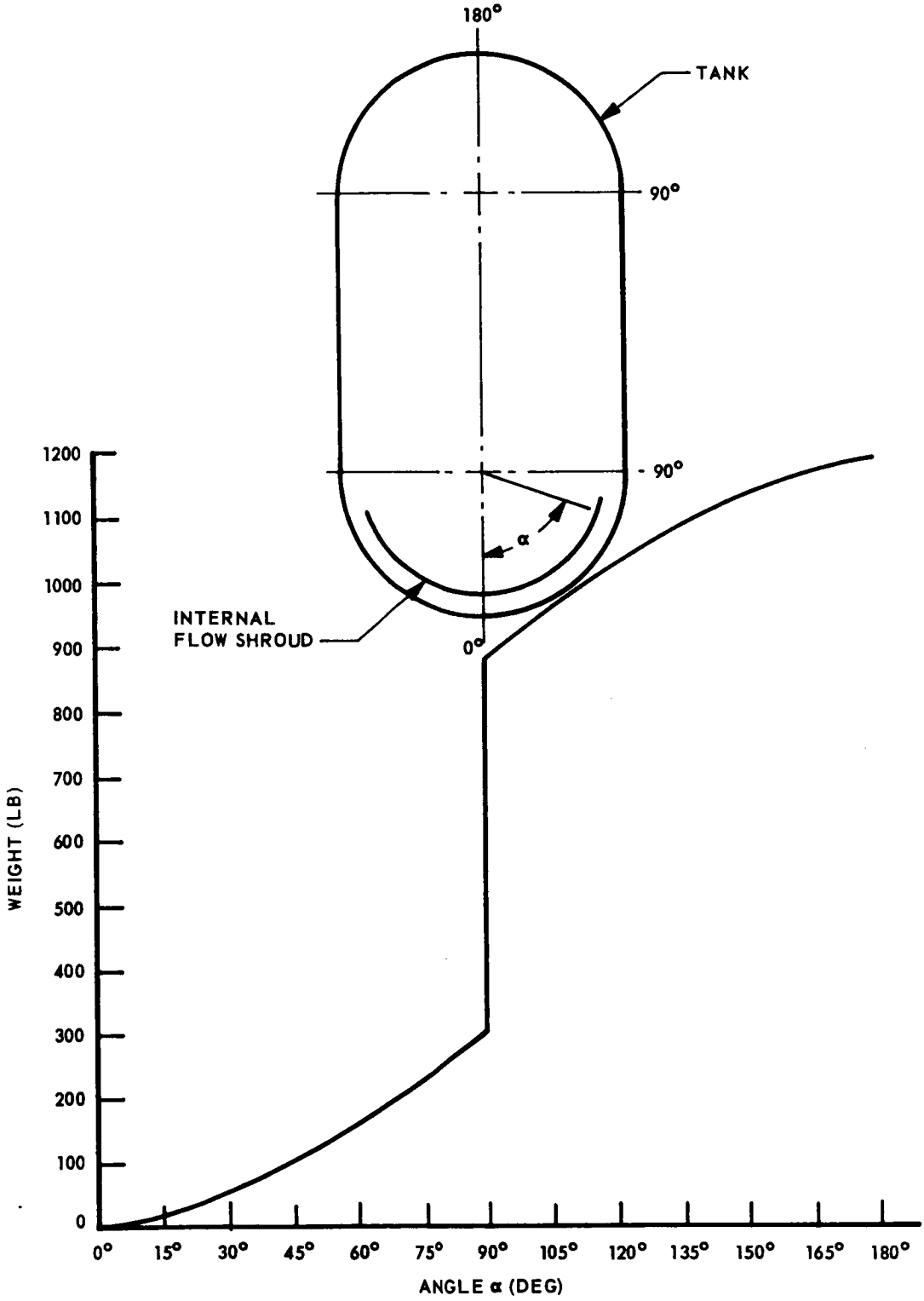

Fig. I-45 Internal Shroud Weight – Mission (3) Vehicle

In the event of small leakage of hydrogen gas from fittings, joints, and from the tubing itself, a degradation in the effectiveness of the thermal protection system will occur. In fact small gas leak rates large enough to increase the interstitial pressure within the insulation to greater than 10^{-5} torr vacuum will rapidly cause the thermal protection system to lose its insulative properties. Such leaks may easily occur in a tank-wall heat exchanger during launch and ascent vibration and acoustic loading. With a compact heat exchanger mounted inside the propellant tank such leaks are of no consequence.

Also in the event a leak or malfunction in the tank-wall heat exchanger is detected during stage assembly, erection, or ground-hold check-out, a large-scale disassembly of the thermal protection system, instrumentation, and other associated subsystems would be required to effect a repair. The repair would have to be made with the vehicle in place on the launch pad. If this were impractical, then the complete stage would have to be removed and replaced with a new stage. The contrast in magnitude of such a repair operation is sharpened when compared to the simple replacement of a 10 to 15 lb thermal conditioning unit having a compact heat exchanger mounted on the inside surface of the easily removed and replaced man-hole cover of the tank.

Because no advantages could be defined for the tank-wall heat exchanger, but several significant and very real disadvantages were defined, no further work on the tank-wall heat exchanger was conducted. On these bases, the compact heat exchanger unit concept was selected for the thermal conditioning system.

Flow Regulator Unit

It is necessary to control both the flow rate and the pressure in the cold side of the heat exchanger so that the heat loads and the available temperature difference are known. If the pressure regulator shown in Fig. I-16 is used, then a flow regulator placed downstream from the heat exchanger is required in the system. Such a device is schematically shown in Fig. I-46.

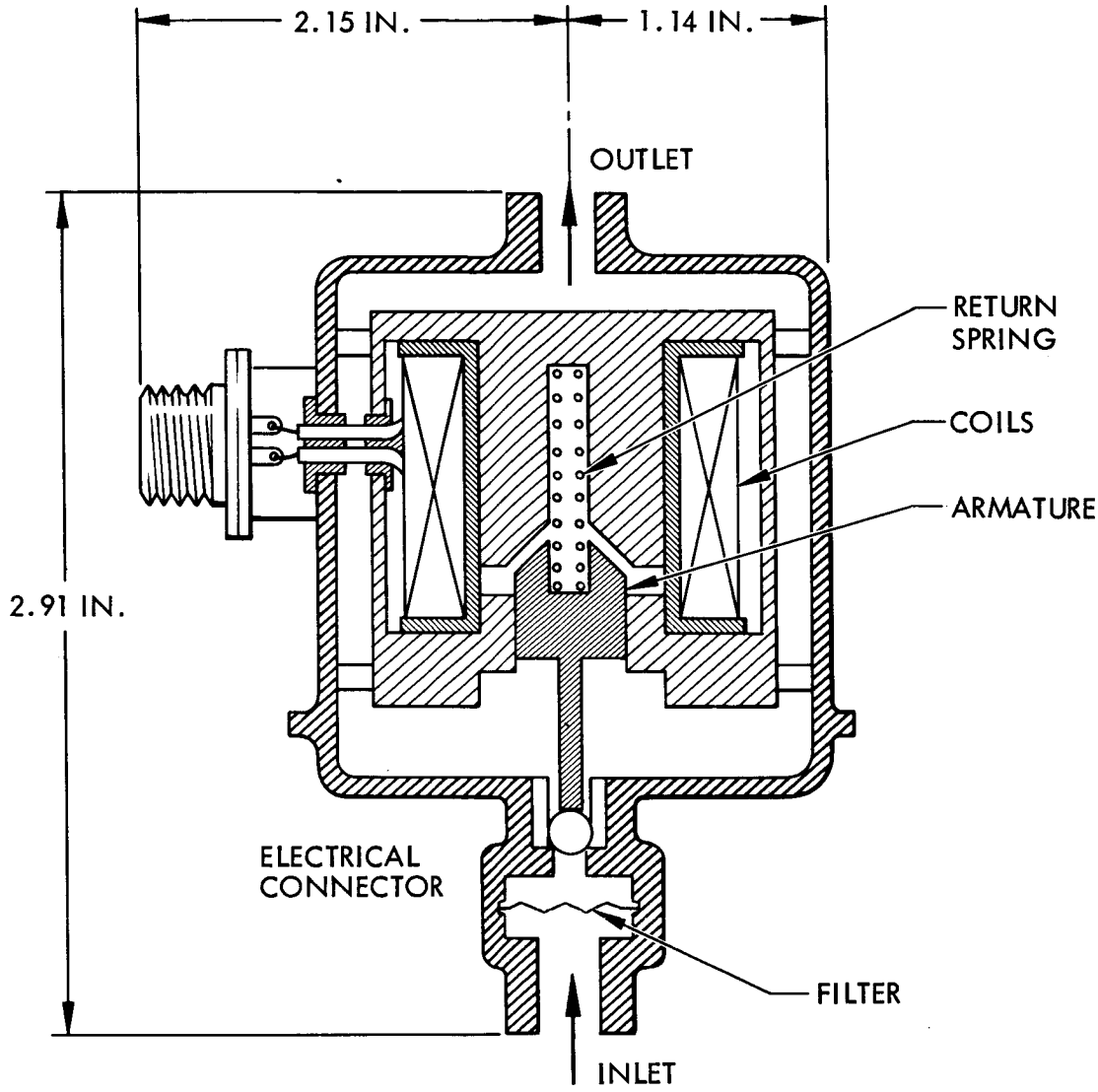

Fig. I-46 Solenoid Valve

This valve unit consists of a solenoid valve with a current limiting assembly located outside the propellant tank. The current limiter is a semiconductor device which will allow a high current to pass for 300 to 500 ms to allow the solenoid to pull in. The current then drops to a low value (about 30 ma) to hold the solenoid valve in the open position. With this approach, no coil compensation is necessary to limit current flow. The resultant holding power requirement is maintained below 1 w.

The flow limiting orifice diameter will be approximately 0.065 in. A filter will be placed downstream of the heat exchanger to prevent particles from plugging the orifice. A built-in filter, as noted previously, will be placed on the pressure regulator (Fig. I-16) to prevent possible particulate contamination from the propellant tank. The weight of the flow regulator unit is about 1 lb.

Mixer Unit

A mixer unit may be required in a thermal conditioning system for one or both of two reasons, as follows:

- To provide the necessary convective velocities through the hot side of the compact heat exchanger
- To provide sufficiently high fluid velocities within the tank to cause hydrogen vapor condensation of bubbles formed by boiling at hot spots on the tank wall wall

The appropriate mixer characteristics are those fulfilling the severest requirements imposed by either of these reasons. In this section of the report, the parametric data covering a wide range of performance for the mixer unit are presented. Specific matching of the mixer unit to the conditions referred to above are treated in later sections of this report.

One of the basic parameters used to determine operational characteristics of the mixer is the specific speed (N_S) which is defined here (using pump terminology) as:

$$N_S = \frac{N\sqrt{Q}}{(H)^{3/4}}$$

The weight and volumetric flow rate and the fluid head and exit velocity are mutually convertible. In Fig. I-47, the weight flow is plotted as a function of the ratio of specific speed to rotational speed with the fluid exit velocity as a parameter. The relationship between the efficiency and the specific speed for various mixer configurations is shown in Fig. I-48. These curves were obtained from various data on pumps. The efficiency values shown are the achievable average values for

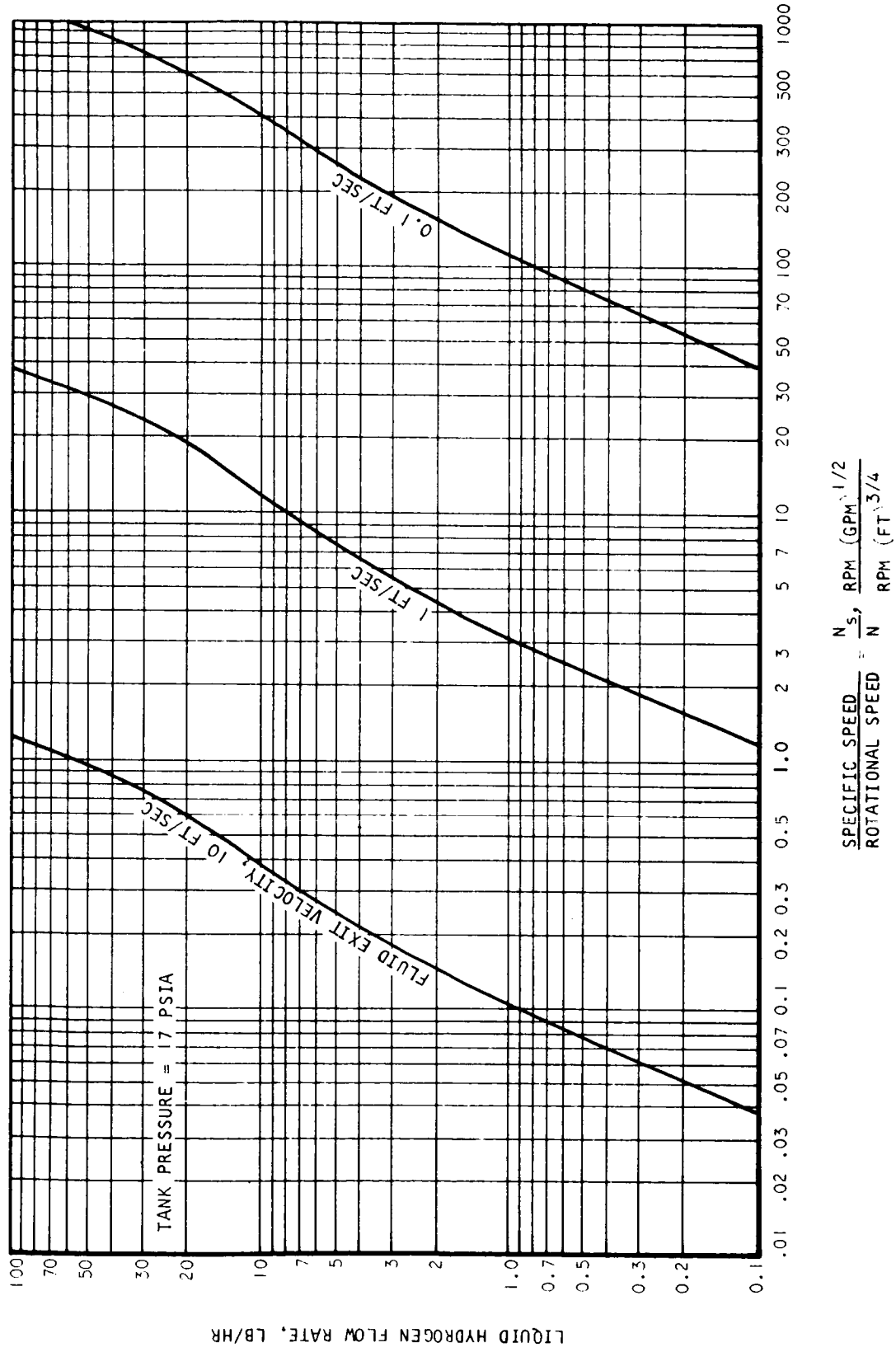

Fig. I-47 Mixer Specific to Rotational Speed Ratio

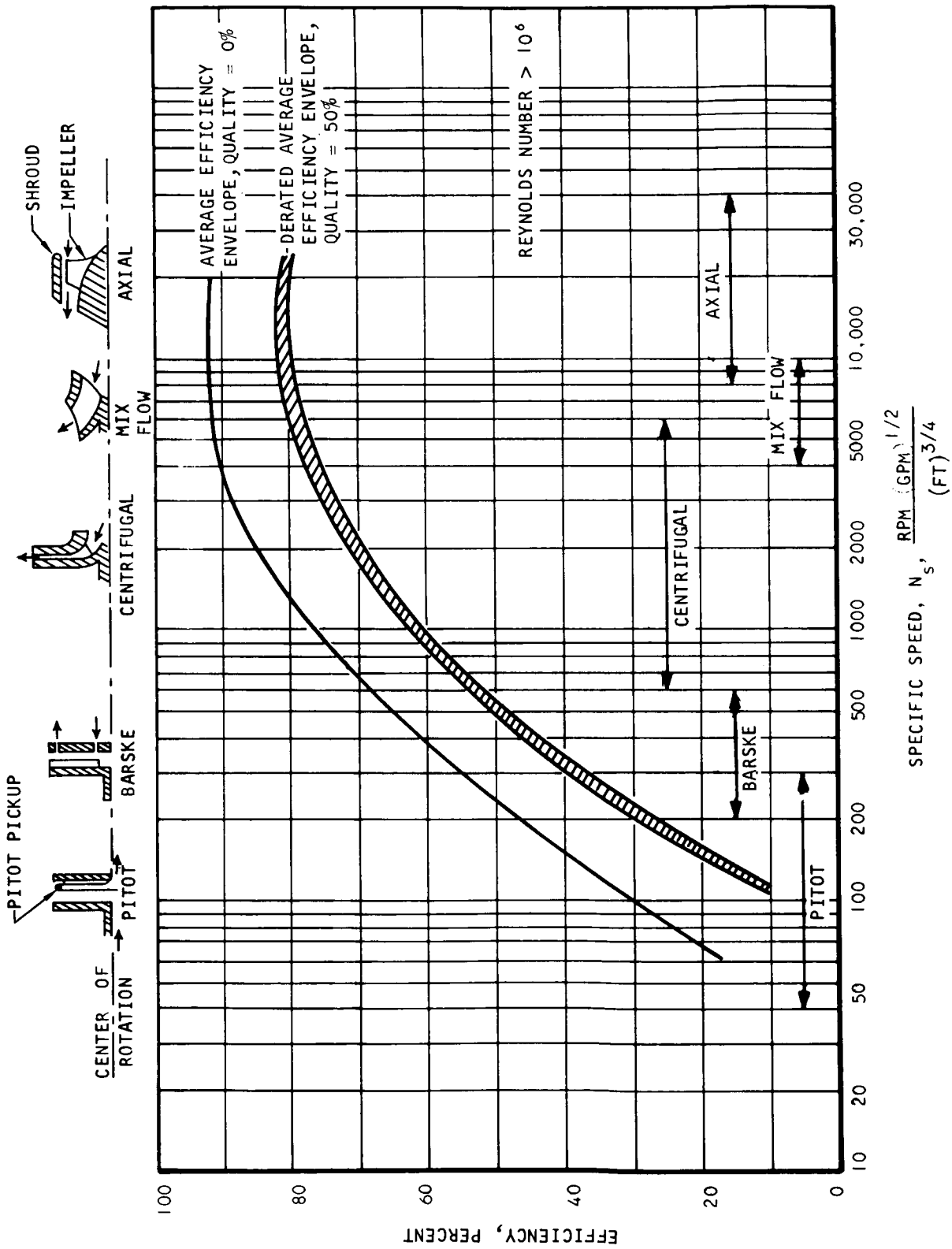

Fig. I-48 Efficiency Characteristics of Various Mixer Types

the different types of machines operating within the ranges noted. The efficiency of a mixer designed for operation in liquid will be decreased when operating in a two-phase mixture. The dotted line in Fig. I-48 is the estimated efficiency envelope for two-phase flow at 50 percent quality. Although a given type of machine can operate over a wide range of specific speeds, it is desirable to design the type of unit which experience has shown to be the most efficient for a given specific speed. For very low specific speeds a pitot unit with a rotating housing is used. The internal blading is designed to produce a solid body of rotating fluid within the fluid housing. Inside the housing one or more pitot tubes are installed with the tip located at the extreme diameter to collect the high pressure rotating fluid. The pitot passes through the housing along the centerline. In the Barske unit, the impeller has radial vanes and fits in the housing with a relatively large clearance. Here also the fluid rotates as a rigid body and is delivered through relatively narrow jets in the housing. In the centrifugal units, the flow is radial and the required pressure rise is obtained by imparting a centrifugal force to the fluid. In the axial unit, the flow is, of course, axial to the center of rotation and this type unit is generally used to obtain high volumetric rates with a small pressure rise. For speeds in the 5000 to 10,000 range the mix flow design is used. Here the flow is partially axial and partially radial to the center of rotation of the impeller.

The efficiency envelope shown is valid for Reynolds numbers greater than 10^6. If the Reynolds number is below 10^6, the efficiency will be decreased significantly for low specific speed machines but only slightly for high specific speed units. The Reynolds number Re is defined as:

$$Re = \frac{DU}{\nu}$$

Once the ratio of the specific speed and the rotational speed is obtained from Fig. I-47, the variable that must be determined is the rotational speed. This can be determined by choosing an appropriate specific speed range that results in high efficiency (Fig. I-48). The rotational speed and rotor size must then be evaluated with respect to the required operating conditions. Figure I-49 is a working chart showing the relationships between rotational and specific speeds.

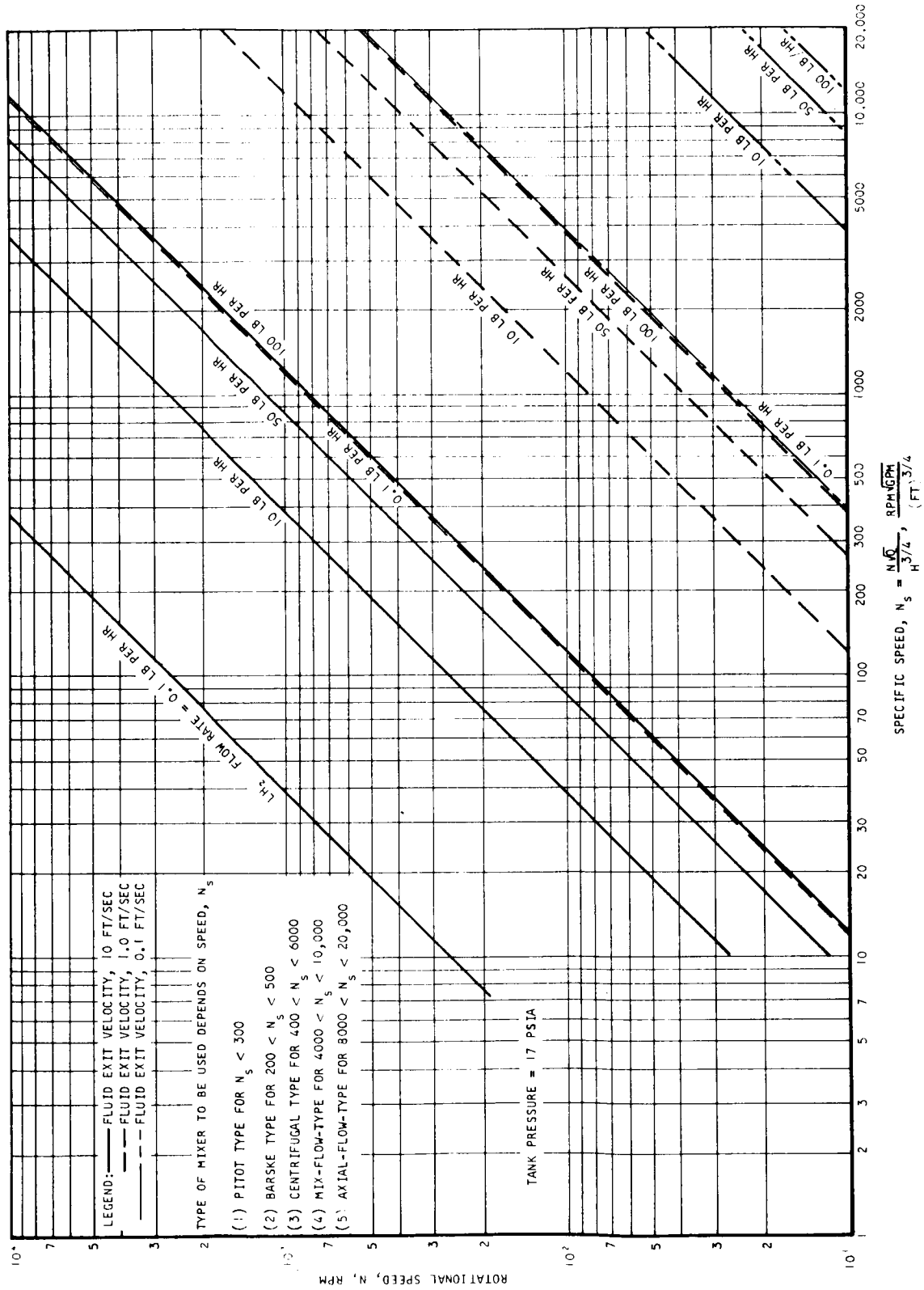

Fig. I-49 Rotational and Specific Speed Chart

The diameter of the rotor (D, in in.) is

$$D = \frac{720\ U}{N\pi}$$

where N is the rotational speed in rpm. Figure I-50 is a working chart showing the relationships between N, U, D, and fluid exit velocity V.

To determine the tip speed, the head coefficient, defined as $H/U^2/g$, must be evaluated. For different blade design and efficiencies, there are corresponding values of head coefficient ψ. The usual ranges of head coefficient are 0.6 to 0.8 for radial blading and 0.4 to 0.6 for backward blading. Radial blading is used in machines with low specific speeds (Barske and pitot) while backward blading is used for large specific speed machines such as centrifugal and axial machines. Two lines, A-A' and B-B', are superimposed on the D-U-N map of Fig. I-49, for ψ values of 0.5 and 0.7. These lines represent the average values for backward and radial blading, respectively. With a given fluid exit velocity and blade design, the tip speed can be determined from Fig. I-50. The diameter of the rotor is determined by moving horizontally from the ordinate (tip speed) to the rotational speed and then moving vertically.

It is desirable to obtain Reynolds numbers in excess of 10^6. This requirement gives rise to two conditions which are also functions of vapor quality, namely:

$DU > 23.8$ for $X = 0$ percent
$DU > 346$ for $X = 50$ percent

Two lines, C-C' and D-D', corresponding to the equality signs of the two conditions, are superimposed on the D-U-N map. To ensure good performance, the chosen rotational speeds should fall to the right of the C-C' and D-D' lines.

Figure I-51 shows the power required to accelerate the fluid to the given velocity as a function of flow rate. The overall shaft power required for the mixer is:

$$\text{shaft power} = \frac{\text{power to accelerate fluid}}{(\eta_X)\ (\eta_{mech})}$$

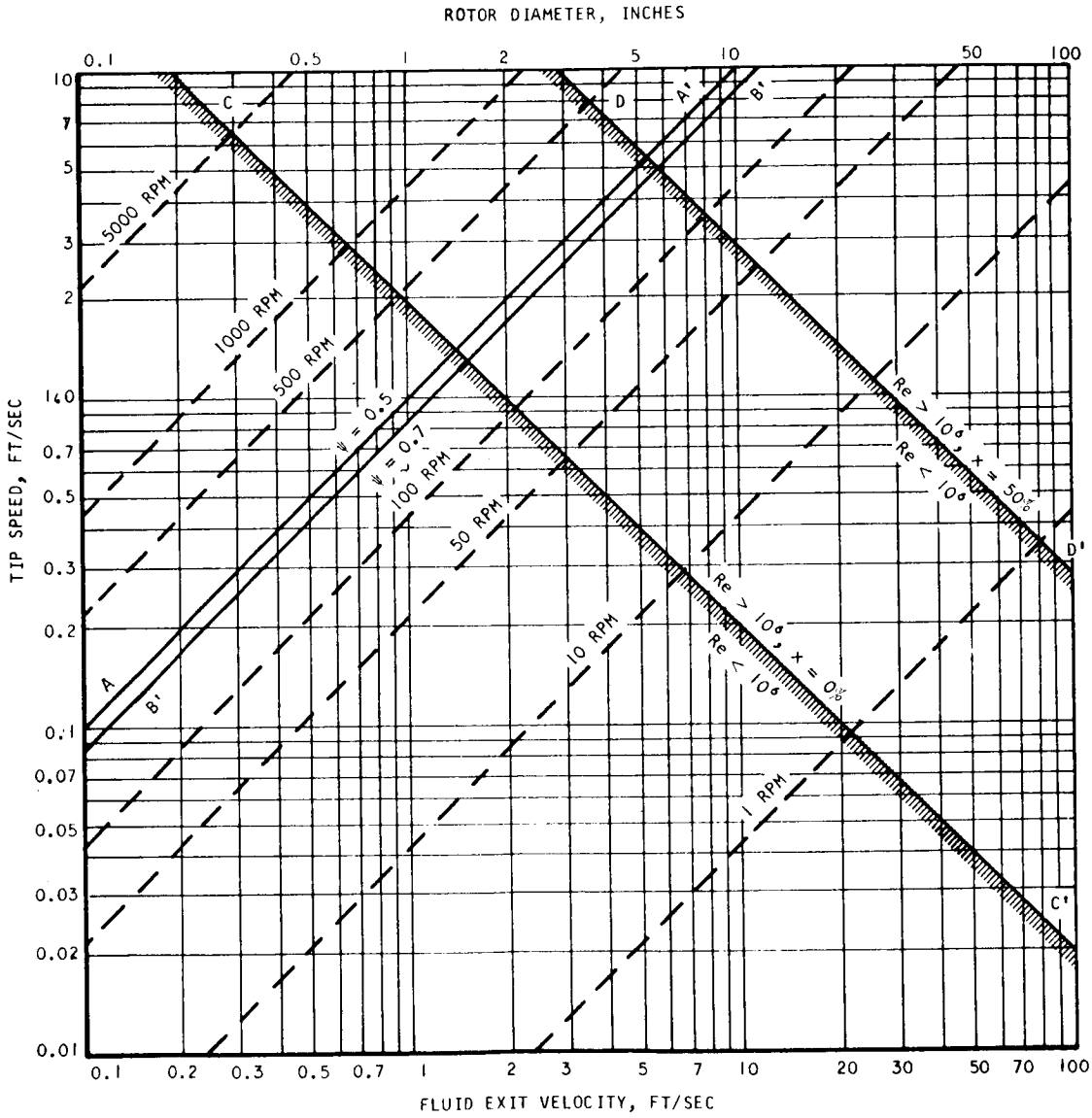

Fig. I-50 Mixer Tip Speed and Rotor Diameter

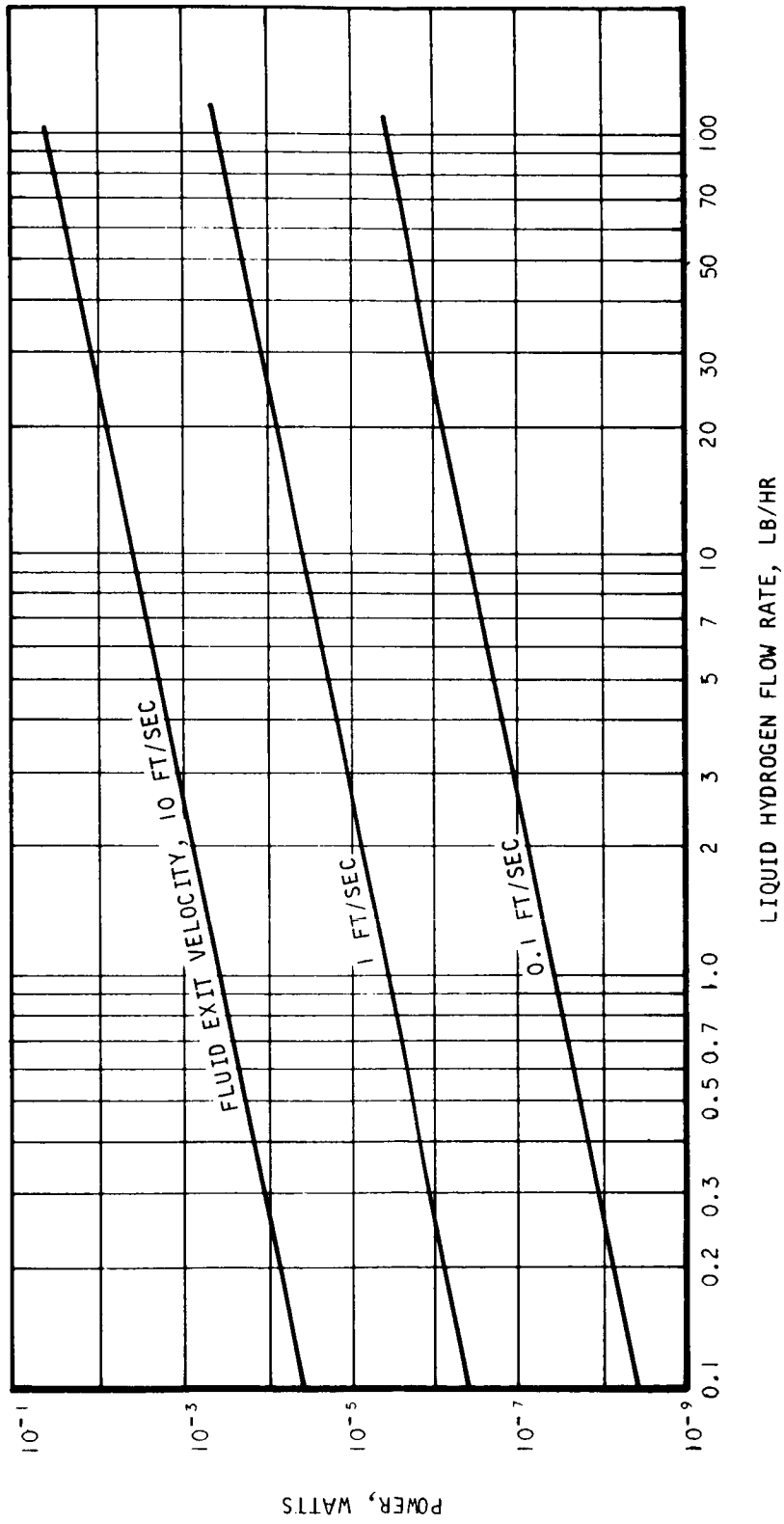

Fig. I-51 Mixer Unit Power Requirements

where η_X is the hydraulic efficiency at the inlet quality and η_{mech} is the overall mechanical efficiency. For the range of the parametric study variables, the power to accelerate the fluid is negligible, as shown in Fig. I-51. For example, the maximum power for the range is only 0.06 w. The actual shaft power will be much greater due primarily to losses associated with bearings and windage. As the power required to accelerate the fluid increases, the mechanical losses become proportionally smaller. Thus, intermittent operation of the mixer with high flows and velocities will improve the overall performance of the unit.

The parametric evaluation of the mixer unit also includes the evaluation of the drive device. This may be either an electric motor or a turbine. The results of the parametric evaluation of the drive devices are discussed below.

Electric Motors. The four types of electric motor drives initially considered for the parametric study were 400- and 2000-cycle ac and brush and brushless dc. It was found that the 2000-cycle ac motor would require heavy conversion equipment and offered no real advantages over the 400-cycle ac motor. For the present study with missions of up to 220 days, conventional brush dc motors are not satisfactory because of life and reliability limitations. Thus, the final parametric study evaluated 400-cycle and brushless dc motors. Brushless dc motors which use photoelectric commutation are now in production. The infrared cell used in the photoelectric pickup loses its sensitivity at liquid hydrogen temperature and therefore photoelectric commutation is not suitable for application in liquid hydrogen. However, the motors can be adapted to liquid hydrogen by changing to an induction coil pickup and using induction rather than photoelectric commutation. This type of motor, specifically designed for use at liquid hydrogen temperatures, has many advantages and is discussed below.

Figures I-52 and I-53 show the weight and volume of 400-cycle ac and brushless dc motors as a function of power output level. The weight of an electromagnetic clutch to transmit the motor output results in roughly a 10 percent increase in the weight and

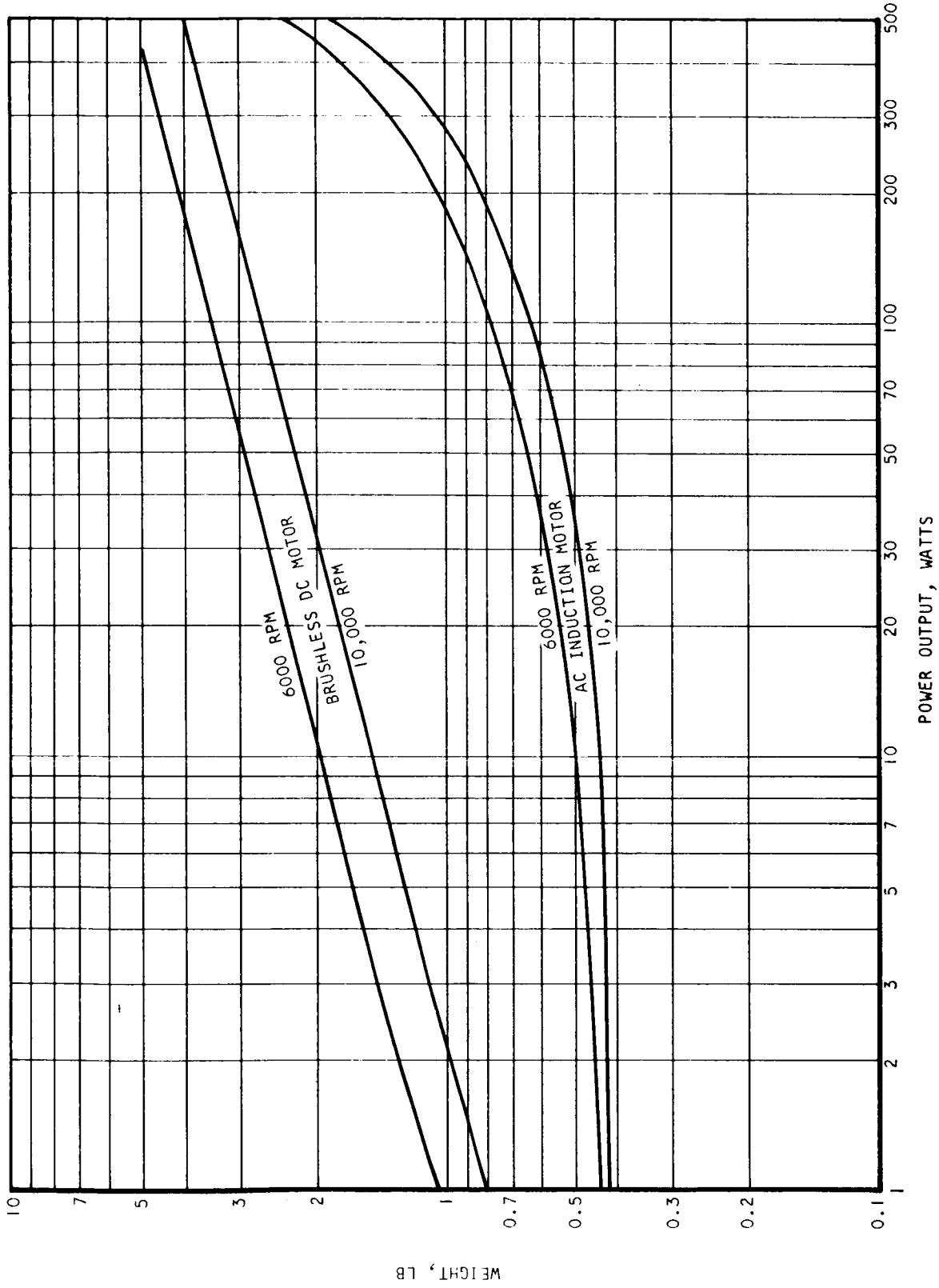

Fig. I-52 Weight of Electric Motors

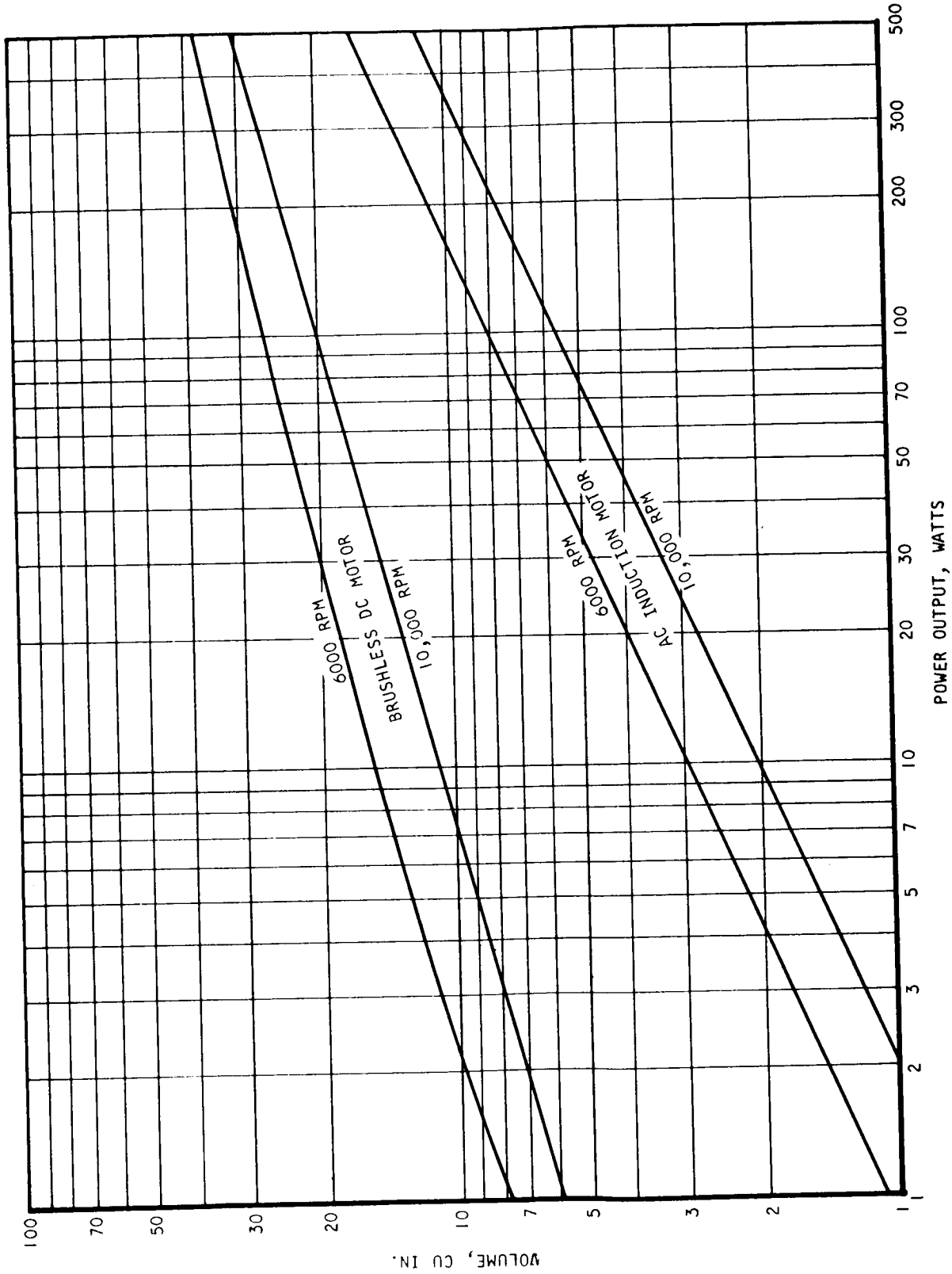

Fig. I-53 Volume of Electric Motors

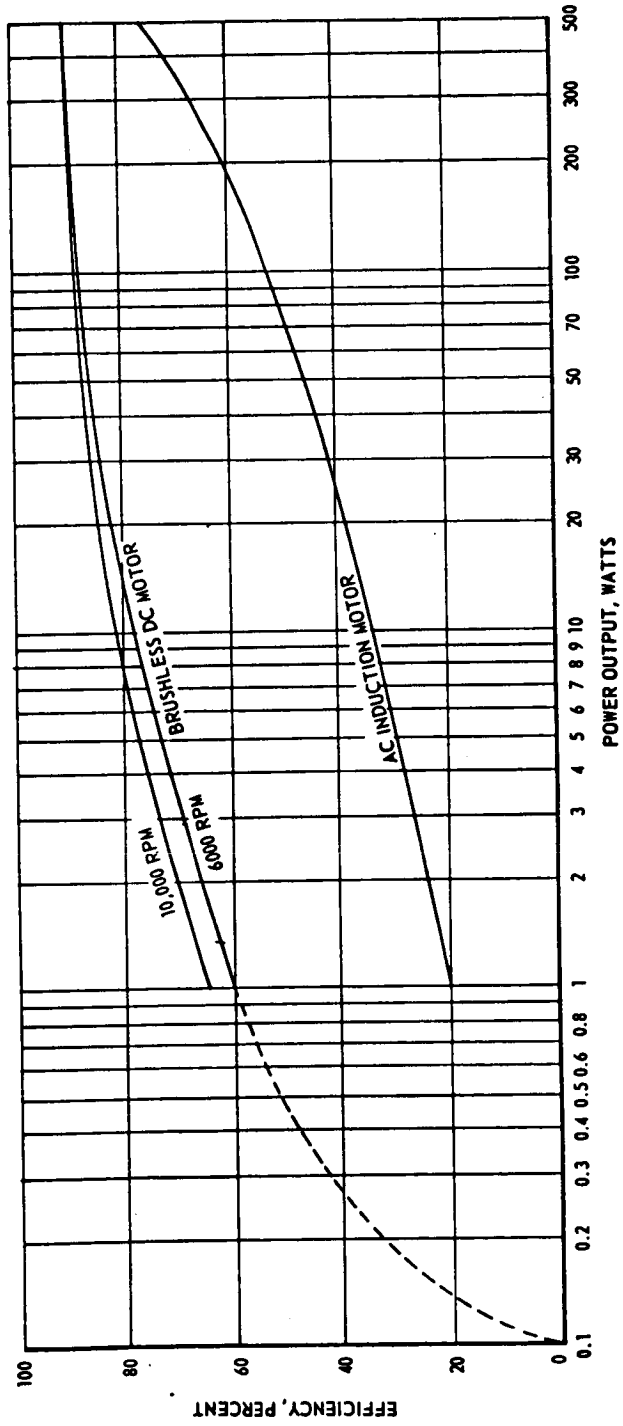

Fig. I-54 Efficiency of Electric Motors

volume of the motor. The ac motor weight and volume do not include an inverter, which would be required if only dc power was available. Direct current power is generated by fuel cell and solar cell systems while ac power is generated by a radioisotope system. The efficiency of the two types of motors is shown in Fig. I-54.

The use of an inverter with the ac motor will reduce the overall efficiency to approximately 80 percent of the values shown. As can be seen from the figures, the brushless dc motor is somewhat larger and heavier and more efficient than the ac induction motor. If a motor is to be placed in the hydrogen tank, a brushless dc motor is recommended because of its higher efficiency. The higher efficiency significantly reduces the heat input to the tank as shown in Fig. I-55. This is especially important for those missions with low tank heat leaks.

Small brushless dc motors are now in production which operate at efficiencies previously thought to be impossible. Figure I-56 shows the characteristics of a brushless two-speed motor now in production. The motor operates at room temperature and, despite its dual-speed characteristic which reduces performance, overall efficiency is 76 percant at the design point. Operation at cryogenic temperature will reduce various electrical losses considerably and will result in higher performance than that obtained at ambient temperatures.

Turbines. The basic configuration selected for all drives consists of a single-stage axial-impulse turbine wheel, with either full or partial flow admission, supported by a set of gas bearings. The bearings considered are foil-type and have the important feature of being inherently stable at any speed. The basic bearing configuration has been developed and successfully used in several small cryogenic turboexpanders.

It is extremely important to determine the most efficient turbine configuration for the given system operating conditions. Since the hydrogen flow rates to be considered are very low as well being at saturation temperatures, miniaturized turbine configuration technology must be applied. The required small turbine sizes may be partially compensated for by increased rotational speeds. However, an increase in rotational speed is accompanied by increased bearing and windage losses. Thus, the overall turbine-drive performance must be considered in the selection of turbine size and speed.

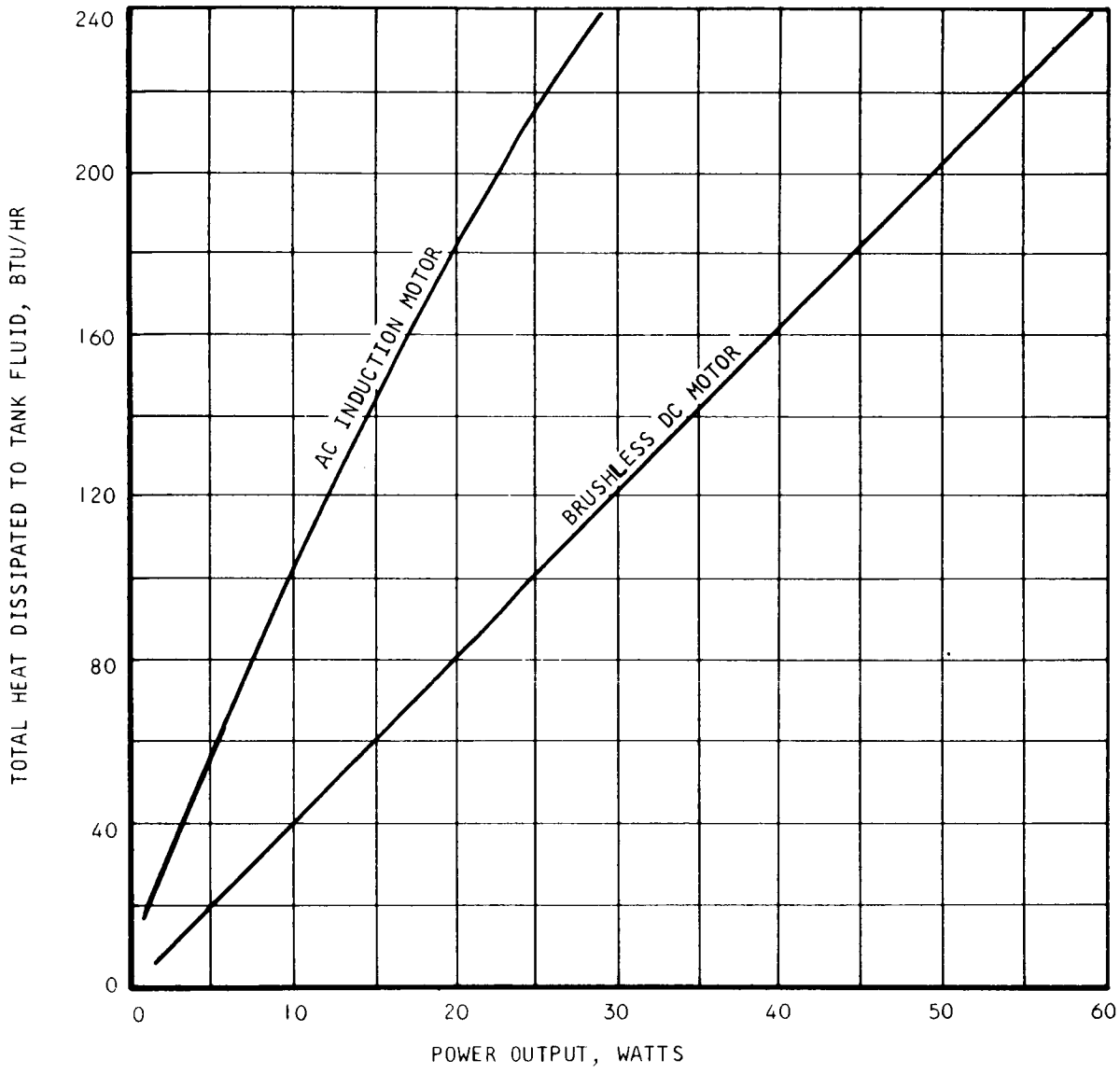

Fig. I-55 Heat Input to Tank Fluid

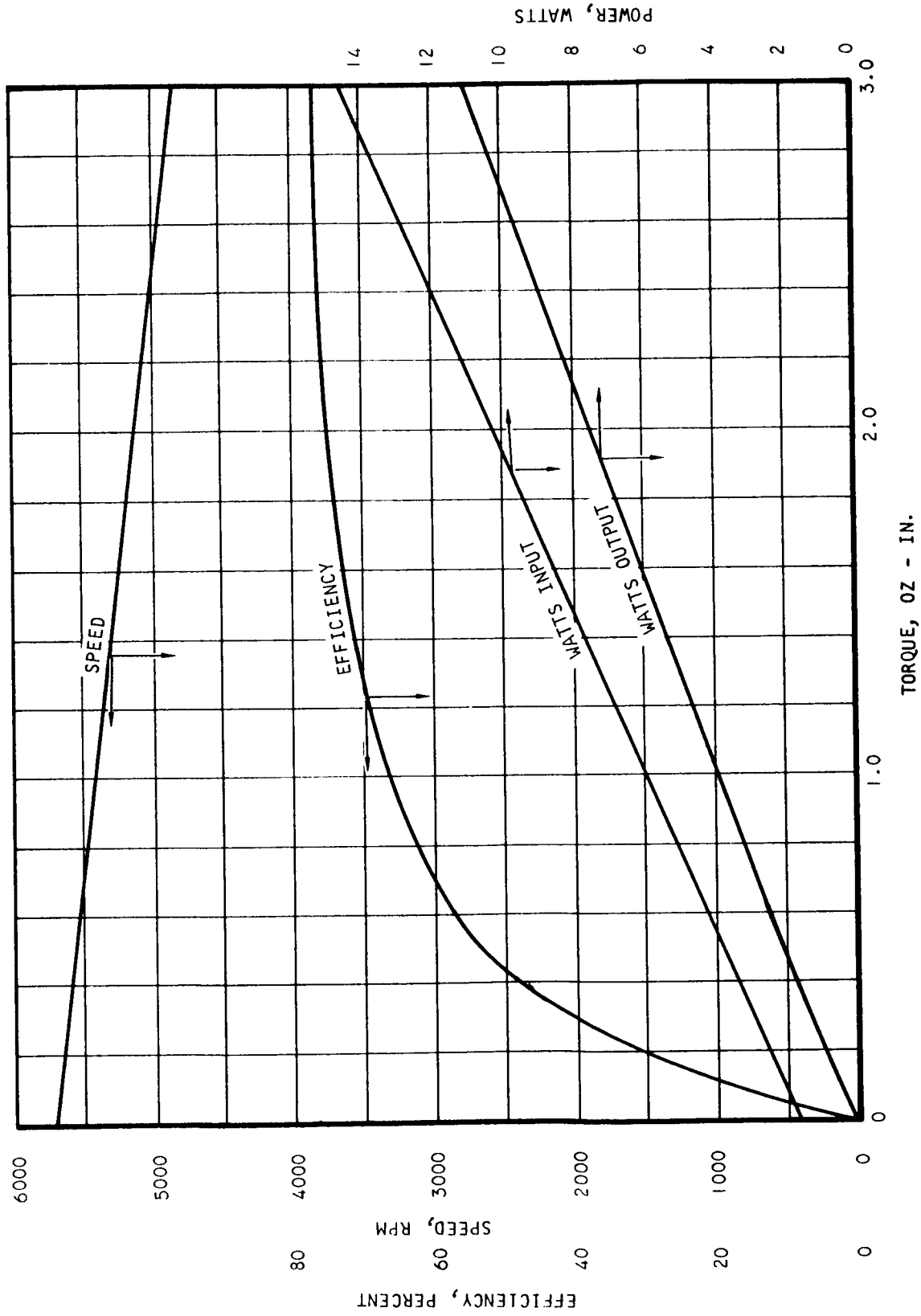

Fig. I-56 Performance of Production Model Brushless DC Motor

Based on analyses and experience with a wide variety of turbines (illustrated in Fig. I-57) including axial, radial, and reentry types (both impulse and reaction), an axial-impulse design has been selected to best meet the turbine-drive requirements.

An axial wheel was selected rather than a radial wheel to avoid the possible problem of a radial-wheel centrifugal field throwing liquid droplets back into the nozzle causing erosion.

Impulse turbines can be designed as axial- or radial-inflow machines. The two types have equal performance capability and the same fabrication techniques can be applied. In impulse turbines, most of the available pressure ratio is used in the nozzle. Little pressure difference exists across the rotor. Therefore, flow leakage and problems associated with axial thrust balancing are essentially eliminated. Some of the other turbine types studied for potential application are discussed below.

A radial-inflow reaction turbine is essentially a 50-percent reaction machine where half of the flow expansion takes place across the nozzle and the remainder takes place in the rotor. Because of the pressure gradient across the rotor, an exducer shroud seal is required to minimize flow leakage. Nonrubbing labyrinth seals must be used. The leakage flow through the finite seal clearance becomes quite substantial for low flow designs, such as the hydrogen turbines considered here. For reliable low-loss gas bearing operation, an additional seal must be installed on the back side of the disk for axial-thrust balancing reasons contributing further to leakage losses. In addition, the maximum efficiency of a reaction turbine occurs at a speed about 45 percent higher than that required by an impulse turbine. The increased bearing losses associated with these higher speeds tend to offset any increase in efficiency. The performance potential for this type of wheel design has not been thoroughly investigated for a partial-admission, high head design. The performance range would be expected to be somewhere between a single-stage axial design and a spot-faced turbine, although the turbine assembly weight may be higher.

The spot-faced impulse wheel (shown in Fig. I-57) has been used in several low-power, short-duration power units. The use of this type of wheel allows the design of an

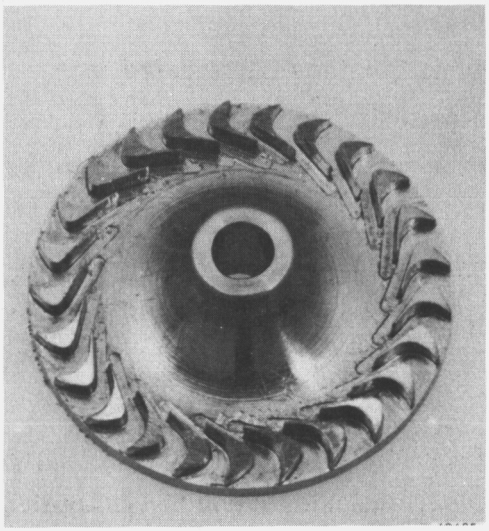

CANTILEVER RADIAL-INFLOW TURBINE WHEEL

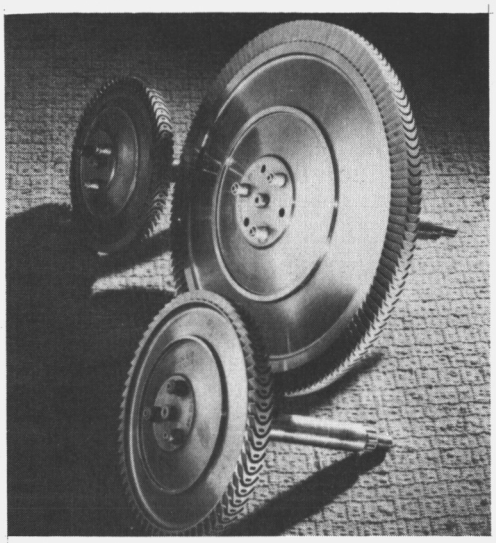

AXIAL-FLOW IMPULSE TURBINE WHEELS

THREE-STAGE RADIAL-OUTWARD FLOW TURBINE WHEEL

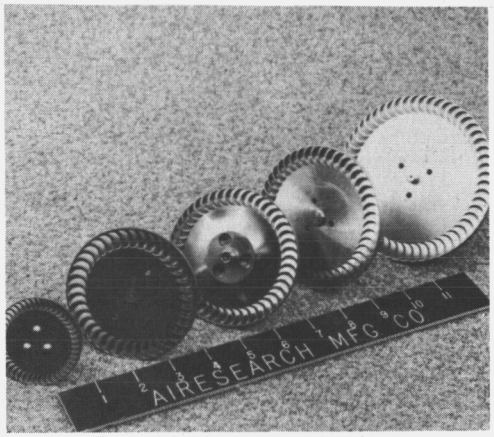

SPOTFACED IMPULSE TURBINE WHEELS

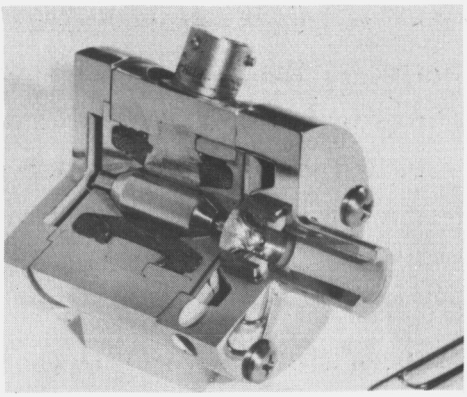

RADIAL REACTION TURBINE WHEEL

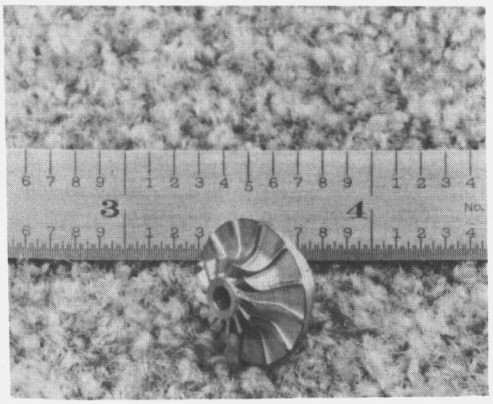

ULTRAMINIATURE TURBOALTERNATOR

Fig. I-57 Various Types of AiResearch Turbines

extremely simple, lightweight, and rugged turbine assembly. However, the efficiencies of present wheel designs are somewhat lower than can be achieved with other types of designs.

Terry-type turbines are almost always a partial admission turbine. The basic flow and performance parameters are similar to a single-stage axial turbine. The bucket design is difficult, however, and it is doubtful if this turbine can show superiority over a conventional axial-flow design. In addition, there are little existing data for small turbine designs.

The drag turbine is essentially a multistage, single-disk design. No stator vanes are provided, and the turbine blades are radial fins. Although the flow process is fairly well understood, there is a lack of empirical data for this design. Drag turbine efficiencies, in general, are lower than an equivalent axial design for a given specific speed.

A reentry turbine allows multistage design on a single disk. The first stage normally acts on a small arc of admission, and the exit fluid from this stage is guided into a duct which carries the fluid back up and over the top of the blade row and into the nozzle of the second stage. The reentry design offers the potential of reduced windage and blade pumping losses over the convential axial-flow design. The full arc can be used to eliminate idle blade losses. This type of design can provide high efficiency, if the leakage losses can be minimized. Four or five stages seem to be the limit of expansion before losses exceed the gain from improved efficiency. It may be difficult for this type of design to actually exceed a multistage axial design in efficiency. This type of turbine is most applicable to much higher energy levels than available from saturated hydrogen.

Bearings. The successful development in several applications have proved the feasibility of utilizing gas-lubricated bearings for high-speed, long-life turbomachinery components. Two basic types of gas bearings – the hydrostatic and hydrodynamic configurations – have been used successfully. The hydrostatic type was eliminated from further consideration for the hydrogen turbine drives, since an auxiliary supply of

pressurized gas is required. With the hydrodynamic bearing type, the pressure required for supporting the load is generated in the small gap between the rotating and stationary bearing surfaces.

The requirements of the gas bearings are:

- Stable operation during startup and at the desired rotational speed
- Sufficient radial and axial load capacity to support the forces imposed by the shaft
- Low power consumption

Dynamic instabilities that are pertinent to machines supported by hydrodynamic fluid film bearings can be divided into three broad classes, those due to: (1) the system critical speeds, (2) the nonsynchronous whirl often called half-frequency whirl, and (3) the resonant whip. The critical speeds usually have no damaging effects unless they occur at or near an operating speed. The damping associated with fluid film bearings permits the rotor to accelerate through the first and second critical speeds with relatively small amplitudes of excitation, if the proper bearing stiffness is used. The bearing mounts must be designed not only to keep the first and second critical speeds far from the operating speeds but also to keep them low to further decrease bearing loads. In addition, the third critical speed must be placed somewhat above the operating speed.

At relatively low speeds, a lightly loaded rotor that has been displaced from the equilibrium position will take a spiral path in its return to the equilibrium point. This whirling type of path results from the tangential component of the fluid film force. The whirl frequency, under certain conditions, can approach one-half of the rotor speed. In this case, the bearing load capacity becomes zero and bearing failure will occur.

Serious consideration must also be given to resonant whip. This condition exists where the tangential component of the fluid film force excites the system critical frequency and the rotor whirls at the critical speed while spinning at a much higher speed. Since the mean fluid velocity is approximately one-half the shaft speed, the fluid is not capable of exciting this type of vibration at spin speeds below approximately twice the

system critical speed. Loads, either static or rotating, forcing the bearing to operate at a high eccentricity ratio, will suppress this type of vibration.

A wide variety of gas bearing configurations may be found in the literature. These range from simple cylindrical journal bearings to grooved journal bearings, journal bearings operating in elliptical journals, and bearings operating on pivoted tilting pads. All of these, with the exception of the tilting pad bearing, are susceptible to half-frequency whirl instability. Another bearing type is the foil bearing. Here, the foil is wrapped about the rotation journal and the load is supplied by the sum of the tension forces. The foil may be made of any of several flexible materials. A configuration which has been successfully applied to cryogenic turboexpanders is the conical overlapping foil bearing (Fig. I-58). In turboexpanders, cone bearings of 3/8 in. in diameter have been run at speeds to 450,000 rpm. In this type of bearing, the shaft, which includes a conical section on either end, runs in conical journals. Foils are installed in the region between the two conical surfaces. The foils are attached at one end only and are arranged such that adjacent foils overlap. Conical bearings have the advantage of being capable of accepting both radial and axial loads. With cylindrical journal bearings, only radial loads are supported. A separate thrust bearing is then necessary to carry axial loading. The actual bearing configuration for a turbine drive can be established only after a detailed design study considering all environmental requirements.

Turbine Characteristics. The configuration selection and performance of the turbine for this application are determined by many variables. The primary design items which effect turbine performance are:

- The throughflow rate
- Available head for expansion
- Turbine wheel tip speed
- Rotational speed
- Degree of flow admission in wheel
- Manufacturing tolerances
- Supersaturation of expanded vapor
- Condensation of the vapor within the turbine
- Bearing and windage losses

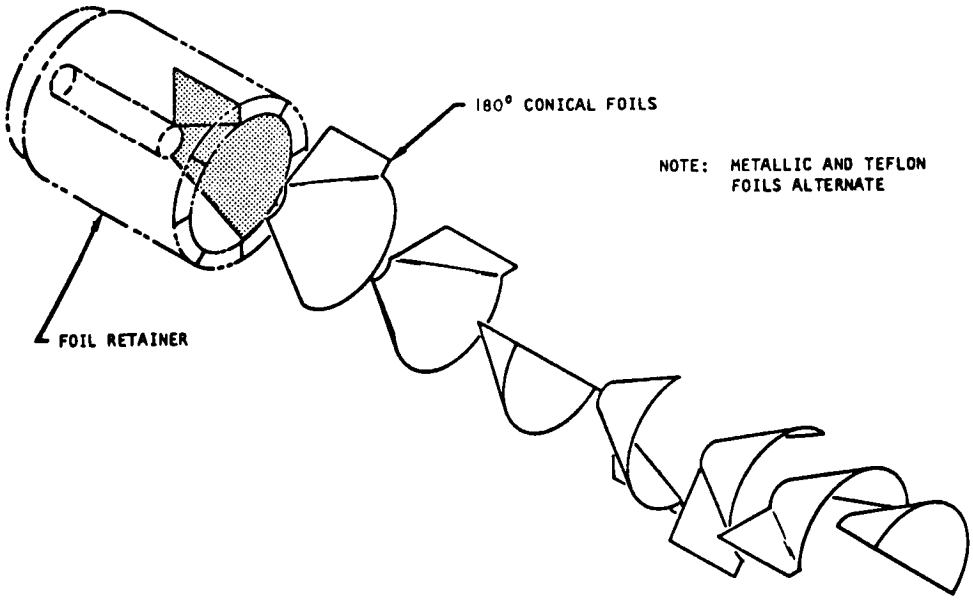

Fig. I-58 Conical Overlapping Foil Bearing

Considering similarity relationships, the efficiency of the turbine is basically a function of the following:

$$\eta_t = f(Re, M, N_S, \rho_o/\rho_i, k)$$

The specific heat ratio, k, affects the turbine performance through the influence on compressibility factors. The other effect of k is in its effect on the turbine velocity vectors with changing density ratio across the turbine. Unless the density ratio remains the constant, the velocity triangles in the turbine passages are modified.

The Reynolds number may also affect turbine performance. There is a certain critical Reynolds number (about 10^6) below which the turbine performance is adversely affected. However, in the range of operation of the subject hydrogen turbines, the Reynolds number effect is small.

Operating at low temperature reduces the velocity of sound. As the tip speed is still high, the possibility of encountering supersonic Mach numbers remains with high-speed miniature turbines. Within a range of Mach numbers up to 1.2 to 1.4 (at the nozzle exit), the effect of supersonic operation can be taken into the design so that only a slight decrease in performance takes place. At higher Mach numbers, a larger penalty in performance can be encountered.

In a review of the data of existing miniature turboexpanders (down to a diameter of 5/16 in.) operating in low temperature refrigeration systems, it is found that: (1) most of them operate within a range of Reynolds number which is not too far from the critical Reynolds number (10^6), (2) most operate within a common range of pressure ratios and density ratios, and (3) the operating Mach number is not high enough to cause a significant penalty in performance.

With these operating conditions, the similarity relationship can be written as

$$\eta_t = f(N_S)$$

This relationship does not introduce any parameter that accounts for the tolerance control or the manufacturing techniques leading to a good fabrication of miniature designs. Thus, for the current study, the physical diameter of the turbine D_T has been included as a design parameter so that generalized performance can be shown for

$$\eta_t = f(N_S, D_T)$$

This performance is shown in Fig. I-59.

An additional study was made for an axial turbine design similar to the type that would be used for the turbine drives. A typical design pressure ratio of 10/1 was selected. The calculated performance of this turbine is shown in Fig. I-60. Also shown on the curve are the effects of partial flow admission in the nozzle stator, down to 1 percent admission. The performances shown in Figs. I-59 and I-60 were compared. This indicated that the performance shown in Fig. I-59 was 4 to 5 percent higher than that shown in Fig. I-60. Consequently, for the analysis and studies, the performance of Fig. I-59 was downrated by a factor of 0.958.

Turbine Bearing and Windage Losses. The performance of any gas bearing system is a complex function of the bearing geometry, surface speed, and gas pressure and viscosity. Analysis of any particular system is extremely complicated. It is assumed that any turbine-drive bearings will be operating in hydrogen gas. However, relevant to this, a small bearing system has been run in flashing Freon.

The variation in windage loss may be approximated as follows:

$$\text{Windage loss} = C\, D^5\, N^3\, \rho$$

As indicated, the determination of the bearing and windage losses is a function of many design variables. For the parametric study, these losses were assumed to be only a function of wheel diameter. The bearing and windage loss was assumed to be 6 w for a 0.40-in. turbine wheel, and to vary directly with wheel diameter. This value is based on recent development test data with this size wheel.

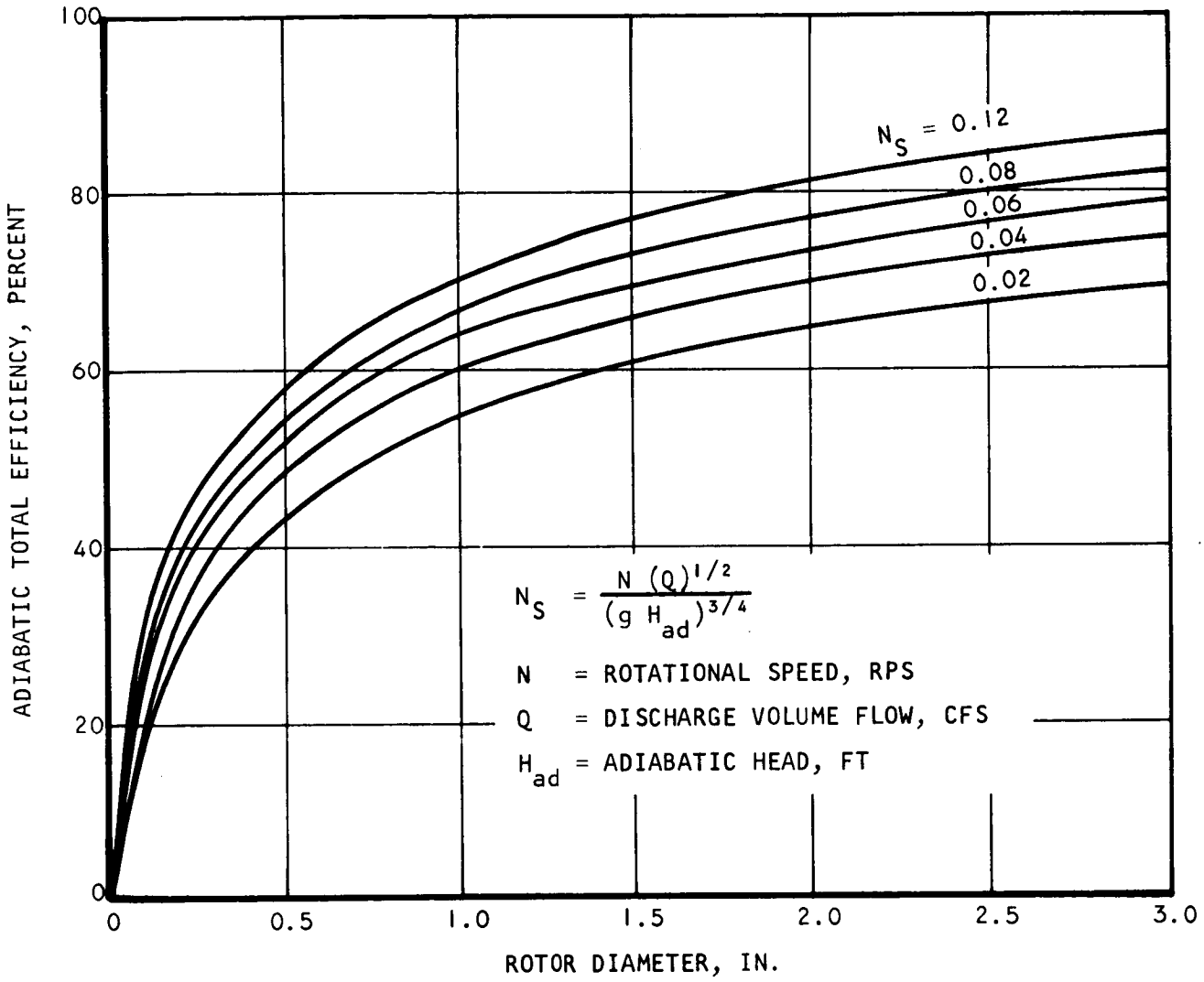

Fig. I-59 Estimated Performance Characteristics of Small High-Speed Turbines

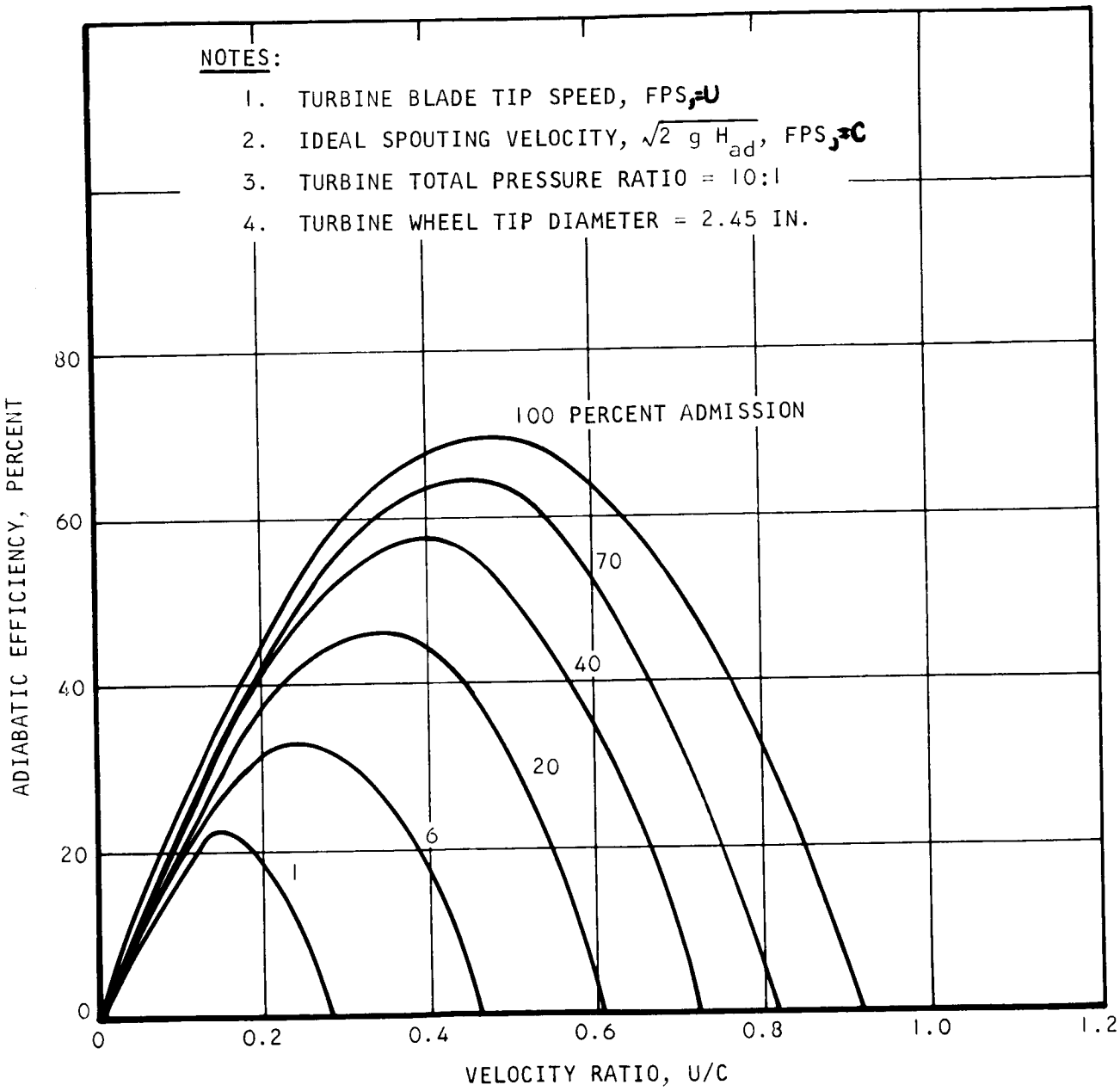

Fig. I-60 Estimated Performance of Impulse Turbine

To optimize turbines over the complete hydrogen flow range is, thus, an involved process requiring the consideration of many variables. Based on preliminary studies and development test data, considering primarily bearing and windage losses and manufacturing tolerances, a maximum speed of 300,000 rpm and a minimum wheel diameter of 0.40 in. were established as design limits for the turbine studies.

Turbine Supersaturation. From the standpoint of the turbine, it is desirable that the inlet conditions be in the superheated region. This would improve turbine performance and reduce the possibility of erosion problems. In operation from the saturation line, the fluid is supersaturated when it is completely a vapor, although standard equilibrium calculations indicate that condensation begins at the instant that the computed quality falls below 100 percent. Expansion from the saturation line represents a condition in which all of the fluid is evaporated but none of it is superheated. An equilibrium expansion shows a mixture of part liquid and part vapor. Heat is given up by the fluid during this expansion. Part of the heat is equal to the product of vapor specific heat multiplied by the reduction in vapor temperature. Another part is equal to the product of the liquid specific heat multiplied by the reduction of the temperature of the previously condensed liquid. The remainder is equal to the product of the mass of liquid condensed by the latent heat of evaporation. Most of the energy given up during the equilibrium expansion comes from fluid condensation. Additionally, the process may differ appreciably from adiabatic conditions at these cryogenic conditions.

The flow process is so rapid that the vapor probably does not have time to condense during the expansion. In this case, the heat given up must equal the product of the specific heat of the vapor by its temperature drop. If condensation does not take place, the temperature for a given pressure is lower than for normal equilibrium and the nozzle passes a higher mass flow.

Thus, if equilibrium conditions are assumed in design and a completely or partially saturated condition is realized in operation, the turbine performance will be greatly reduced. To achieve a given velocity diagram, a turbine designed for equilibrium flow could differ considerably from one designed for supersaturated flow. The blade height would be smaller for the supersaturated state than for the equilibrium state.

The actual condensation process is strongly dependent on the rate of formation of droplets of a certain critical droplet size. This, then, also is dependent on the condition of the inlet fluid, whether it is dry saturated or wet saturated.

Turbine Condensation. The ultimate equilibrium state of expansion has two undesirable effects: (1) it lowers turbine efficiency and (2) it promotes erosion. Once condensation begins to take place and the droplets exceed their critical value, they rapidly grow and attain significant inertial forces. The condensate may then flow in contact with the stator or rotor blades. Condensate striking the nozzle flows with little velocity and must be accelerated to rotor speed by the rotor. The energy for this acceleration must come from the working fluid. Thus, the efficiency of the turbine decreases in proportion to the amount of fluid condensed. Since the turbine must do work on the condensate, the decrease in efficiency can be expected to exceed the liquid content in the working fluid. Various experiments and data seem to confirm that approximately 1 percent is lost for each percent of condensate in the turbine. The value used for the turbine performance studies, and which seems to be a reliable figure for steam turbines, has been a charge to the turbine of 1.3 percent for each percent of liquid indicated by equilibrium expansion.

Although no data has been found on blade erosion from hydrogen, this should not be as severe a problem as it has been with other heavier working fluids.

Turbine Performance. Figure I-61 shows the available head, or enthalpy, as a function of the turbine pressure ratio for inlet pressures of 10, 50 and 135 psia. One significant point indicated by these curves is that the available head is less at the higher inlet pressure of 135 psia for a given pressure ratio. The peak energy actually occurs in the pressure range of 60 to 80 psia. Thus, maximum turbine power available from a drive unit will occur in the pressure range below 80 psia. Vapor quality as a function of the same variables is also shown in Fig. I-61. The quality shown is that indicated by an isentropic expansion under equilibrium conditions. At the higher inlet pressure, these curves show that turbine performance is lower and the potential is much higher for liquid in the turbine. The steps as indicated in the quality lines are due to the fluid passing through the triple point (1 psia). An increase in the vapor to fluid ratio occurs as the fluid transforms from the liquid phase to the solid phase thus providing an improvement in the vapor quality.

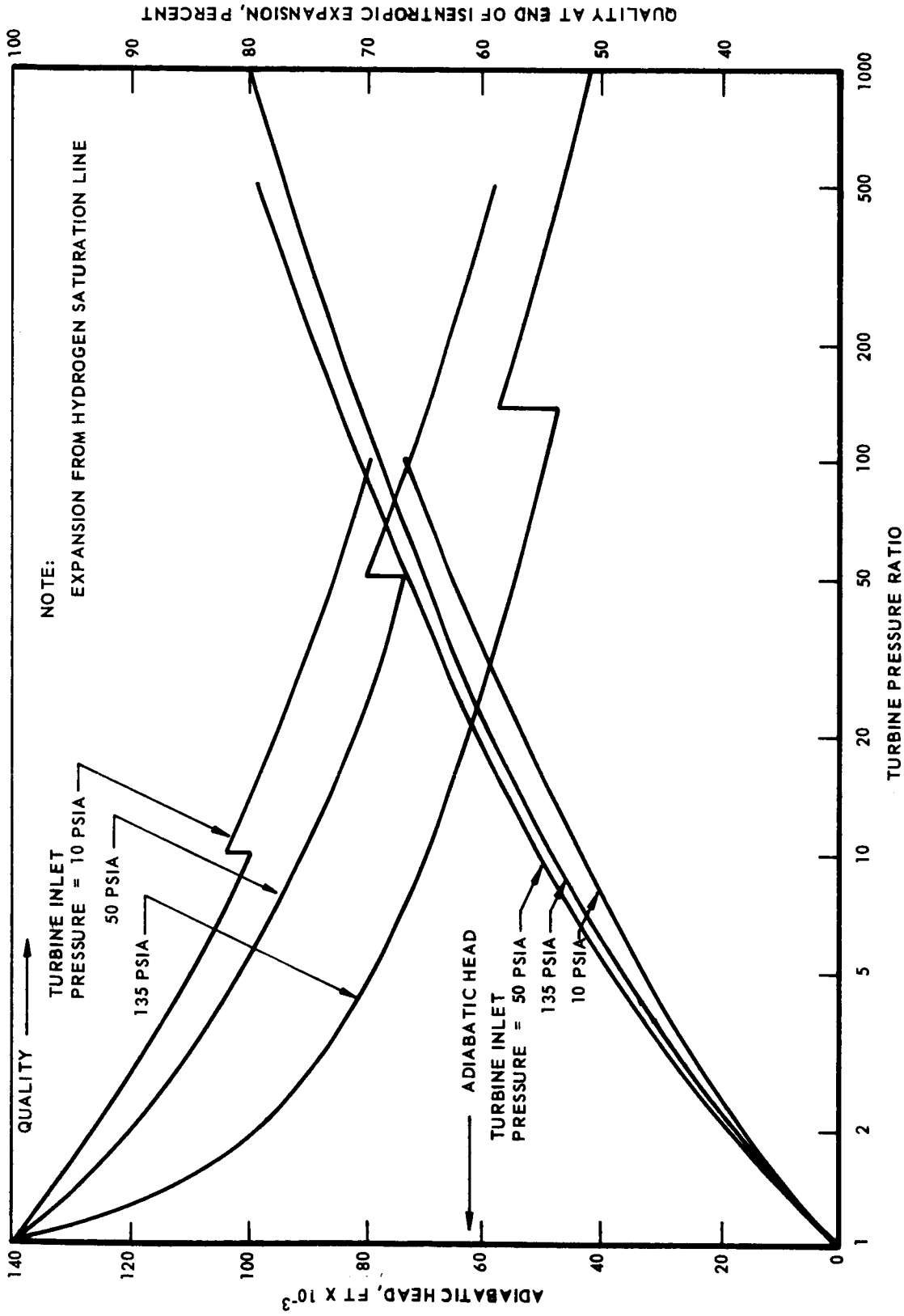

Fig. I-61 Thermodynamic Characteristics of Saturated Hydrogen

Figures I-62, I-63, and I-64 show turbine-drive characteristics for an inlet total pressure of 10 psia at pressure ratios of 10:1, 100:1, and 5:1 . In the flow range of 30 to 60 lb per hr, the turbine is basically sized to accommodate the high throughflow. For these conditions, size will remain unchanged for the various pressure ratios. However, higher speeds are required for compatibility with the higher pressure ratios. At the low flow conditions, the maximum speed is attained and partial-admission miniature turbines are required approximately 0.5 in. in diameter. The turbine at the zero output power conditions has been sized for maximum turbine efficiency; whereas, at the higher flow conditions, the speed was selected for maximum turbine efficiency. The over-overall diameters shown on these curves allow for installation mounting. The actual wheel diameters are about 1 in. less than the overall diameters shown on the curves.

Figures I-65, I-66, and I-67 show the same turbine-drive characteristics as above except for a total inlet pressure of 50 psia. As indicated, for the high flow rates, the size and weights of these drive units are much less than for the 10 psia units. This is due to smaller flow area requirements with the higher pressures for a given flow. For maximum efficiency operation and for the smaller sizes, the rotational speeds are increased until the 300,000 rpm limit is attained. Again, at the lower flows and constant speed of 300,000 rpm, the turbine wheel size is selected for compatibility with maximum turbine efficiency. The effects of partial admission are also considered. Partial admission effects on peak efficiency speed are indicated in Fig. I-60.

As mentioned previously, the operating speeds shown in Figs. I-62 through I-67 were selected for maximum efficiency. For a given set of operating conditions, the turbine output power and torque, as a function of speed, will vary approximately as shown in Fig. I-68. The various speeds would normally be obtained through a reduction gearbox with the turbine still operating at peak efficiency.

Figure I-69 indicates the influence of turbine inlet pressures below 10 psia on the various design variables. These curves are most valid for the high inlet flow conditions in the range of 30 to 60 lb per hr. For lower flow rates, the diameter and weight values obtained will be somewhat higher due to existing partial-admission designs. However, in this range, the weights and sizes are quite small so that the absolute numbers should be valid for further system tradeoff studies.

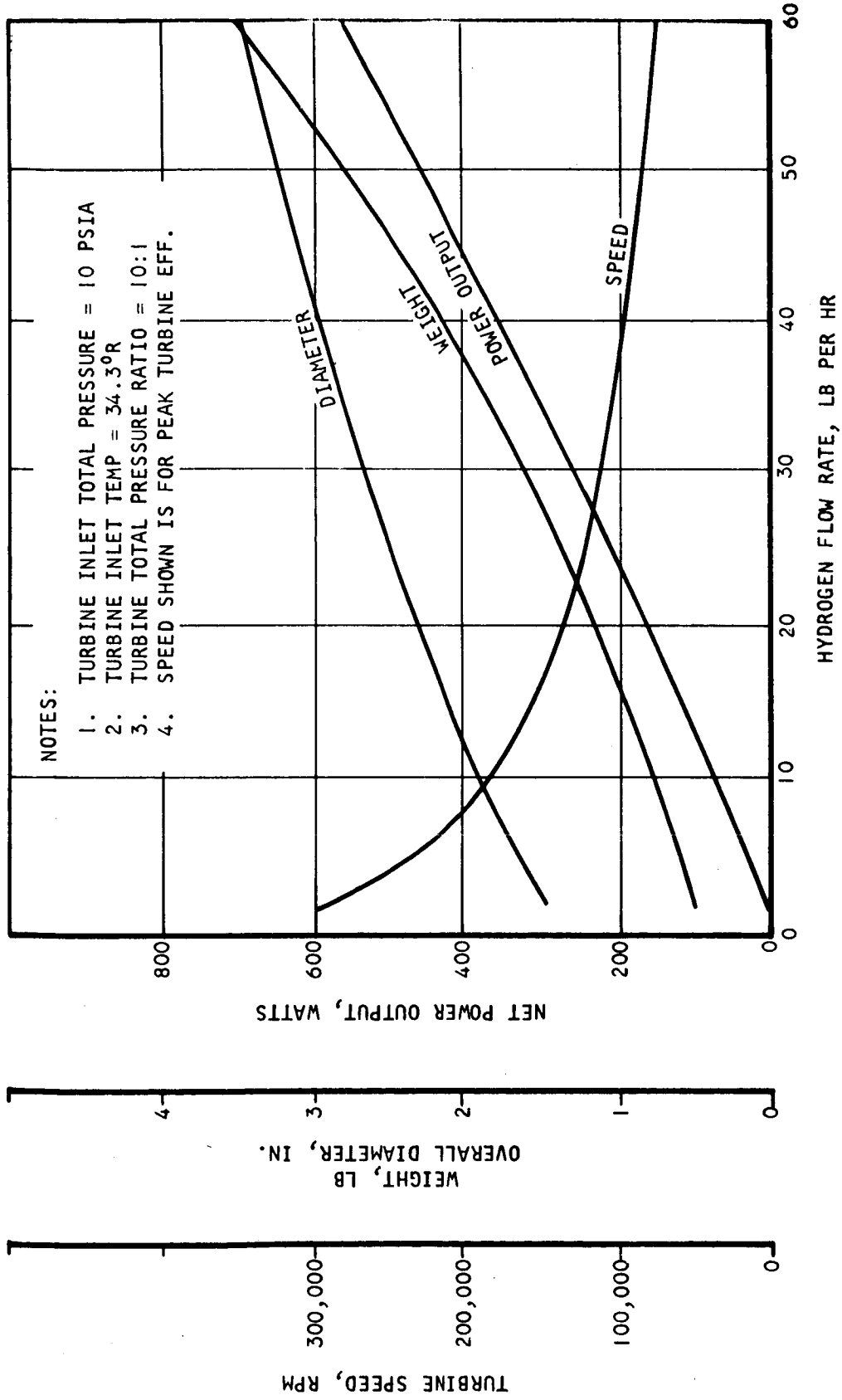

Fig. I-62 Estimated Turbine-Drive Characteristics

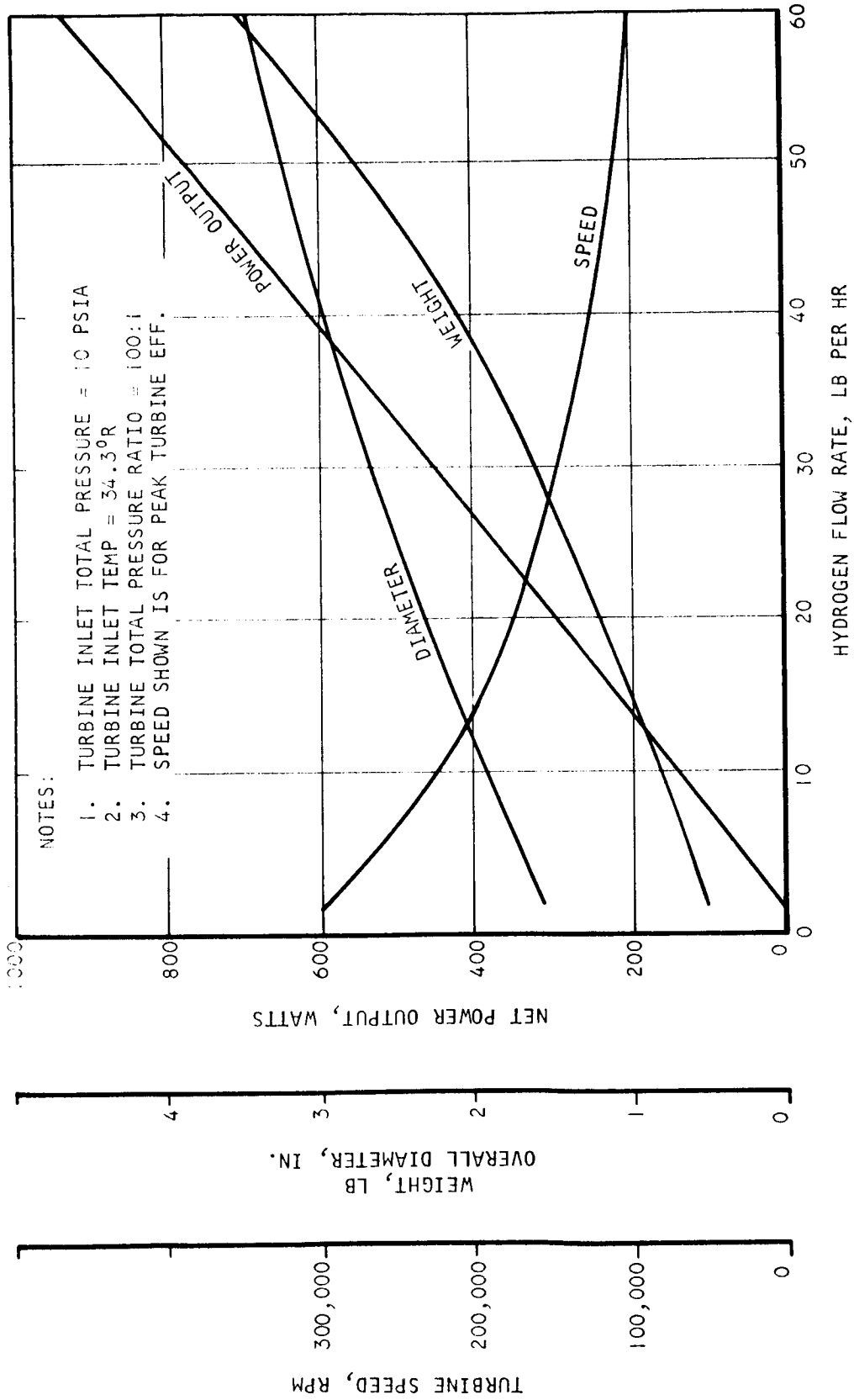

Fig. I-63 Estimated Turbine-Drive Characteristics

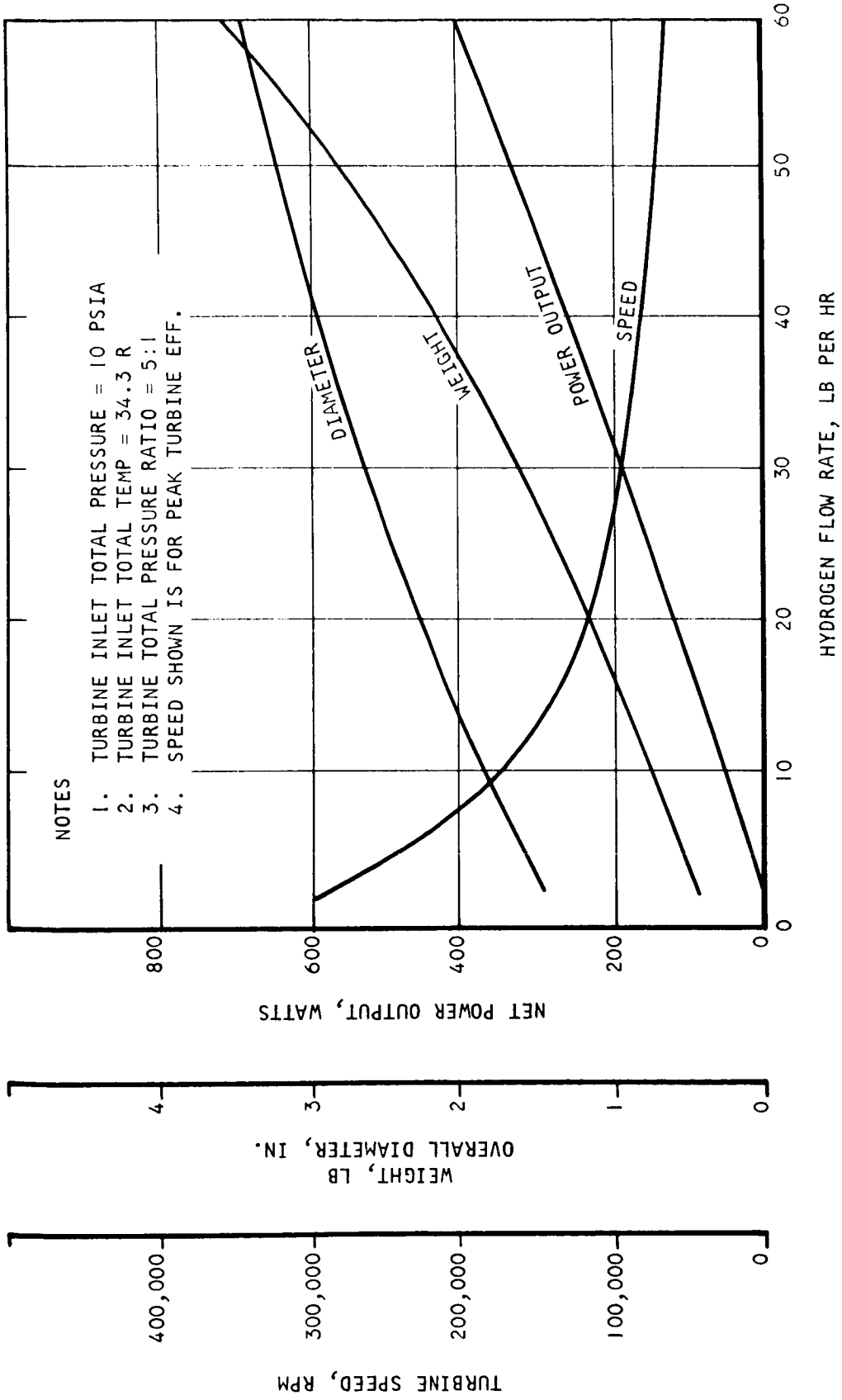

Fig. I-64 Estimated Turbine-Drive Characteristics

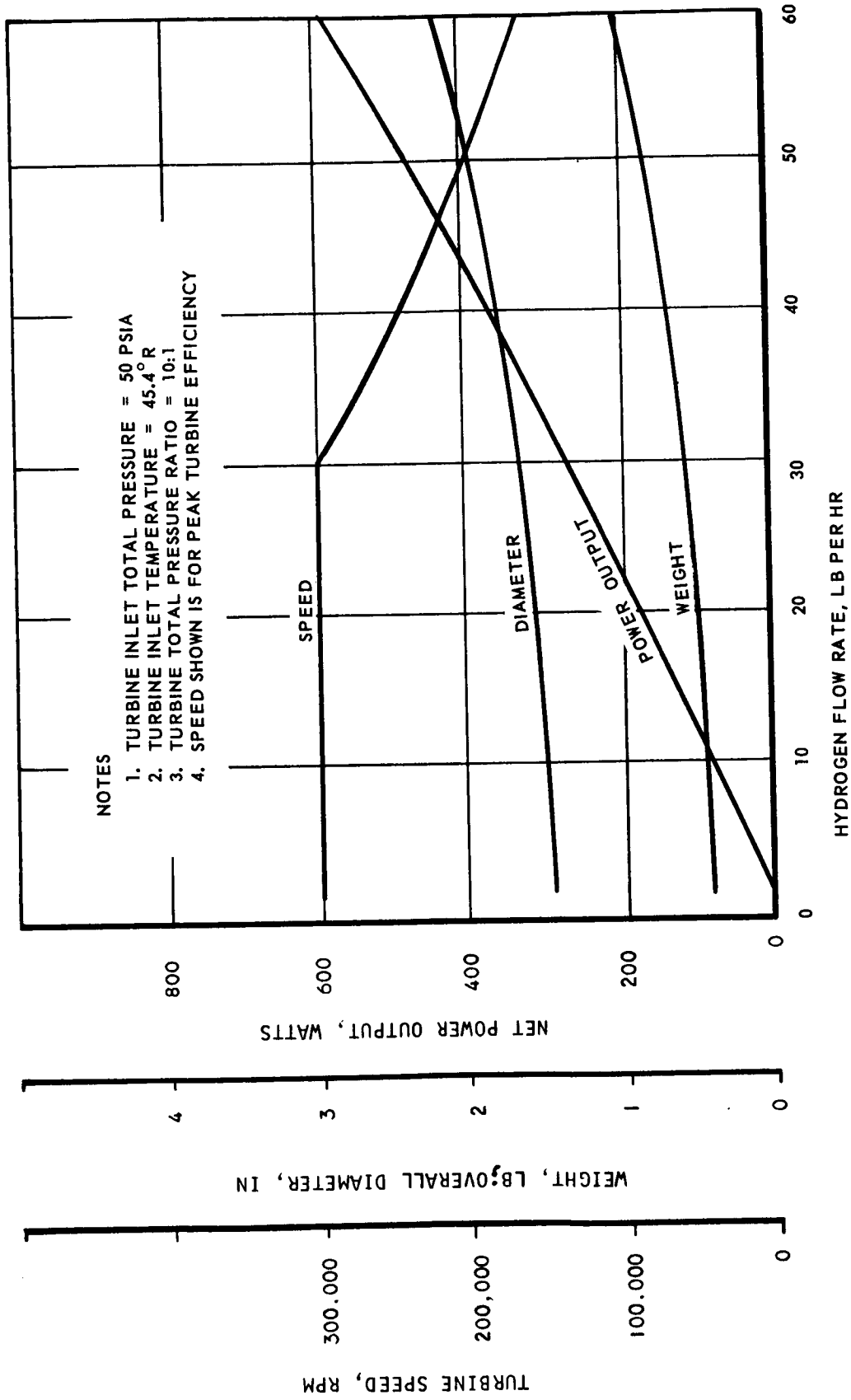

Fig. I-65 Estimated Turbine-Drive Characteristics

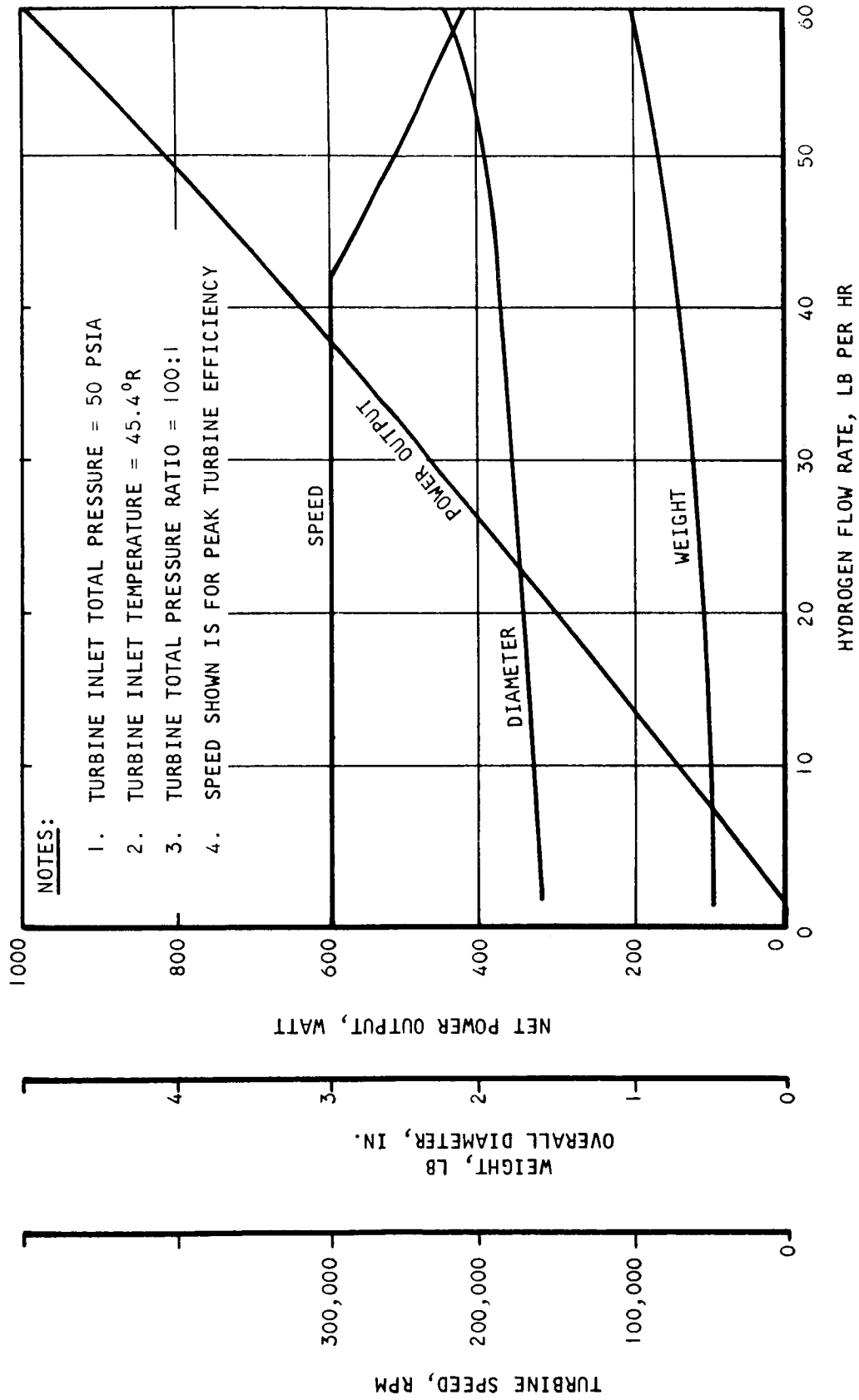

Fig. I-66 Estimated Turbine-Drive Characteristics

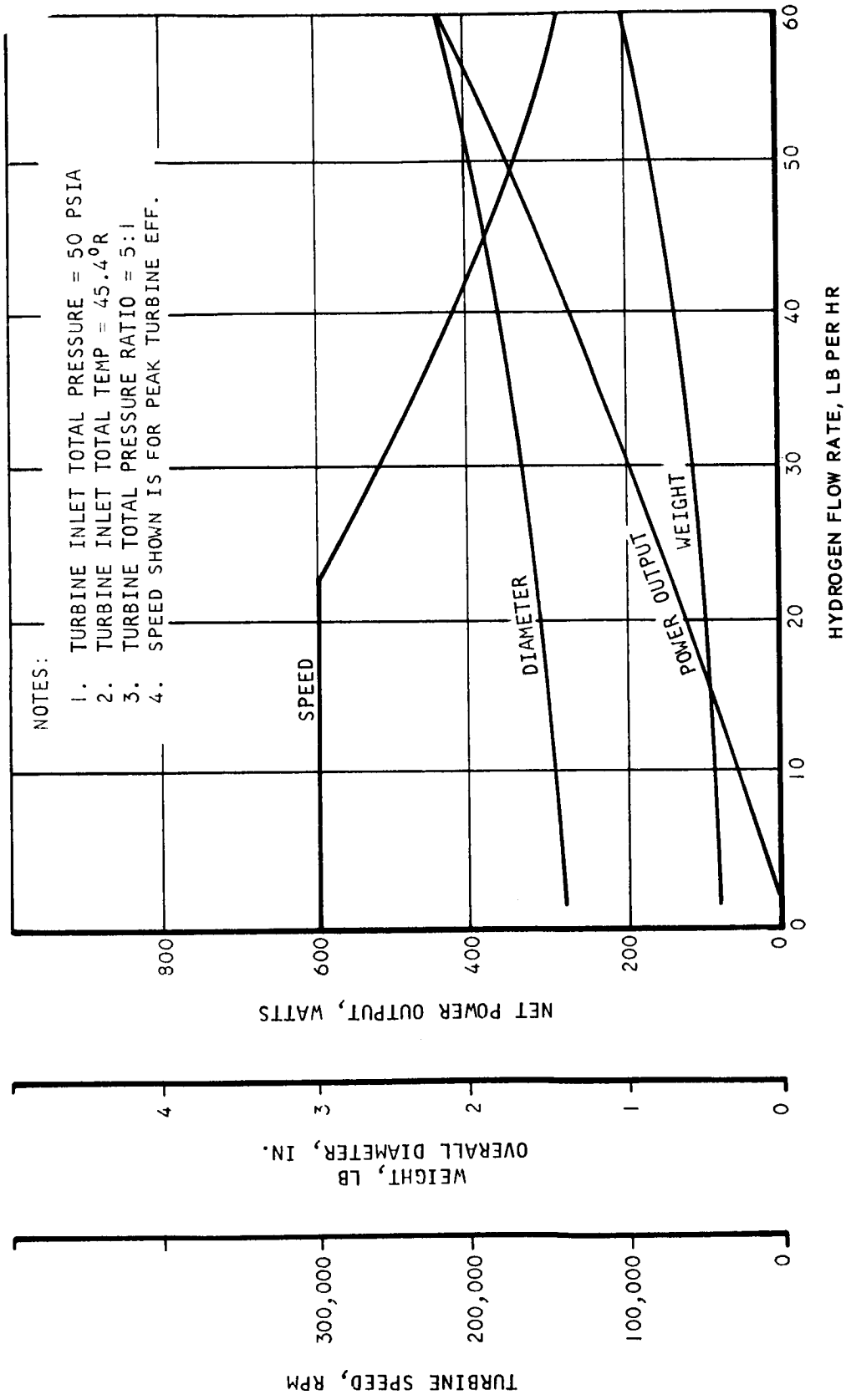

Fig. I-67 Estimated Turbine-Drive Characteristics

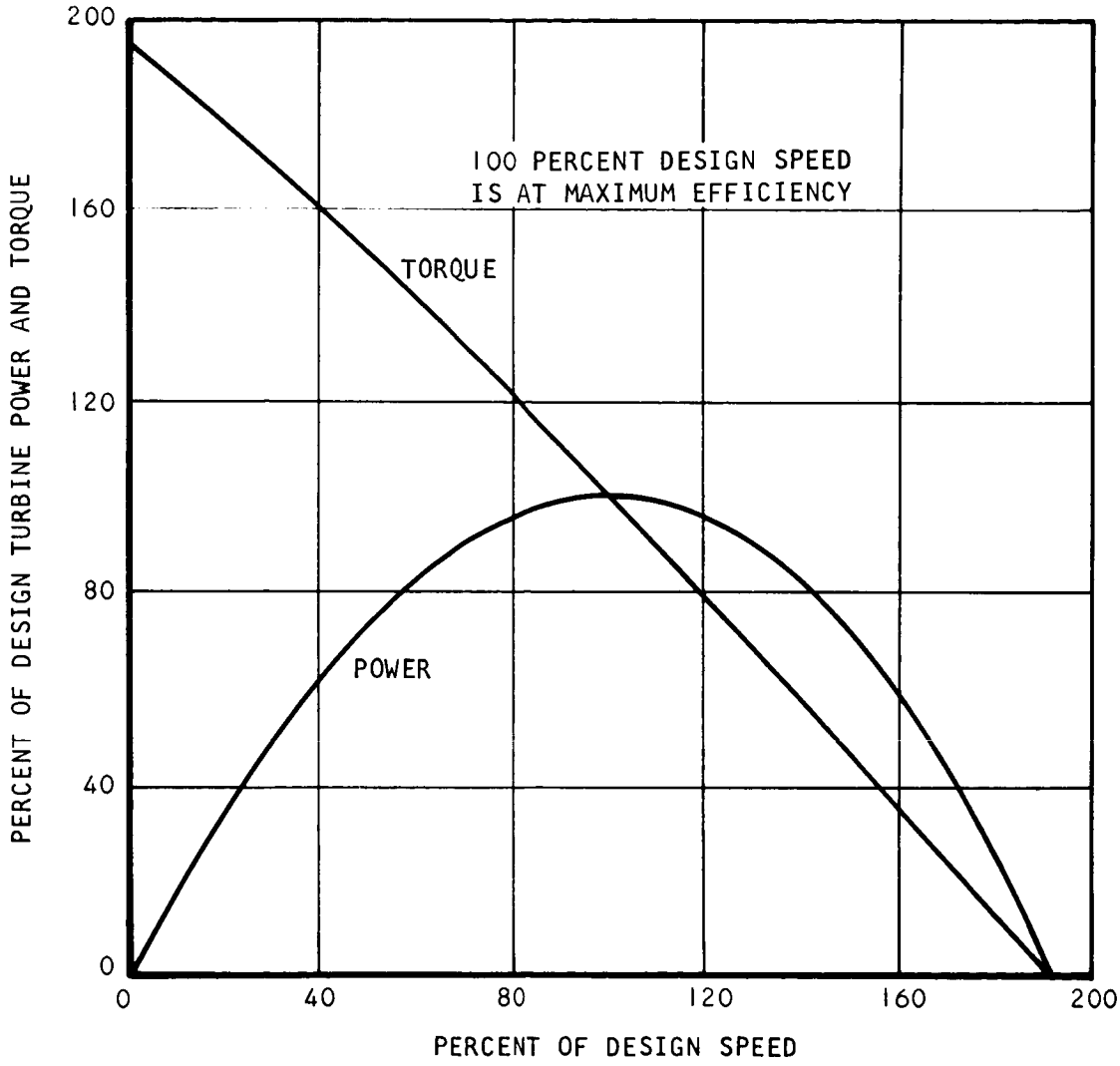

Fig. I-68 Typical Impulse Turbine Off Design Torque-Speed-Power Characteristics

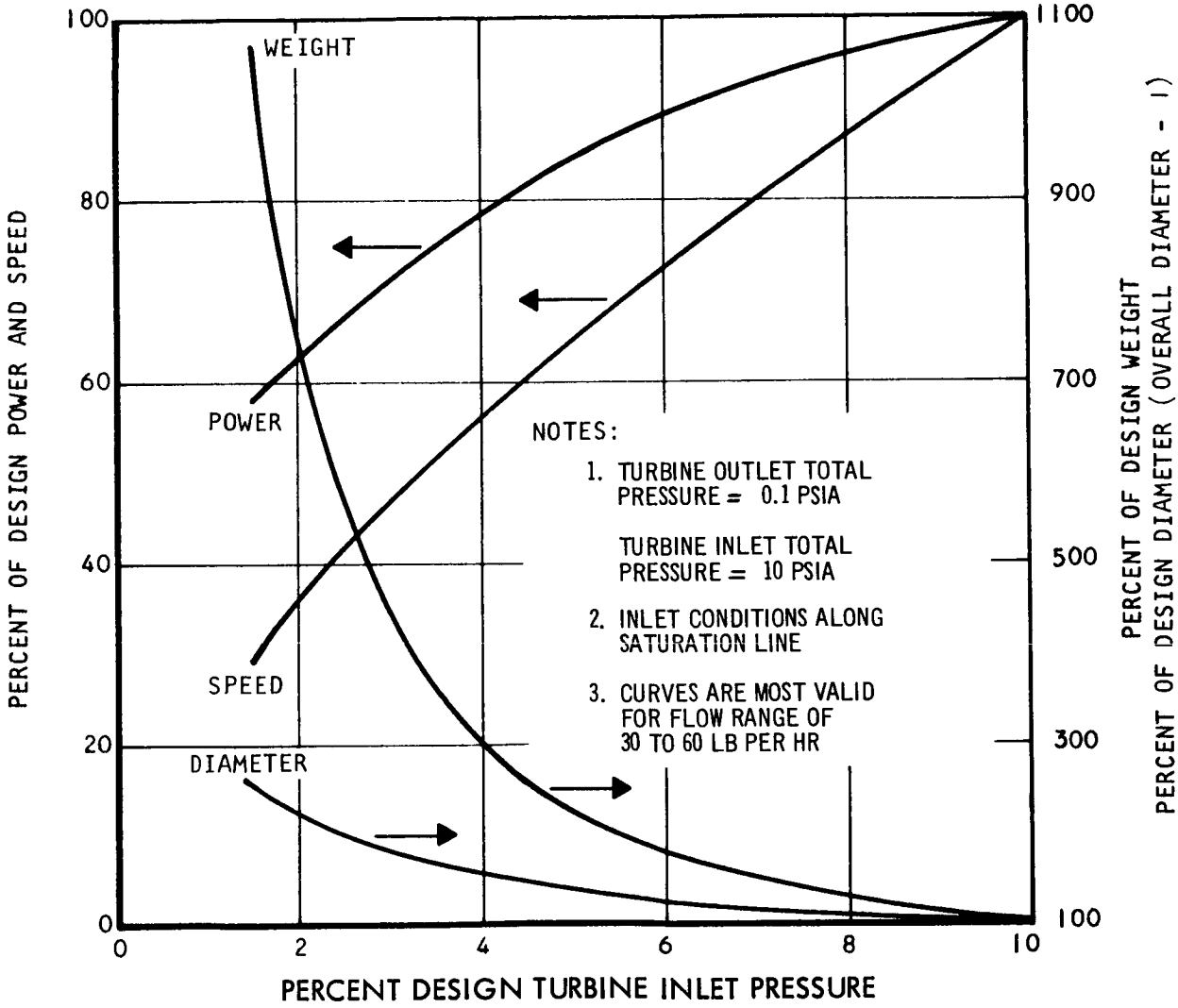

Fig. I-69 Typical Off Design Turbine-Drive Characteristics

For operation at higher inlet pressures of 50 to 135 psia, size and weight will be reduced only slightly at the high flows and will essentially remain unchanged at the low flow rates. Above 50 psia, power output will increase slightly. At 135 psia, it will actually be about 20 percent less than that available at 50 psia for a given pressure ratio and flow rate.

Although the study was conducted only for 100 percent saturated vapor conditions, as mentioned previously, operation in the superheat region would certainly be desirable for the turbine. For each degree of superheat, the turbine output power will increase about 1 percent. The other design variables studied would not change significantly.

From these parametric data, it may be concluded that turbine drives for the mixer unit are possible. However, complete thermal conditioning system design evaluations are required to compare system performance, reliability, response, and weight before the best drive may be selected.

SYMBOLS AND ABBREVIATIONS

The symbols and abbreviations used in this report are presented at the end of each section, and in the order in which they occur.

LH_2 – Liquid Hydrogen

GH_2 – Gaseous Hydrogen

He – Helium

ΔP_f – Fluid Drag Through Wick Screen, lb/ft^2

ΔP_L – Static Pressure Across Wick

ΔP_B – Capillary Pressure Across Liquid-Vapor Interface, lb/ft^2

W – Weight of Capillary Standpipe, lb

R – Tank Radius, ft

L – Tank Height, ft

ρ – Material Density of the Capillary Standpipe, lb/ft^3

δ – Thickness of the Capillary Standpipe, ft

u – Tip Speed, ft/sec

g – 32.2 ft/sec^2

P_v – Vapor Pressure, lb/ft^2

ρ_ℓ – Liquid Density, lb/ft^3

η_{sep} – Separation Efficiency

η_p – Hydraulic Efficiency of Separator

K – Work Coefficient, used in performance of dynamic separator

x – Quality of Inlet Fluid

L – Latent Heat of Vaporization, Btu/lb

J – Energy-Work Conversion Factor

L_{BV} – Load of Belleville Spring, lb

L_{CB} – Load of Coil Springs and Bellows, lb

L_P – Load of ΔP Across Poppet

P_1A – Actuation Pressure Times Bellows Area, lb

P_2A – Deactuation Pressure Times Bellows Area, lb

G – Mass Flux Through Heat Exchanger, lb/hr-ft^2

D_H – Hydraulic Diameter, ft

P_1 – Expansion Valve Inlet Pressure, psi

P_2 – Expansion Valve Outlet Pressure, psi

P_3 – Final Saturated Vapor Pressure, psi

NTU – Number of Transfer Units

E – Heat Exchanger Effectiveness

h – Heat Transfer Coefficient, Btu/hr-ft^2-^{o}R

η – Fin Effectiveness

A – Heat Transfer Area, ft^2

T – Temperature, ^{o}R (Th-warm side, tc-cold side, tw-wall)

uA – Product of Overall Heat Transfer Coefficient and Area, Btu/hr-^{o}R

C – Heat Capacity, Btu/hr-^{o}R

r – Radial Distance Along Tank-Wall From Tank-Wall Heat Exchanger Attachment, ft

k – Thermal Conductivity, Btu/hr-ft-^{o}R

q – Heat Flux, Btu/hr-ft^2

n – Arbitrary Constant

β – h/kt

a – Point Attachment Radius for a Tank-Wall Heat Exchanger

t – Tank Wall Thickness, ft

h – Convective Heat Transfer Coefficient Between Tank Contents and Wall, Btu/hr-ft^2-^{o}R

h_i – Convective Coefficient Within the Tube, Btu/hr-ft^2-^{o}R

k_w – Thermal Conductivity of Tank Wall, Btu/hr-ft-^{o}R

ΔT – Temperature Difference Between Tank Contents and Fluid Within Heat Exchanger, ^{o}R

K_0 – Modified Bessel Function of Zero Order

K_1 – Modified Bessel Function of First Order

Q – Heat Transfer Rate, Btu/hr

N – Number of Pins

ω – Vent Fluid Flow Rate, lb/hr

λ – Latent Heat of Vaporization, Btu/lb

L – Tube Length, for Tank Wall Heat Exchanger, ft

D – Diameter of Tube, ft

f – Friction Factor

g_c – Gravitational Constant

μ – Viscosity, lb/hr-ft

ρ – Density, lb/ft^3

σ – Surface Tension, lb/ft

$\frac{\Delta P}{\Delta L}$ – Pressure Drop Per Unit Length, psi/ft

N_s – Specific Speed, $NQ/(g H_{AD})^{3/4}$

N – Rotational Speed, rpm

Q – Volumetric Flow Rate, ft^3/sec

H – Head Rise, ft

R_e – Reynolds Number, DU/V

D – Rotor Diameter, ft

U – Rotor Tip Speed, ft/sec

ν – Fluid Kinematic Viscosity

η_x – Hydraulic Efficiency at Inlet Quality

η_{mech} – Overall Mechanical Efficiency

Ψ – Head Coefficient

η_t – Adiabatic Efficiency Based on Inlet Total to Exit Total Pressure

M – Mach Number

K – Specific Heat Ratio of Gas

H_{AD} – Adiabatic Head, ft

ρ_o/ρ_i – Density Ratio Across Turbine

C – Disk Friction Coefficient

D – Effective Wheel Diameter, ft

ρ – Cavity Gas Density

Section II

PROPELLANT MIXING REQUIREMENTS

When a liquid hydrogen tank is being heated, temperature stratification will occur unless some means of distributing the heat is used other than conduction and natural convection through the fluid. Stratification increases the rate of pressure rise in the tank and, therefore, the vent frequency. In the extreme event that a thermal conditioning system only locally cools the tank propellant because of improper mixing, hot spots (outside the mixing zone) on the tank could control the tank pressure. Such an event, of course, would result in a failure of the vehicle mission.

In a 1-g gravity environment, buoyant forces create a boundary layer flow of warm fluid towards the top of the tank. This warm fluid is deposited in a stratified layer at the vapor-liquid interface and partially vaporizes into the ullage. In zero gravity, these buoyant forces are nonexistent, and stratification takes the form of heated propellant, vapor generation, and superheat at the tank wall.

Stratification reduction may be accomplished by forced convection mixing, and there are several criteria for reducing stratification by this means. Those investigated in this program as applicable to a thermal conditioning system are as follows:

- Suppression of boiling
- Sweeping of boiling vapor bubbles from the tank walls
- Condensation of trapped vapor pockets

Consideration of the appropriateness of these criteria to mixing requirements will be applied to zero- and low-gravity conditions. One-g gravity ground-hold and high-gravity ascent flight effects on the thermal conditioning system design and performance will be evaluated in a later section of this report.

If liquid hydrogen boiling is to be completely suppressed everywhere in the tank, then the design conditions for the mixing requirements will be established at the points of highest heat flux. These points are at the tank support and plumbing attachments. From Fig. I-33 it can be seen that these high heat flux points are widely dispersed.

The necessary velocity for suppression of boiling can be estimated by simultaneously matching the forced convection and nucleate boiling correlations. This matching is shown in Fig. II-1, where the Forster-Zuber correlation is used to extrapolate the available nucleate boiling data. All of the available pool boiling data found to date are summarized in Fig. II-2, which is reproduced from References 8 through 16. Noting that typical cryogenic vehicle support and plumbing heat flux ranges from 30 to 300 Btu per hr-ft^2, it is evident that local forced convection velocities far in excess of 10 ft/sec will be required on a continuous basis to suppress boiling. To provide a cooling jet of liquid hydrogen only 1/4-in. thick and flowing at 10 ft/sec across the equator of the Mission (2) vehicle tank requires a power input to the liquid hydrogen of 187 Btu/hr whereas the heat leaks from all other sources into the propellant tank average from 11.5 to 160 Btu/hr for typical vehicles (see Table I-1). Such power dissipation is obviously unacceptable. It may be concluded, therefore, that propellant mixing requirements are not to be based upon suppression of boiling.

Inasmuch as boiling must be permitted in the hydrogen tank, the velocity requirements for sweeping vapor bubbles created on the tank walls during boiling should be established. If such velocity requirements are small, then sweeping such vapor bubbles into cooler zones of the propellant tank and even through the thermal conditioning system will cause them to collapse by condensation.

The liftoff volume of bubbles from horizontal surfaces is well established theoretically and experimentally as a function of liquid surface tension, density, and the contact angle. Unfortunately, a search of technical literature offered no information which would enable the calculation of the critical size of a bubble attached to a vertical surface. If such data were available, dynamic pressure forces could be substituted for

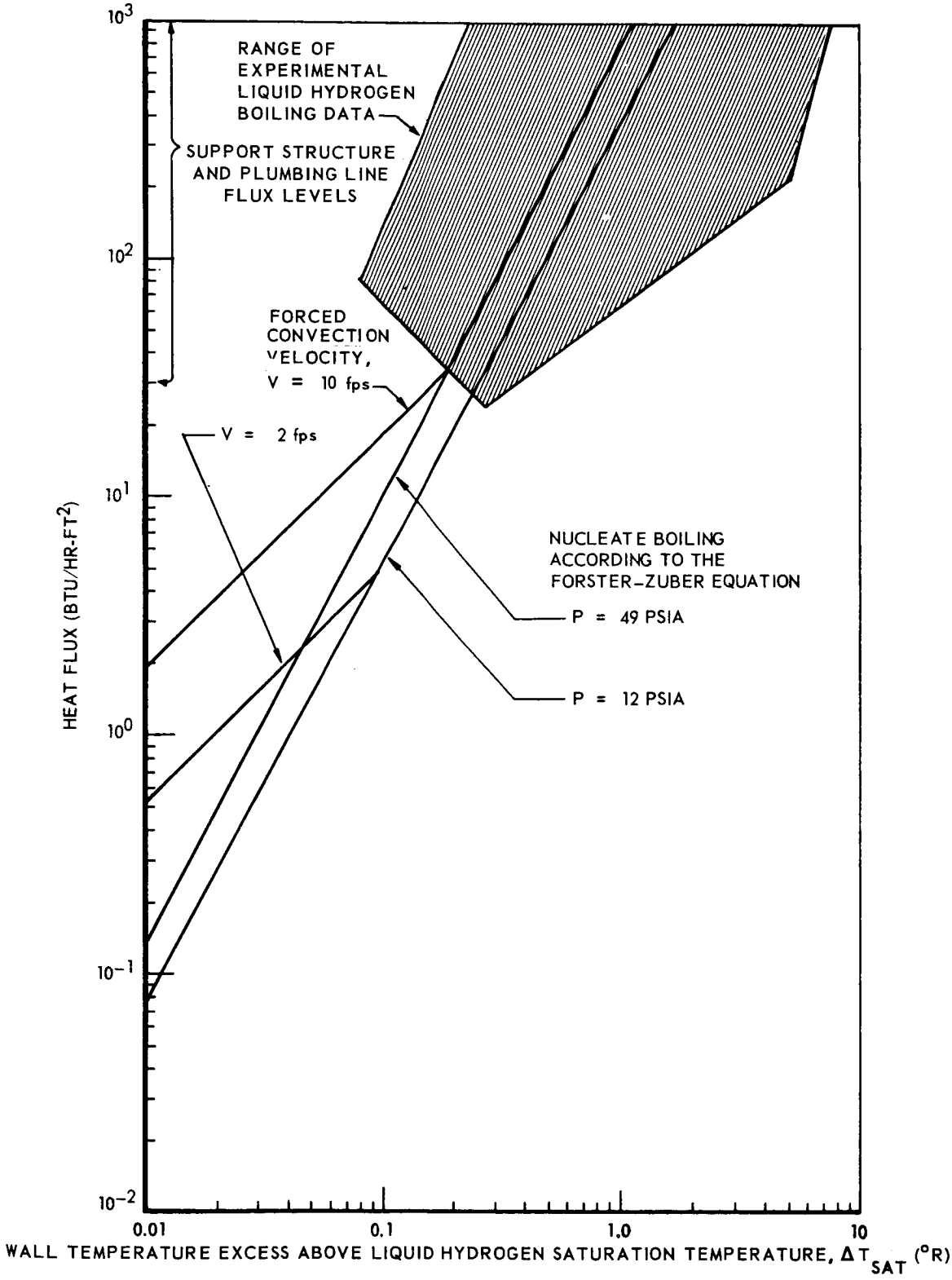

Fig. II-1 Forced Convection Requirements to Suppress Liquid Hydrogen Boiling on a Tank Wall

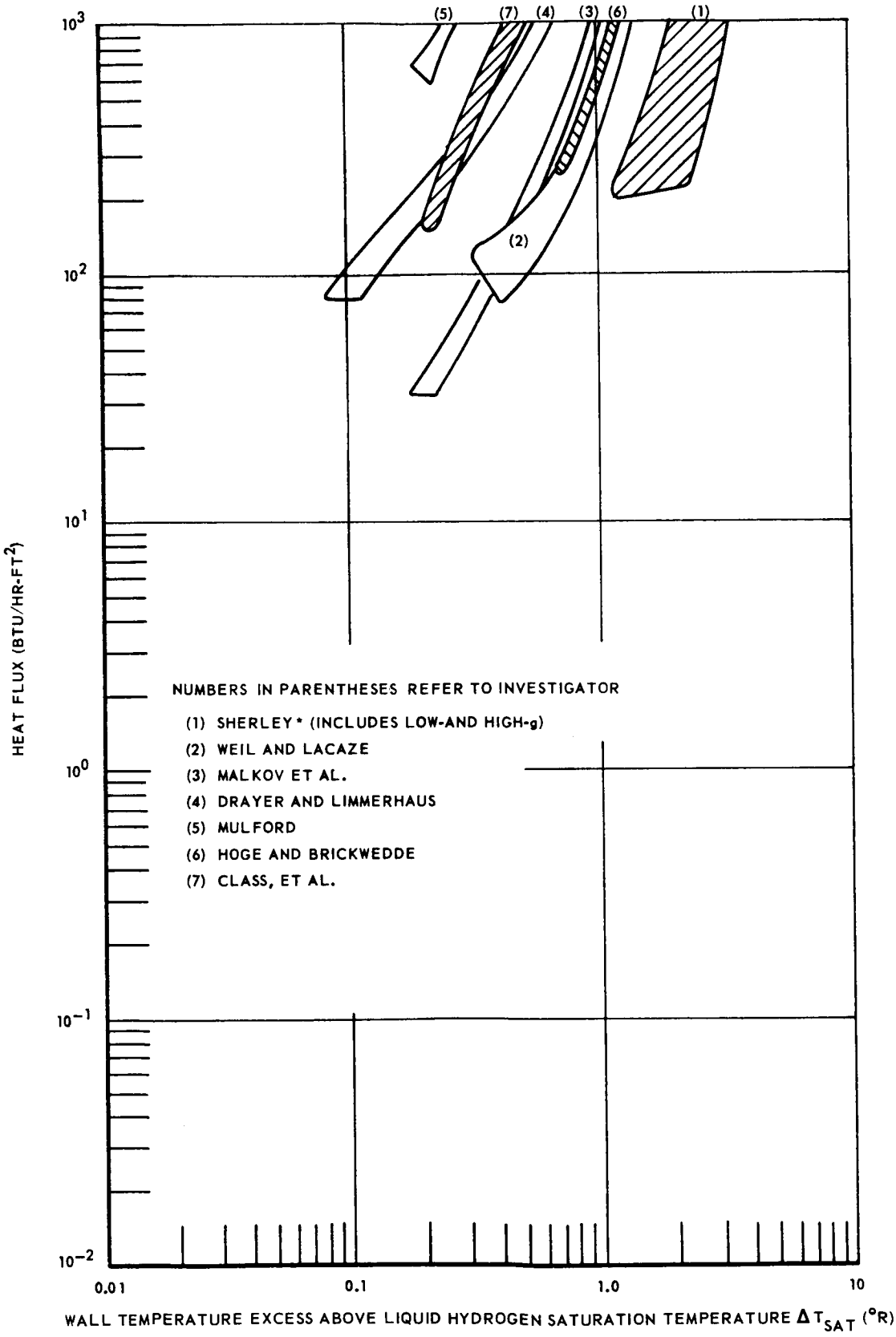

Fig. II-2 Experimental Pool Boiling of Hydrogen

buoyant forces, enabling calculation of the necessary velocity for a given size bubble. Lacking the necessary relation, a simple theory was developed as a means of obtaining a rough estimate of velocity requirements and is presented in detail in the Appendix A of this report. The results of the theory are presented in Fig. II-3.

From Fig. II-3, it can be seen that local liquid hydrogen velocities required to detach bubbles of modest size are very low. For example, a velocity of about 0.1 ft/sec will detach vapor bubbles greater than 0.1 in. in diameter from the tank wall. For vapor bubbles greater than 0.5 in. in diameter, a local liquid velocity of only 0.05 ft/sec is required. Sweeping of vapor bubbles from tank walls is therefore a practical concept in that low local velocities are adequate for this purpose.

Unfortunately this criteria is not applicable everywhere in the tank. Portions of the propellant tank are blocked to effective propellant circulation by baffles used for propellant slosh suppression. Figure II-4 shows such baffles as they would appear in a Mission (2) vehicle, for example. The three baffles are 6-1/2 in. wide with a vertical spacing of 12.9 in. The middle baffle is located on the tank equator, and all baffles have a preferred setting of 1/2 in. from the tank wall, but in no case greater than 1 in.

Unless extraordinary means, such as direct pumping of the trapped vapor, are employed to sweep vapor trapped within these slosh baffles, it must be presumed that vapor within these baffles will remain locked — independent of tank general circulation velocity. In that event, such trapped vapor must be effectively cooled by condensation at the point of origin.

The forced convection requirements for condensation of such "locked" vapor generated at the tank wall were investigated. A search of the technical literature revealed that no experimental data or theory were available for predicting the rate of vapor condensation to a cooling stream of liquid. Therefore, the theoretical relations for predicting the coefficient of heat transfer between a pure saturated vapor and a colder moving stream of liquid in a zero-gravity field were derived by Sterbentz and Bullard. The development of these theoretical relations is somewhat similar to the works of Nusselt.

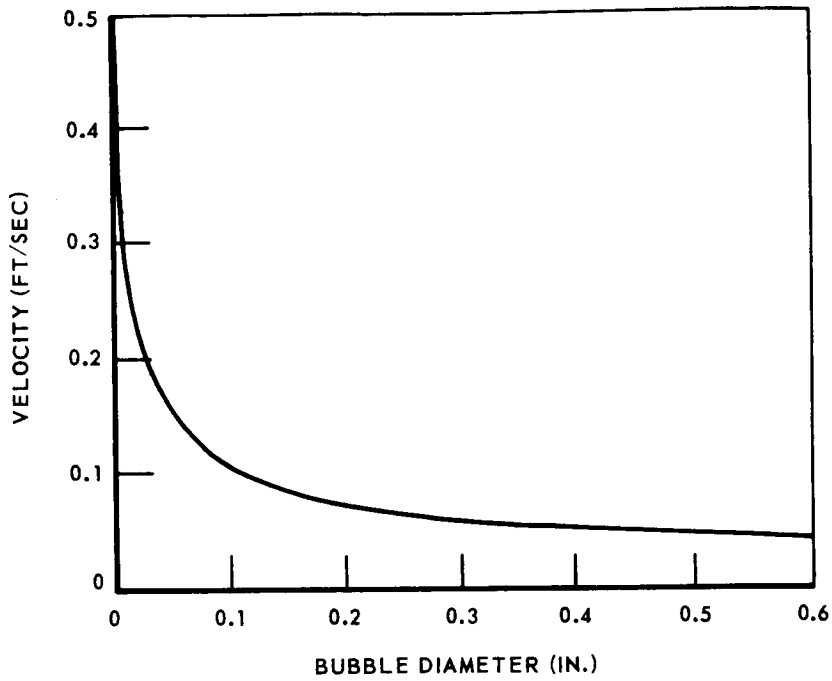

Fig. II-3 Local Velocity Required to Detach Hydrogen Vapor Bubbles in a Zero-Gravity Field

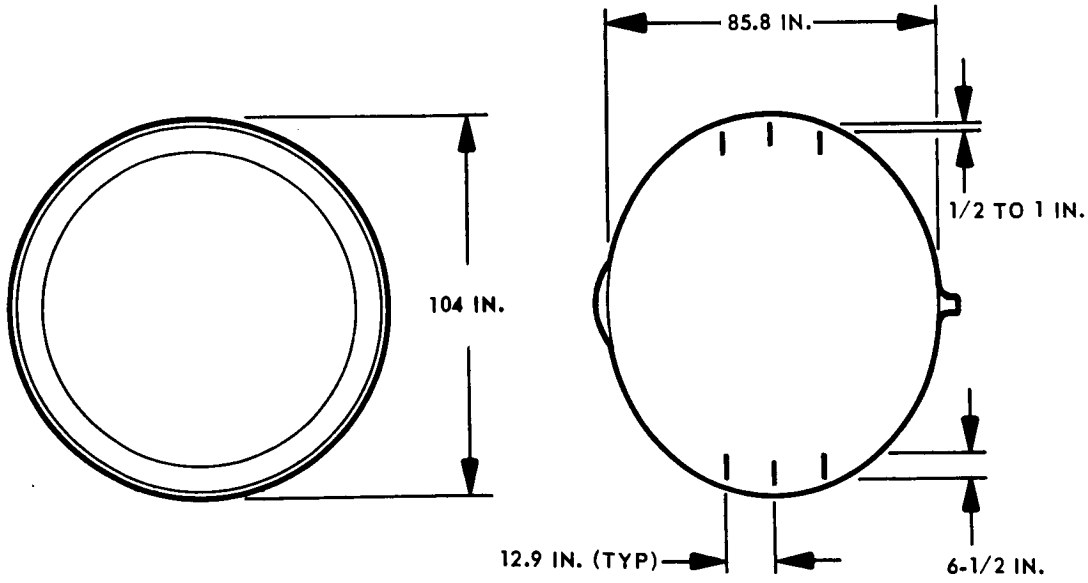

Fig. II-4 Mission (2) Vehicle Slosh Baffle Requirements

In 1916, Nusselt derived theoretical relations for predicting the heat transfer coefficient between a pure saturated vapor and a colder surface. In his work, it was assumed that the force of gravity alone causes the flow of condensate over the cold surface, thus neglecting the possible effect of vapor velocity upon the thickness of the condensate film. By employing the definition of viscosity in streamline motion and assuming zero velocity of the condensate at the cold surface and a maximum velocity at the liquid-vapor interface, Nusselt obtained the thickness of the condensate film at a given point on the surface. By assuming that the total thermal resistance lies in the film of condensate through which the latent heat of condensation is conducted, but neglecting the cooling of the condensate, the locat heat transfer coefficient may then be calculated. A complete development and evaluation of Nusselt's work is given in Ref. 17. The two forms of interest of the theoretical dimensionless equations of Nusselt for film-type condensation on vertical surfaces are as follows:

$$h_m = 0.943 \left(k_\ell^3 \rho_\ell^2 g \lambda / \mu_\ell L \Delta T \right)^{1/4} \tag{1}$$

and

$$h_m \left(\frac{\mu_\ell}{k_\ell^3 \rho_\ell^2 g} \right)^{1/3} = 1.47 \left(\frac{4\Gamma}{\mu_\ell} \right)^{-1/3} \tag{2}$$

Figure II-5, taken from Ref. 17, presents a comparison of Eq. (2) with experimental data taken from a 1-g gravity field with steam condensing on vertical tubes and plates. It can be seen that the theory yields good agreement with the experimental data, although the theoretical values are generally low. This effect is possibly due to the downward flow of vapor, thereby reducing the condensate film thickness, and to mixing action of the ripples in the condensate film.

In the work of Sterbentz and Bullard, it has been assumed that the streamline flow of liquid over the vapor alone causes the flow of condensate at the cold liquid-vapor interface in a zero-gravity environment. By employing the definition of viscosity in streamline flow to the condensate film and assuming a zero-velocity of the condensate at the vapor-condensate interface and a maximum velocity at the condensate-liquid

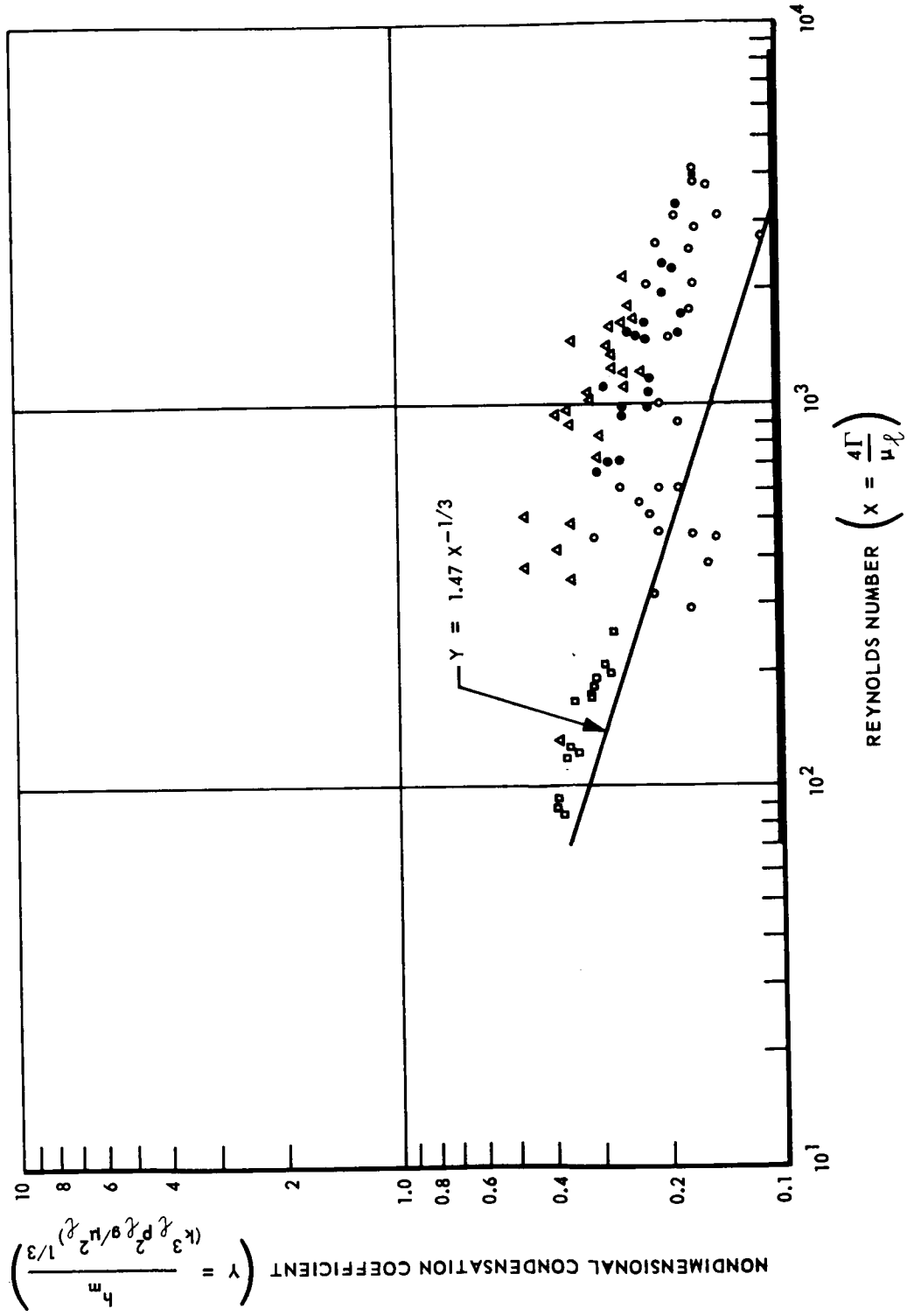

Fig. II-5 Comparison of Nusselt Correlation with Experimental Steam Data

interface, the thickness of the condensate film at a given point on the liquid surface is obtained. Then, as in the work of Nusselt, the local heat transfer coefficient may be calculated on the basis that the total thermal resistance lies in the film of condensate through which the latent heat of condensation is conducted. Cooling of the condensate is neglected. Equation (3) defines the heat transfer coefficient derived in this manner. The detailed derivation is given in Appendix B of this report

$$h_m = 1.12 \left(k_\ell \, \rho_\ell \, u_o \lambda / L \, \Delta T \right)^{1/2} \tag{3}$$

Figure II-6 presents the heat transfer coefficient as calculated from Eq. (1) for gravity dominated situations and from Eq. (3) for forced convection cases.

The fact that the results of the theories are convergent is significant and indicates that conditions can exist where condensation is either gravity dominated or forced convection dominated. These domains may be identified by equating Eqs. (2) and (3), yielding the following expression:

$$\left(\frac{u_o}{gL}\right)\left(\frac{1}{\Delta T}\right) = 0.84 \left(\frac{k_\ell}{\mu_\ell \, \lambda}\right) \tag{4}$$

The right-hand side of Eq. (4) is a property function of the fluid. The left-hand side is a Froude number given a temperature difference between the vapor and the condensation surface. If this Froude number exceeds approximately 0.002 for a 1° R temperature difference for liquid hydrogen, then condensation induced by forced convection is more rapid than that induced by gravitational forces. The implication of this result is that in a low-gravity field very gentle mixing of the propellant will bring about a more rapid drop in tank pressure than would be induced by a tank-wall cooler or heat exchanger without a mixer.

After the first firing of the engines of a space vehicle, the ullage contains helium gas. When a mixture of a condensable vapor and a noncondensable gas is exposed to a surface colder than the dew point of the mixture, some condensation occurs. A layer of

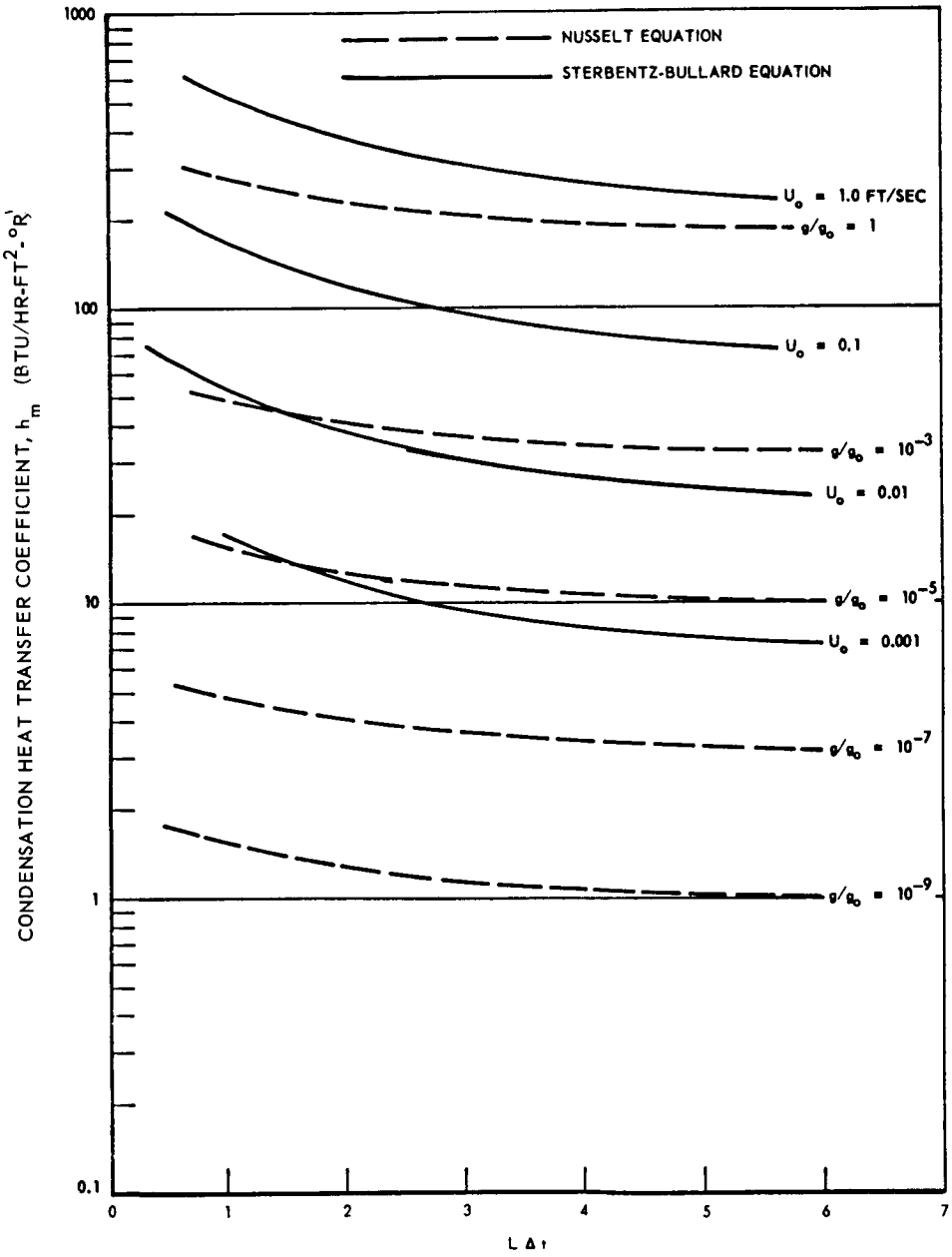

Fig. II-6 Vapor Condensation Correlations, 0g and 1g

condensate collects on the cooling surface and a film mixture of noncondensable gas and vapor forms next to the condensate layer. The concentration of vapor in the gas film is lower than in the main body of the mixture due to condensation of hydrogen. Because of the difference in partial pressure of the vapor between the main body of the mixture and at the interface between the gas and condensate films, the vapor diffuses from the main body through the gas film to liquify at the interface.

In forced convection condensation however the moving liquid and condensate film cause the vapor to move with the film as a result of viscous shear. The resulting drag causes a circulation of the vapor and gas to produce a continuous convective replacement of the low vapor concentration film next to the condensate film with a fresh mixture of higher concentration from the main body of vapor and gas. The mechanism is obviously quite intricate.

The effects of the addition of the helium noncondensable gas to the hydrogen condensable vapor are to lower the coefficient of heat transfer as computed from Eq. (3). However, no estimate is currently available for determining the magnitude of the effect.

Having established the values of the heat transfer coefficient for a condensing vapor cooled by a moving liquid stream, the local forced convection requirements for tank pressure decay must next be examined. The rate of change of tank pressure is described by Eq. (5).

$$\frac{dP}{d\theta} = \gamma P \left(\frac{\rho_\ell}{\rho_g}\right) \left(\frac{\Delta T}{\rho_\ell \lambda}\right) \left(\frac{A}{v_g}\right) h_m \tag{5}$$

The expression, derived in Appendix C, is general and may be applied to various ullage volumes and heat transfer areas. If the worst situation is assumed wherein the tank pressure is diminished only by cooling the vapor trapped between the slosh baffles, Eqs. (3) and (5) yield the following expression:

$$\frac{dP}{d\theta} = \gamma P \left(\frac{\rho_\ell}{\rho_g}\right) \left(\frac{\Delta T}{\rho_\ell \lambda}\right) \left(\frac{bL}{v_T}\right) \left(\frac{v_T}{v_g}\right) \left[\frac{k_\ell \rho_\ell U_o \lambda}{L \Delta T}\right]^{1/2} \tag{6}$$

From Eq. (6), it can be seen that the pressure response in a hydrogen tank is dependent upon the tank and slosh baffle geometry, the ullage volume ratio, the tank pressure, the temperature difference between the cooling liquid stream and the vapor pocket, and the local stream velocity. Equation (6) is plotted in Figs. II-7, II-8, and II-9 for the three reference vehicles and shows a marked decrease in pressure response as the ullage volume increases. Also shown are the ullage volumes prior to each of the firings; it can be seen that very low velocities will lower the pressure within a few minutes – even near the end of the mission. For example, if the thermal conditioning is activated when the tank pressure reaches 20 psi and shuts off when it drops to 17 psi, the Mission (2) vehicle system will operate for 230 sec with a velocity of 0.1 ft/sec at the propellant-vapor interface.

For efficient pressure response, the heat transfer rate between the vapor and circulating fluid must be as high or higher than the energy vent rate, that is,

$$\frac{hA\,\Delta T}{\dot{v}\,\omega\,\lambda} \geq 1$$

Therefore

$$1.12 \left[\frac{k_\ell \rho_\ell u_o \lambda}{L \Delta T}\right]^{1/2} \frac{bL}{\omega \lambda} \geq 1$$

For liquid hydrogen, this is satisfied if

$$\left(\frac{bL}{\omega}\right) \left(\frac{u_o}{L \Delta T}\right)^{1/2} \geq 22$$

This condition is easily met for even high vent flow rates of 10 lb/hr where the required cooling stream velocity should be equal to or greater than 0.0084 ft/sec.

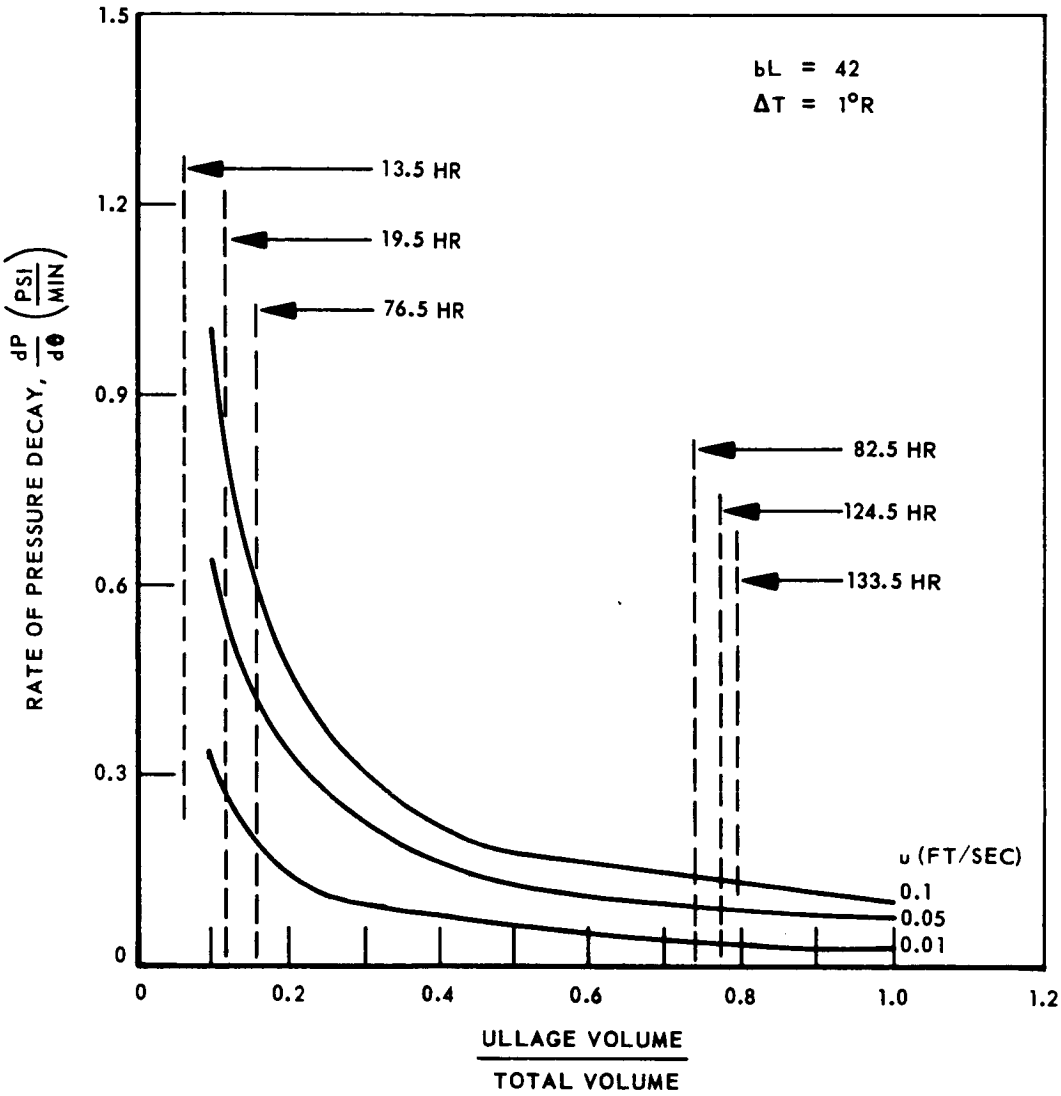

Fig. II-7 Tank Pressure Response – Mission (1) Vehicle

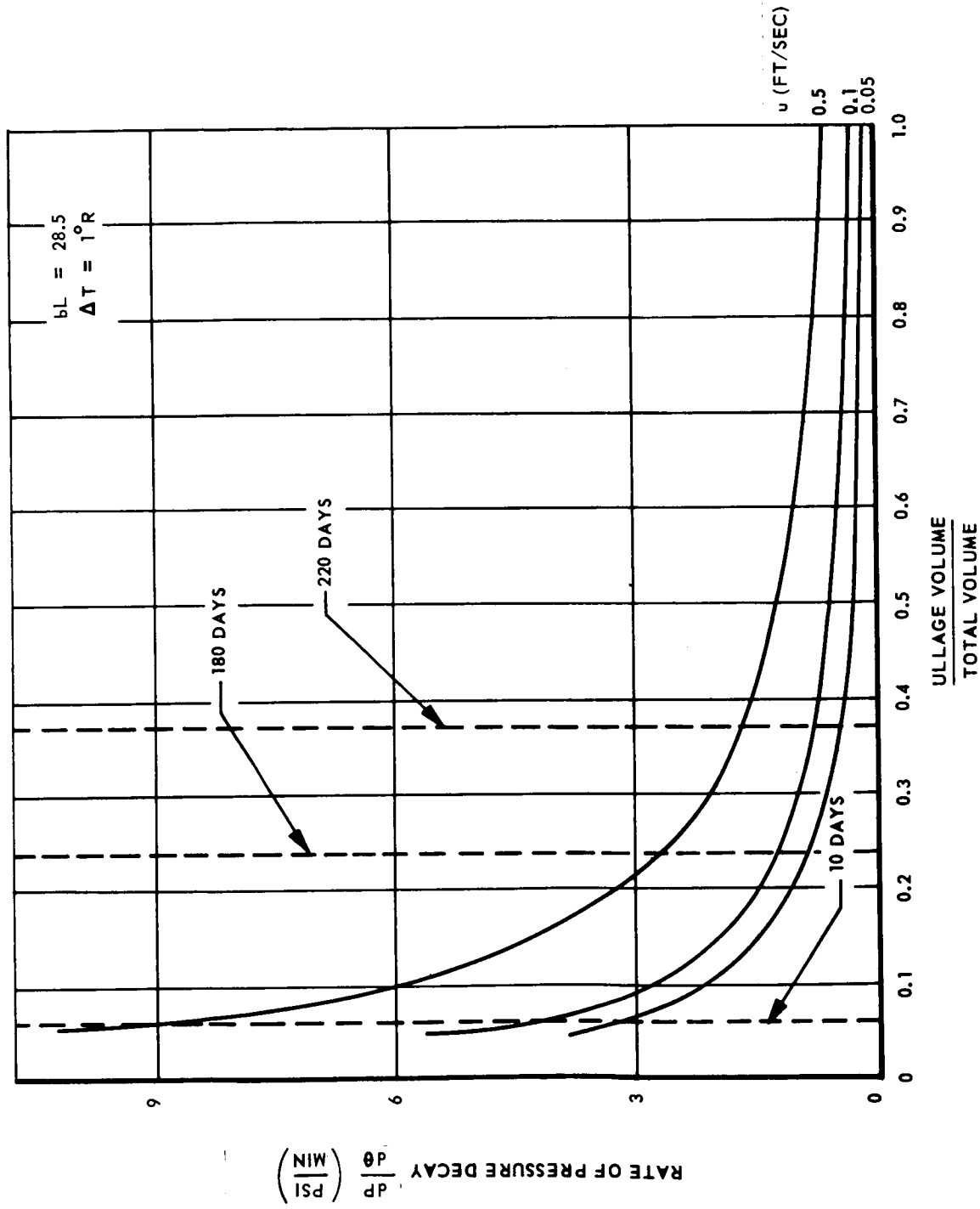

Fig. II-8 Tank Pressure Response – Mission (2) Vehicle

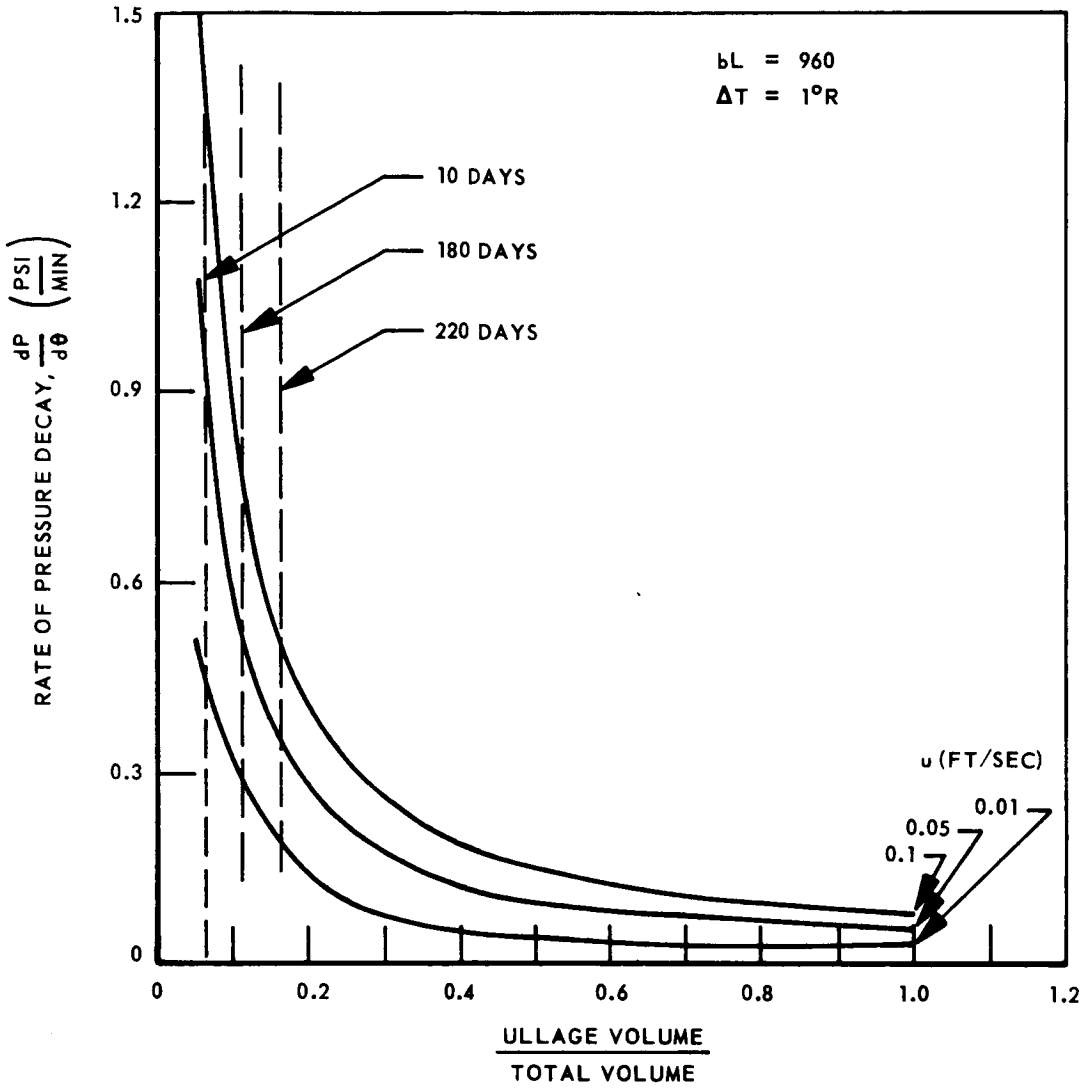

Fig. II-9 Tank Pressure Response – Mission (3) Vehicle

Also of interest is the determination of the rate of pressure rise in the propellant tank in a perfectly stratified condition. With this condition, as shown in the sketch below, a layer of vaporized propellant will form on the tank wall.

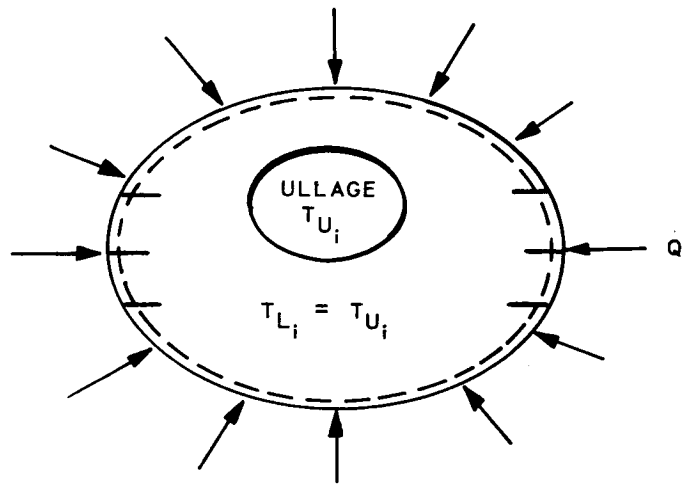

A heating rate Q enters the tank and creates vapor such that, at some time θ, the conditions indicated by the dotted lines exist. The newly created vapor occupies approximately 40 times the volume it did as liquid. Considering the liquid to be incompressible relative to the vapor, this expansion of liquid upon vaporizing creates a change in pressure by compressing the initial ullage and restricting the growth of the newly created vapor layer.

As shown in Appendix D of this report, Eq. (7) represents the most rapid rate of pressure rise that is possible in the propellant tank.

$$\left(\frac{\Delta P}{\Delta \theta}\right)_{max} = \frac{R}{(V_g/V_T)\, C_P} \left(\frac{Q}{V_T}\right) \tag{7}$$

The term V_g/V_T is the minimum percent ullage volume (about 5 percent for cryogenic stages). The term Q/V_T is the heating rate per unit tank volume, and the reference missions encompass a wide spectrum of value for $\dot{Q}/V_T$. Equation (7) is plotted in Fig. II-10 showing the variation of tank pressure rise rate with heat rate and tank

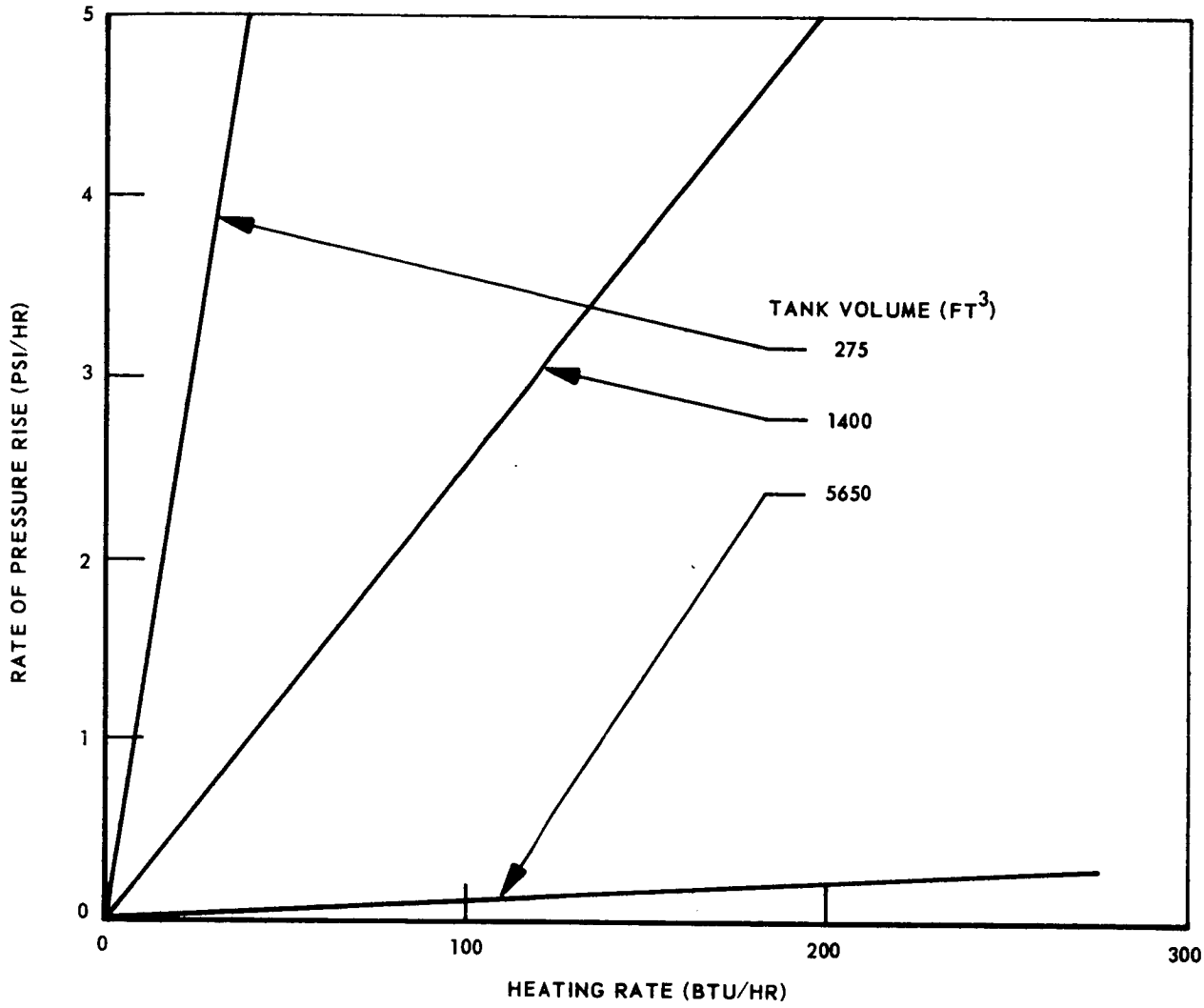

Fig. II-10 Tank Pressure Rise Rate With Only Ullage Heating (Ratio of Ullage Volume to Tank Volume Equals 0.05)

volume for an ullage volume ratio of 5 percent. From these data, the resulting maximum rates of pressure rise for these three missions are:

$$\text{Mission (1): } (\Delta P/\Delta\theta)_{max} = 4.8 \text{ psi/hr}$$

$$\text{Mission (2): } (\Delta P/\Delta\theta)_{max} = 2.2 \text{ psi/hr}$$

$$\text{Mission (3): } (\Delta P/\Delta\theta)_{max} = 0.04 \text{ psi/hr}$$

From these values it is clear that the vent frequency in the absence of mixing does not impose severe response requirements upon the components of a thermal conditioning system.

From Fig. II-6 it will be recalled that, in the absence of forced convection, fairly high heat transfer coefficients are estimated by Nusselt's Eq. (1). In fact, for an acceleration environment as low as 10^{-9} g, heat transfer coefficients of greater than 1 Btu/^{o}R-ft^{2}-hr are obtained. For vapor trapped within the slosh baffles of the Mission (2) vehicles, heat will be transferred across the vapor-liquid interface at a rate of about 54 Btu/hr if the vapor-liquid interface area is equal to (bL) of the baffles. This rate is well in excess of the average total heat leak into the tank of 11.7 Btu/hr. Therefore, from these data, it might be inferred that the propellant tank contents may be more mixed than highly stratified as in the case described by Eq. (7). Consequently, an analysis of a cycle was performed for a completely mixed propellant for the Mission (2) vehicle. The results are shown in Figs. II-11 through II-14.

For such a system, the regulator controlling the vent cycle would open at a preselected tank pressure and would reseat at a preselected lower pressure. Figure II-11 shows the time between vent cycles as a function of the regulator operating band and the average heating rate. Values are shown for 0 days and 220 days. For a given operating band, the vent cycle is shorter later in the mission because the available heat sink is less and results in a faster rate of pressure rise.

Figure II-12 shows the quantity of propellant vented during each vent period as a function of the valve operating band and the propellant heating rate. It will be noted

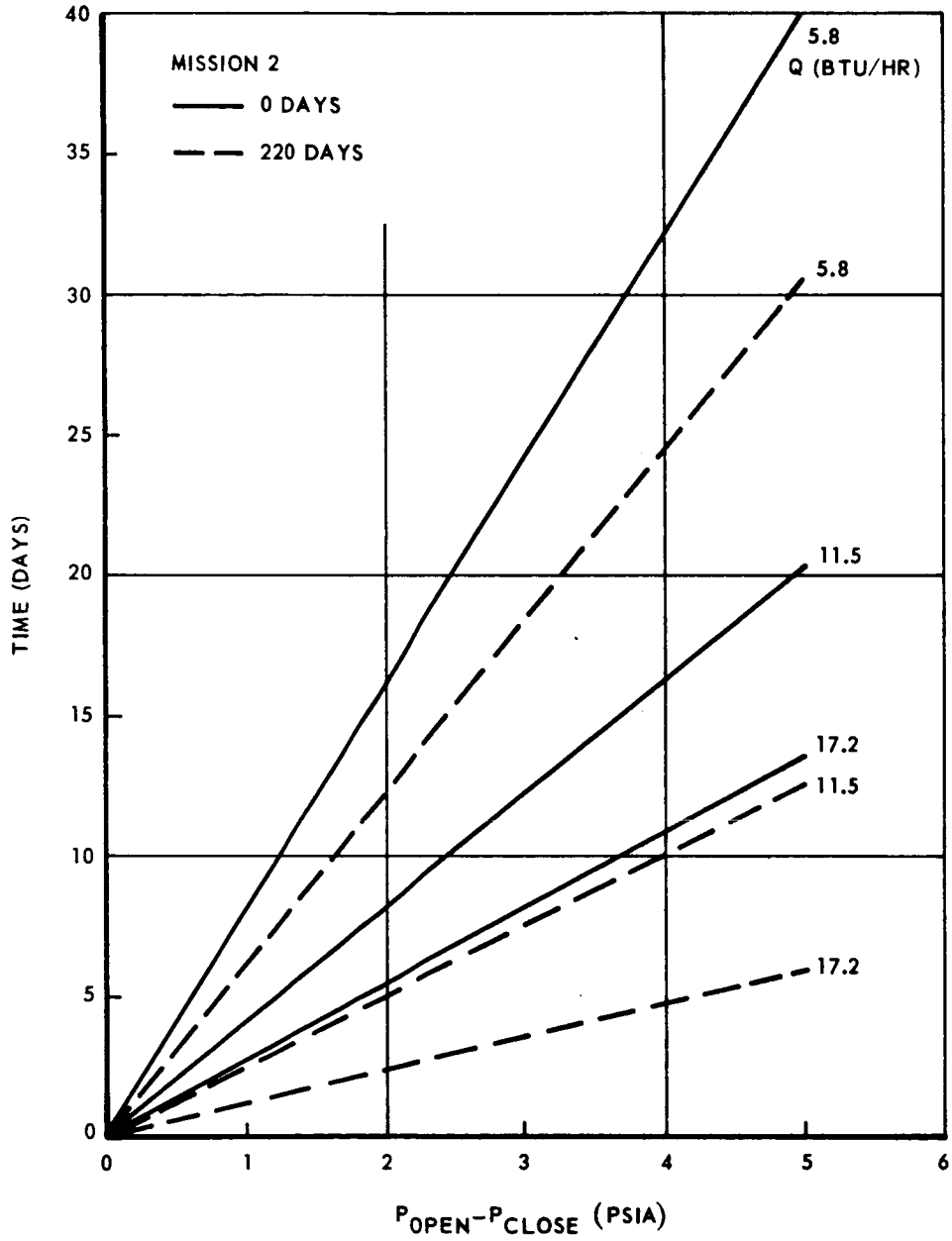

Fig. II-11 Valve-Closed-Position Duration for 0- and 220-Day Times After Launch

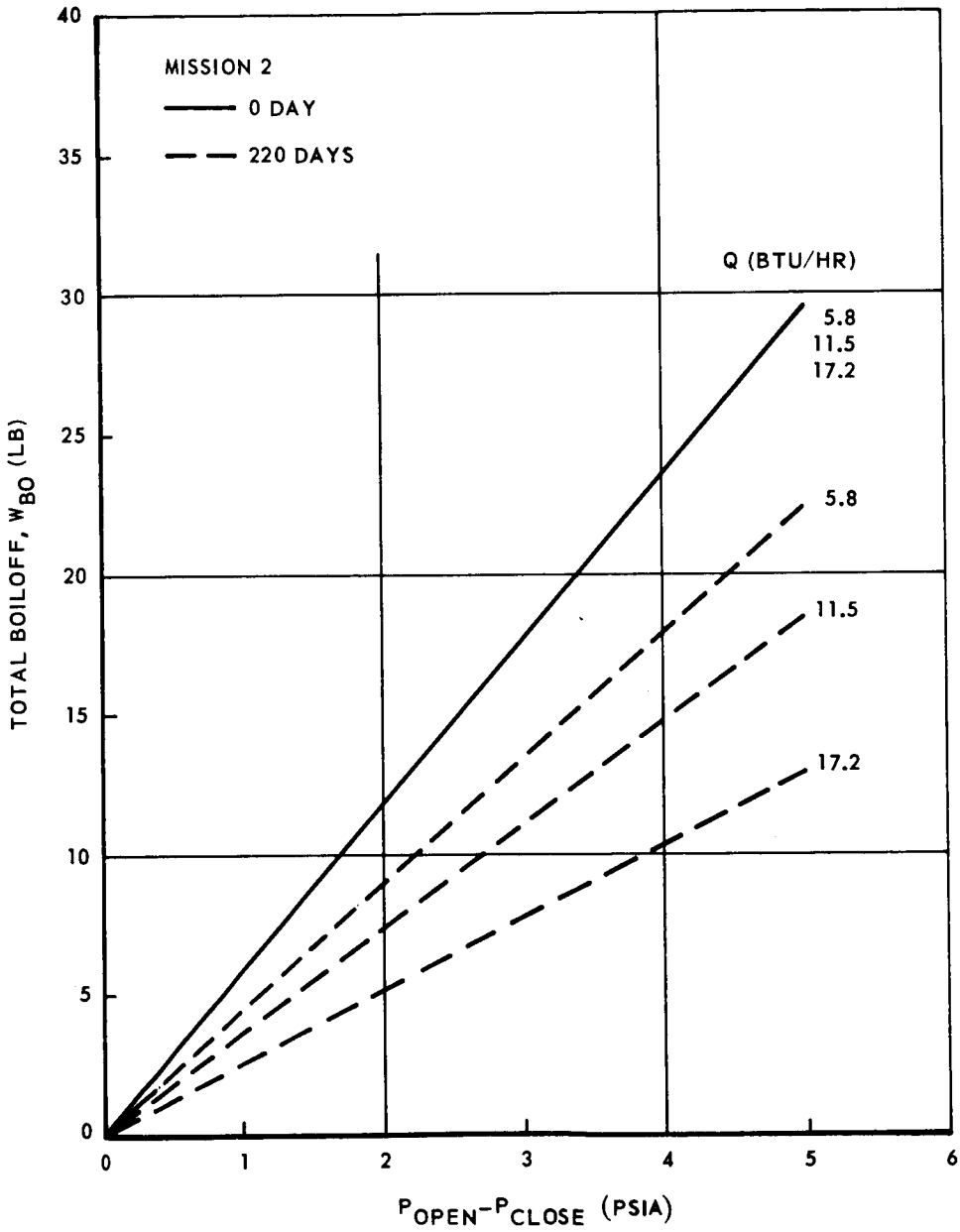

Fig. II-12 Amount of Hydrogen Expelled During Valve Opening for 0- and 220-Day Times After Launch

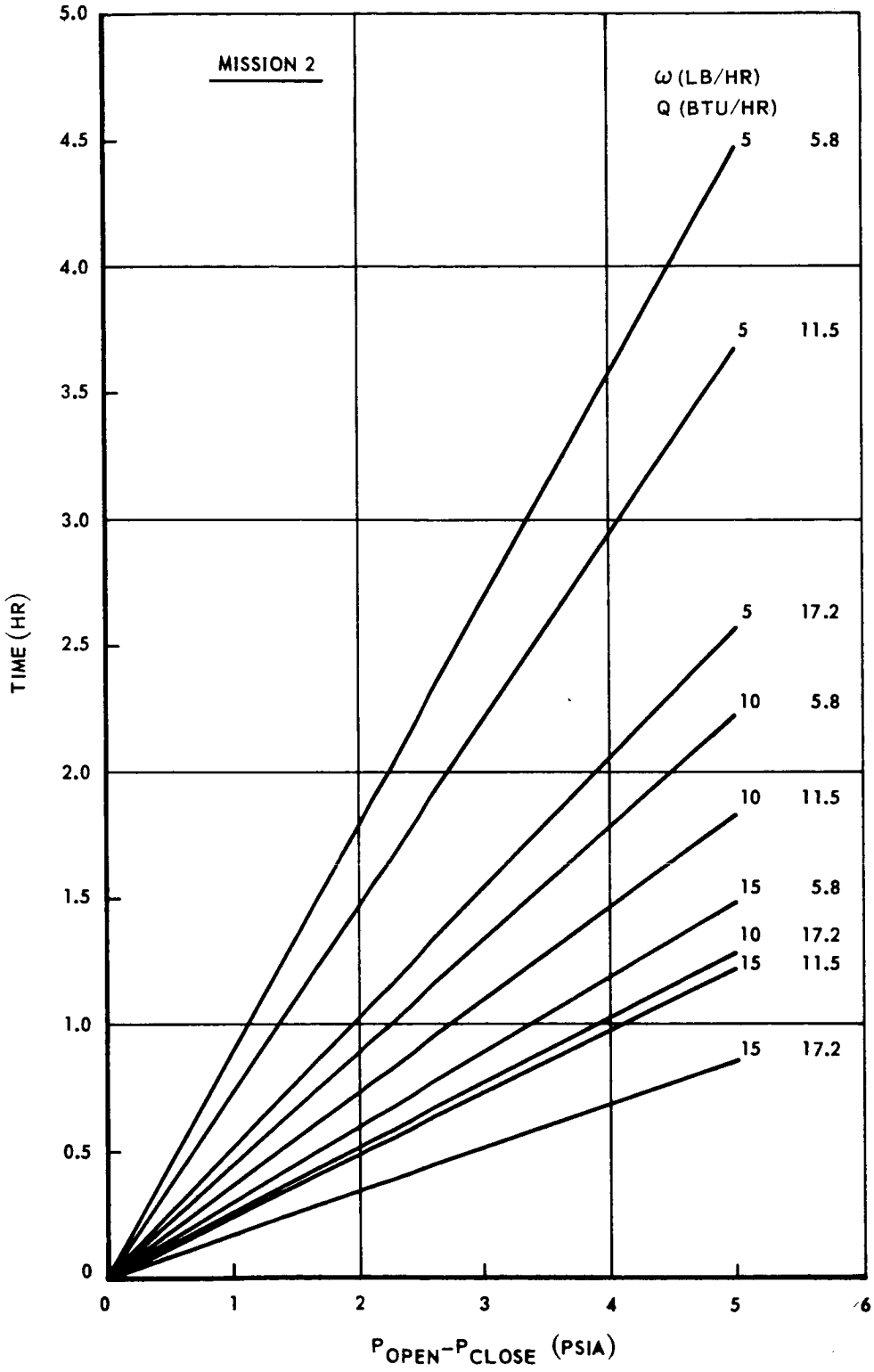

Fig. II-13 Valve-Open-Position Duration at 0 Days After Launch

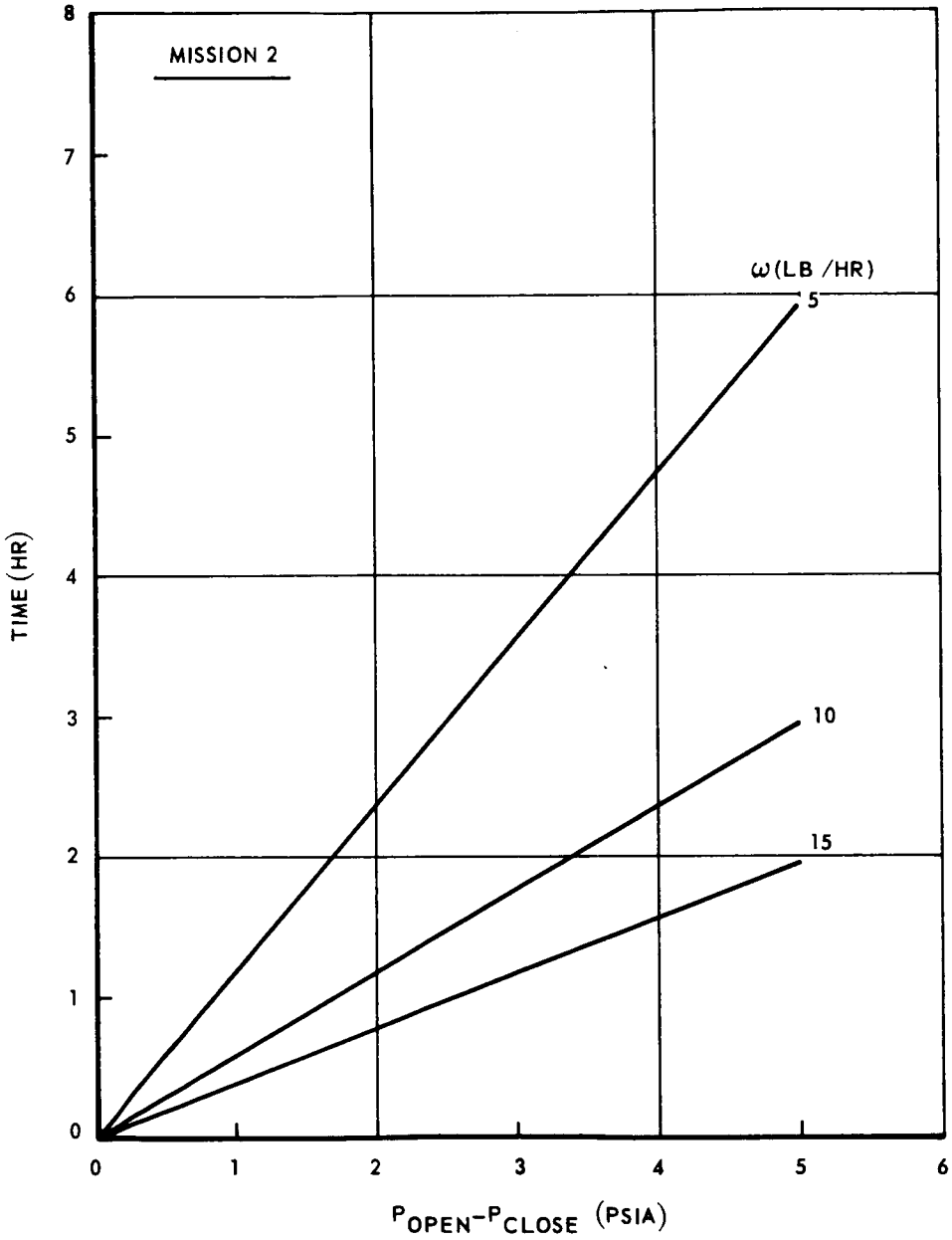

Fig. II-14 Valve-Open-Position Duration at 220 Days After Launch

that heating rate does not change the expelled fluid quantity at the beginning of the mission, but it does near the end of the mission. The expelled propellant is proportional to the heat sink capacity of the remaining tank contents. If a high heating rate occurs throughout the mission, the available heat sink at the end is reduced by boiloff and results in a higher vent frequency but less expelled fluid per cycle.

Figures II-13 and II-14 show the blowdown time as a function of the pressure control band and the vent rate.

From these data, it is clear that if a large degree of propellant stratification occurs in a propellant tank, the thermal conditioning system will operate for many short vent cycles. If a more nearly mixed propellant condition occurs in the tank, then the thermal conditioning system will vent the tank over a relatively few longer vent cycles. The specific degree of mixing or stratification that will occur in any propellant tank is a function of the specific vehicle and payload geometry and the details of vehicle orientation, rotation, flight attitude, and maneuvers. A properly designed thermal conditioning system should not be restricted by such considerations. As such, the optimum thermal conditioning system will have the capability to reliably meet the off-on operation of the many vent cycles demanded by a stratified propellant condition, as well as meet the demands of longer duration shut down and venting of the mixed propellant condition.

The foregoing analyses define the functional requirements of a mixer, in terms of fluid circulation velocities, which can be related to the vehicle and mission parameters. These circulation velocities can be provided by a mixer that either expels a jet radially along the tank wall or by one that expels a jet axially in the tank. In either case, it remains to relate the characteristics of the device to its functional requirements. These requirements are discussed next.

Consider first in detail the radially expelled or single wall-bound jet. Since no analytical model of a single wall-bound jet into a spherical tank was found in the literature, the mixing phenomenon in a propellant tank in a zero-gravity field was predicted from an analysis originated by Schwind. A jet leaving a mixer at the bottom of a tank will quickly become a wall jet almost in pure radial outflow. This becomes a two-dimensional wall jet at the tank equator, then approaches a radial inflow jet as it progresses in the upper half of the tank. Separation from the wall will occur somewhere in the upper part of a full

tank, and some of the wall jet fluid returns down the vertical axis of the tank to the mixer inlet. The natural thickening of the wall jet is partially counteracted in the lower half by the axisymmetric thinning effect of increasing circumference; and the thickening is aided by this effect in the upper half. When the jet flow is initiated, the central fluid is at rest; but it gradually arrives at a steady-state motion of a non-isentropic toroidal vortex. At this steady-state condition, the core flow is separated from the wall jet by an axisymmetric stream sheet, shown as a stream line in the cross section cut through the tank in the following schematic. Friction on this dividing stream line near the mixer exit provides an energy input to the vortex which is partially

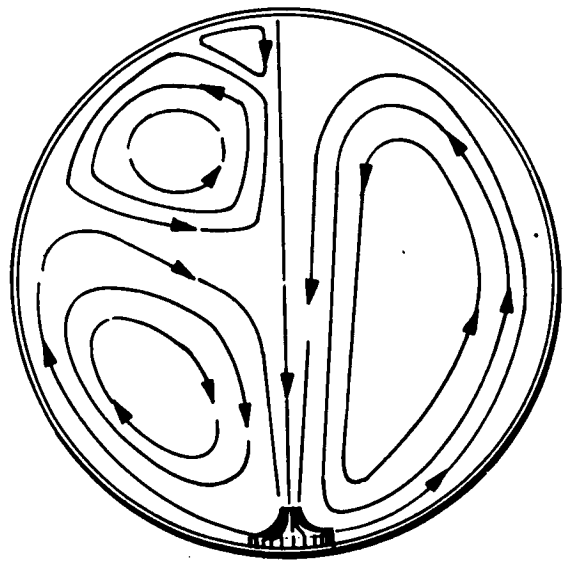

SCHEMATIC OF
TWO POSSIBLE FLOW CONFIGURATIONS

redeemed elsewhere where the vortex will help drag the wall jet along. For axisymmetric steady flow, an integral condition can be shown (Ref. 18) to the effect that the net diffusion of (radius) x (vorticity) across the dividing streamline is zero. Boundary layer separation may even occur not too far above the equator, and one more or even several more closed vortexes may form as shown in the left half of the above sketch. For a given full tank and starting wall jet, geometry dimensional analysis shows that the fluid motion is solely a function of a characteristic jet Reynolds number.

The effect of the toroidal vortex, while no doubt very important, has been neglected in this analysis, as only the most sophisticated, costly computer programming could include the vortex at this time. From results of this analysis, an estimate can be made of the toroidal vortex strength and its effect on the wall jet.

Applying the moment of momentum about the center of a sphere, the continuity of mass, and the viscous wall velocity profile matched to a free jet velocity profile at the jet maximum velocity point, a number of equations can be derived which define the maximum velocity in the jet, the distance between the tank wall and the maximum jet velocity streamline, jet momentum, and total jet thickness. These results have also been applied to the equations of heat transfer to obtain a measure of the heat transfer coefficient at the tank wall for application to the tank-wall heat exchanger unit. A detailed development of these relations is presented in Appendix E of this report.

The results of these analyses are shown in Figs. II-15 through II-20. Figure II-15 shows the decay of the velocity and the heat transfer coefficient. Figures II-16 through II-19 show the growth of the boundary layer as well as the velocity decay for a range of radius-to-jet-height ratios and various Reynolds numbers. The effect of jet Reynolds number on layer growth and velocity decay is shown in Figs. II-19 and II-20 for various angular locations and two different radius-to-jet-size ratios. Figure II-21 shows the appearance of the loci of velocity ratios U/U_m for a Reynolds number of 10^5 and different initial jet thicknesses. Figure II-22 shows typical values of maximum jet velocities along the tank for a Reynolds number of 10^5 and different values of initial jet thickness.

It is of interest to note from Fig. II-21 that the jet maximum velocity displaces slowly from the tank wall. Although these profiles are representative of clean tank circulation patterns, the thinness of the maximum velocity jet profile is encouraging. With slosh baffles displaced from the tank wall, a reasonable degree of propellant circulation between the tank wall and the baffles might be expected.

For the central or axial jet mixer, the fluid stream is ejected from one end of the tank generally along an axis of the propellant tank. With an axial jet, the velocity

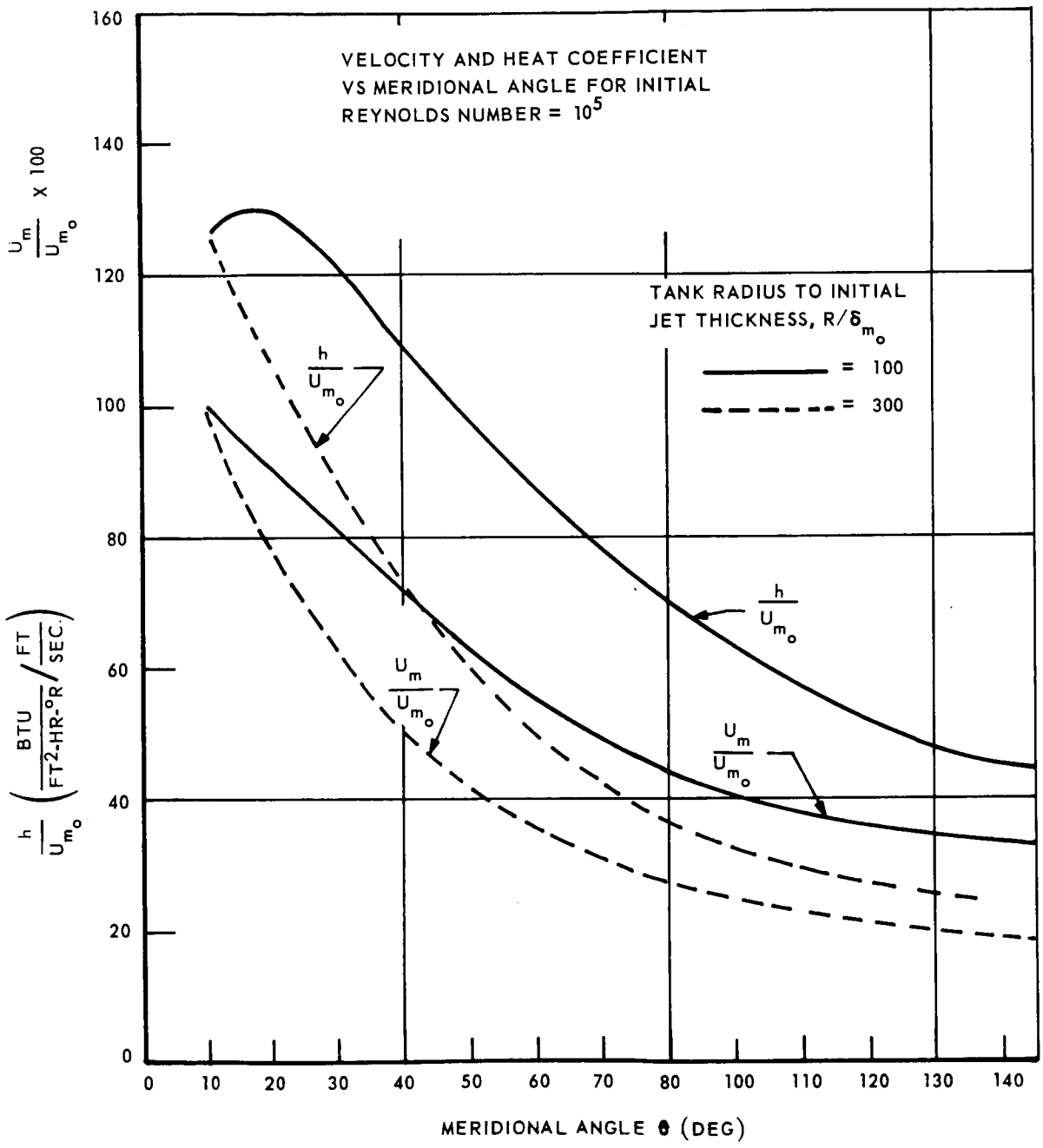

Fig. II-15 Velocity and Heat Transfer Coefficients in a Wall-Bound Axisymmetric Jet

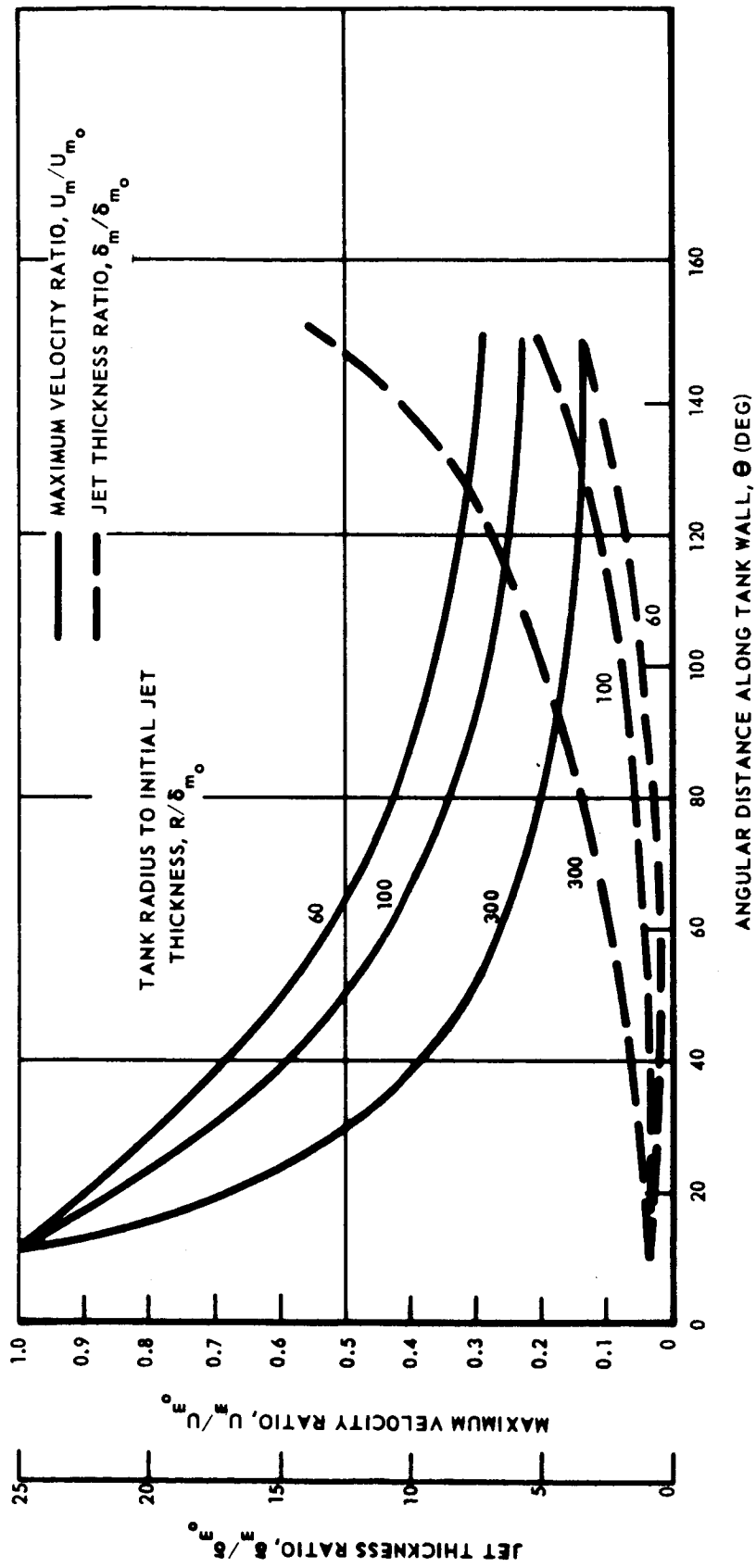

Fig. II-16 Single Wall-Bound Jet Degradation, Reynolds Number = 10,000

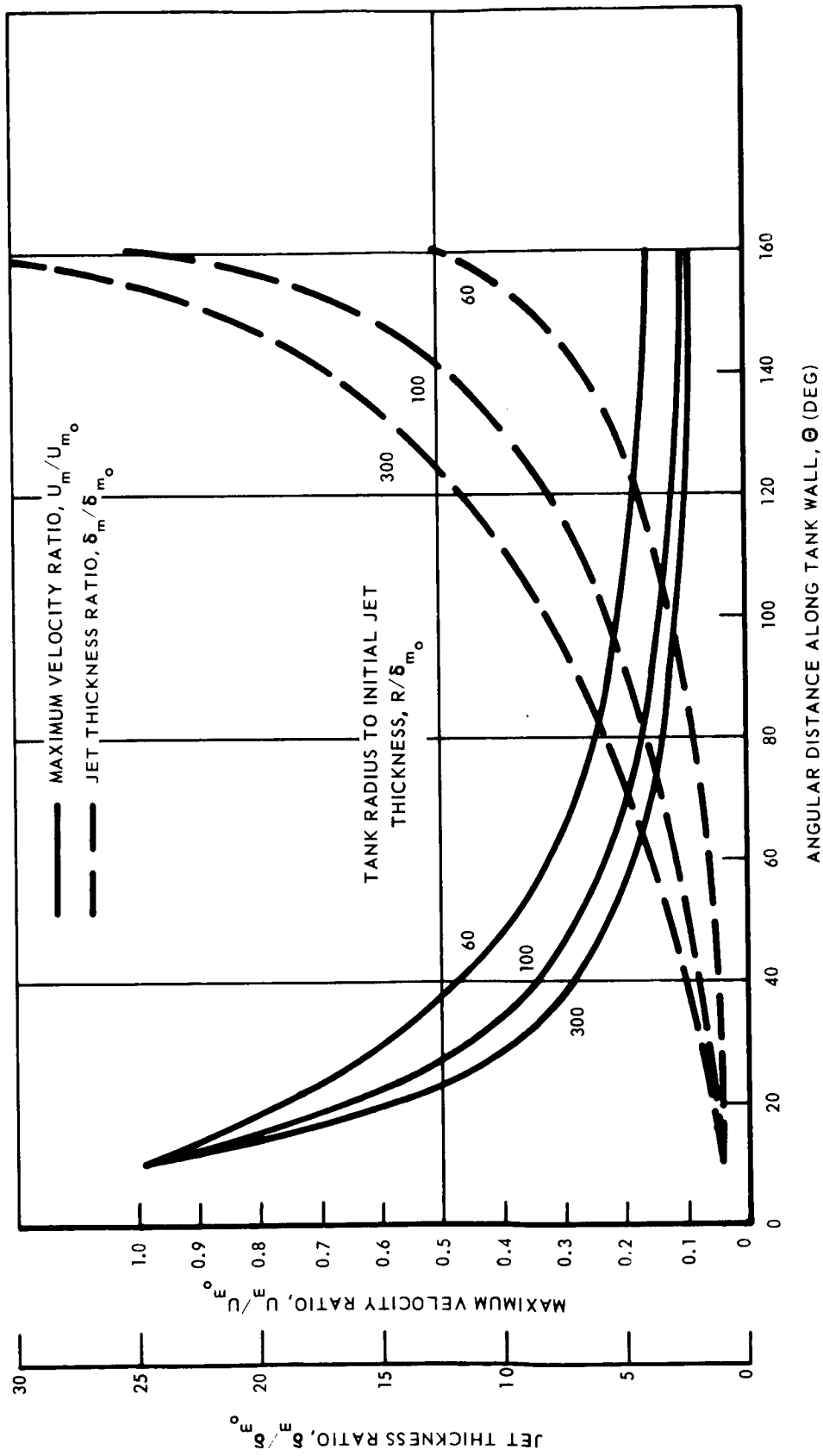

Fig. II-17 Single Wall-Bound Jet Degradation, Reynolds Number = 1,000

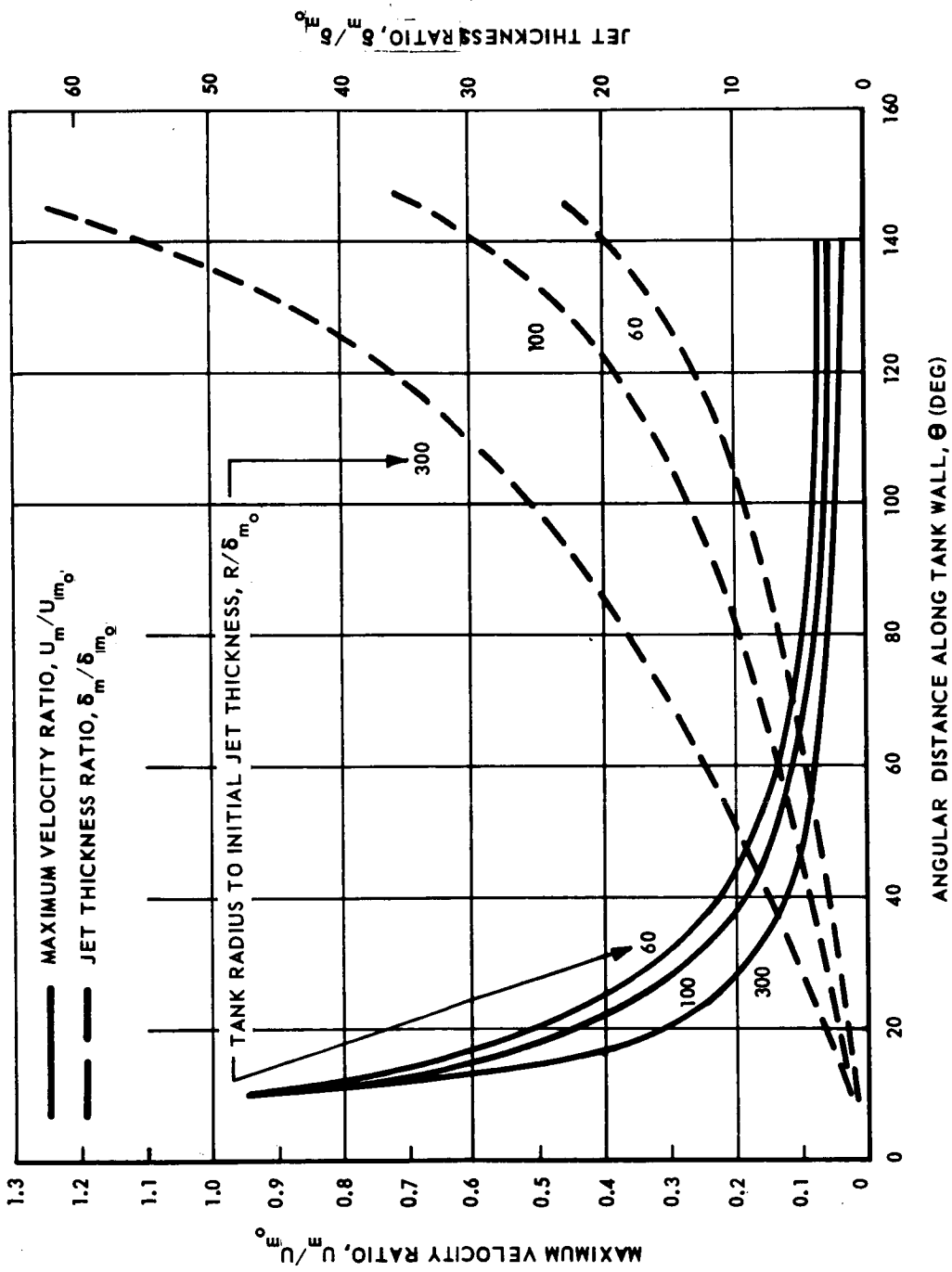

Fig. II-18 Single Wall-Bound Jet Degradation, Reynolds Number = 100

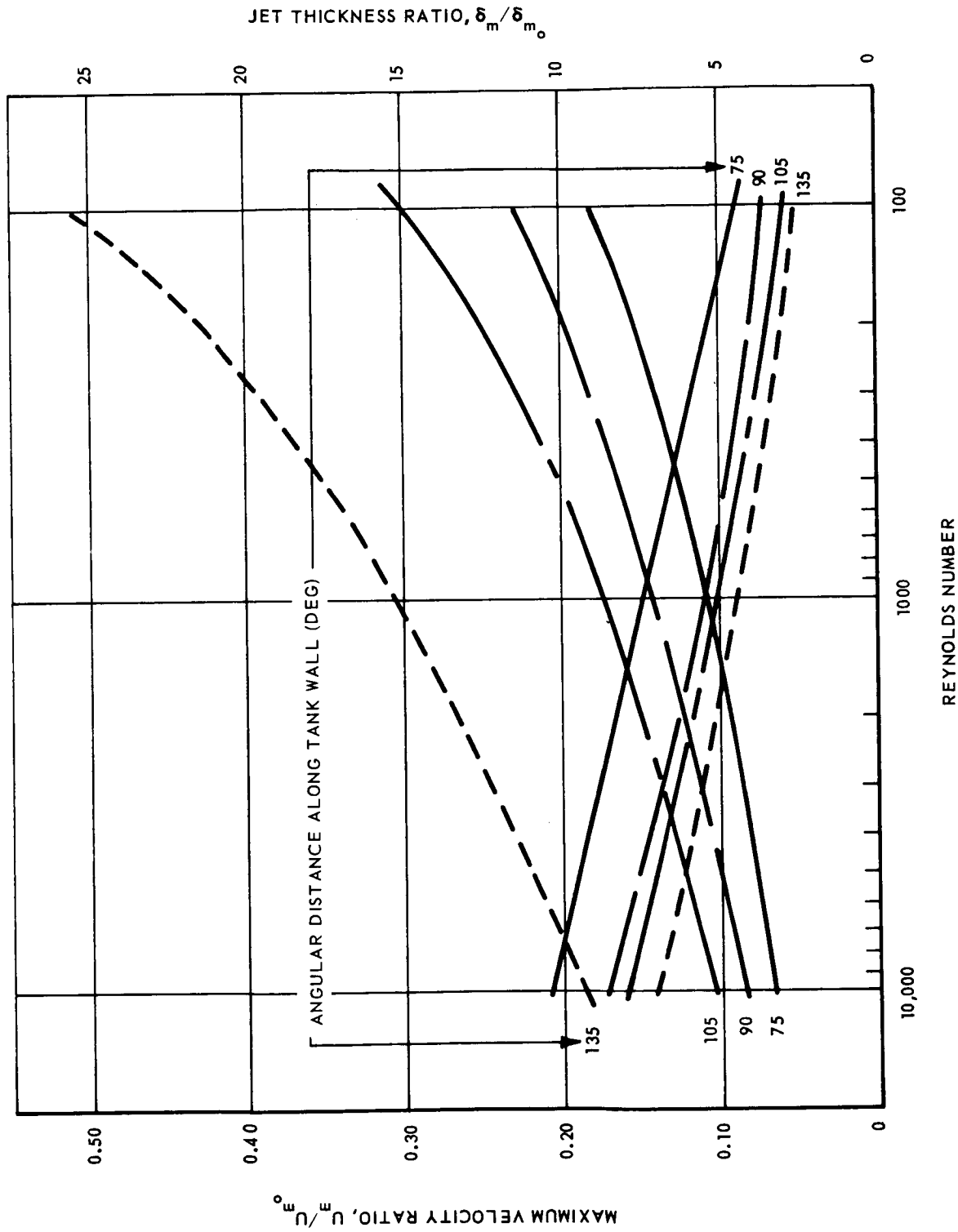

Fig. II-19 Effect of Jet Reynolds Number on Wall-Bound Jet Degradation (Radius Ratio, $R/\delta_{m_o} = 300$)

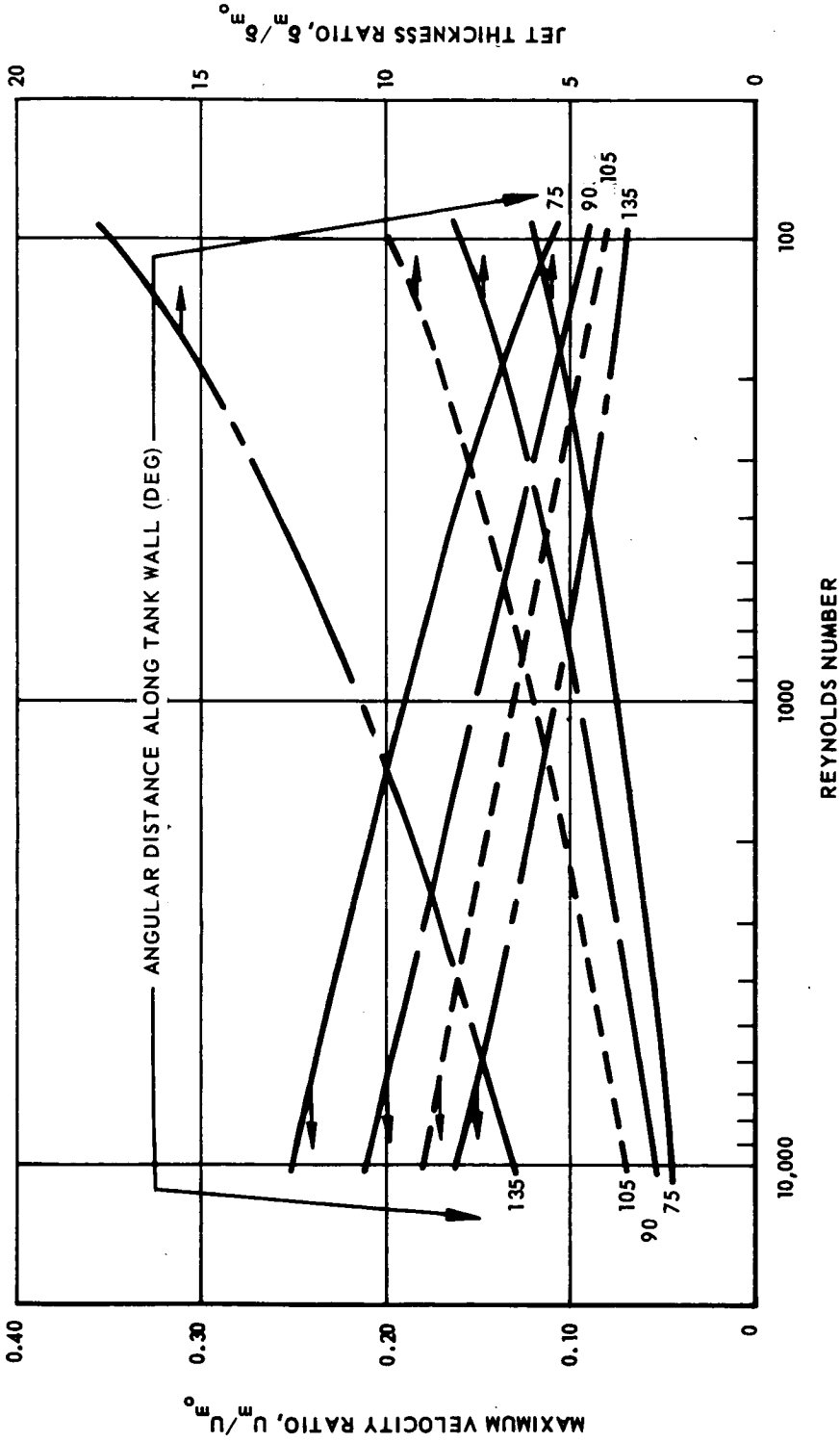

Fig. II-20 Effect of Jet Reynolds Number on Wall-Bound Jet Degradation (Radius Ratio, $R/\delta_{m_o} = 200$)

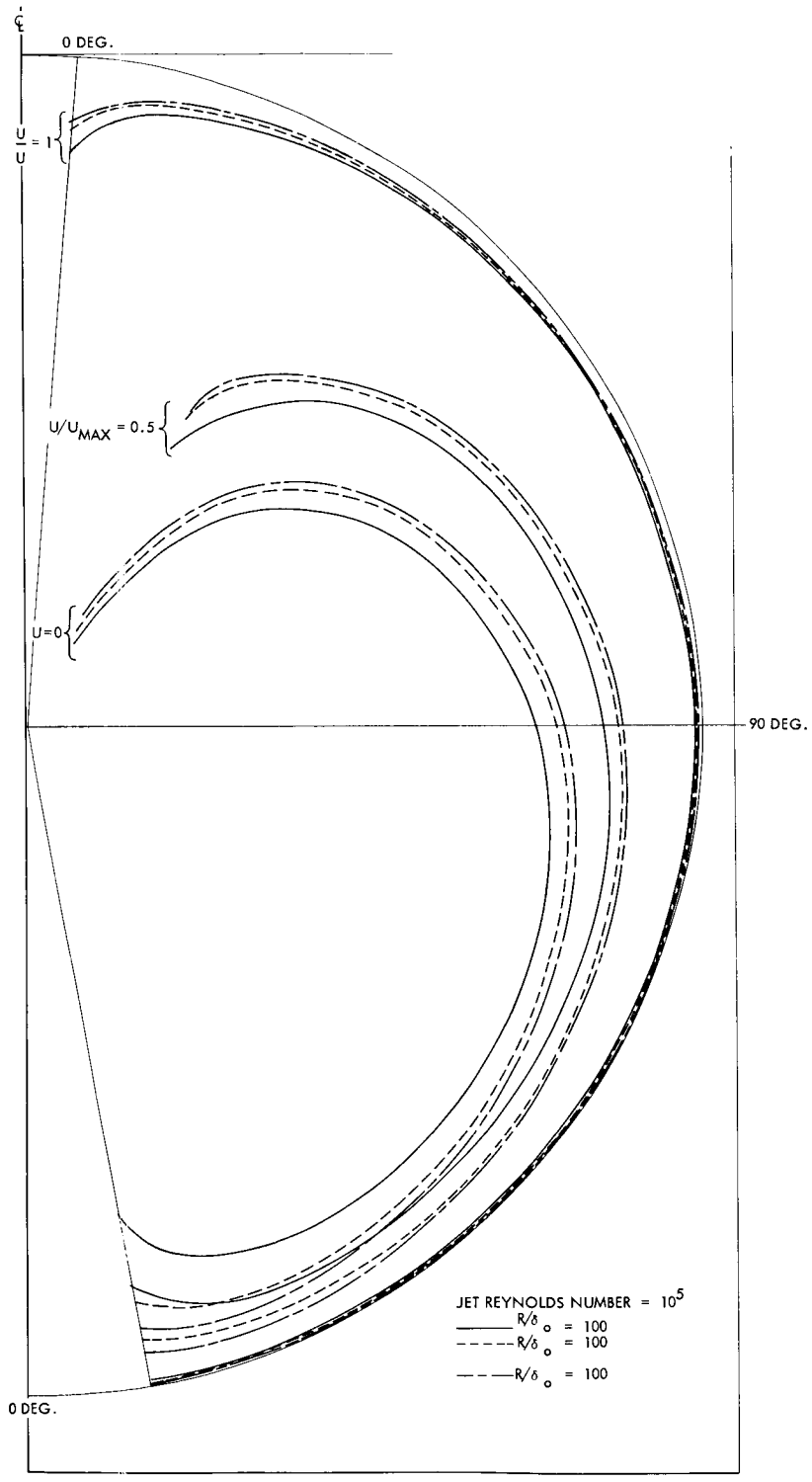

Fig. II-21 Wall Jet Velocity Loci in Sperhical LH_2 Tank

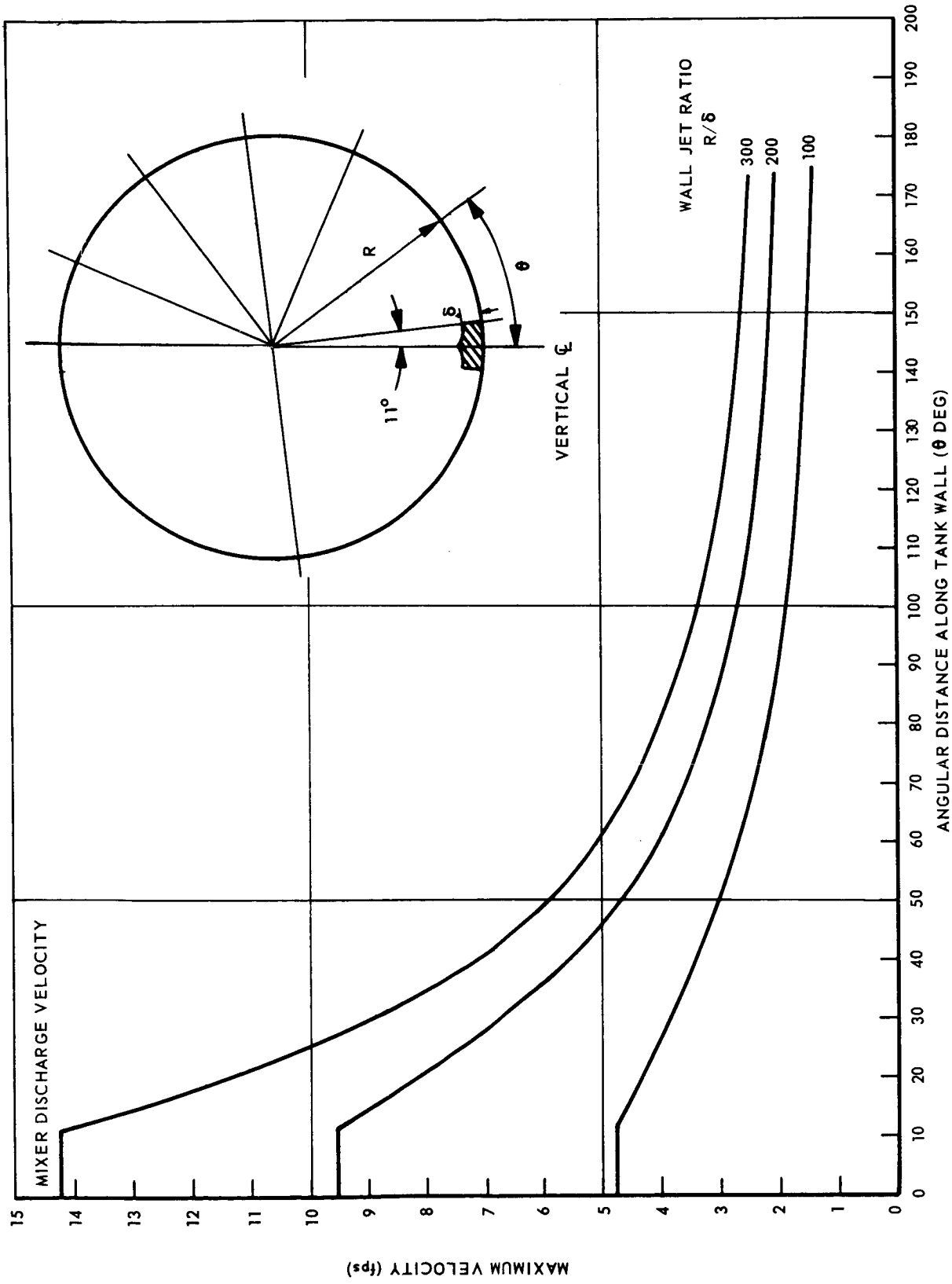

Fig. II-22 Magnitude of Velocities Along Loci of Maximum Velocity Profile in Spherical LH_2 Tank With a Wall Jet

profile, velocity decay, and spreading angle are adequately described by free jet theories and experiments, except near the opposite wall of the tank. On the opposite wall, jet separation and a stagnation region will develop which permit the jet to spread radially along the wall as a single wall-bound jet.

This stagnation region may, in fact, be a region of high heat flux where plumbing penetrations are located (see Fig. I-33). In a zero-gravity field, a large vapor bubble may be generated and attached to the tank wall at this location. Unless this bubble (if it exists) is removed from the wall, it may control tank pressure independently of the action of the thermal conditioning system. A mixing criterion, therefore, has been defined for an axial-jet mixer wherein the mixer jet velocity must be high enough to penetrate and sweep the vapor bubble from the tank wall opposite the mixer unit.

Consider the condition illustrated in the sketch below:

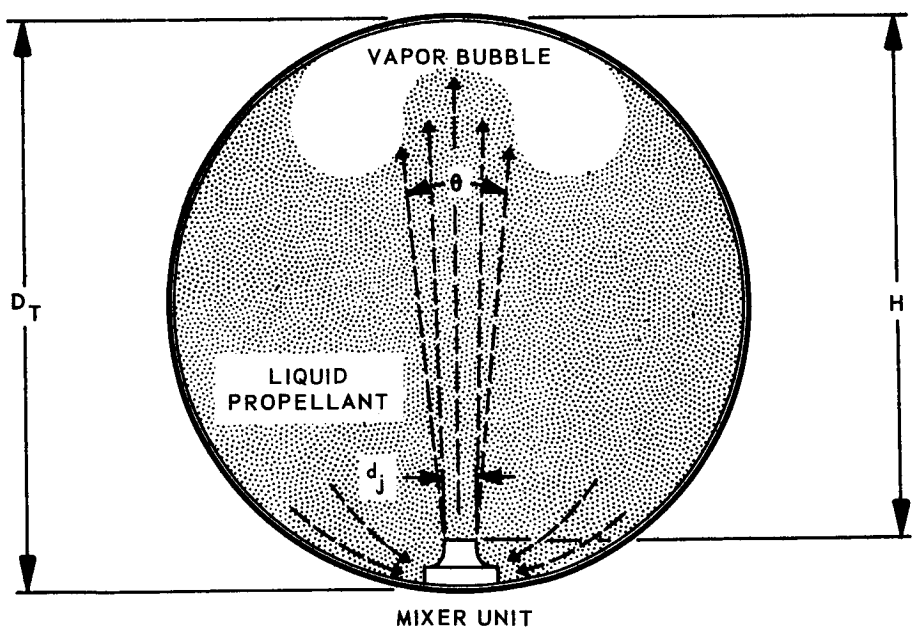

SCHEMATIC OF CENTRAL JET FLOW

In a zero-gravity field, only inertial and viscous forces act on the jet. If a vapor bubble is in the path of the jet, the surface of the bubble will be distorted by the jet dynamic forces being opposed by the bubble surface tension forces. If these dynamic forces are large enough, the jet will break through the bubble. If these dynamic forces are not large enough, the jet will be deflected by the bubble and will not reach the opposite wall.

A complete analysis of this phenomenon is developed in Appendix F. From this analysis, it has been shown that the critical local Weber number of the stream to break through the vapor bubble is given by:

$$W_{e_{cr}} = 4 \tag{8}$$

Utilizing the conservation of momentum relations in the jet, this local critical Weber number may be related to the required mixer jet Weber number.

$$W_{ej_{cr}} = \frac{\rho U_j^2 d_j}{\sigma} = 4 \left(1 + \frac{H}{d_j} \tan \theta\right) \tag{9}$$

As an example, applying Eq. (9) to the reference mission vehicles and assuming a 2-1/2 in. mixer jet diameter, the data shown on Fig. II-23 were calculated. It can be seen that for the Mission (2) vehicle, the mixer unit can throw the jet stream from one wall of the tank to the other if the jet mixer exit velocity exceeds 0.4 ft/sec. A jet velocity in excess of 1.2 ft/sec is required for the Mission (3) vehicles.

To establish the validity of this criterion, a two-dimensional apparatus (Fig. II-24) was fabricated for simulated zero-gravity experiments. The apparatus is constructed of two flat transparent plates, spaced 1/8-in. apart. This spacing is adequate for assuring that liquid flowing between the plates will remain attached to both surfaces. Thus when the plates are placed in a horizontal position, the fluid flowing between them is governed by only dynamic, viscous, and surface tension forces. The gravity forces are negligible, thereby simulating a zero-gravity environment.

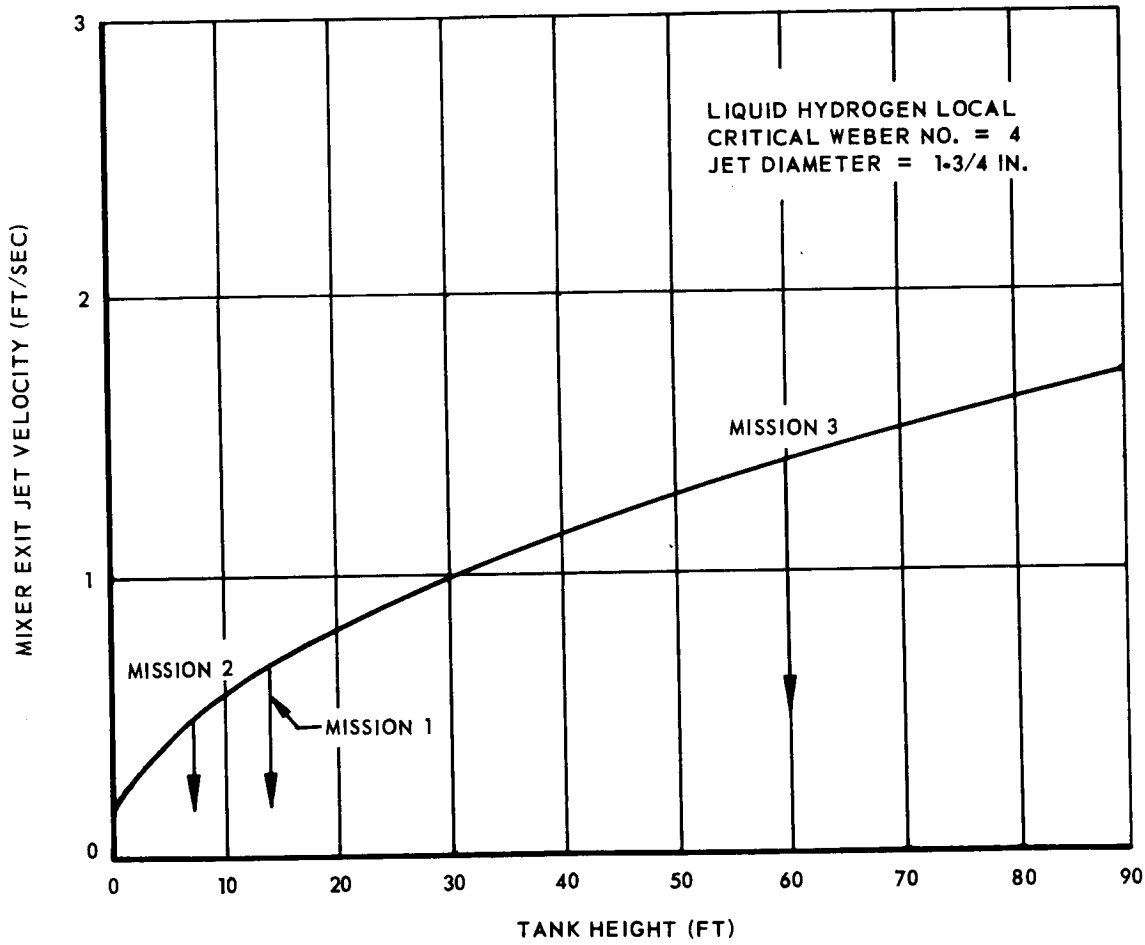

Fig. II-23 Theoretical Mixer Jet Velocity Requirements in Zero Gravity for Complete Circulation

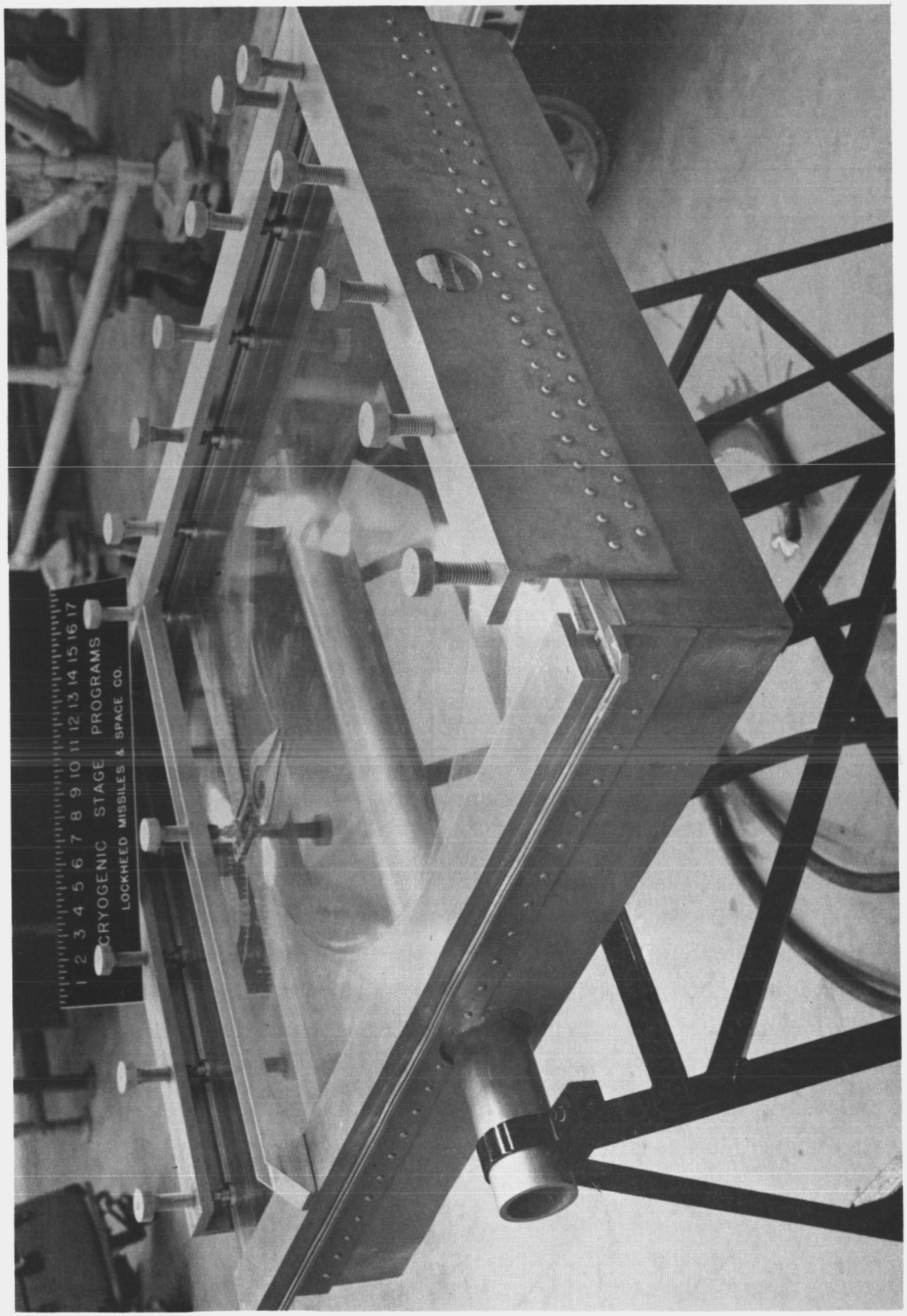

Fig. II-24 Two-Dimensional Flow Test Apparatus

Equation (9) for the three-dimensional jet cannot be used to describe the flow to be expected in the two-dimensional apparatus. However, the same basic principles are governing. As developed in the appendix of this report, the critical Weber number for complete penetration of a vapor bubble in the two-dimensional apparatus is given by:

$$W_{e_{cr}} = \frac{\rho U_x^2 t}{\sigma} = 2\left(1 + \frac{t}{d_x}\right) \tag{10}$$

Equation (8) is the three-dimensional counterpart.

Relating this critical Weber number to the conditions at the mixer jet discharge Eq. (10) becomes:

$$W_{ej_{cr}} = \frac{\rho U_j^2 t}{\sigma} = 2\left(1 + \frac{H}{d_j}\tan\theta\right)^2 \left[1 + \frac{t}{d_j}\left(\frac{1}{1 + \frac{H}{d_j}\tan\theta}\right)\right] \tag{11}$$

Here the Weber number has been arbitrarily based upon plate spacing t and could have been based upon the other jet dimension d_j.

Figure II-25 presents the critical jet Weber number calculated from Eq. (11). A spreading angle of 13 deg was used wherein the angle was determined from numerous photographs of the spreading jet. Experimental data obtained from experiments with the two-dimensional apparatus shown in Fig. II-24 are also plotted in Fig. II-25. Tests were performed with both water-air mixtures and with alcohol-air mixtures in 1-ft and 2-ft diameter tanks. The theory predicts the proper trend but the critical Weber number tends to be low by a factor of 2. It might be noted that the dashed line through the data is nearly coincident with the theory if a spreading angle of 20° is used in Eq. (11).

Table H-1, in the appendix presents a complete listing of all the experiments conducted with the apparatus. These include several tests with the central jet in a clean tank

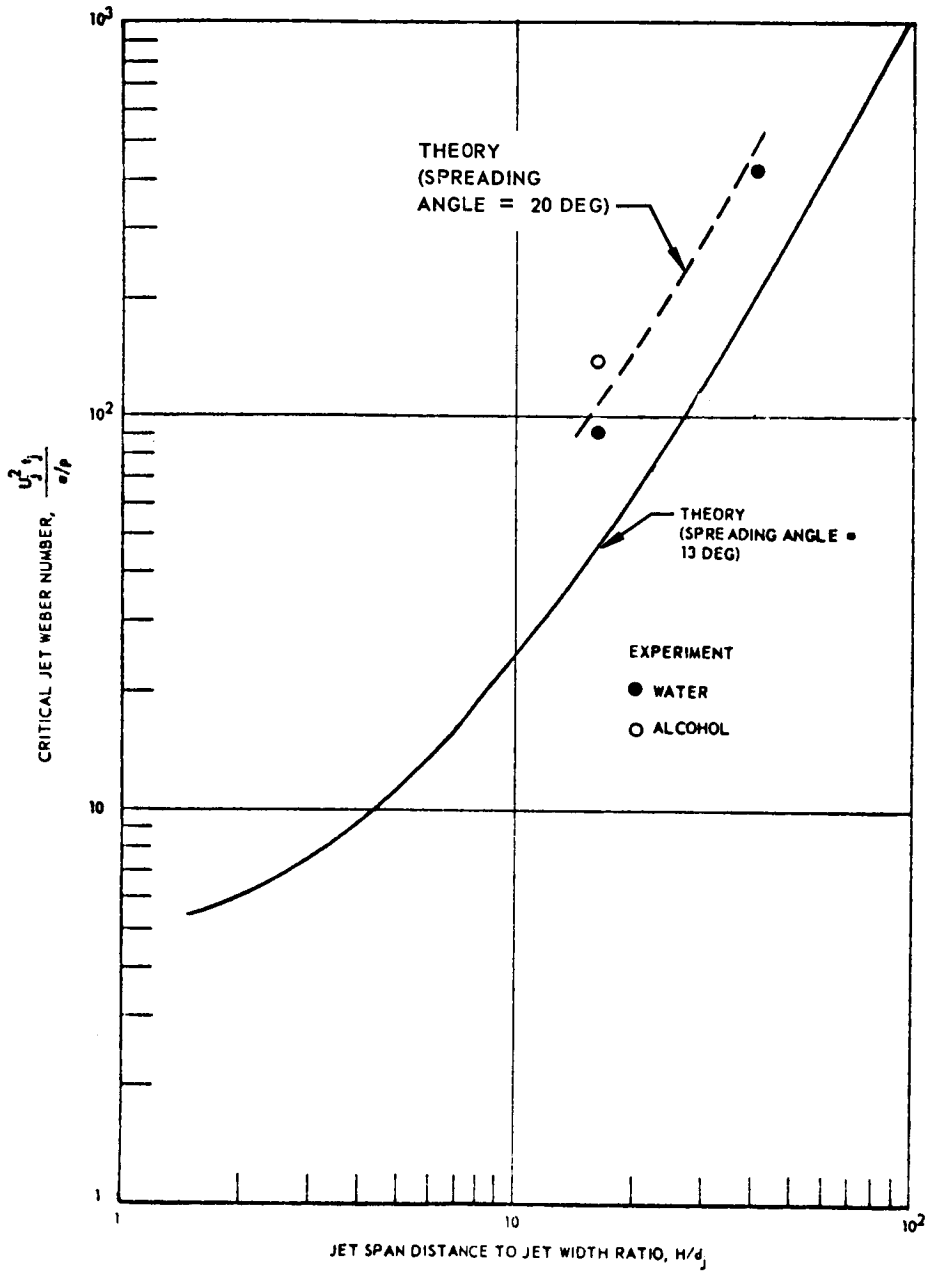

Fig. II-25 Comparison of Theory With Experimental Data for Mixing by an Axial Jet (Two-Dimensional Apparatus)

which provided the basis for comparison with the critical Weber number criteria, as discussed above. Figure II-26 shows some typical liquid-ullage patterns obtained with this configuration; the flow rates range from subcritical to well above that needed for complete circulation.

Tests were also conducted to determine the effect of baffles on central jet mixing patterns. The three slosh baffles for the Mission (2) vehicle were scaled down linearly and simulated in the two-dimensional apparatus. This simulation included two configurations – the baffles installed against the tank wall, and installed with a gap between the baffles and wall. In the latter case, the gap was scaled linearly based upon 1 inch being allowed in the vehicle. When the baffles were attached directly to the wall, it was not possible to break up or dislodge a large gas bubble trapped between baffles. However, with the gap, the circulating fluid could flow behind the baffles if the flow rate was high enough. It was found that a flow rate approximately 30 percent higher than the clean tank "critical" value for the submerged axial jet was sufficient to break through a vapor bubble behind the farthest baffle.

A wall bound jet in the two-dimensional tank was also investigated. A simulated pipe was installed to represent the case of mixer intake and discharge occurring on opposite ends of the tank as shown in Fig. II-27. This series of tests included the baffles with scaled displacement from the tank wall. Again it was found that progressively higher jet velocities were needed to break through vapor bubbles located in the gaps behind successive baffles. This is shown in Fig. II-28. However, the jet would break through behind all three baffles when the flow rate was approximately equal to the critical value for the submerged central jet. Also shown in Fig. II-28 is a critical velocity for the same apparatus but with the baffles removed. The velocity was just sufficient to completely sweep the bubbles off the tank wall. This velocity is slightly higher than that required to break through behind all three baffles which tends to indicate that the wall bound jet remains sufficiently thin to move through the gap between baffle and tank wall without a noticeable loss in momentum. Figure II-29 shows typical liquid-ullage patterns for a range of jet velocities with this jet configuration. During tests a bar was placed over the flat plates of the test apparatus (Fig. II-29) to prevent a separation of the plates under internal fluid pressure. This bar obscures observation of the flow duct as shown in Fig. II-27.

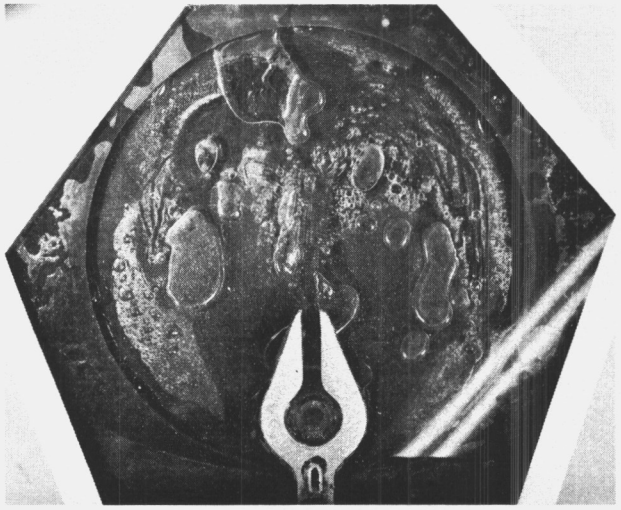

Below Critical Circulation

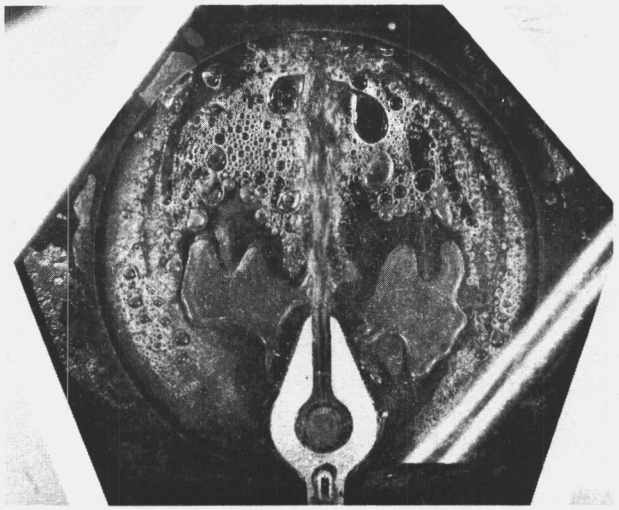

Critical Circulation

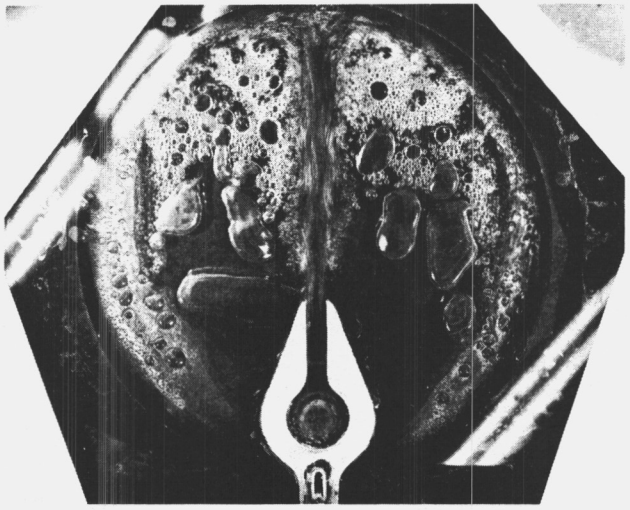

Above Critical Circulation

Fig. II-26 Typical Liquid-Ullage Patterns With an Axial Jet

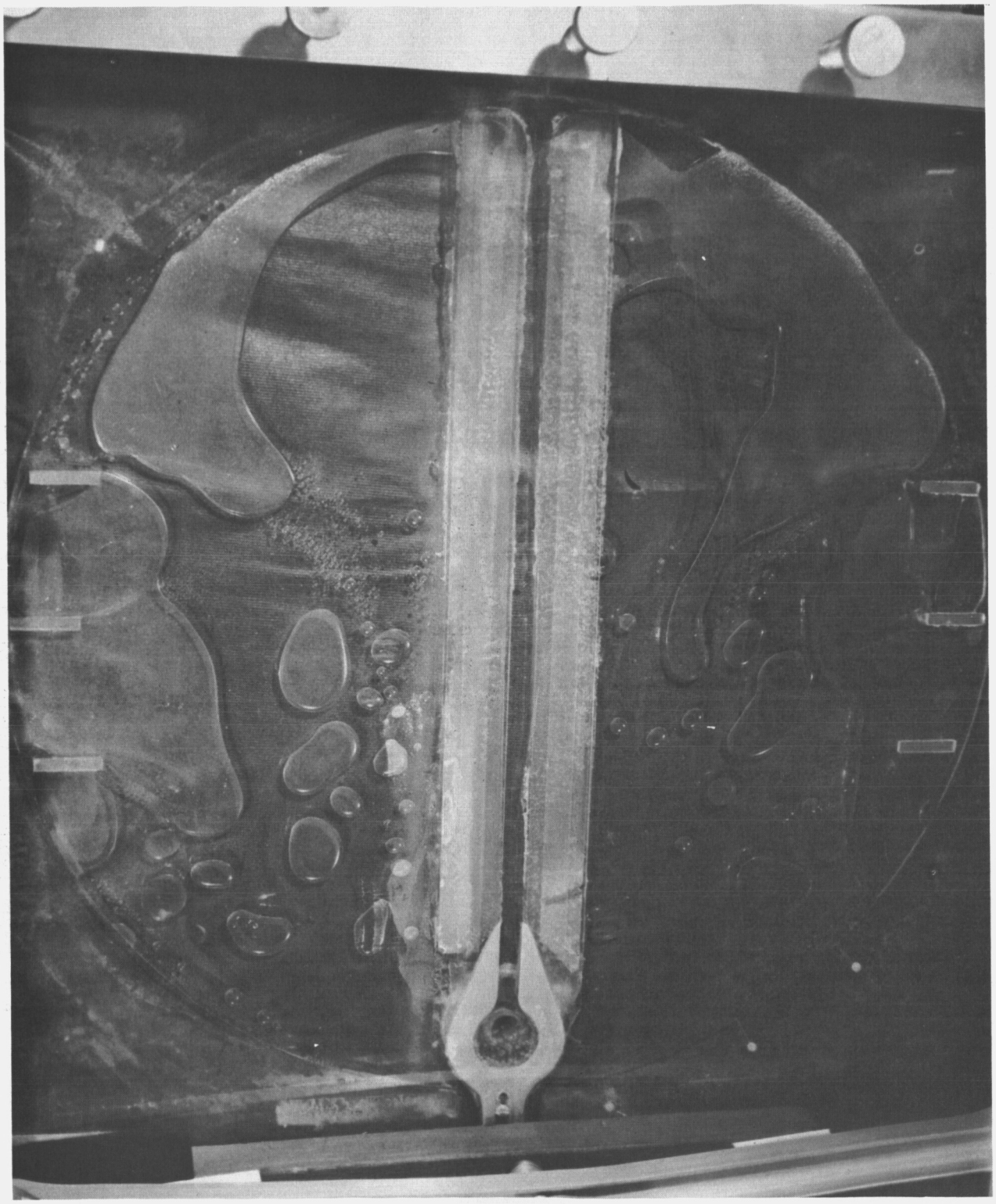

Fig. II-27 Two-Dimensional Flow Test Apparatus With A Single-Wall Bound Jet

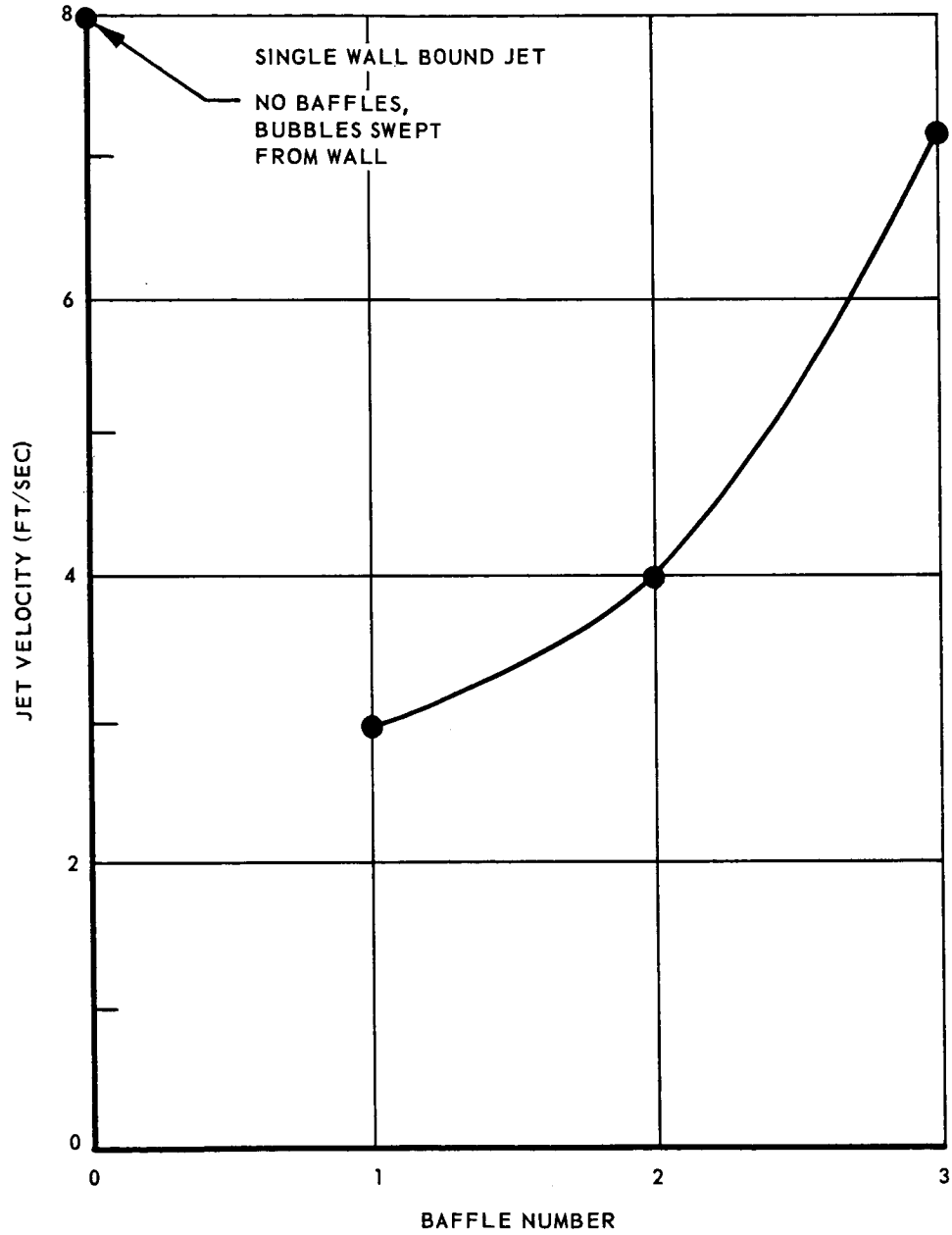

Fig. II-28 Jet Velocities Required to Break Through a Gas Bubble Located Behind a Given Baffle in the Two-Dimensional Test Apparatus

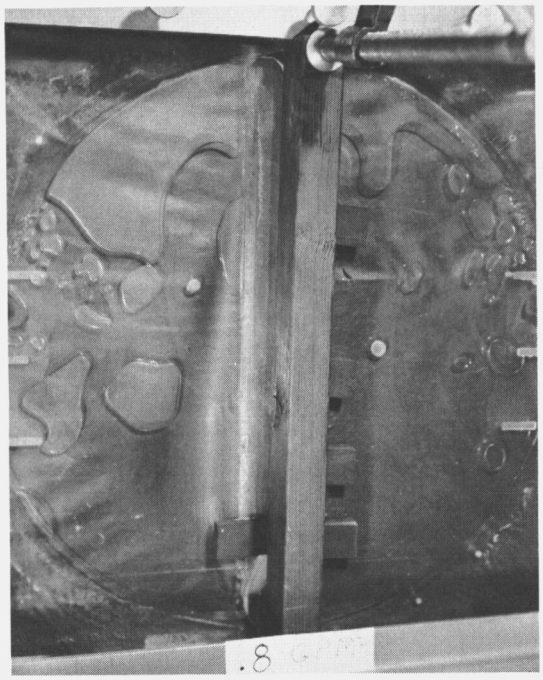

JET VELOCITY = 1.7 FT/SEC

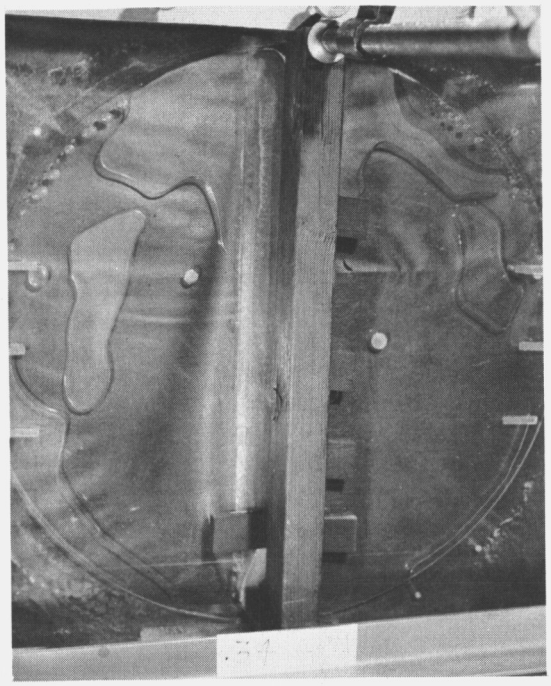

JET VELOCITY = 4.1 FT/SEC

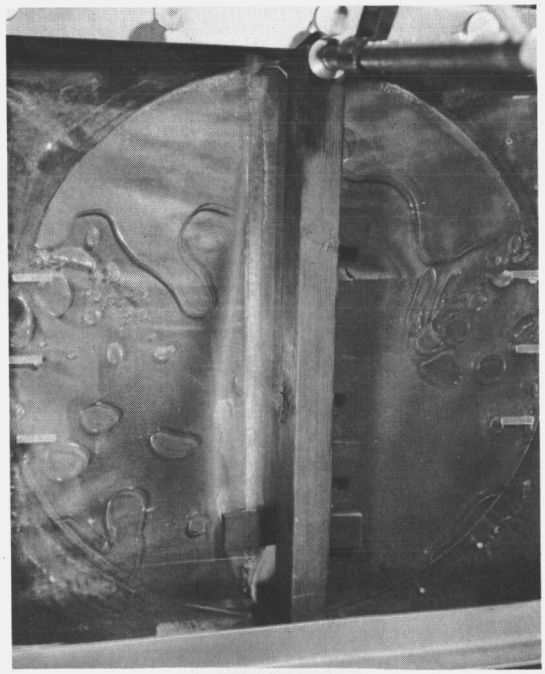

JET VELOCITY = 7.1 FT/SEC

Fig. II-29 Typical Liquid-Ullage Patterns With a Single Wall-Bound Jet

In summary, the experimental program has provided both qualitative and quantitative data need for specification of liquid propellant tank mixing requirements. The program has verified the theory for the central jet and has also shown that the inclusion of slosh baffles will not impose unreasonable penalties on the mixer power requirements. It can be concluded that if these requirements are established with the assumption that condensation occurs only at one face of the bubble, the requirements will be conservative because some liquid was observed to flow between the baffle and the tank wall.

SYMBOLS AND ABBREVIATIONS

h_m – Condensation Coefficient, Btu/hr-ft^2-°R

K_ℓ – Thermal Conductivity of Liquid Propellant, Btu/hr-ft-^{o}R

ρ_ℓ – Density of Liquid Propellant, lb/ft^3

g – Gravitational Acceleration, ft/sec^2

λ – Latent Heat of Vaporization of the Liquid Propellant, Btu/lb

μ_ℓ – Viscosity of the Liquid Propellant, lb/ft-sec

L – Distance Between Baffles, ft

ΔT – Temperature Superheat of the Vapor, ^{o}R

Γ – Mass Flow Parameter, lb/ft-sec

U_o – Liquid Velocity at the Liquid-Vapor Innerface, ft/sec

$\frac{dp}{d\theta}$ – Rate of Tank Pressure Change, psi/sec

γ – Ratio of Specific Heats for Propellant Gas

A – Innerface Area Between Liquid and Vapor, ft^2

V_g – Ullage Volume, ft^3

ω – Mass Flow Rate, lb/hr

b – Tank Circumference, ft

Q – Heating Rate, Btu/hr

V_T – Tank Volume, ft^3

C_P – Specific Heat of Ullage Gas, Btu/lb

U_m – Maximum Velocity in the Jet at Angle θ, ft/sec

U_{m_o} – Maximum Initial Velocity in the Jet, ft/sec

We_{cr} – Critical Weber Number at Liquid Vapor Innerface

Wej_{cr} – Critical Weber Number at Jet Nozzle

t – Plate Spacing, ft

d_j – Jet Diameter, ft

H – Tank Height Above the Jet Nozzle

U – Jet Velocity, ft/sec

U_j – Jet Velocity at Nozzle Exit, ft/sec

σ – Surface Tension, lb/ft

Section III

SYSTEM DESIGN METHOD

Having established the parametric requirements for the components of basic liquid propellant thermal conditioning system concepts as well as propellant tank mixing requirements, a general method for matching components and optimizing systems for each of the three reference missions is required.

The general design method for evaluation and optimization of the liquid propellant thermal conditioning system is described in this section of the report. The approach is quite general. The final curves relate the system weight penalty to liquid hydrogen withdrawal rate, tank pressure, and pressure ratio across the expansion valve. The system weight penalty includes the fixed weight of the system, the hydrogen weight loss associated with the work (heat) input from the mixer unit to the bulk fluid, and the electrical power penalty if any.

The data evaluated in the parametric analysis section are used in the system design method and, when applicable, this data is repeated in this section to illustrate its use. Some of the components, such as expansion valves, tank-wall heat exchangers, passive liquid removal units, etc., were previously eliminated as not being suitable for use in a liquid propellant thermal conditioning unit. However, two classes of systems remain that are applicable to a wide range of missions and vehicles. Systems design methods are presented for both classes.

AXIAL-IMPULSE, TURBINE DRIVEN, COMPACT HEAT EXCHANGER SYSTEM

The design method is applied first to a compact heat exchanger system with a turbine as the drive unit for the mixer. A fan is used to force the tank fluid through the heat exchanger and to mix the tank contents. The components considered are as follows:

a. Fluid removal unit
b. Expansion valve

c. Compact heat exchanger

d. Fan

e. Turbine drive

The turbine will be used to drive the heat exchanger fan and the dynamic separator, where applicable. The object of the general design method is the development of a parametric system weight curve for various tank pressures (Fig. III-1). The actual data to be used in the design method are shown in Figs. III-2 through III-13.

It should be noted that the design method can be used for tank pressures to 150 psia and for hydrogen withdrawal rates to 60 lb/hr. As an exception, however, when a dynamic separator is considered, the method is limited to low tank pressures. As noted earlier at high tank pressures, extremely high power requirements make this device impractical as a liquid removal unit. Data for a dynamic separator are presented for a tank pressure of 17 psia. For Missions (1), (2), and (3), the tank pressure during coast periods is 17 psia. Figures III-5 and III-12 have been included in the report to show more detail on turbine power output and weight at the lower pressures associated with these missions.

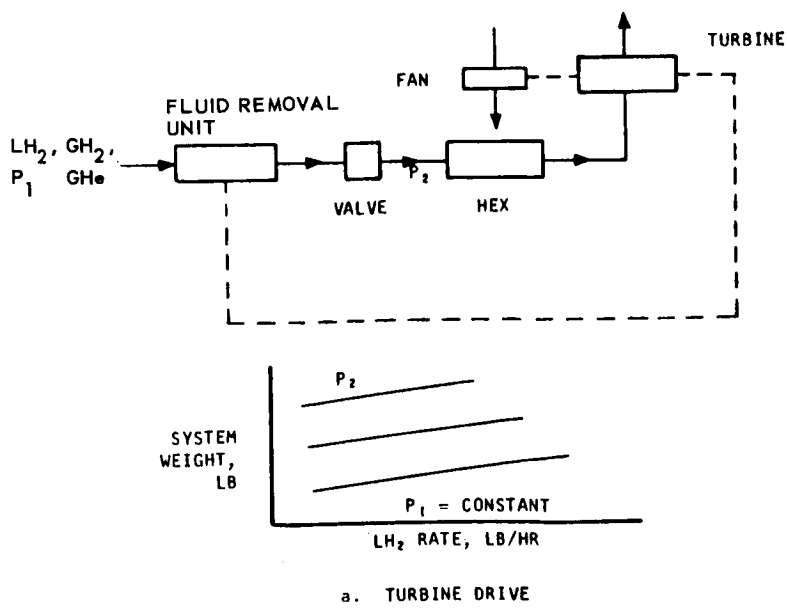

Fig. III-1 Typical System Weight Curve, Turbine Drive System

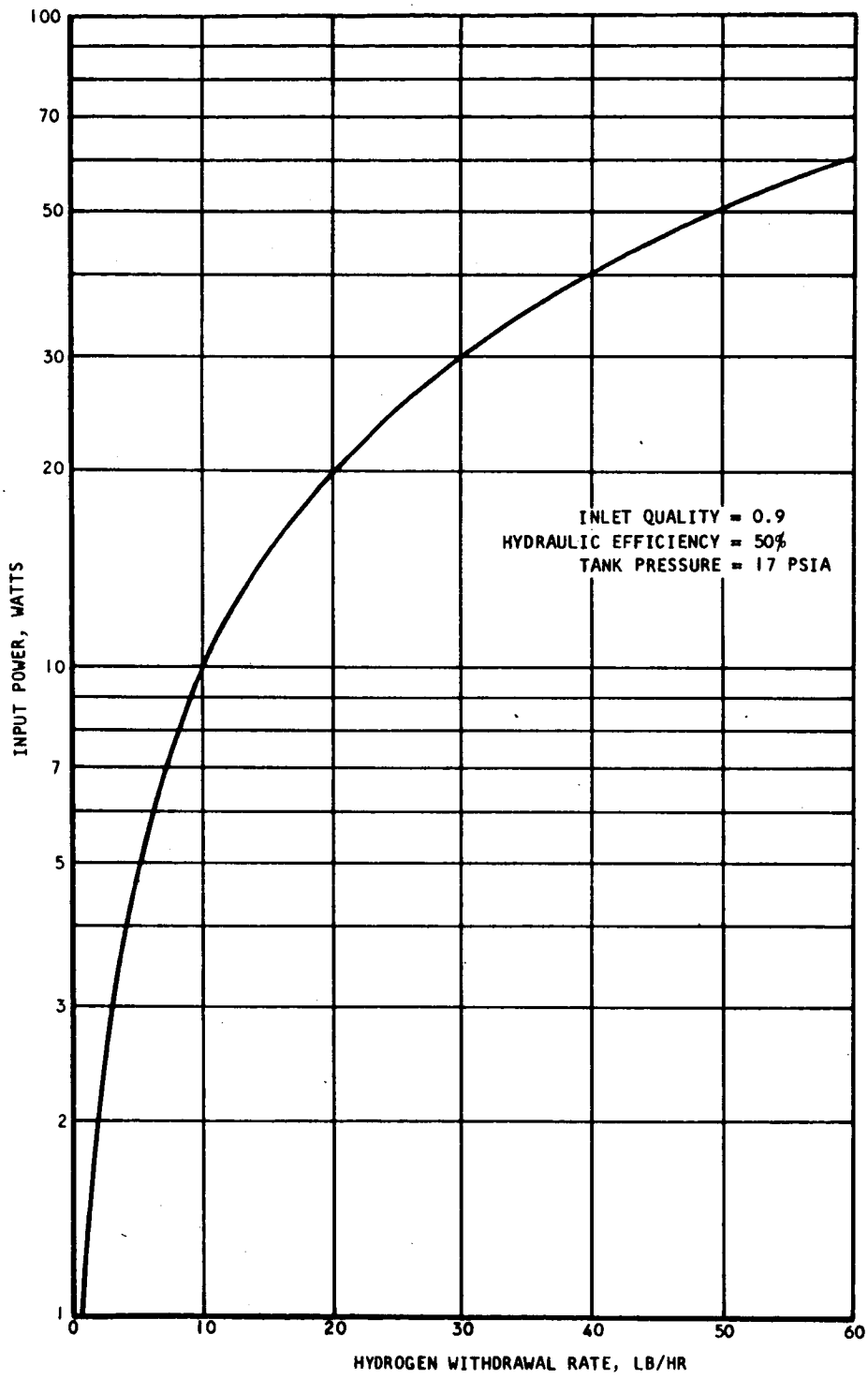

Fig. III-2 Dynamic Separator Power Requirement

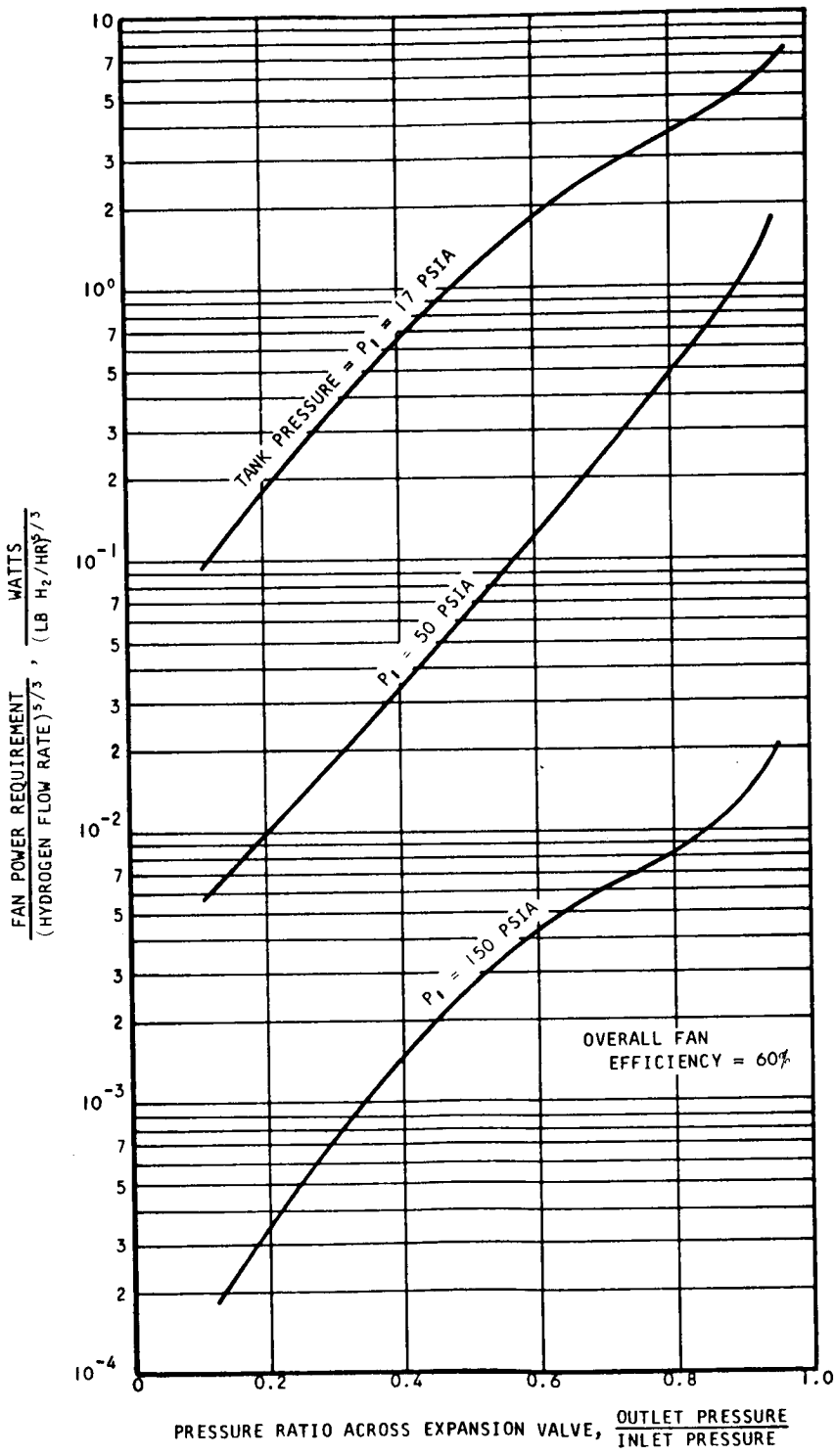

Fig. III-3 Fan Power Requirement

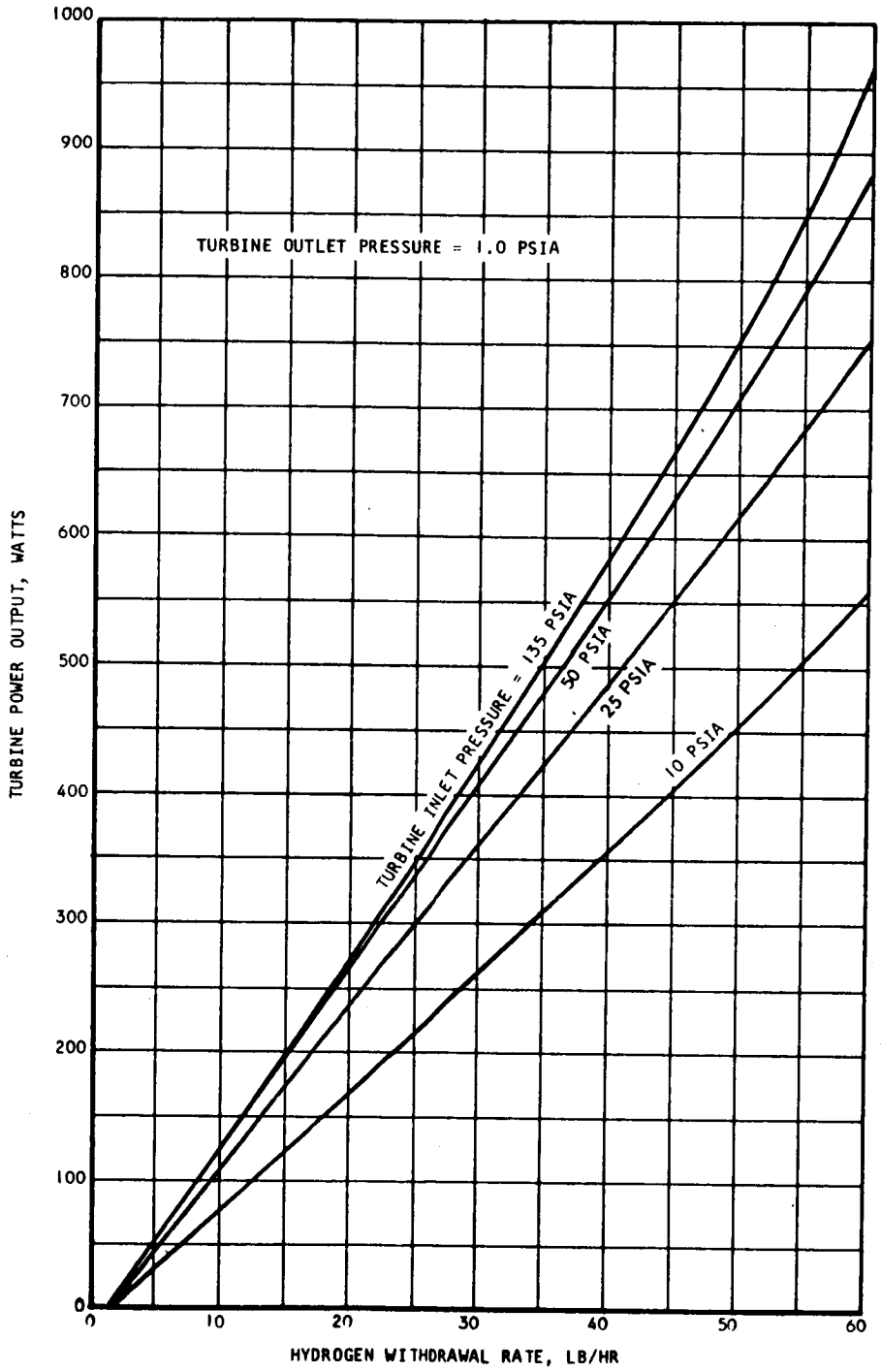

Fig. III-4 Axial-Impulse Turbine Output Power

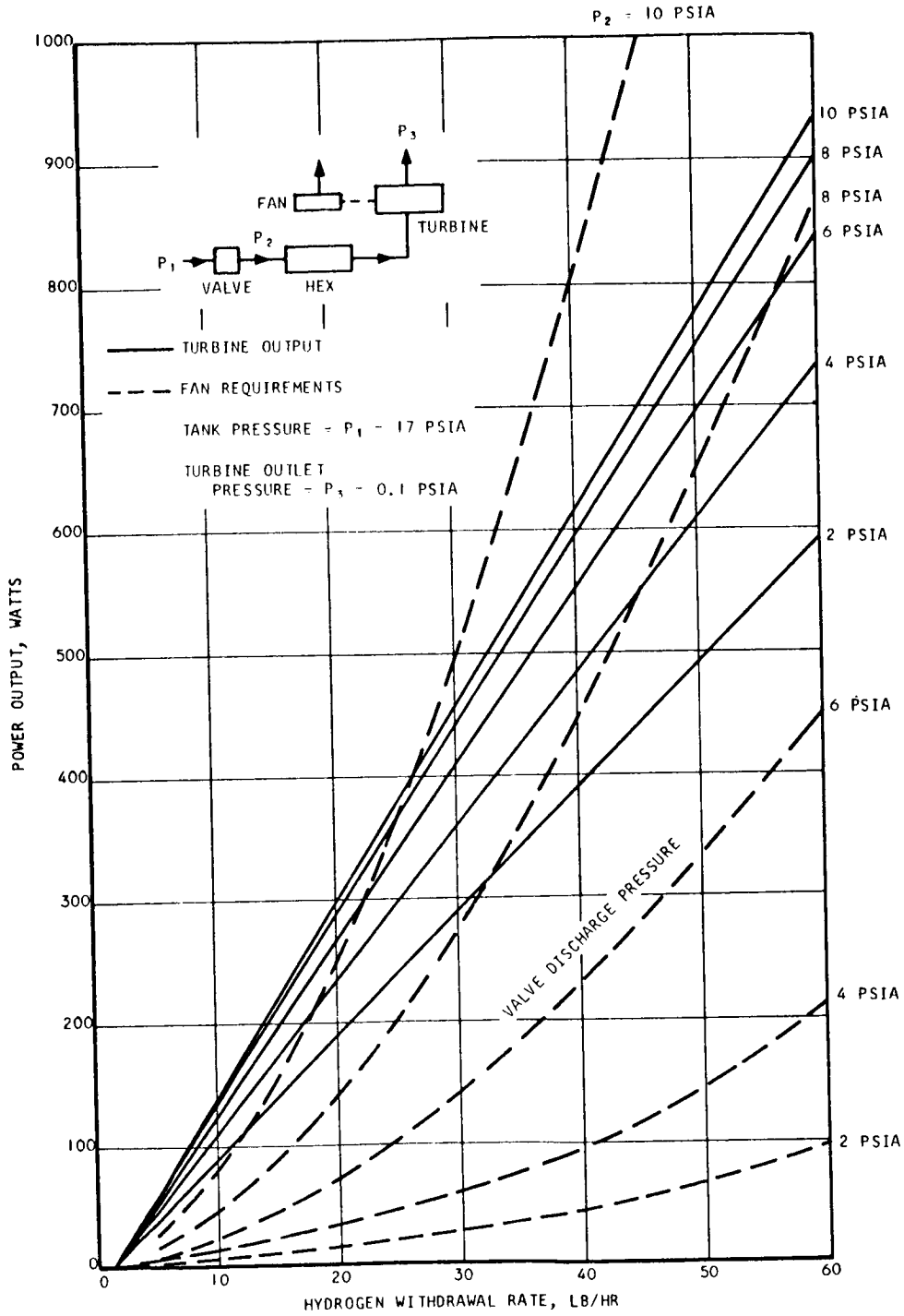

Fig. III-5 Typical Turbine Output and Fan Input Power Matching Characteristic

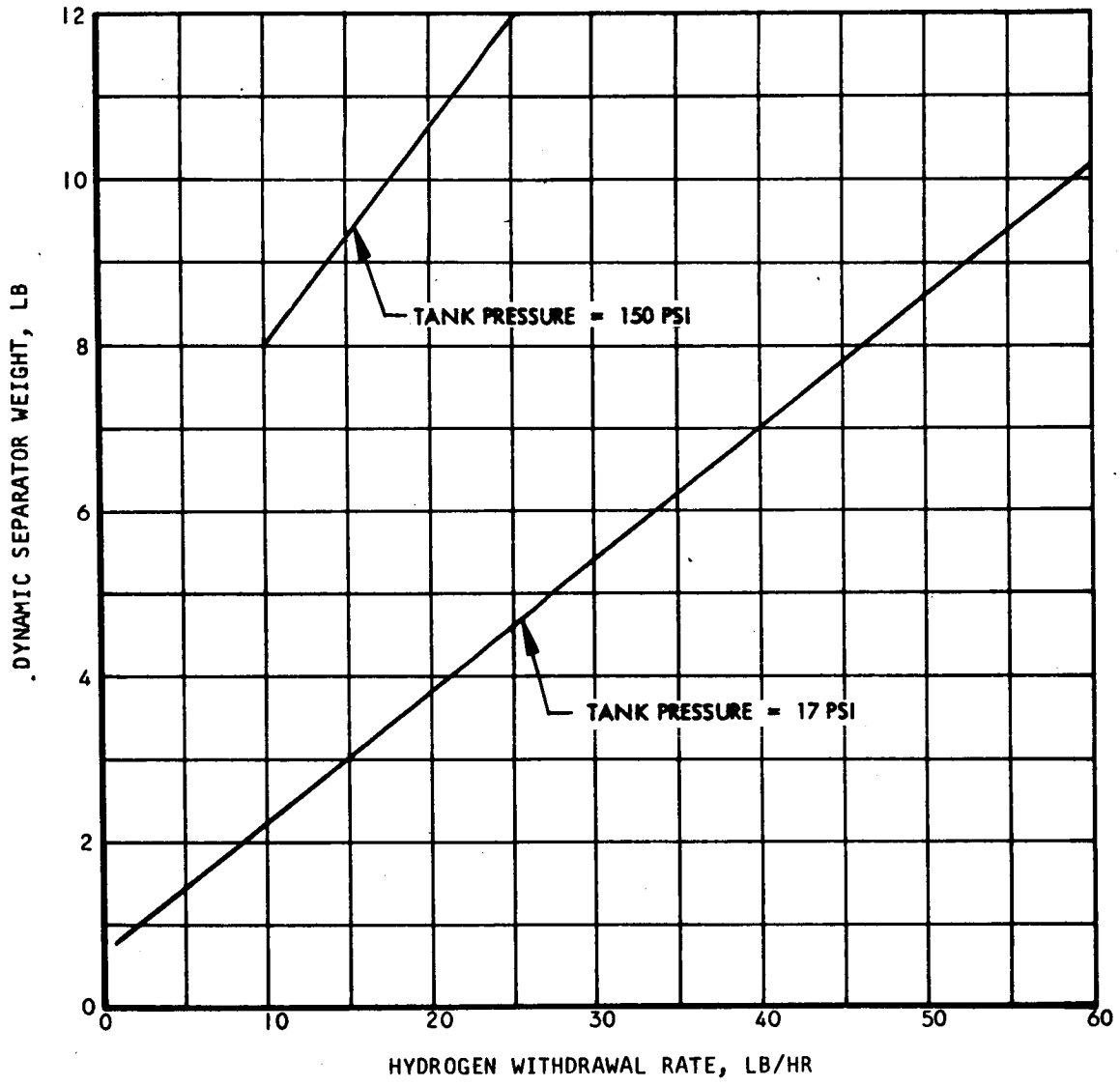

Fig. III-6 Dynamic Separator Weight (Inlet Quality = 0.9)

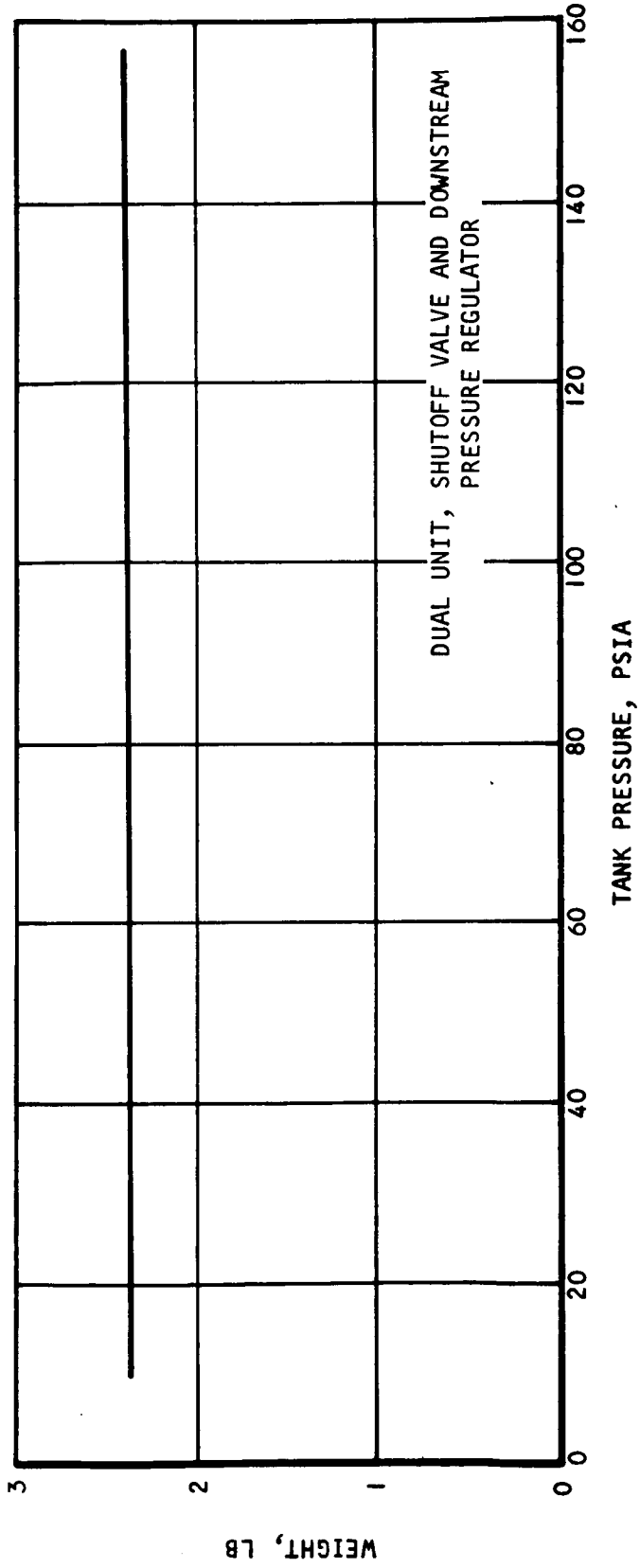

Fig. III-7 Expansion Valve Weight

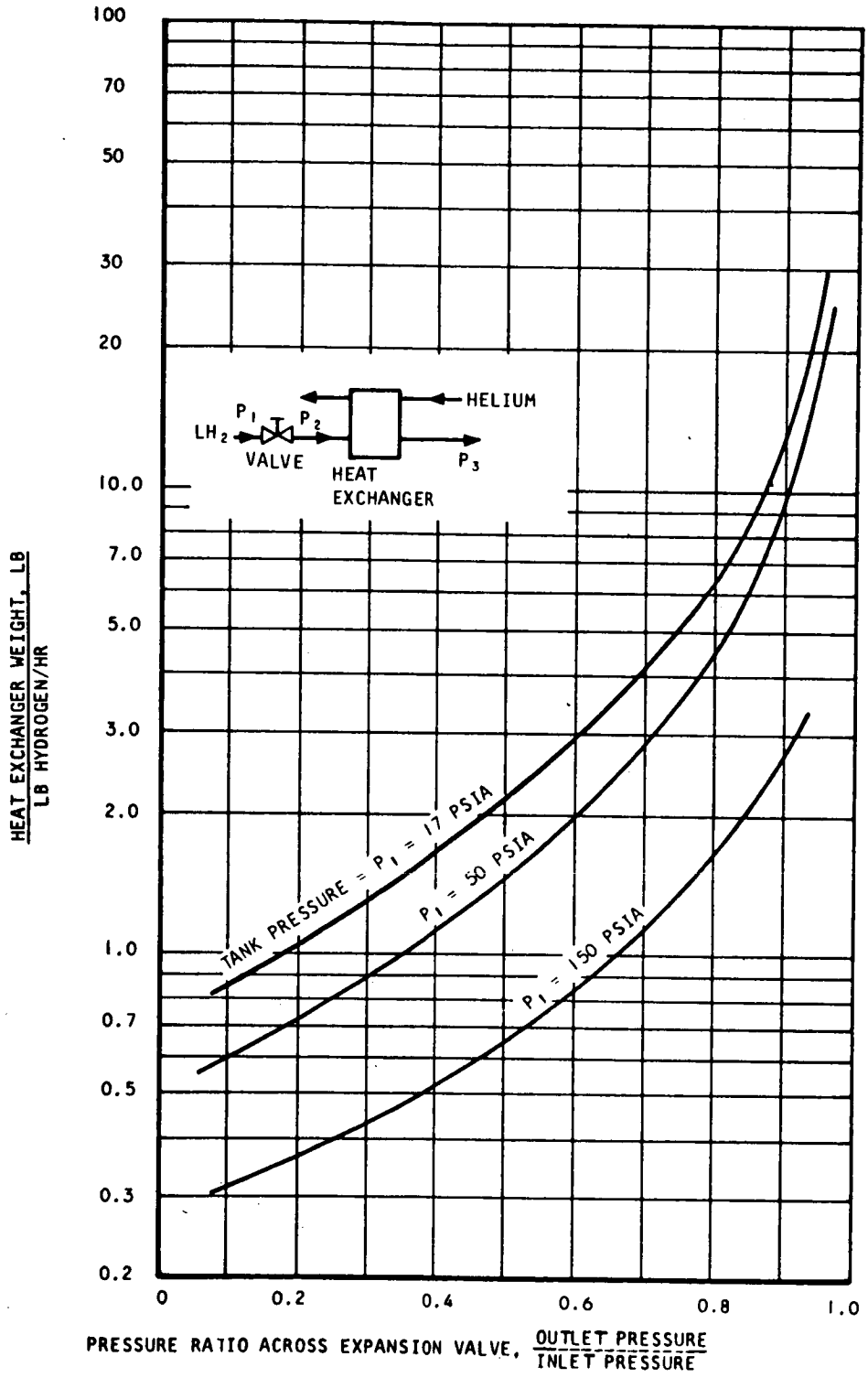

Fig. III-8 Heat Exchanger Weight

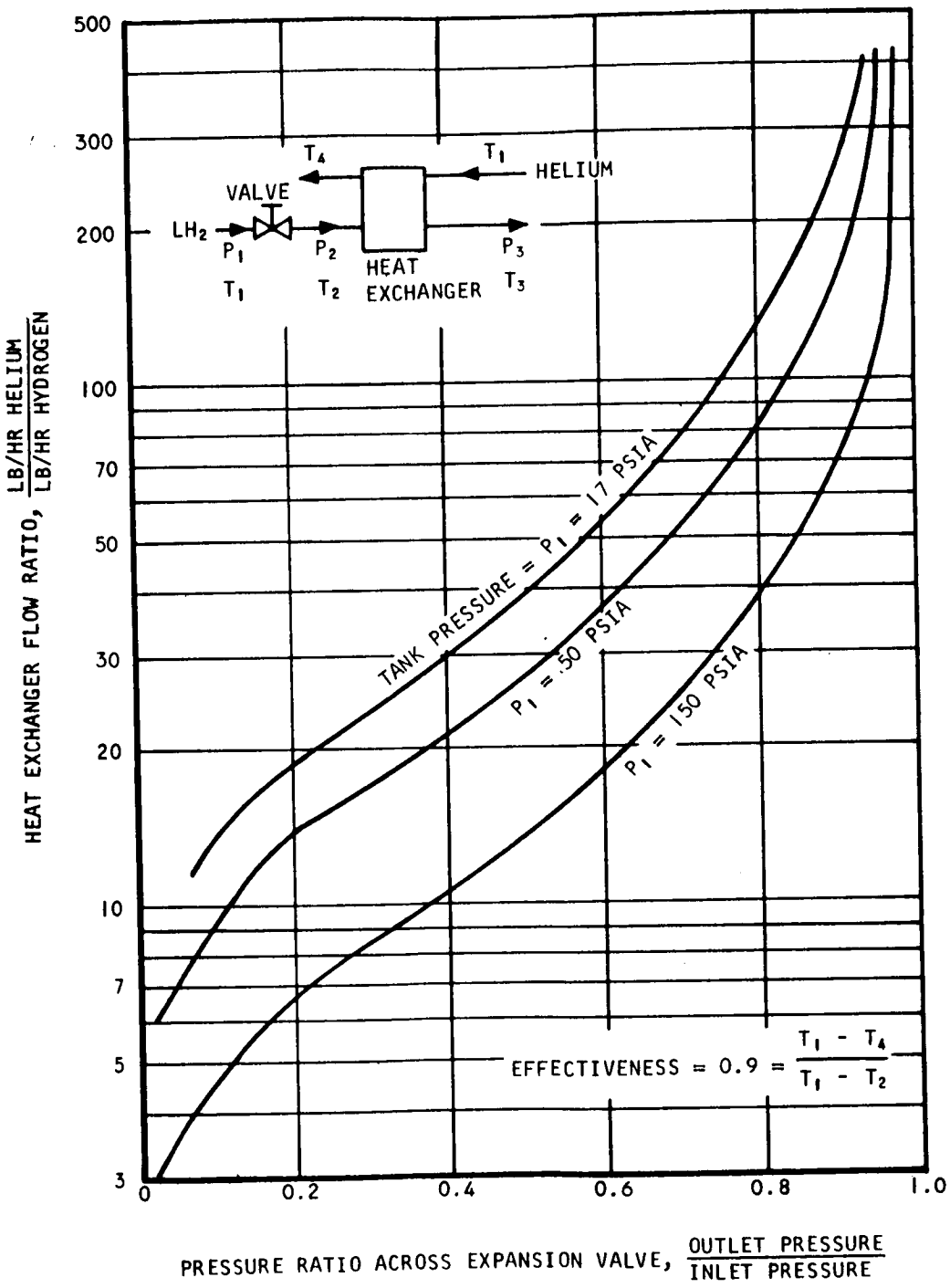

Fig. III-9 Heat Exchanger Flow Ratio

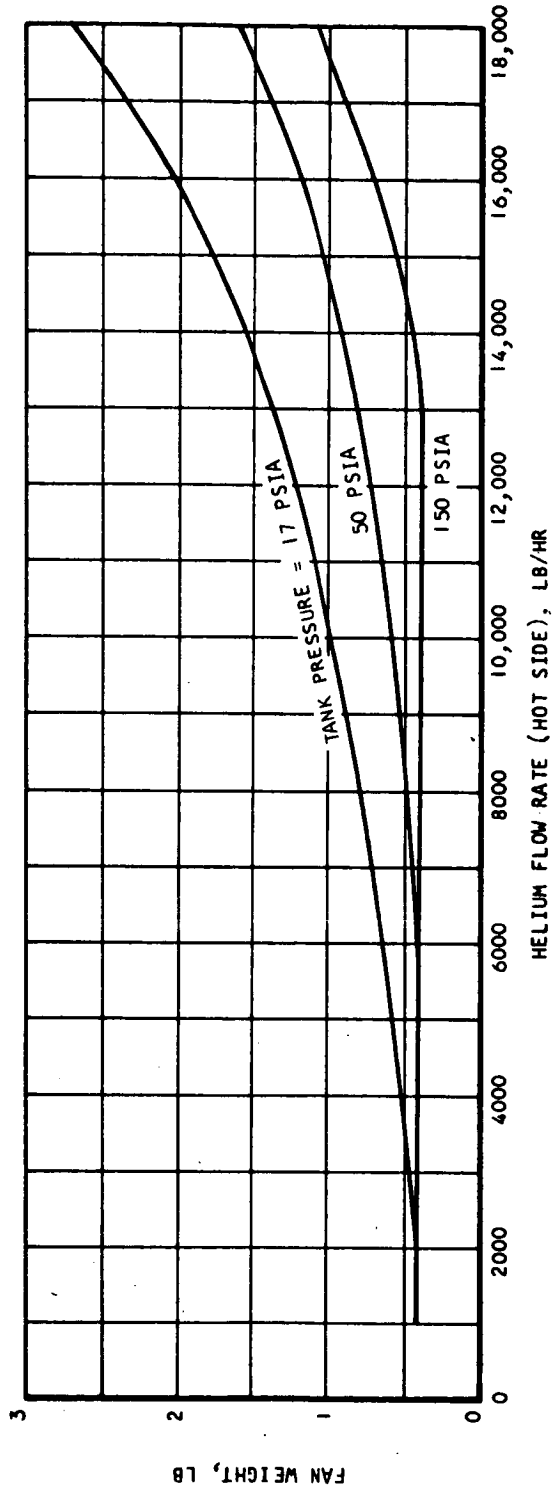

Fig. III-10 Heat Exchanger Fan Weight

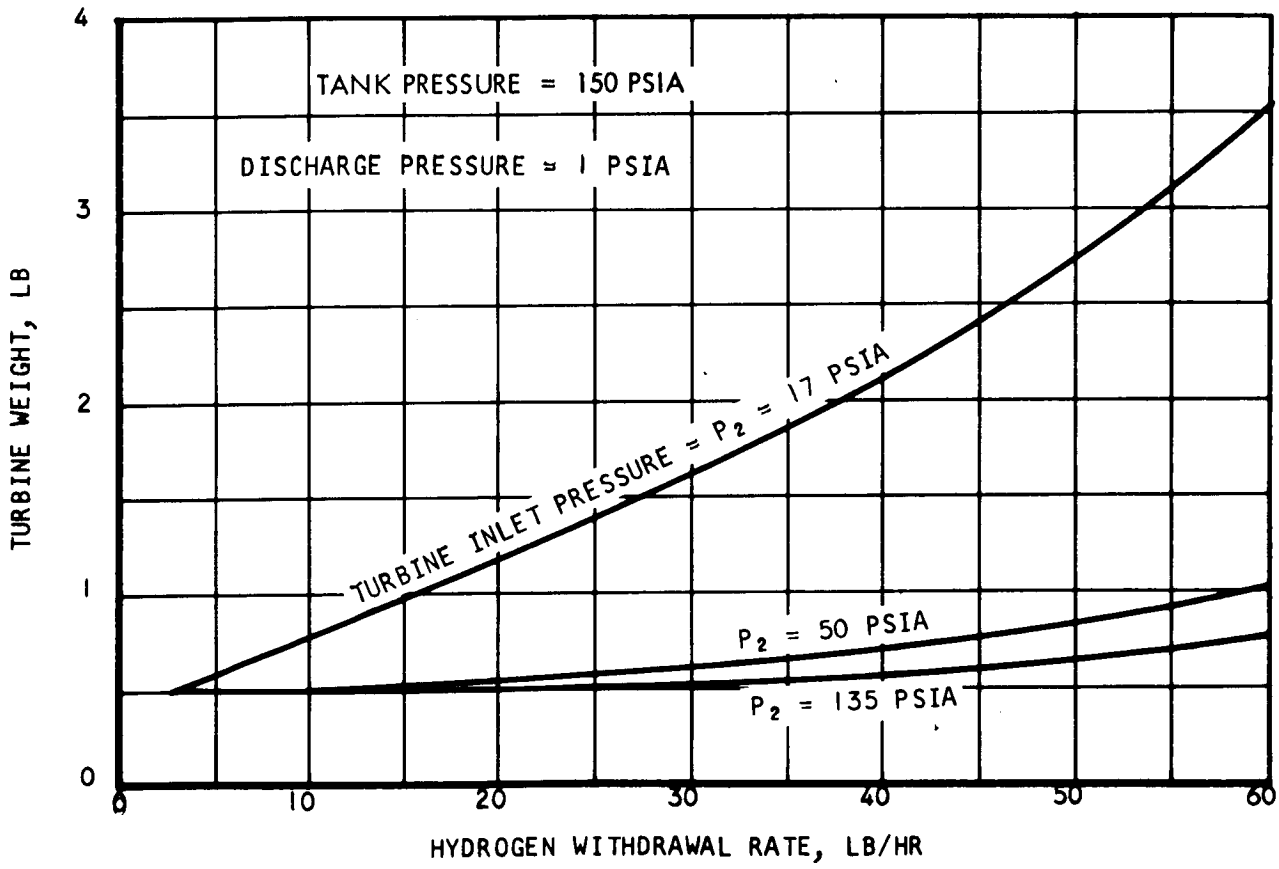

Fig. III-11 Turbine Weight – High Inlet Pressures

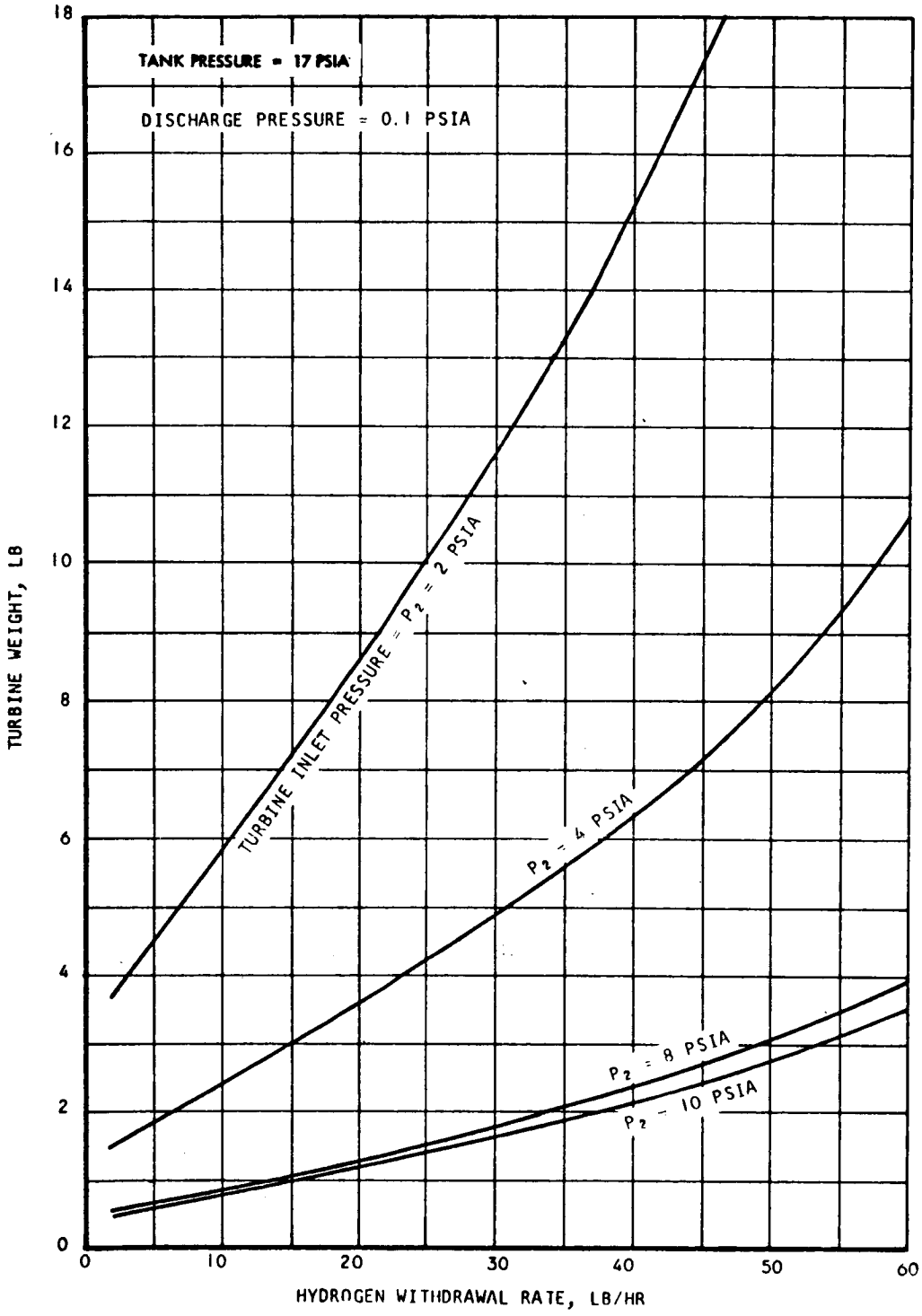

Fig. III-12 Turbine Weight – Low Inlet Pressures

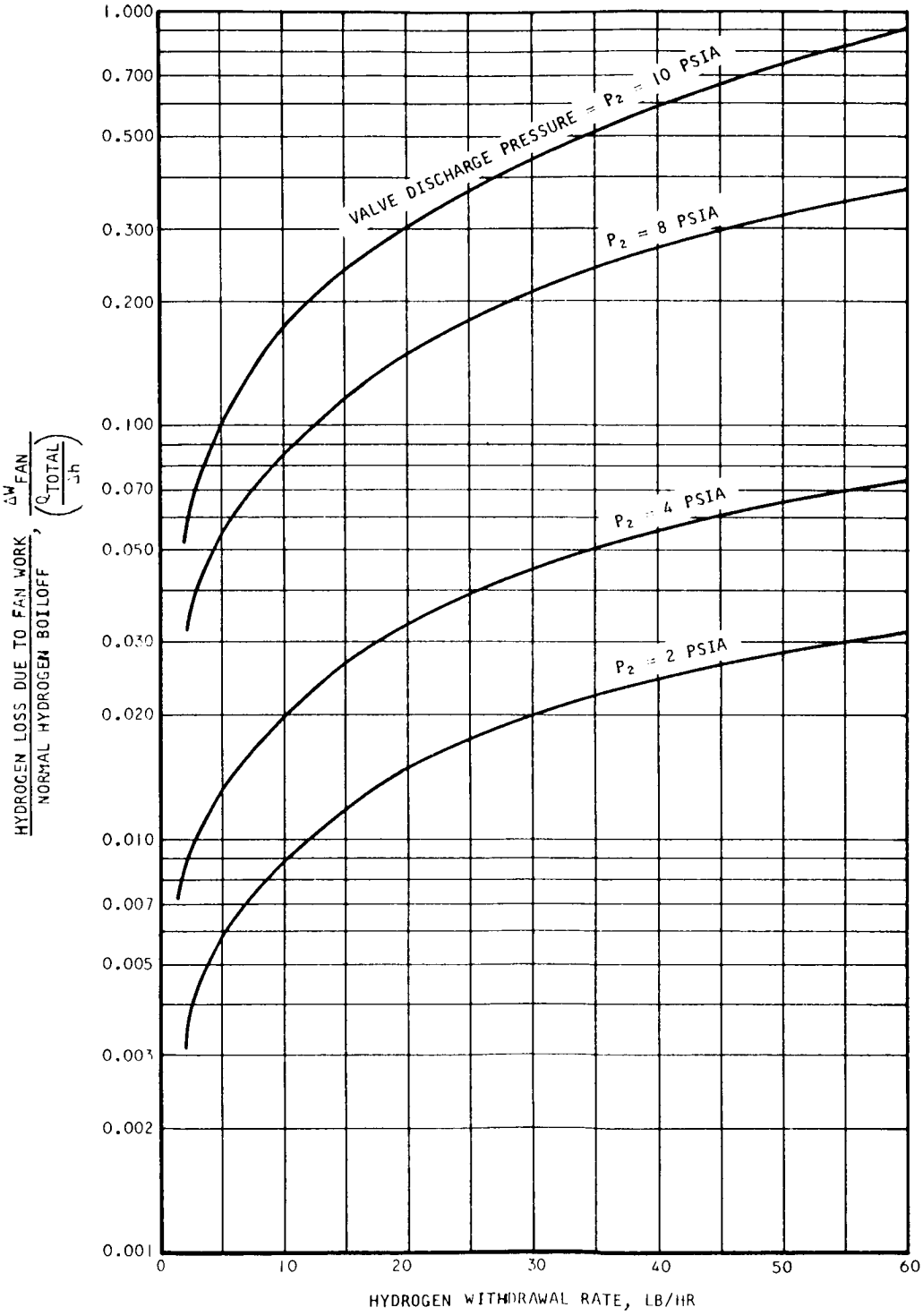

Fig. III-13 Normalized Fan – Work Weight Penalty

The overall system weight curves for the turbine drive system can be obtained as follows:

Step 1. Select a fluid removal unit (fluid filter or dynamic separator).

Step 2. Select a tank pressure P_1.

Step 3. Select a valve discharge pressure P_2.

Step 4. Select a liquid hydrogen flow rate W_{H_2}.

Step 5. If the liquid removal unit is a dynamic separator, determine power requirements from Fig. III-2.

Step 6. Determine heat exchanger fan power requirements from Fig. III-3. Fan power is determined from warm side heat exchanger 100 percent hydrogen gas.

Step 7. Determine turbine output power from Fig. III-4.

Step 8. Add the power required for the separator, when applicable, and heat exchanger fan (Steps 5 and 6). If the turbine output power is equal to or greater than the sum of the heat exchanger fan and dynamic separator requirements, a power balance can be made; proceed to Step 9. If the turbine output power is less than required, the system is not feasible; return to Step 3 and choose a lower valve discharge pressure P_2. It should be noted that a trial and error process is not necessary if a generalized plot is made of turbine output and fan input requirements. This was done for Missions (1), (2), and (3) (Fig. III-5). It can be seen that the turbine output is greater than the fan input requirements for valve discharge pressures less than 8 psia over the entire flow range considered.

Step 9. Determine the weight of the dynamic separator unit from Fig. III-6, if used.

Step 10. Determine the expansion valve weight from Fig. III-7. The valve weight is 2.3 lb for the pressure and flow rates considered here.

Step 11. Determine the heat exchanger weight from Fig. III-8.

Step 12. Determine the hot side (helium) flow rate from Fig. III-9.

Step 13. Determine the fan weight from Fig. III-10.

Step 14. Determine the turbine weight from Figs. III-11 or III-12.

Step 15. The fixed weight of the system is determined by adding the weights of the individual components determined in Steps 9, 10, 11, 13, and 14. To obtain the overall system weight penalty for the turbine drive system, the heat addition due to the work performed by the fan must be evaluated (it is assumed that heat addition due to turbine inefficiencies is removed by the withdrawn hydrogen). The work (heat) input to the tank fluid is removed by withdrawing an additional amount of hydrogen: The weight penalty in terms of fluid can be found from:

$$\Delta W_F = \frac{p(3.413)}{(h_3 - h_2)} \left[\frac{q\,t}{W_{H_2}(h_3 - h_2) - p(3.413)}\right]$$

Using the above equation and Fig. III-3, the weight penalty is shown in Fig. III-13 for the general case and in Fig. III-14 for Mission (2).

Thus, the total weight penalty for a given system, P_1, P_2/P_1, and W_{H_2} is:

$$W = W_{LR} + W_V + W_H + W_F + W_T + \Delta W_F$$

Step 16. Return to Step 4 and reiterate for various liquid hydrogen withdrawal rates. The result will be a curve of system weight as a function of flow rate for a given valve discharge pressure.

Step 17. Return to Step 3 and repeat for various valve discharge pressures. The result will be a series of curves of system weight as a function of flow rate for various valve discharge pressures.

Step 18. Return to Step 2 and repeat for various tank pressures. The result will be several graphs of system weight for various tank pressures for a given system.

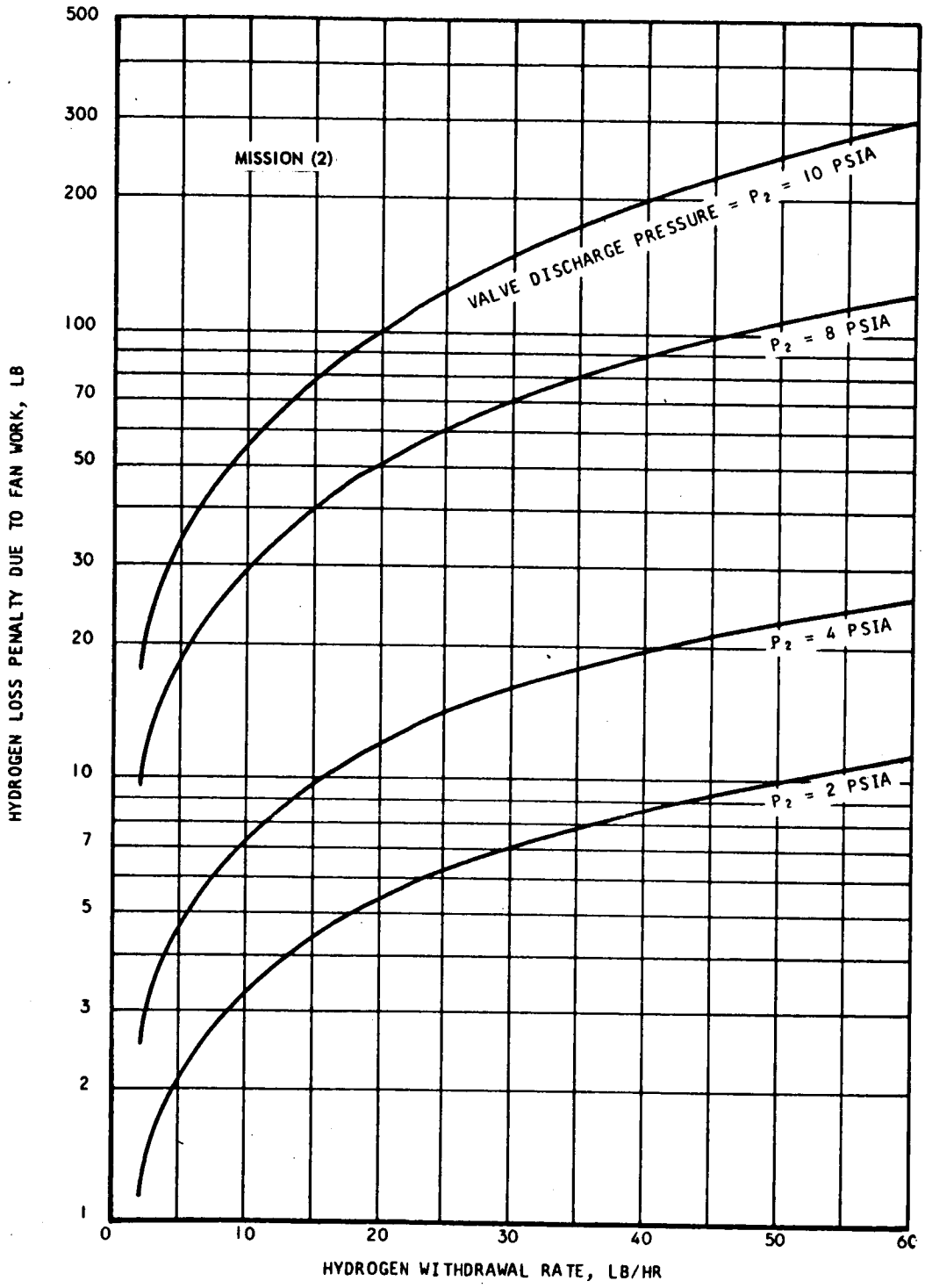

Fig. III-14 Mission (2) Fan Work Weight Penalty

ELECTRIC MOTOR DRIVEN COMPACT HEAT EXCHANGER SYSTEMS

The general approach for the systems using an electric motor drive (Fig. III-15) is similar to the approach used for the turbine drive systems. A power weight penalty is included for the electric motor. This penalty is a function of the time that the electric motor is used. The number of hours, θ, that the electric motor will be running (or the thermal conditioning system operating time) is simply the term shown in brackets in Step 15 above or

$$\theta = \frac{q\,t}{W_{H_2}(h_3 - h_2) - p(3.413)}$$

The procedure for developing the system weight curves for an electric motor is quite similar to that for turbines. The steps below marked same are identical to those for the turbines which were discussed previously.

Step 1. Same
Step 2. Same
Step 3. Same
Step 4. Same
Step 5. Same

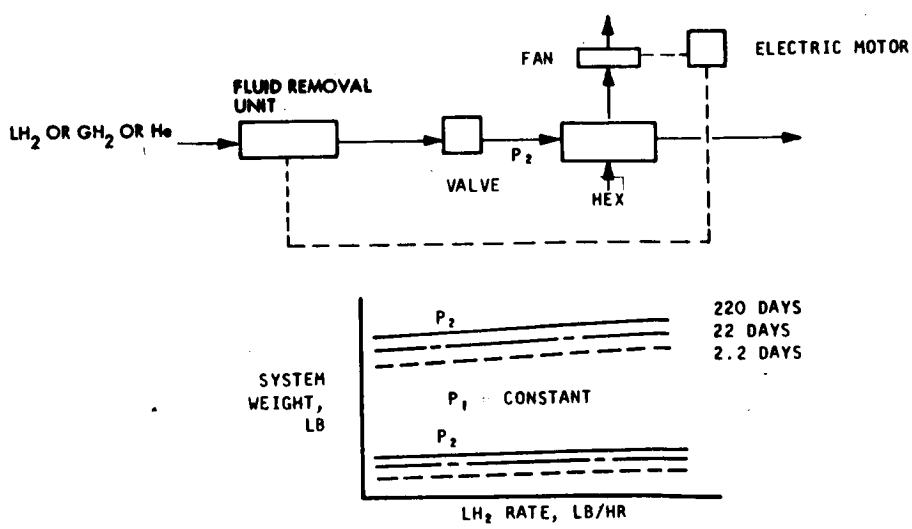

b. ELECTRIC MOTOR DRIVE SYSTEM

Fig. III-15 Typical System Weight Curves, Motor Drive

Step 6. Same

Step 7. Add the power required for the separator, when applicable, and the heat exchanger fan (Steps 5 and 6). This is the output power required from the electric motor.

Step 8. The electrical power weight is determined from the electric motor characteristics (Fig. III-16), assuming a fuel cell power source. The fuel cell power weight is based on the Apollo fuel cell. The cell weighs about 300 lb (including radiator) and has a 2-kw output power level. The specific reactant usage rate is roughly 0.9 lb/hr-kw. Assuming that the oxygen and hydrogen are stored in cryogenic tanks, the weight storage for the reactants is roughly 0.25 lb/lb O_2 and 2 lb/lb H_2. The overall power weight is thus:

$$W_P = 0.00135\, w\theta + 0.15\, w$$

The fan power required (Fig. III-3) is identical to the motor output. From Fig. III-16, the motor power draw can be determined. The power weight can be obtained by evaluating the operating time of the system, θ, and by using the above power weight equation. The power weight for the various system operating times is shown in Fig. III-17. The electrical power for Mission (2) is shown in Fig. III-18.

Step 9. Same

Step 10. Same

Step 11. Same

Step 12. Same

Step 13. Same

Step 14. Determine the electric motor weight from Fig. III-19.

Step 15. The fixed weight of the system is determined by adding the weights of the individual components determined in Steps 9, 10, 11, 13, and 14. The total system weight is determined by adding (1) the electrical

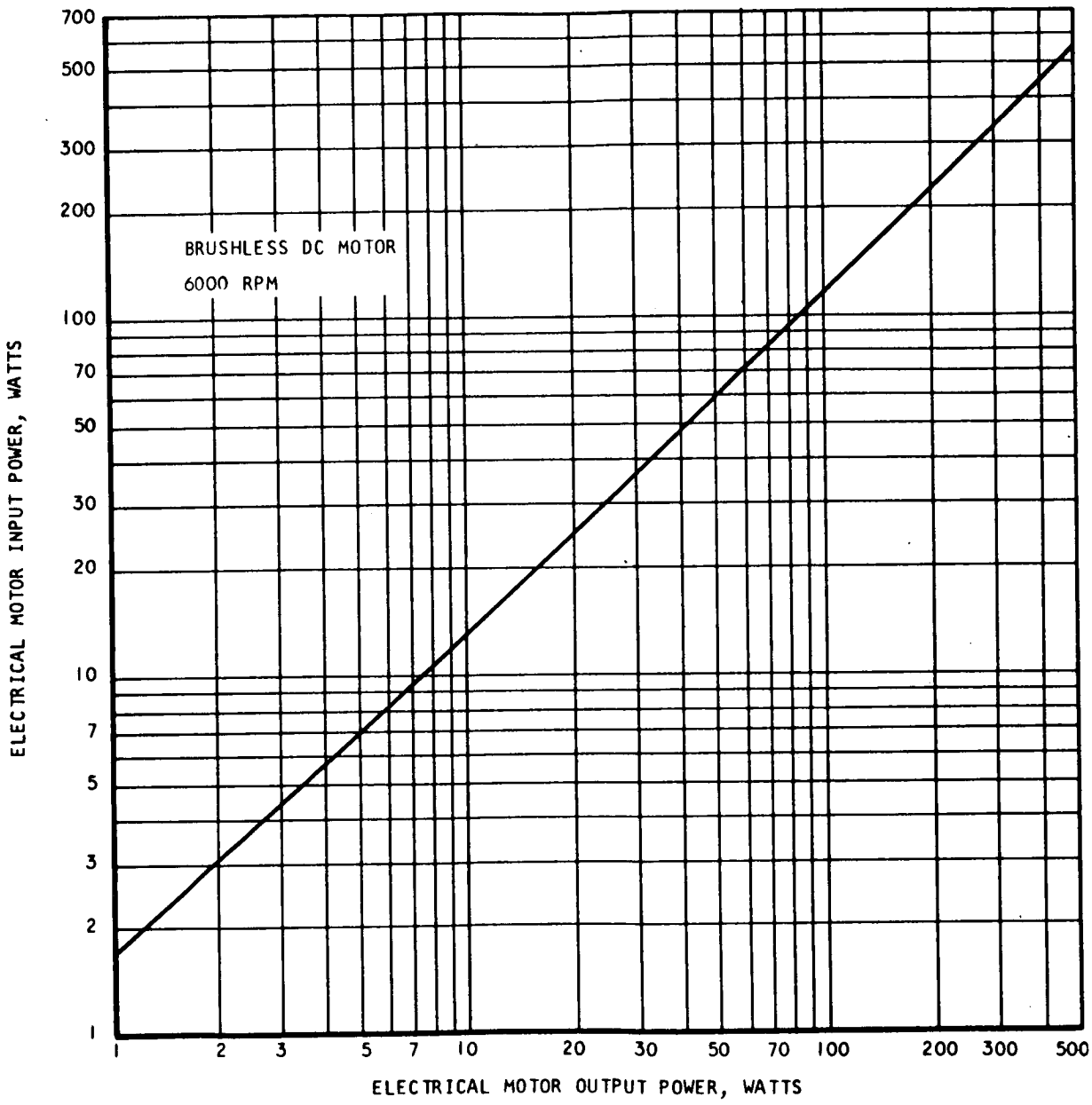

Fig. III-16 Electrical Motor Input and Output Power

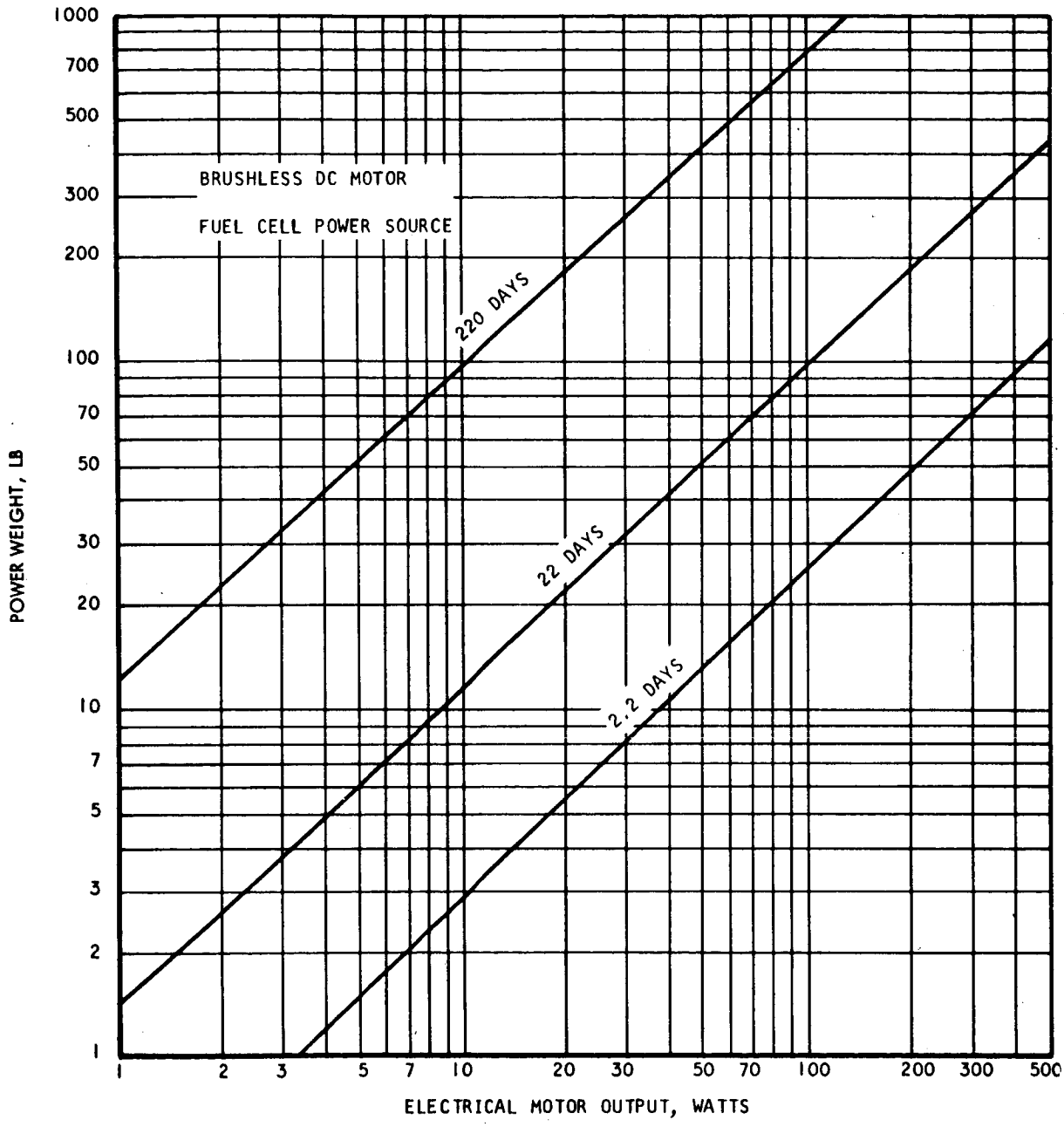

Fig. III-17 Electrical Power System Weight

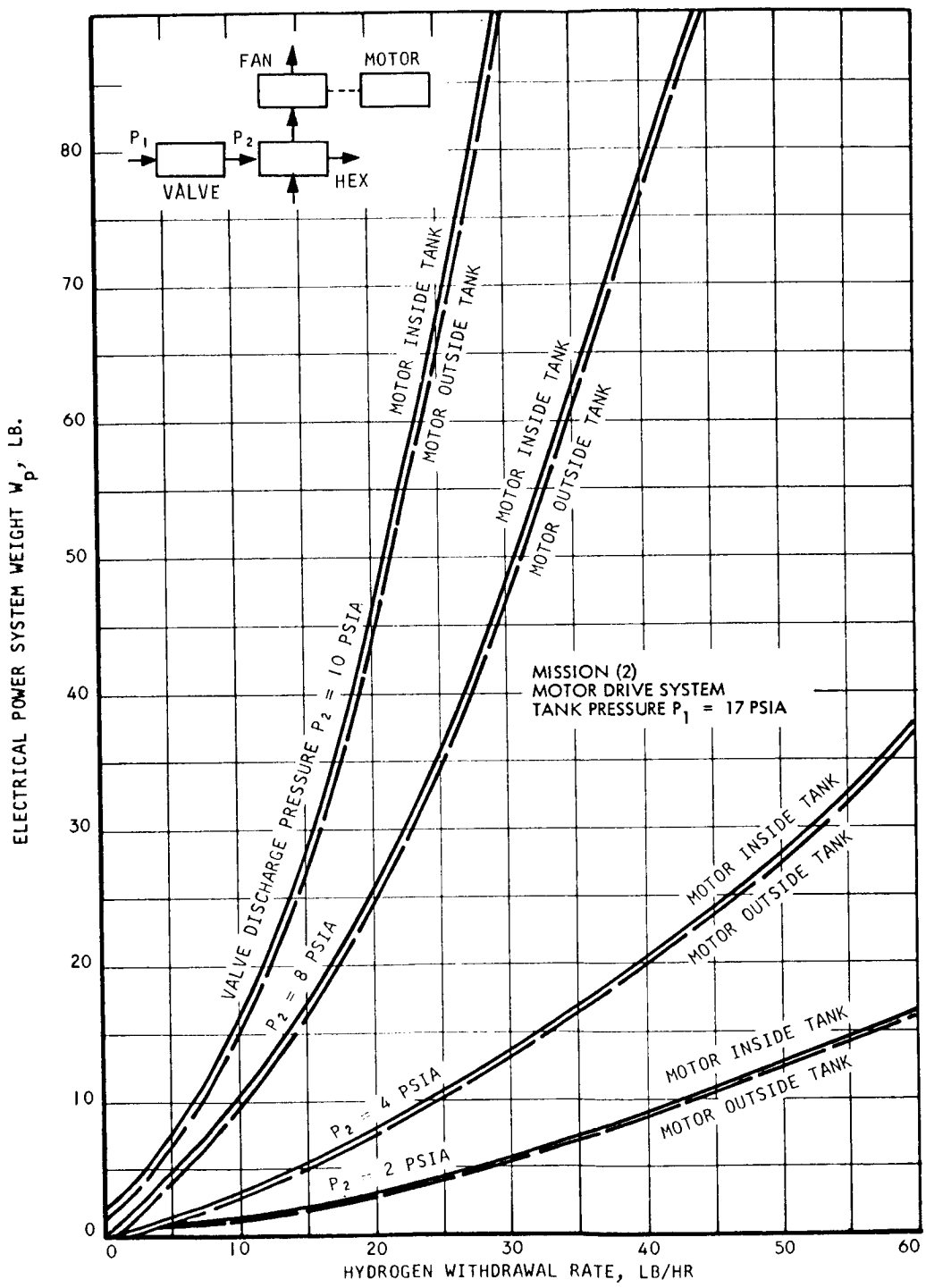

Fig. III-18 Mission (2) Electrical Power System Weight

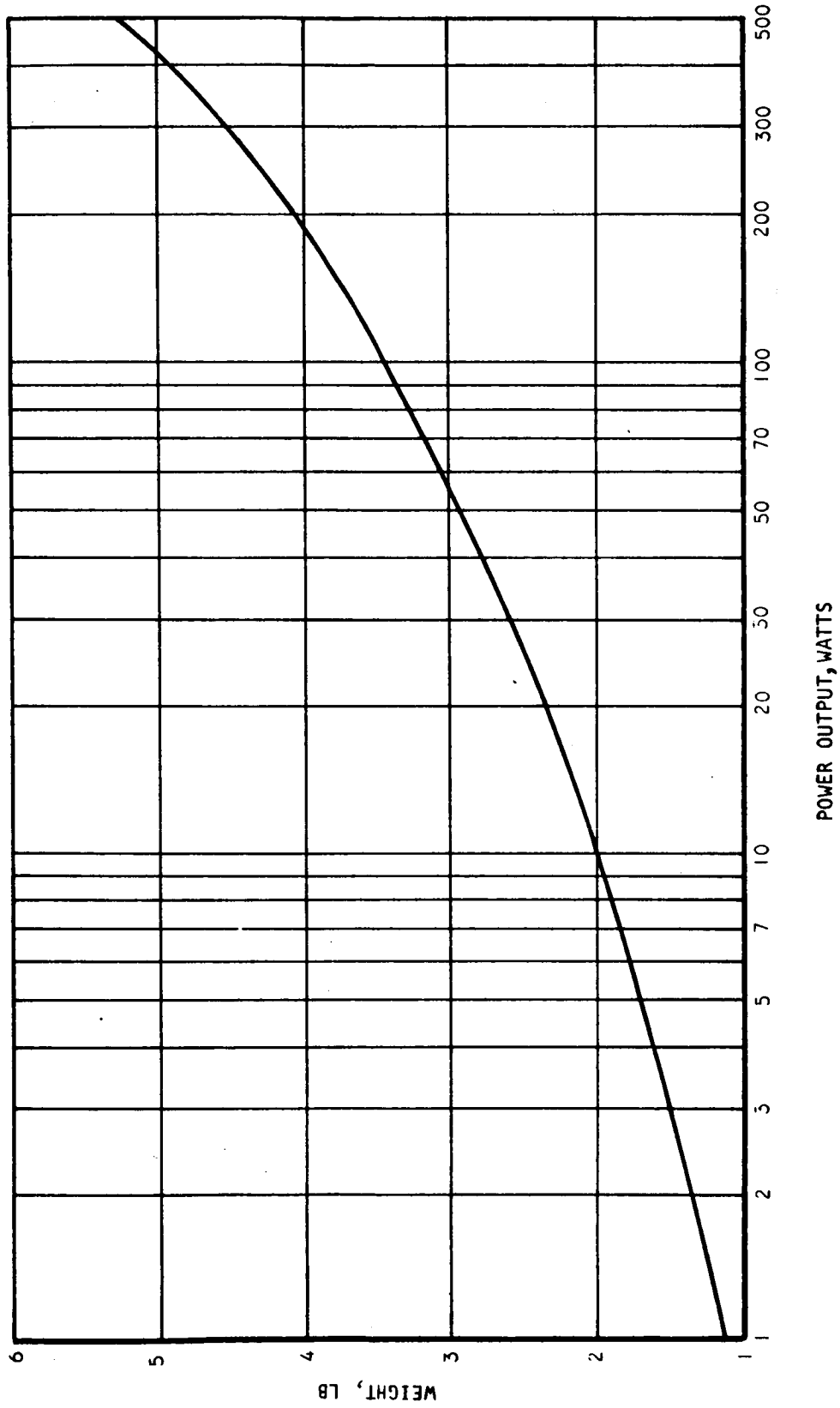

Fig. III-19 Brushless DC Motor Weight

power system weight and the boiloff due to fan or electrical motor input energy and (2) the fixed weight. The electrical power was determined in Step 8. The input energy required for circulating fluid over the warm side of the heat exchanger is discussed in two cases. In the first case, the electrical motor is mounted outside of the tank and the heat given off by the motor (electrical and mechanical inefficiencies) is transferred to the venting fluid after it leaves the tank. For this case, the boiloff is due only to the fan input energy. This is identical to that for turbines (Fig. III-20). For the other case, where the motor is located inside the tank, the electrical motor input power is substituted for the fan input power in the fluid loss equation. The energy weight contribution is shown in Fig. III-13 for the general case and in Fig. III-20 for Mission (2).

Thus, the total weight for the system containing an electrical motor for a given P_1, P_2/P_1, and W_{H_2} is:

$$W = W_{LR} + W_V + W_H + W_F + W_E + W_P + \Delta W$$

Step 16. Same

Step 17. Same

Step 18. Same

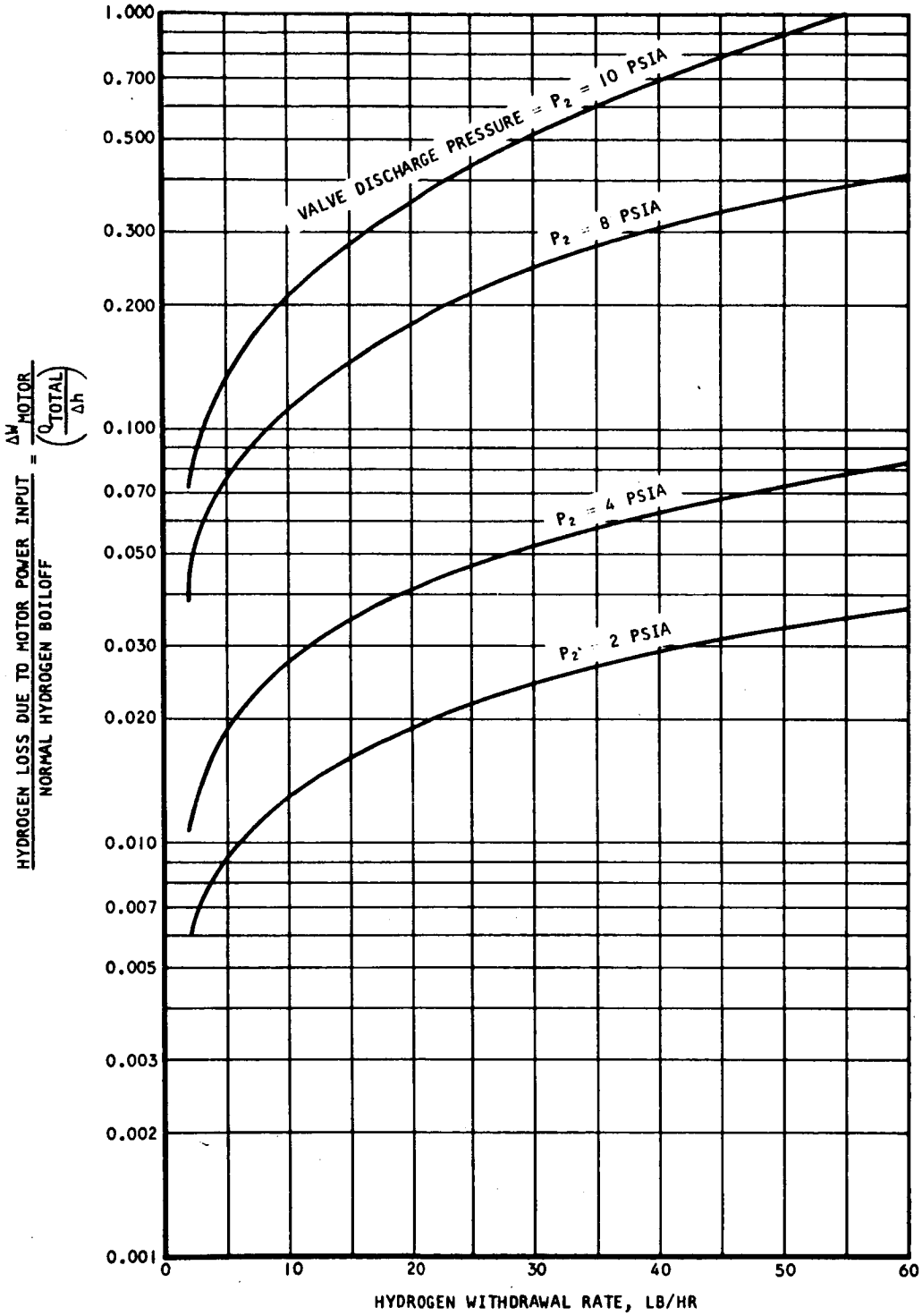

Fig. III-20 Normalized Motor Energy Weight

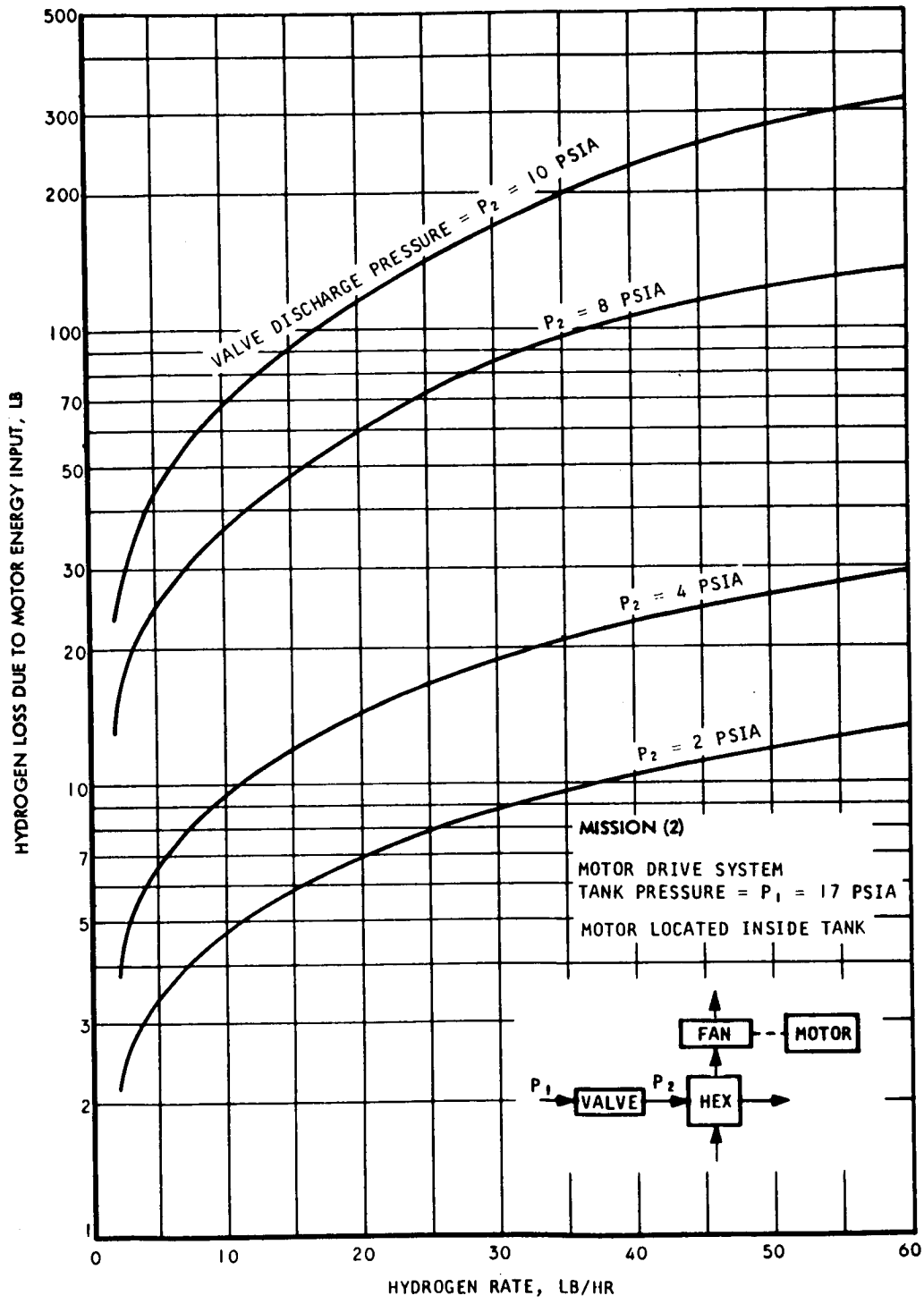

Fig. III-21 Mission (2) Motor Energy Weight

SYMBOLS AND ABBREVIATIONS

P_1 – Tank Pressure, psi

P_2 – Valve Discharge Pressure, psi

W_{H_2} – Hydrogen Withdrawal Rate, lb/hr

P – Fan Input Power, watts

q – Average External Heat Leak for Vehicle, Btu/hr

t – Mission Time to Last Firing, hr

h_3-h_2 – Enthalpy Change of Vented Fluid Across Heat Exchanger, Btu/lb

W – Total System Weight, lb

W_{LR} – Weight of Liquid Removal Unit, lb

W_V – Weight of Expansion Valve, lb

W_H – Weight of Heat Exchanger, lb

W_F – Weight of Fan, lb

W_T – Weight of Turbine, lb

ΔW_F – Fluid Loss Due to Fan Input Energy

W_P – Electrical Power Weight, lb

w – Power Draw, watts

θ – Total Time of Power Draw, hr

W_E – Weight of Electric Motor, lb

Note: NO SYMBOLS AND ABBREVIATIONS IN SECTIONS IV OR V

Section IV

APPLICATION OF DESIGN METHOD

The design method outlined in the preceding section was used to make an optimization analysis of thermal conditioning systems for Missions (1), (2), and (3).

Mission (2), the primary mission, uses an Earth-Mars kickstage, and will require thermal conditioning of the liquid hydrogen propellant tank for 220 days (launch to last firing of engine). The average heat leak for this mission is specified as 11.5 Btu/hr, giving a total heat leak for the mission of 60, 720 Btu. Mission (1), a lunar logistic mission, will operate for 133.5 hr. The average heat leak will be 160 Btu/hr, and the total heat leak will be 21,360 Btu. Mission (3), the Mars manned mission, is a 220-day mission with an average heat leak of 22 Btu/hr and a total heat leak of 116, 160 Btu.

This analysis considered the use of both turbine-driven and electric motor-driven mixers with a compact heat exchanger. Further, for the electric motor-driven fan, both internal and external (to the tank) motor mounting was considered. For all conditions, the total system weight (fixed equipment plus expendables such as electrical energy and additional hydrogen boiloff due to equipment heat losses) was calculated as a function of hydrogen withdrawal rate with valve pressure P_2 as a parameter. The systems considered can operate with any inlet fluid quality; thus, the weight of the fluid removal device (a fluid filter) is included in the system weight curves as a part of the expansion valve weight.

The selection of a system which can operate efficiently on any fluid quality rather than one which can operate only upon all gas or all liquid removal is based upon the following considerations:

- Retention of helium pressurant gas
- System reliability

Control of the vent system and proper evaluation of the associated boiloff are affected by considerations involving the retention of helium pressurant for multi-start vehicles. If the tank is maintained at a fixed total pressure equivalent to the loading pressure (17 psia), then the retention of helium pressurant after an engine firing results in a decrease in the hydrogen partial pressure. Decreasing the hydrogen partial pressure causes the bulk of the propellant to be cooled (by boiling) to the partial pressure saturated temperature. If, however, the tank contents are maintained at a constant temperature (i.e., constant hydrogen partial pressure), there is no boiloff, and some savings in helium gas and system weight are obtained. Figure IV-1 shows a weight comparison of these two control methods, with systems designed to remove only liquid or only ullage gas. In the latter system, it was assumed that all of the helium was lost between firings.

The lightest of the three systems compared in Fig. IV-1 is the constant temperature control, liquid removal only system. This system is idealistic, however, for two reasons. First, the control of tank pressure by saturated propellant temperature measurement requires a uniform temperature throughout the tank at all times if either over pressure conditions or excessive tank venting are to be avoided. Second, the measurement of temperature must be extremely accurate – on the scale of a few-tenths of a degree Rankine. Note that the saturated temperature of liquid hydrogen varies about 0.3°R per psi.

Practical control of tank pressure presently must be based upon tank pressure measurement. From Fig. IV-1 it is clear that for a Mission (2) vehicle, less than a 5-lb difference in effective helium pressurization system weight is estimated when comparing a thermal conditioning system which removes only liquid hydrogen to one which removes only ullage gas. The weights of a dielectrophoretic or dynamic separator exceed this weight difference. Therefore, for the Mission (2) vehicle, a lighter venting and pressurization system is obtained with a thermal conditioning system which removes either liquid hydrogen or ullage gas during venting.

The only liquid removal units which were identified for possible application were the dielectrophoretic and dynamic separator units. Either unit is obviously much more

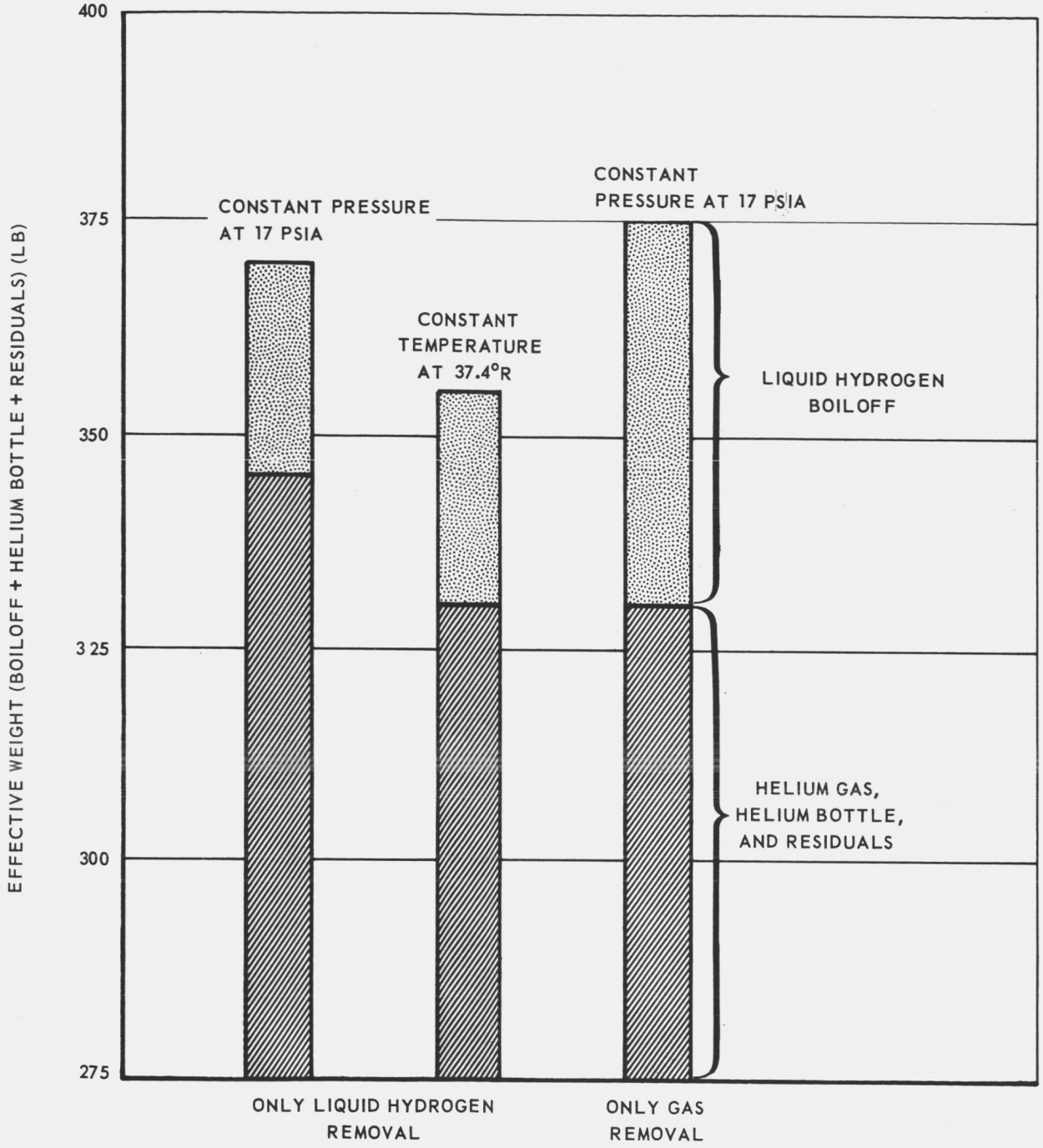

Fig. IV-1 Effect of Liquid or Gas Removal on Helium System and Boiloff Weights (Mission 2)

complex than a single screen filter. In the event that the pressurization and venting systems are designed for liquid removal only and helium pressurant gas is provided on a no loss basis, then a failure in the liquid removal unit probably would mean a failure to perform the mission. Thus from cursory reliability considerations, a thermal conditioning system based only upon liquid removal is less reliable than a system designed to efficiently operate with any inlet fluid quality.

TURBINE-DRIVEN FAN, COMPACT HEAT EXCHANGER SYSTEM

The system weight comparison for systems using a turbine-driven fan is shown in Figs. IV-2, IV-3, and IV-4 for Missions (1), (2), and (3) respectively. The total system weight increases with increasing hydrogen withdrawal rate and with increasing valve discharge pressure. Figures IV-5 through IV-8 break down the total system weight into fixed equipment weight and heat exchanger weight. It should be noted that the total weight in these figures applies only to Mission (2); however, the heat exchanger and fixed weight curves apply to all missions. The fixed weight includes the expansion valve, heat exchanger, fan, and turbine. As can be seen from the figures, the heat exchanger makes up an increasing percentage of the total fixed weight as the valve discharge pressure increases. As the valve discharge pressure increases, the temperature change across the valve decreases. This presents a smaller driving force for heat transfer in the heat exchanger and, therefore, a larger area and weight requirement.

The difference between the total weight and the fixed equipment weight is the increased hydrogen boiloff due to the fan power.

ELECTRIC MOTOR-DRIVEN FAN, COMPACT HEAT EXCHANGER SYSTEM

The system weight comparison for systems using an electric motor-driven fan is shown in Figs. IV-9, IV-10, and IV-11 for Missions (1), (2), and (3) respectively. All weights are expressed as a function of the same variables used with the turbine drive system. In addition, the weight depends on whether the motor is mounted internally or externally to the tank. For an internally mounted motor, all input power will eventually be transferred to the tank fluid as heat and will appear as an additional hydrogen boiloff weight.

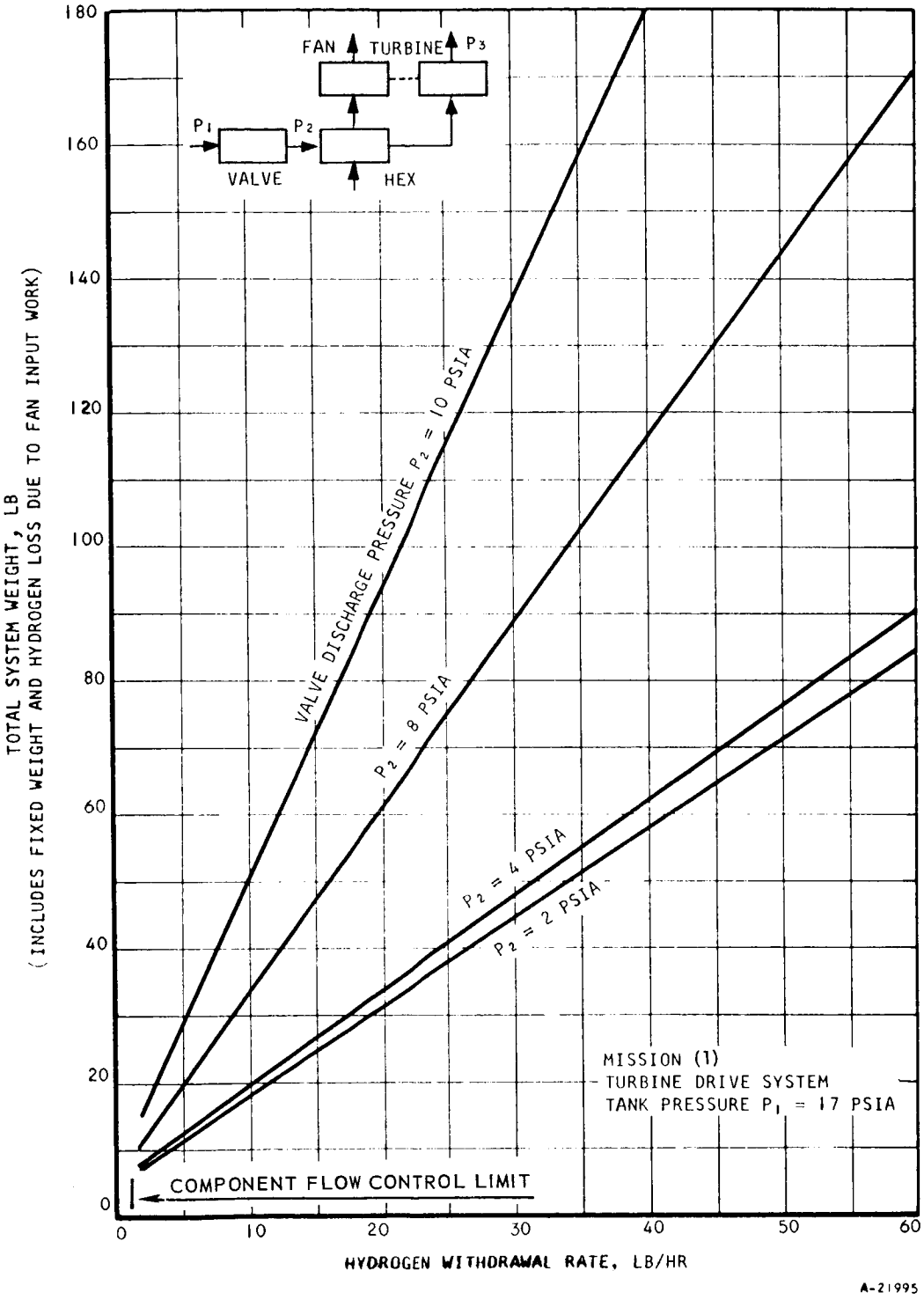

Fig. IV-2 Mission (1) System Weight Comparison, Turbine Drive

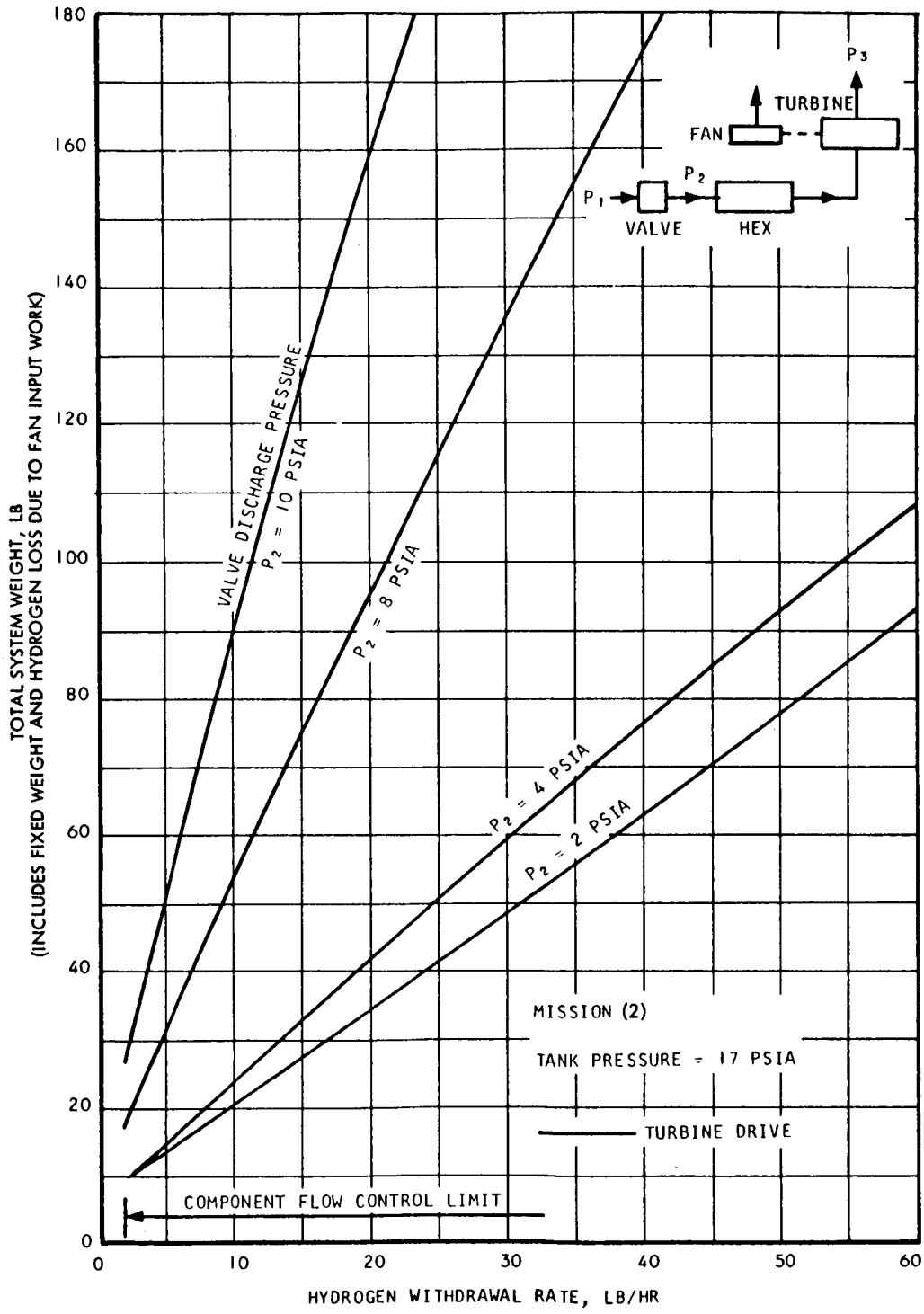

Fig. IV-3 Mission (2) System Weight Comparison, Turbine Drive

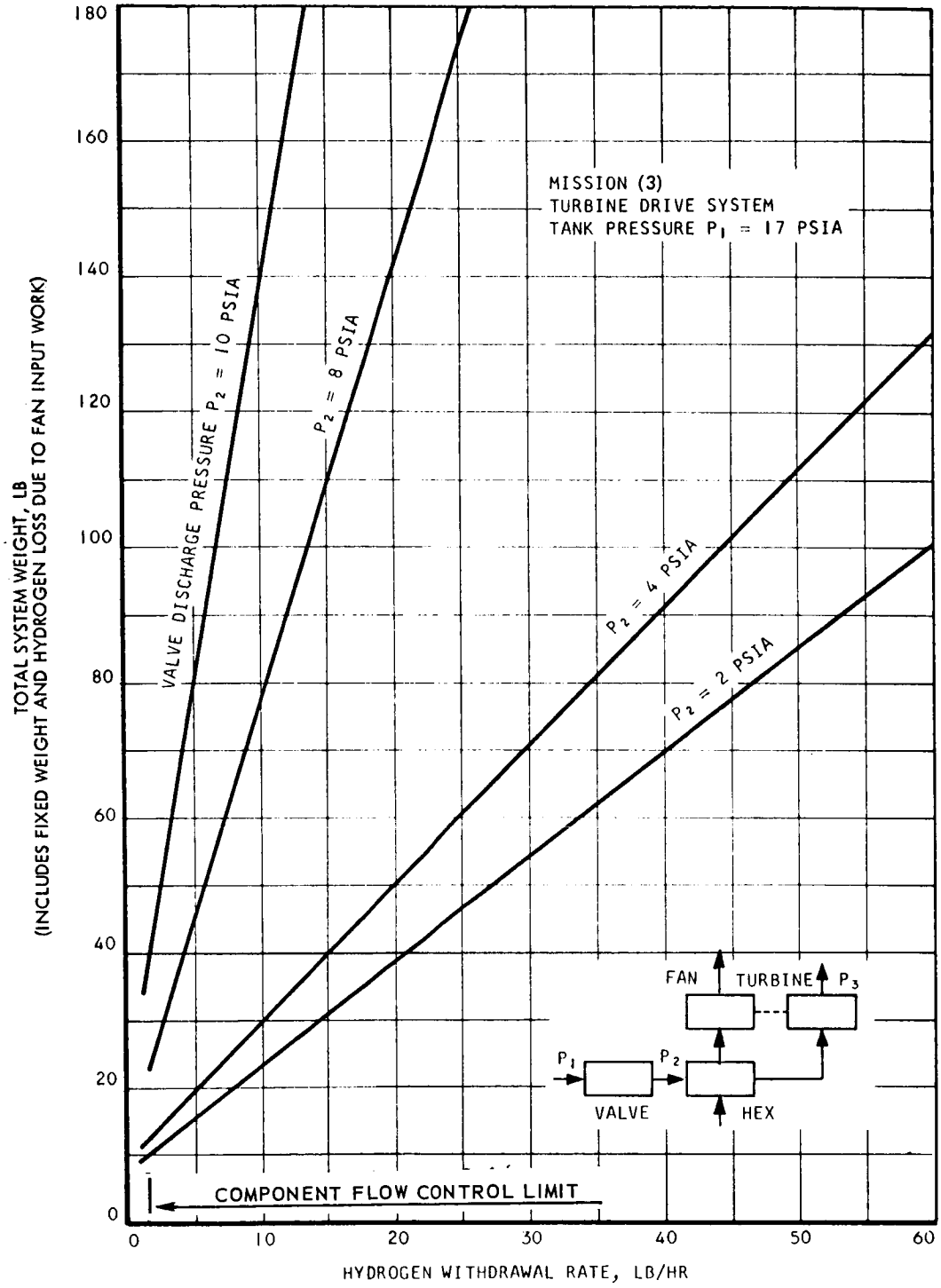

Fig. IV-4 Mission (3) System Weight Comparison, Turbine Drive

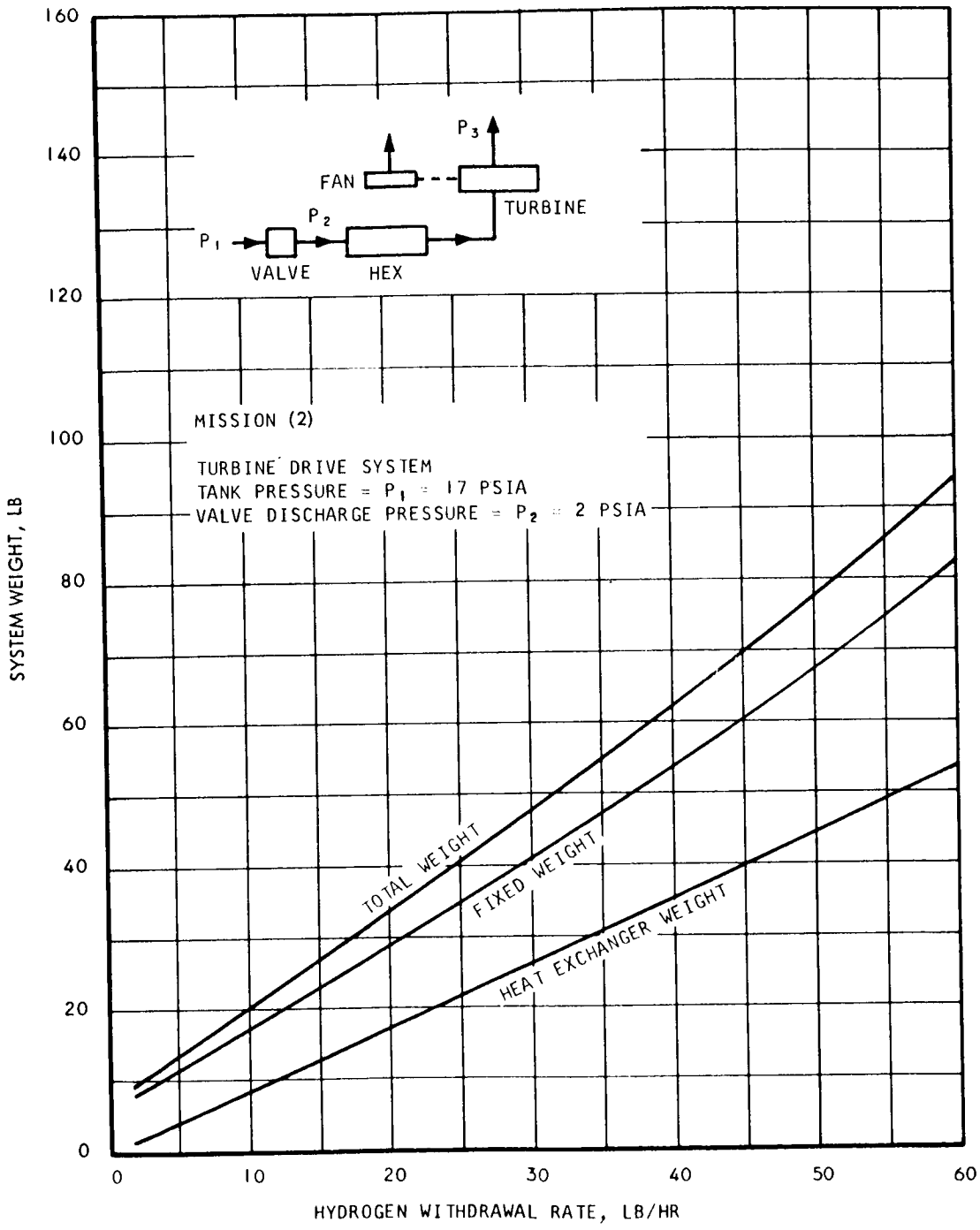

Fig. IV-5 Mission (2) System Weight, Turbine Drive (P_2 = 2 psia)

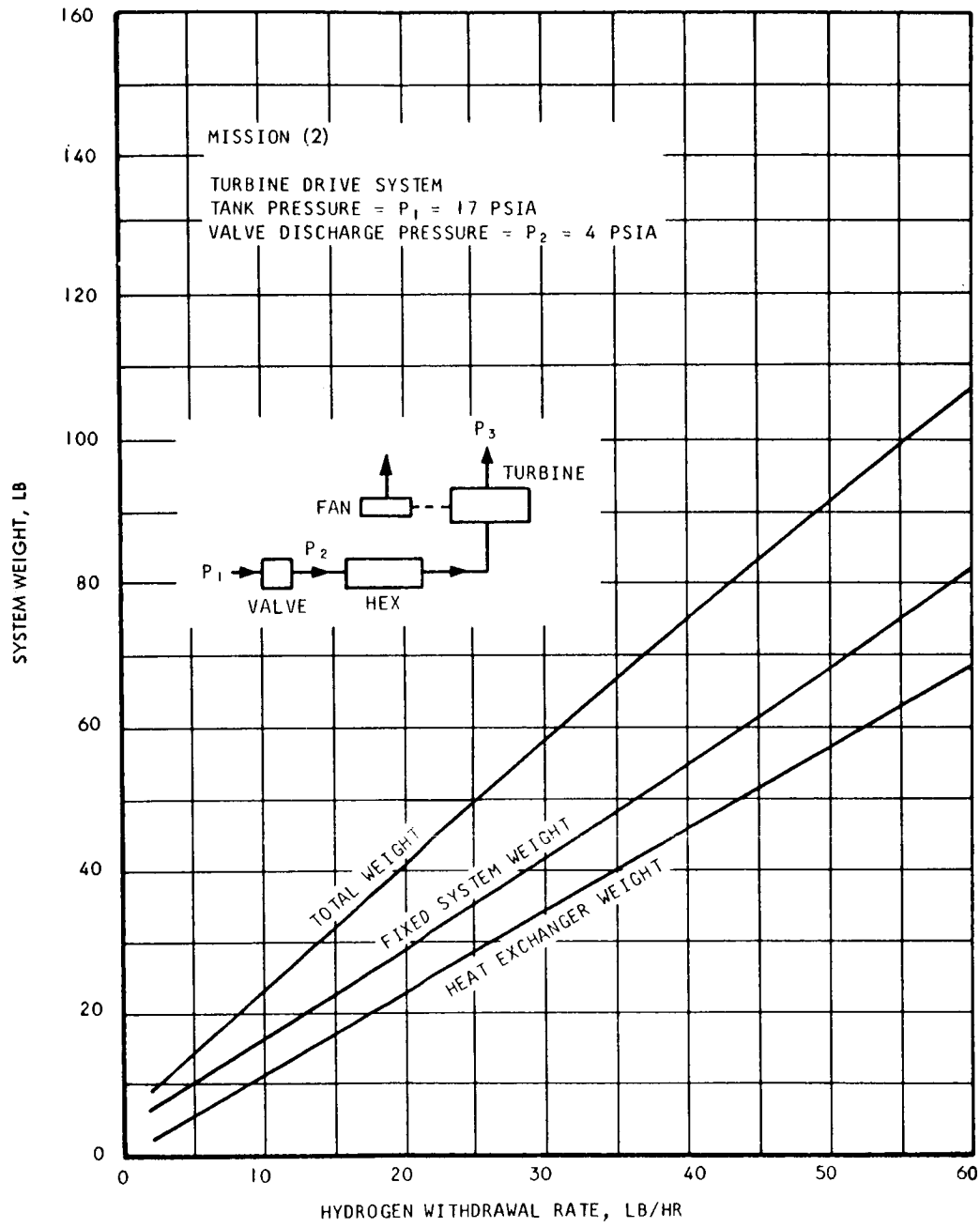

Fig. IV-6 Mission (2) System Weight, Turbine Drive (P_2 = 4 psia)

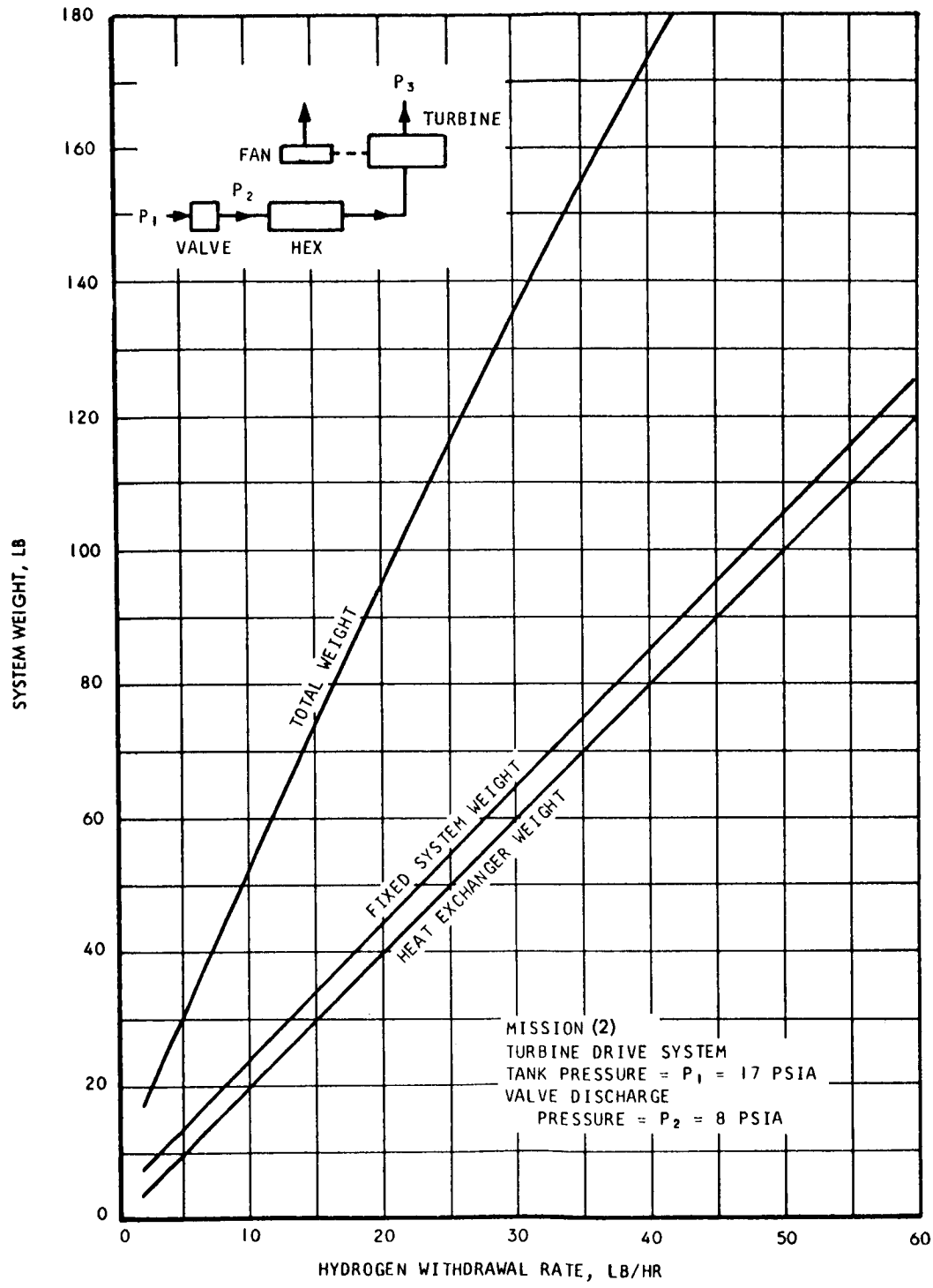

Fig. IV-7 Mission (2) System Weight Turbine Drive (P_2 = 8 psia)

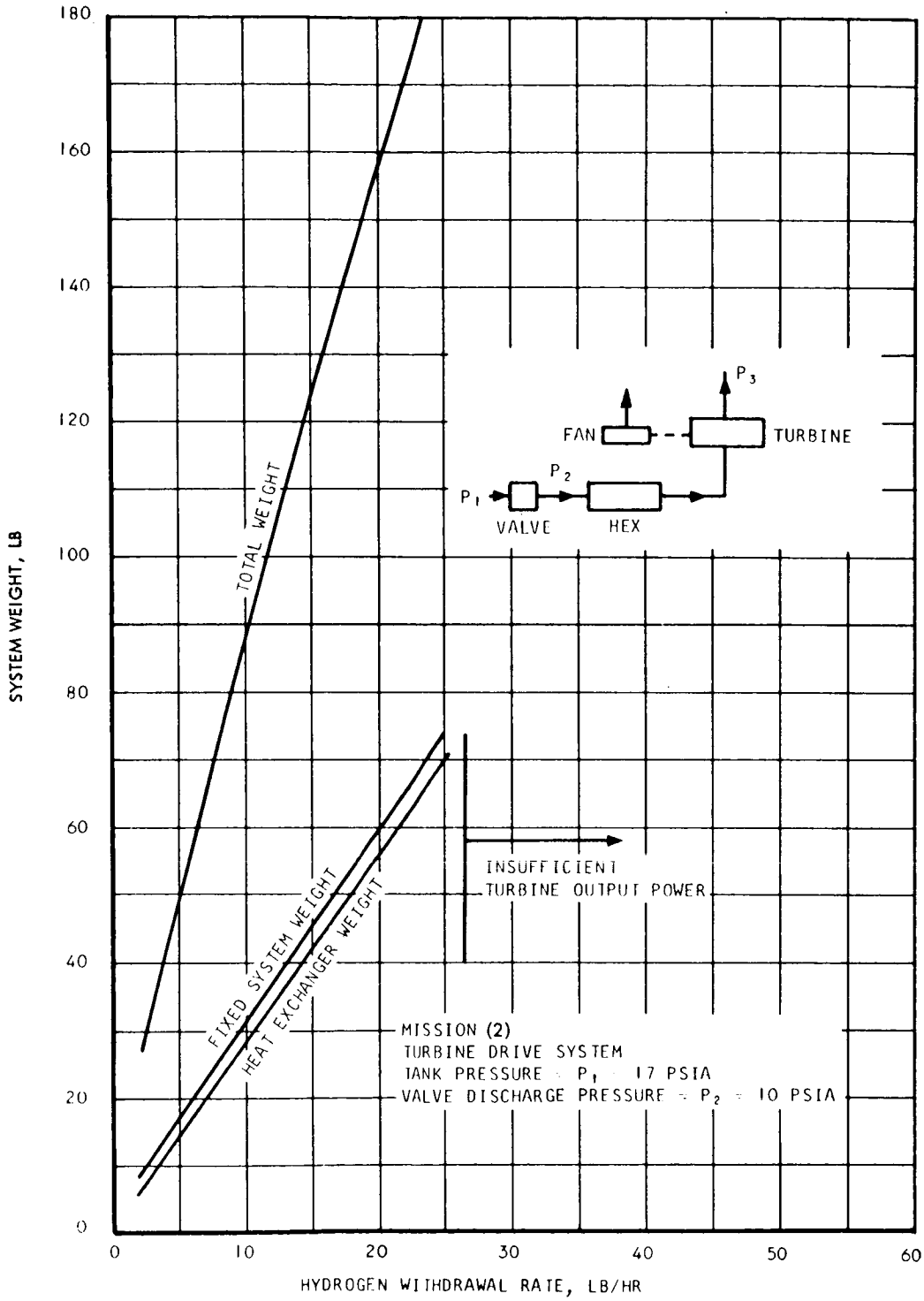

Fig. IV-8 Mission (2) System Weight, Turbine Drive (P_2 = 10 psia)

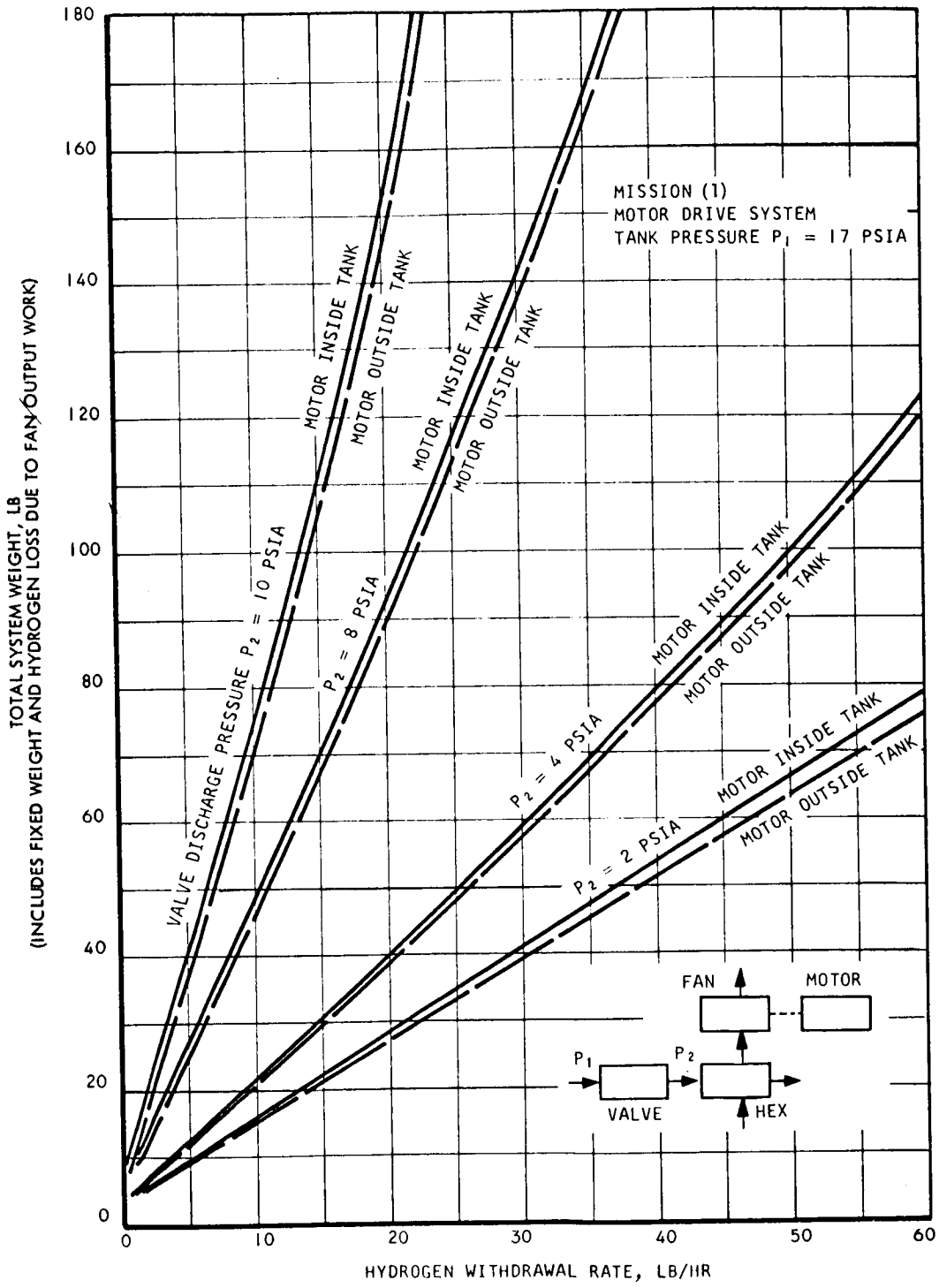

Fig. IV-9 Mission (1) System Weight Comparison, Motor Drive

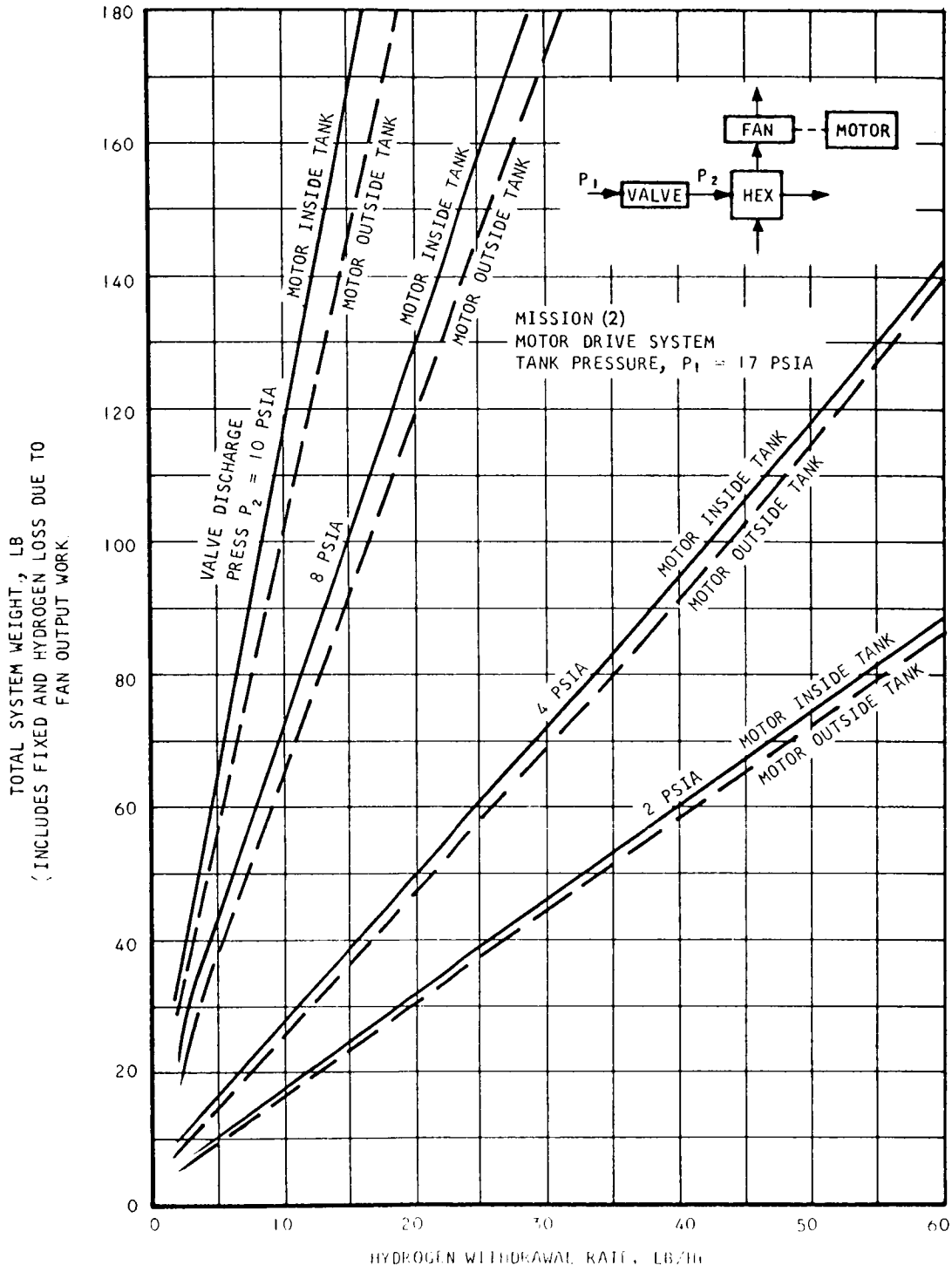

Fig. IV-10 Mission (2) System Weight Comparison, Motor Drive

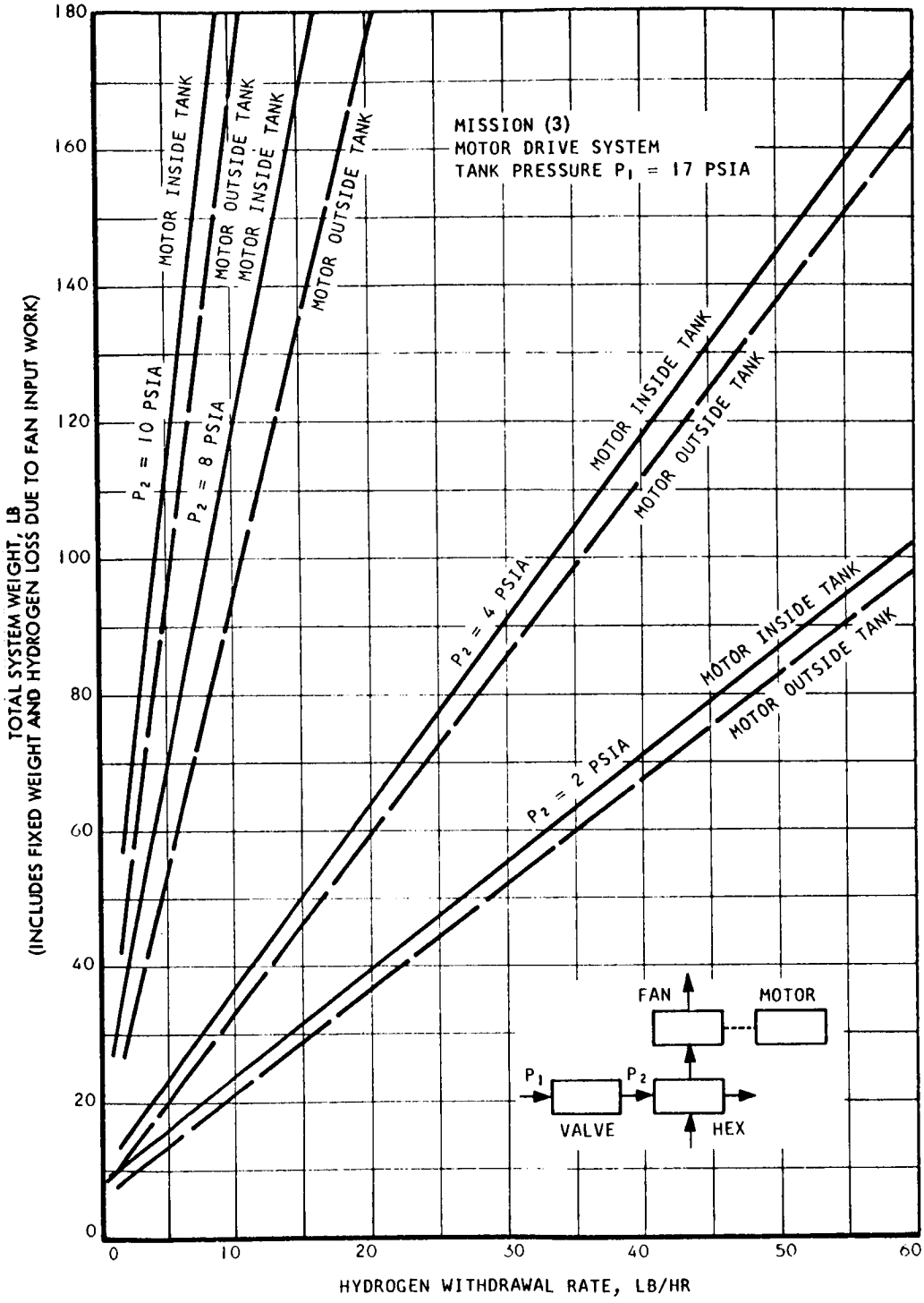

Fig. IV-11 Mission (3) System Weight Comparison, Motor Drive

For an externally mounted motor, only the fan work will be transferred to the tank contents. This situation is identical to that for a turbine drive. All motor losses (I^2R , windage, bearing) will be removed by submerging the motor in the vented hydrogen flow. It is assumed that using this means of motor cooling will impose no additional weight on the system.

Figures IV-12 through IV-15 give the total and fixed weight breakdowns for the electric motor-driven system. Again, the total weight in these figures applies only to Mission (2); however, the heat exchanger and fixed weight curves apply to all missions. For this system, the fixed weight includes the expansion valve, heat exchanger, fan, and motor. The difference between the total weight and fixed weight represents the electrical power system weight and the hydrogen boiloff weight due to motor operation.

COMPARISON OF DRIVE SYSTEMS

A comparison of the total weight for the turbine and for the electric motor drive systems is shown in Figs. IV-2 through IV-11 and IV-16. For the low withdrawal rates desired for the missions, the selected withdrawal rate will be based on component limitations, and will probably be less than 5 lb/hr. For these low flow rates and for low valve discharge pressures, the overall weight for the turbine and electric motor drive systems are almost identical. Therefore, selection of the drive system must be based on system characteristics other than weight. Some of the advantages of each type of drive are discussed below.

The advantage of the turbine drive system is that the unit is self-contained, and no external source of power is required. If electrical power is extremely critical, a turbine drive system may be necessary. However, based on a power associated with a fuel cell power source, the power weight increment is not severe.

The electric motor drive system appears, therefore, to have significant advantages over the turbine drive system. These are:

a. The heat exchanger fan can be used for mixing tank fluid when no fluid is being withdrawn from the tank.

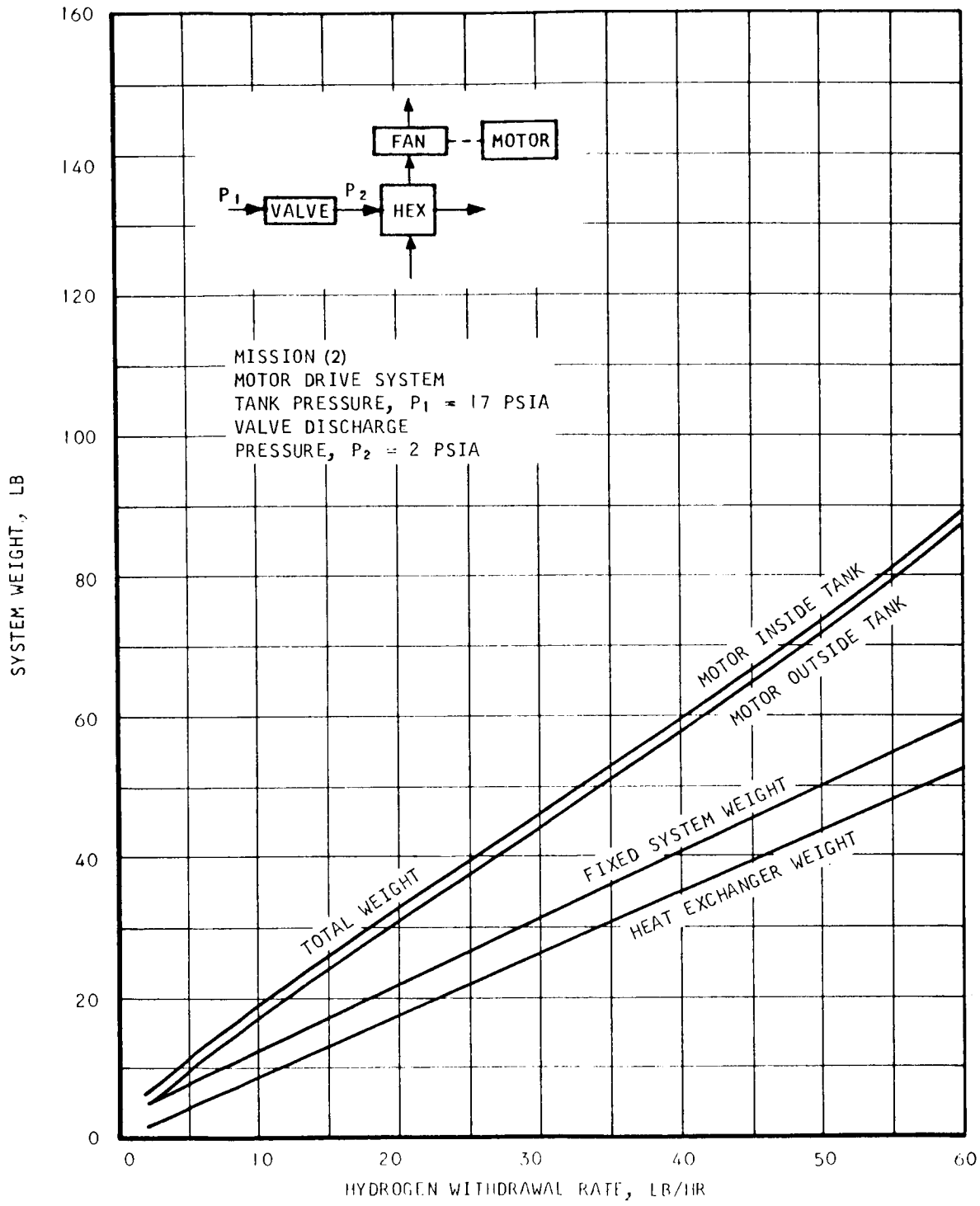

Fig. IV-12 Mission (2) System Weight, Motor Drive (P_2 = 2 psia)

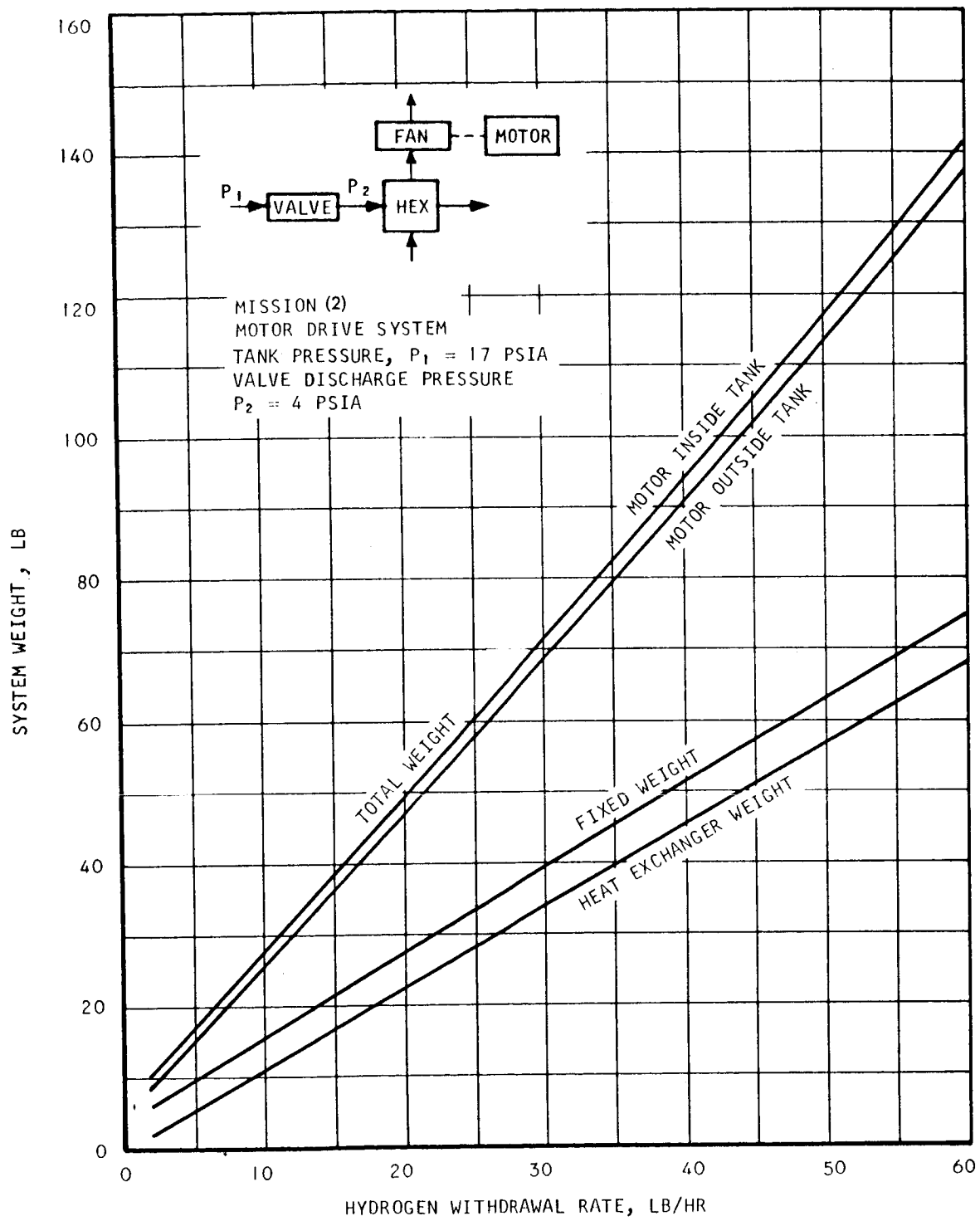

Fig. IV-13 Mission (2) System Weight, Motor Drive (P_2 = 4 psia)

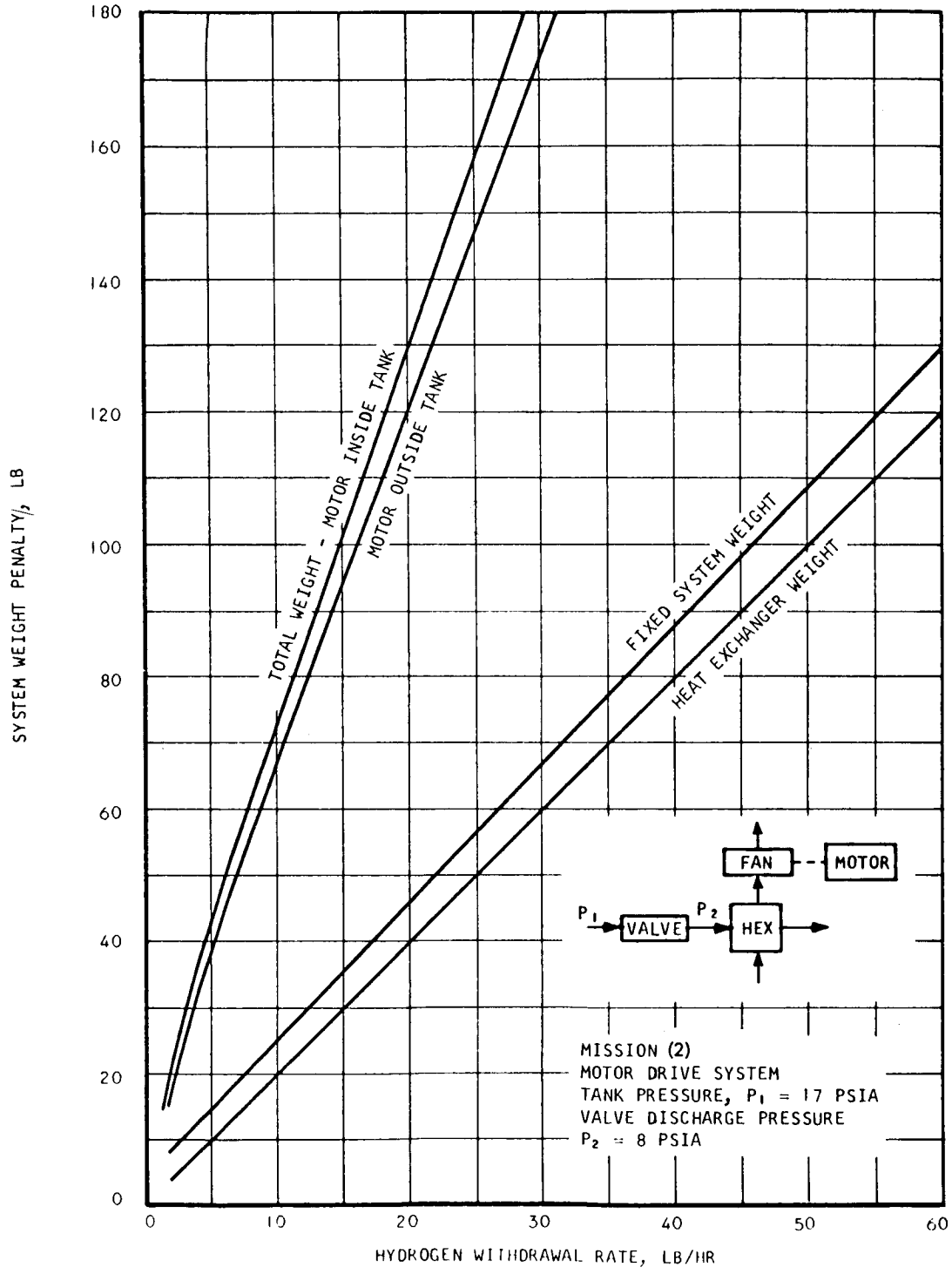

Fig. IV-14 Mission (2) System Weight, Motor Drive (P_2 = 8 psia)

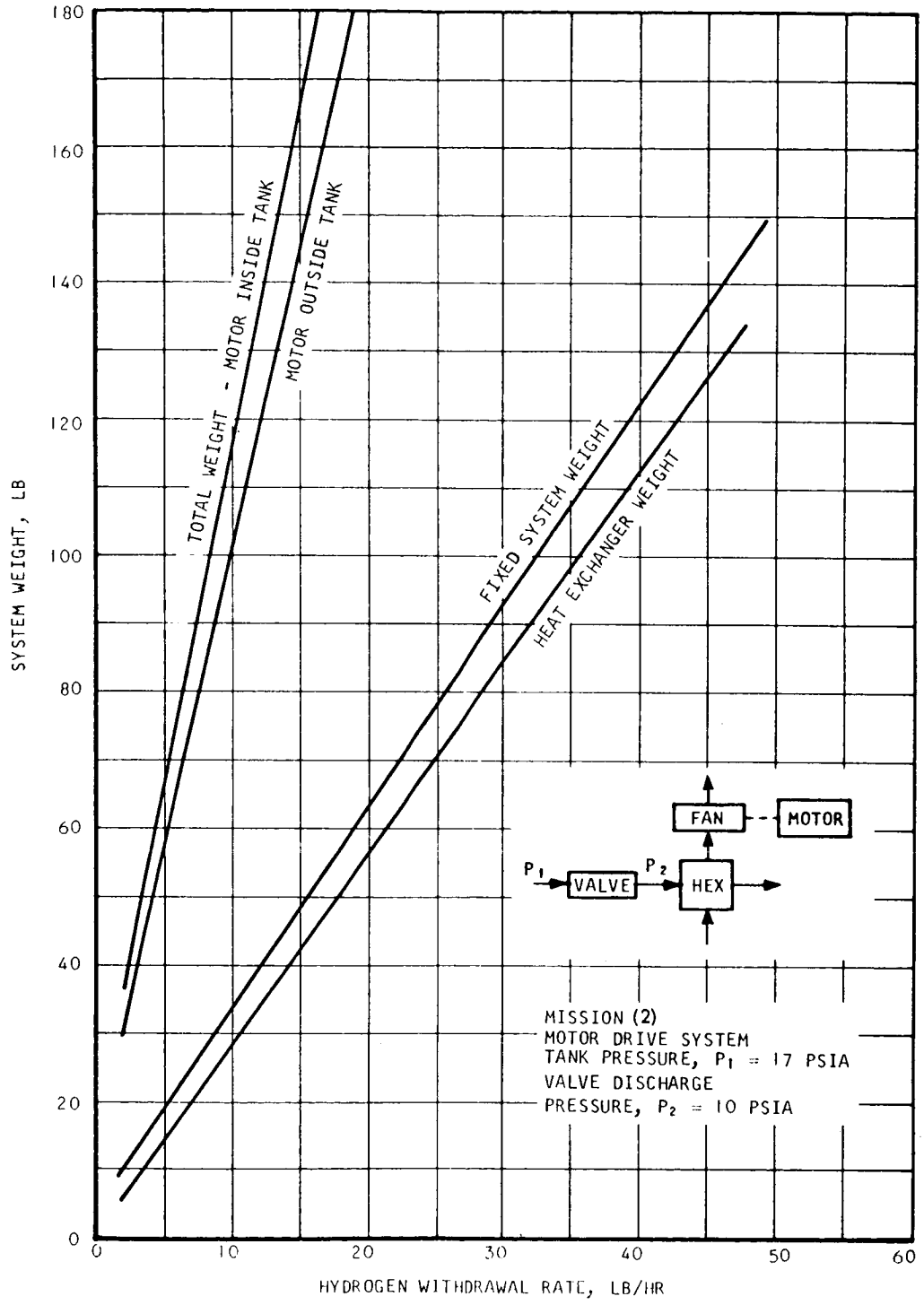

Fig. IV-15 Mission (2) System Weight, Motor Drive (P_2 = 10 psia)

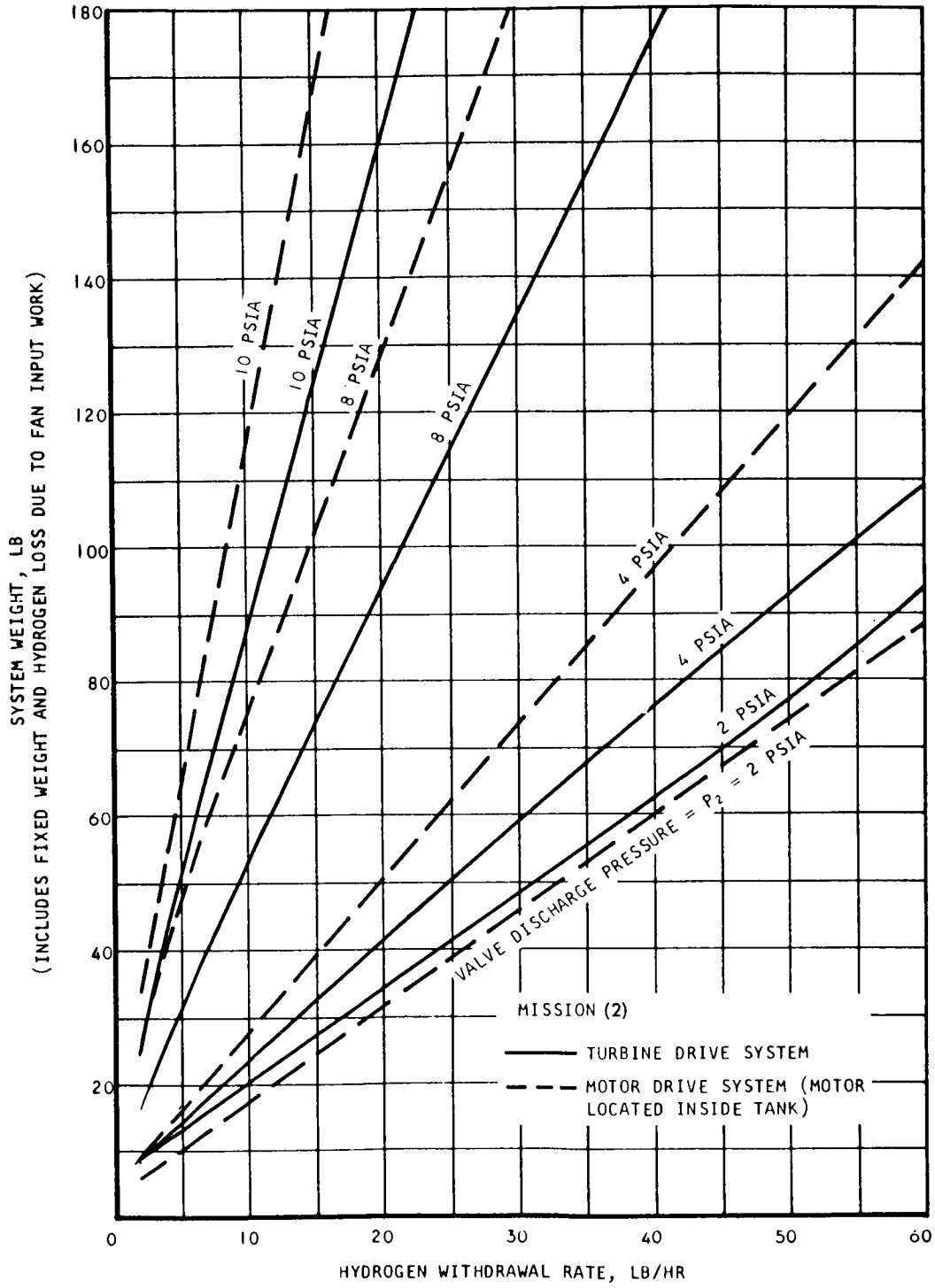

Fig. IV-16 Mission (2) Weight Comparison of Turbine- and Motor-Driven Systems

b. A speed match can easily be made between the fan and the drive unit.

c. The starting transient can be made less severe by designing for a very high starting torque or by operating the fan before the expansion valve is opened.

d. The cost of the system may be lower and the development requirements are less severe.

e. Exhaust duct pressure can be higher which reduces the tendency of solid hydrogen buildup in the exhaust duct.

A comparison was made of ac and dc motors. A preliminary analysis was also conducted to determine startup characteristics of the drive system. This work, discussed below, indicates that the drive unit should be a brushless dc motor.

Several characteristics of brushless dc motors make them a better choice than ac induction motors even though brushless dc motors have not been built to operate at cryogenic temperatures. The design of a brushless dc motor for liquid hydrogen operation will involve experience gained with cryogenic ac motors (bearing design, etc.) and experience with brushless dc motors designed for operation at ambient temperatures. The advantages of brushless dc motors over ac induction motors are:

a. Higher efficiency and, thus, lower heat input to the tank fluid

b. Less power draw from the electrical power system

c. High starting torque to reduce the startup transient

d. Ease of limiting power consumption during startup and operation

The first two advantages for a motor with a 5-w output power rating (this corresponds roughly to a liquid withdrawal rate of 5 lb/hr with a valve discharge pressure of 4 psia) will be considered. For Mission (2) the hydrogen loss due to the heat input from the motor is 9.9 lb for the brushless motor and 26.5 lb for the ac induction motor. With a fuel cell power source and an 80-percent efficient inverter (dc to ac), the electrical power weight is 1.7 lb for the brushless dc motor and 5.6 lb for the ac induction motor.

The starting speed torque characteristics of a typical ac motor are shown in Fig. IV-17. The starting torque is generally within 30 percent of the operating torque. Slight improvements can be made in starting torque by changing the design, but this reduces the efficiency at the normal operating point. For a brushless dc motor, the starting torque increases at a constant rate as the speed decreases (Fig. IV-17). Starting torques of 10 to 100 times the operating torque are, thus, possible. The brushless dc motor will, therefore, arrive more quickly at operating speed; i.e., the hot-side fluid rate through the heat exchanger will reach the steady-state value more quickly. This will ensure that the heat exchanger is functioning soon after the expansion valve is opened and, thus, reduce the possibility that liquid hydrogen will be vented overboard.

With liquid on the hot side of the heat exchanger, the flow requirements are reduced, and the required overall power draw is less. However, the motor will tend to slow down and increase power draw. With the dc motor, the power draw can be controlled easily by electronic circuitry. In addition, if desired, the power draw during startup can be limited or designed so that it is the same as during steady-state operation.

An analysis was made to determine if a turbine-driven system would start up with little or no hydrogen liquid loss before steady-state operation was reached. It was found that, for the conditions considered, the turbine would not develop sufficient torque to overcome the breakaway friction of its own bearings. This condition is caused by (1) the relatively high ratio of breakaway bearing torque to turbine running torque encountered in small, very high-speed turbines, and (2) by the low volumetric rate through the turbine due to the high gas density obtained at cryogenic temperatures. Thus, a turbine-driven system is definitely not feasible for the vent rates under consideration.

The analysis of the startup characteristics was based on ideal conditions that would facilitate a fast startup. This was done to simplify the analysis and to determine quickly if startup was possible. If startup was not possible under the assumed ideal conditions, it surely would not be possible under the actual conditions encountered in an operating system. The ideal conditions assumed were: (1) the fluid entering the turbine nozzle was saturated hydrogen vapor; and (2) during expansion through the

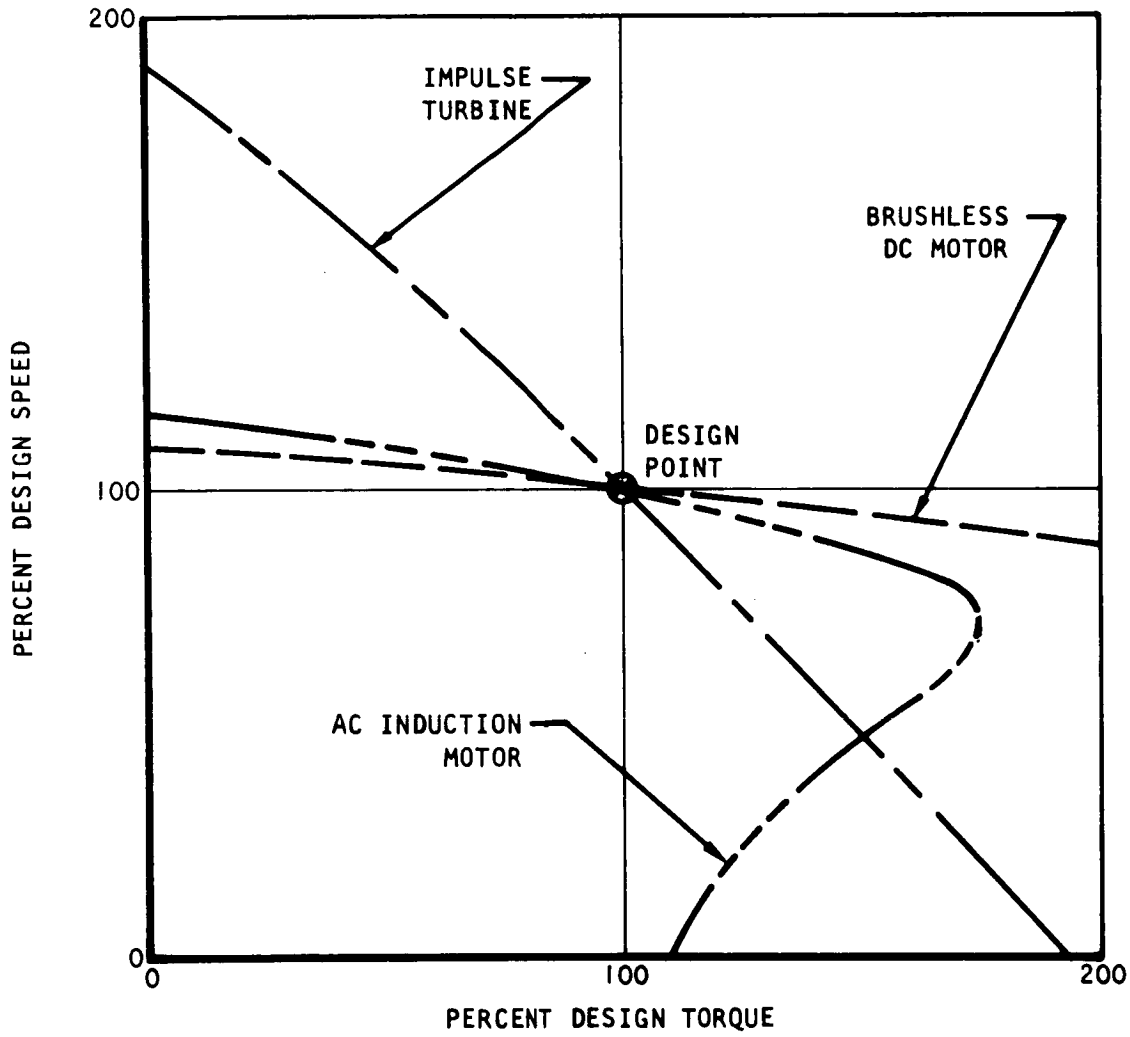

Fig. IV-17 Typical Speed Torque Characteristics for Drive Systems

nozzle, the gas was heated so that saturated hydrogen vapor entered the turbine blade. The flow rate considered was 5 lb/hr with an inlet pressure of 4 psia and an outlet pressure of 0.1 psia. The saturated vapor assumptions are very optimistic, since if liquid hydrogen is expanded from 17 psia to 4 psia, the quality is only 8 percent. The assumption, thus, yields much higher nozzle velocities than would actually be encountered. For the impulse turbine configuration, the enthalpy difference between inlet and outlet is converted into kinetic energy in the nozzle. The resultant nozzle exit velocity is approximately 1000 ft/sec.

The force acting on the turbine wheel is due to the change of momentum of the vapor in passing through the turbine blade row. Typical blade angles were used, 15 deg at the entrance and 19 deg at the exit. Since the blade is not moving initially, the vapor is forced to turn through 146 deg in passing by the blade. The change in momentum for the conditions considered results in a starting torque of 0.69 in.-oz. for a 1-in. wheel. The axial force (or thrust) is 0.000384 lb. Test data on gas bearings were evaluated to determine the probable starting or breakaway torque of a 1-in. turbine wheel supported by foil bearings. The starting torque was estimated to be, as a minimum, 1.5 in.-oz. Therefore, the torque exerted on the turbine wheel is less than 50 percent (under ideal conditions) of the torque required for starting the turbine alone. It should be noted that additional starting torque is required for the fan and for the electromagnetic gear train. Thus, the turbine will not start without an external source of power and should not be considered as the drive system for the fan.

Section V

SYSTEMS OPTIMIZATION

The results obtained thus far indicate that the thermal conditioning system design should reflect the following:

a. A compact heat exchanger unit with a brushless dc motor-driven fan is the preferred selection.

b. Since system should be capable of efficiently accepting either liquid or gas from the propellant tank, the fluid-removal unit is a single filter screen over the intake port of the expansion valve.

Before a system can be synthesized for the three reference missions, additional information is required on flow and pressure control, on the effect of the heat exchanger warm-side flow rate, and on the operation of the fan and motor. The analysis of these items and the development of the recommended propellant thermal conditioning system are discussed next.

FLOW AND PRESSURE CONTROL

It is necessary to control both flow rate and pressure in the cold side of the heat exchanger so that heat loads and available temperature difference are known. The flow rates required for the three reference missions are very low, less than 1 lb/hr on a continuous basis. An expansion valve discharge pressure of 4 psia is optimum. It is sufficiently above the triple point (1 psia) to prevent solid hydrogen from forming in the heat exchanger core and, in addition, yields a low system weight (Fig. IV-9). It also provides sufficient pressure for actuation of the expansion valve by the bellows and allows a choked orifice to be placed downstream from the heat exchanger for flow control.

A shutoff valve downstream from the heat exchanger is required to prevent an expansion below the triple point. (This would occur if the exhaust line from the heat exchanger were ducted directly to space.) The valve can also be a flow-limiting device that will improve system operation. The fluid state downstream from the heat exchanger will always be vapor, whether gas or liquid enters the expansion valve. Pressure at the flow-limiting orifice will be maintained at a constant value of approximately 4 psia. For all conditions, the vapor will be within a few degrees of tank temperature. Thus, the orifice will ensure that the flow through the system will be essentially constant, whether gas or liquid enters the system. This allows the heat exchanger cold-side flow rate to be closely matched to system requirements. If there were no flow-limiting device downstream from the heat exchanger, there would be large variations in rate; this would result in a larger heat exchanger requirement. Figure V-1 shows various possible pressure and flow control methods which use an orifice in the valve downstream of the heat exchanger to control the flow rate.

The preferred method of pressure and flow control is shown in Fig. V-1A. The system is actuated by a pressure switch located outside of the propellant tank. When the tank pressure exceeds the design value, the switch causes the solenoid shutoff valve to open and simultaneously turns on the electric motor. As the pressure in the heat exchanger decreases below 4 psia, the regulator opens and maintains downstream pressure. The solenoid contains a calibrated choked orifice, which limits flow to the design value. When the tank pressure drops to the lower limit of the pressure switch control band, the solenoid closes, the motor is turned off, and the pressure regulator closes.

The flow-limiting orifice diameter will be approximately 0.065 in. A filter downstream from the heat exchanger will prevent particles from plugging the orifice; a built-in filter on the regulator will prevent possible particulate contamination from the propellant tank.

Figure V-1B shows another approach in which the dual-function valve (shown in Fig. I-11) opens when the tank pressure exceeds the design value and, in addition, regulates downstream pressure. An electrical switch actuated by the valve stem is

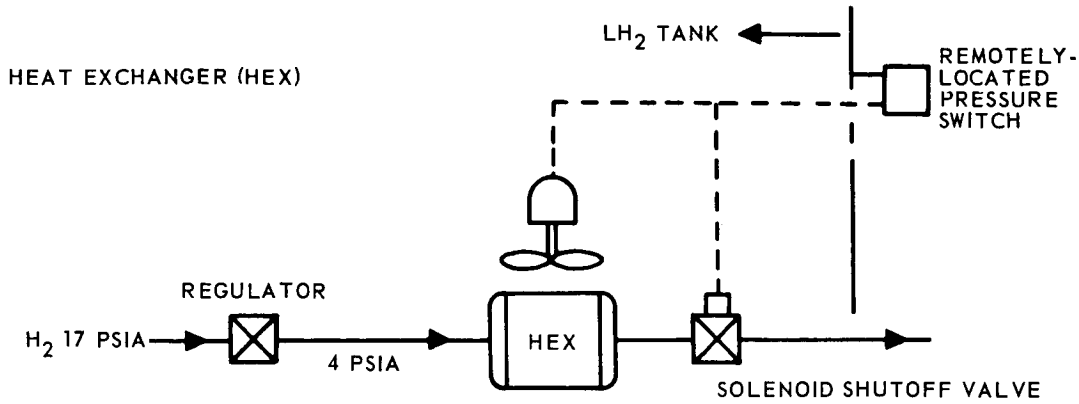

A.

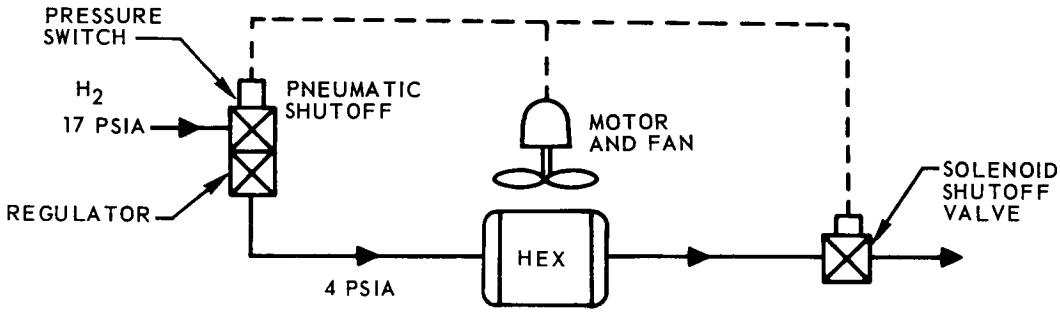

B.

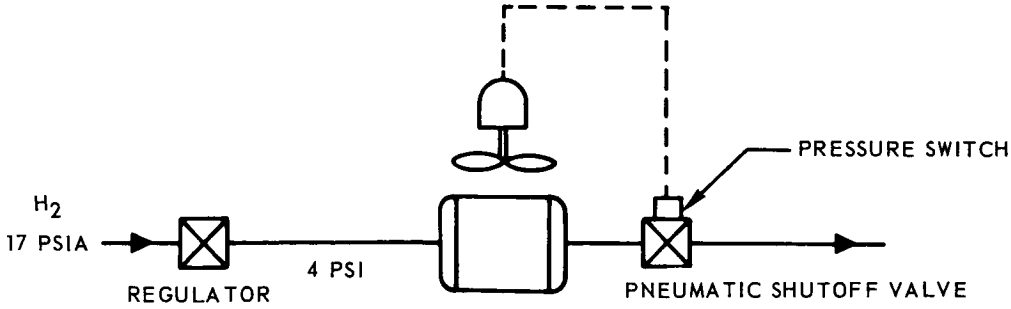

Fig. V-1 Pressure and Flow Control Methods

mounted on top of the shutoff portion. Thus, when the pneumatic shutoff valve opens, the motor starts and the downstream solenoid valve also opens. This approach is not recommended because two valves are used for essentially the same function; therefore, the reliability of the cryogenic electrical switch is questionable.

A third method of controlling flow and pressure is illustrated in Fig. V-1C. A pneumatic valve, rather than a solenoid, is used as the shutoff valve and flow limiter. The shutoff valve downstream from the heat exchanger is the upper portion of the dual-function valve shown in Fig. V-1B. A switch on top of the valve is actuated by the valve stem. This system is undesirable because the reliability of the switch is questionable. In addition, the system cannot be shut off when the tank is pressurized during engine firing or during the initial launch phase. A solenoid shutoff valve allows more flexibility in system operation.

The systems described above have a flow-limiting orifice/shutoff valve located downstream from the heat exchanger. This device was necessary, as previously noted, to prevent an expansion below the triple point in the heat exchanger. With this system, fluid will be trapped between the 4-psia regulator and the shutoff valve when the tank pressure drops below the design point of the pressure switch and the solenoid valve closes. The trapped fluid will receive heat from the tank contents and, finally, will reach bulk fluid temperature. If the fluid in the system is gaseous hydrogen when the valve closes, the pressure will increase to 5 psia. If the fluid is a mixture of liquid and gaseous hydrogen, the pressure will increase to 17 psia during standby. If the trapped fluid is a mixture of helium and liquid hydrogen, the pressure will rise to about 28 psia during standby. In all cases, the pressure in the heat exchanger will be greater than 4 psia when the motor and solenoid valve are reactivated. This results in a desirable built-in time delay, since the motor and fan will force fluid through the heat exchanger before the regulator valve is opened. It should be noted that the amount of fluid between the regulator and solenoid valve is very small even if liquid hydrogen is passing through the system when the valve closes. The volume of the system for the three reference mission is less than 0.1 cu ft; there is less than 0.03 lb of hydrogen in the system. A pressure relief valve can be built into the regulator valve body to reduce the pressure in the heat exchanger when the pressure differential between the exchanger and the tank reaches a given level.

HEAT EXCHANGER AND FAN ANALYSIS

The analyses show that, for a minimum weight system, the cold-side rate and the expansion valve discharge pressure should be as low as possible. A further analysis was performed to determine heat exchanger/fan characteristics for a nominal liquid hydrogen flow rate of 5 lb/hr and a valve discharge pressure of 4 psia.

The first heat exchanger design was based on the assumption of a counter-flow configuration with a warm-side temperature effectiveness of 0.90. Fluid flow over the warm side of the heat exchanger can be liquid hydrogen, gaseous hydrogen, gaseous helium, or a mixture of all three fluids. The worst design condition is gaseous helium on the warm side. This condition was chosen in order to give a conservative design. With a temperature effectiveness of 0.9, with no superheat on the heat exchanger cold side, and with a liquid hydrogen flow rate of 5 lb/hr, the required helium (warm-side) flow rate is approximately 100 lb/hr. Two different heat exchanger face areas were used to determine the effect of this variable. The face areas used were 3.0 by 3.0 in. and 6.0 by 6.0 in. The heat transfer rate for all heat exchangers was 870 Btu/hr. Table V-1 summarizes the important data for these units.

The lower core volume of the 3.0- by 3.0-in. face unit is achieved at the expense of increased pressure drop and pumping power. These heat exchangers are fairly large for the relatively low heat transfer rate of 870 Btu/hr because of the high temperature effectiveness (0.9) used for the warm side. With high effectiveness, the log mean temperature difference will be lower; and a larger exchanger is required for a given heat transfer rate. If a higher warm-side flow rate is used, the effectiveness will be lower, the heat transfer coefficient will be higher, and the required heat transfer will be smaller.

The warm-side flow rate was doubled to determine the influence of effectiveness on heat exchanger size. The valve inlet and outlet pressures were held constant at 17 psia and 4 psia, respectively. Also, the cold-side liquid hydrogen flow rate was held constant at 5.0 lb/hr. These conditions resulted in a warm-side temperature

Table V-1

HEAT EXCHANGER DESIGN AND PERFORMANCE DATA

	3- by 3-in. Face	6- by 6-in. Face	3- by 3-in. Face
Heat transfer rate (Btu/hr)	870	870	870
Warm-side flow rate (lb/hr)	100 (GHe)	100 (GHe)	200 (GHe)
Cold-side flow rate (lb/hr)	5.0 (LH_2)	5.0 (LH_2)	5.0 (LH_2)
Warm-side effectiveness	0.90	0.90	0.45
Length (in.)	16.0	7.48	7.86
Volume (cu in.)	144	270	70.7
Weight (lb)	13	23	9.5
Core pressure drop (in. H_2O*)	0.135	0.0220	0.217
Manifold pressure drop (in. H_2O*)	0.086	0.0054	0.337
Total pressure drop (in. H_2O*)	0.221	0.0274	0.554

*Warm side only, cold-side pressure drop is negligible.

LOCKHEED MISSILES & SPACE COMPANY

effectiveness of 0.45. The new heat exchanger design and performance data are shown in Table V-1, which reveals that a further reduction in weight was achieved and that the pressure drop was not excessive.

The selection of a particular configuration must take into account motor-fan characteristics and mixing requirements; therefore, the steady-state performance of the fan-motor unit operating in liquid hydrogen was analyzed. The fan-motor will be designed for operation in gaseous helium since this represents the worst condition from the standpoint of heat exchanger design. However, it is possible that during fan-motor operation, liquid hydrogen will enter the warm side of the system. This will present no heat transfer problem if the fan-motor can pump sufficient liquid hydrogen through the heat exchanger. The heat transfer coefficient will be higher than with gaseous helium; the hydrogen will be subcooled and will cause some gaseous hydrogen to condense at the liquid-gas interface, which will lower tank pressure.

The liquid hydrogen flow condition will determine the motor size needed. Brushless dc motors have fairly flat speed-torque characteristics (Fig. IV-17); therefore, the volumetric flow rate will not decrease to a great extent. Because of the large mass flow rate, the power requirement will be much greater for the liquid flow case than for the gaseous helium case. Thus, the motor selected will probable operate at a relatively low efficiency when gaseous helium (or a helium/hydrogen mixture) is flowing through the system.

To estimate the performance differences of the fan-motor unit under both liquid and gas flow conditions, data for an actual brushless dc motor were used. Fan performance was estimated under different flow conditions. The motor characteristics used in the analysis are shown in Fig. III-16. The warm-side flow rate was taken as 100 lb/hr of gaseous helium at the heat exchanger design point. The heat exchanger used in the analysis was the 6- by 6-in.-face-dimension unit discussed in the previous section. It was assumed that a duct exit velocity of 25 ft/sec was required for mixing. The performance data for the fan-motor unit are given in Table V-2.

Table V-2

FAN-MOTOR PERFORMANCE

Characteristic	Warm-Side Fluid	
	Gaseous Helium	Liquid Hydrogen
Flow rate (lb/hr)	100	2300
Fan-motor speed (rpm)	5700	5000
Fan-motor input head (ft-lb/lbm)	12.2	8.03
Fan-motor pressure rise (in. H_2O)	0.50	6.80
Fan efficiency	0.80	0.73
Motor efficiency	0.24	0.77
Motor input power (w)	2.40	12.2

The characteristics of the brushless dc motor ensure that it will not stall in liquid hydrogen and that high flow rates will be obtained. These flow rates are more than sufficient to prevent capillary binding within the heat exchanger, the ratio of dynamic to capillary forces being 8 to 1. For the 6- by 6-in.-face-area heat exchanger, the major pressure head is associated with accelerating the fluid to 25 ft/sec. Mixing analyses presented earlier indicate that much lower velocities are required. Thus, it is possible to reduce motor input requirements much below those in Table V-2, which are given for comparative purposes only.

The cold-side design flow rate of the thermal conditioning system must be sufficient to maintain tank pressure under the condition of maximum heat leak. The flow rate on the hot side of the heat exchanger can be dictated by heat transfer requirements or by the tank circulation requirements.

The basic cold-side rate shown in Table V-3 is based on the maximum heat leak to the propellant tank with saturated fluid out of the heat exchanger. The design cold-side flow rate was obtained by adding a 10-percent margin for heat input from the fan and motor and another 20 percent to account for sizing of the flow-limiting orifice. The helium rate was based on a warm-side effectiveness of 0.45, which yields a small

Table V-5

REFERENCE MISSION FLOW RATES

Mission No.	Cold-Side Rate (lb/hr)		Warm-Side Rate (lb/hr)		Mixer Jet Velocity (ft/sec)	Mixer Jet Diameter (in.)
	Basic (Continuous) Value	Design Value	Helium	Liquid Hydrogen		
1	1.06	1.4	57.4	1320	5.0	1.75
2	0.0971	0.13	5.25	121	0.5	1.75
3	0.226	0.3	12.2	280	1.1	1.75

LOCKHEED MISSILES & SPACE COMPANY

heat exchanger without prohibitive power and heat leak penalties. The warm-side rate with liquid hydrogen is based on a brushless dc motor fan drive which slows down only slightly when liquid hydrogen passes through the system.

The flow rates shown in Table V-3 were used to synthesize systems for three reference missions. These systems would be operating for approximately 45 to 67 percent of the mission. A schematic of the system is shown in Fig. V-1A. Table V-4 shows the characteristics of the systems developed, based on a vent flow rate approximately 30 percent greater than the maximum flow rate. All components, except the heat exchanger and fan/motor, are the smallest practicable size. The table reveals that the fixed weight of the system is not greatly reduced for the low-flow requirements of Mission (2).

The power requirements shown in Table V-4 are based upon the use of a brushless dc motor. However, the variation in power requirements among the three missions is much less than the variation in warm-side flow rate. Also, for the flow rates being considered, a comparison of the power requirements for helium and liquid on the warm side reveals that the power is only moderately affected by fluid density. This is due to two factors: (1) In decreasing the flow from the Mission (1) to the Mission (2) requirements, the fan efficiency will be reduced by about 50 percent owing to the lower specific speed and smaller size of the unit; and (2) as the motor output requirements are reduced below 1 w, the motor efficiency drops rapidly because of the nearly fixed losses associated with bearings and windage (Fig. I-54). With liquid hydrogen, the motor efficiency was estimated at 62 percent for Mission (1) and at 40 percent for Mission (2). With the lower fan power requirements with helium flow, motor efficiency was only 10 percent for Mission (1) and 3 percent for Mission (2). Since the overall efficiency of the fan-motor combination is the product of the individual efficiencies, the overall power requirements are not greatly reduced by reduced flow or fluid density over the power range of interest. The result is that more electrical energy per unit mass of vented flow is required for Missions (2) and (3) than for Mission (1).

Table V-4

SYSTEM CHARACTERISTICS (FLOW-MATCHED SYSTEMS)

	Reference Missions		
	1	2	3
Cold-Side Flow Rate (lb/hr)	1.4	0.13	0.3
Warm-Side Flow Rate (lb/hr)			
Helium	57.4	5.25	12.2
Liquid Hydrogen	1320	121	280
System Weight (lb)			
Pressure Regulator	1.0	1.0	1.0
Heat Exchanger	7.0	2.0	3.0
Motor and Fan	1.5	1.0	1.0
Solenoid Shutoff Valve	1.5	1.5	1.5
Pressure Switch	1.0	1.0	1.0
Filter, Tubing, and Support Structure	3.0	2.5	2.5
	15.0	9.0	10.0
Motor Power Requirements (w)			
Helium	0.9	0.6	0.6
Liquid Hydrogen	2.3	0.7	1.4
Heat Exchanger Size (in.)	3x3x7	0.9x0.9x7	1.4x.4x7

The overall system weight can be found by adding the fixed weight (Table V-4) and the weights associated with supplying the electrical power and the additional heat of the motor and fan. Table V-5 shows the total weight of the system when helium or liquid hydrogen passes through the warm side of the heat exchanger. The electrical power weight for a battery is based on a weight factor of 40 w-hr/lb. For the fuel cell, the electrical power penalty is given by $Wp = 0.00135\ WT + 0.15w$.

For Missions (2) and (3) (220-day duration), the electrical and heat input weights are much greater than the fixed weight for the flow-matched system. This is due to the low motor and fan efficiencies obtained at the low rates associated with these missions. The Mission (1) design flow rate can be used for Missions (2) and (3). This would reduce the overall time that the system was operating, resulting in a significant saving in the overall system weight. This effect is shown in Figs. V-2 and V-3 showing the total effective weight for the three missions. It can be seen that the weight for all systems is nearly optimum at the same vent rate whether the electrical power is supplied by battery or fuel cell. This optimum vent rate corresponds to the Mission (1) flow-matched system, which is a value of 1.4 lb/hr.

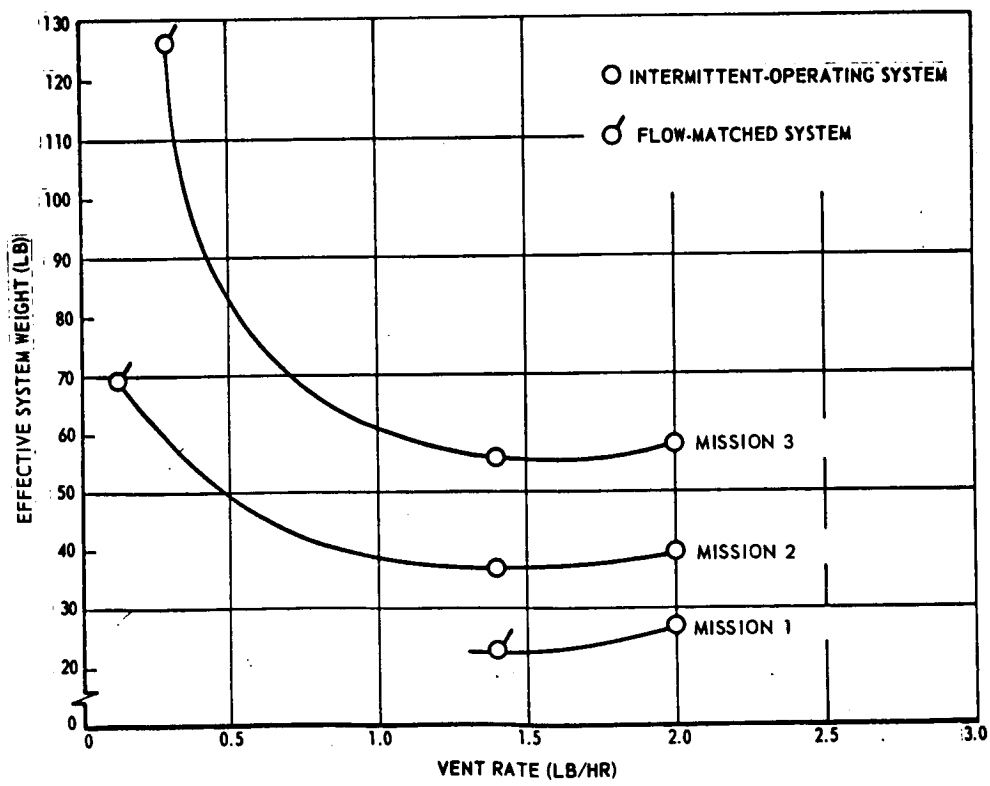

Fig. V-2 Optimum Thermal Conditioning System Vent Flow Rate for Three Missions (Battery Power Source)

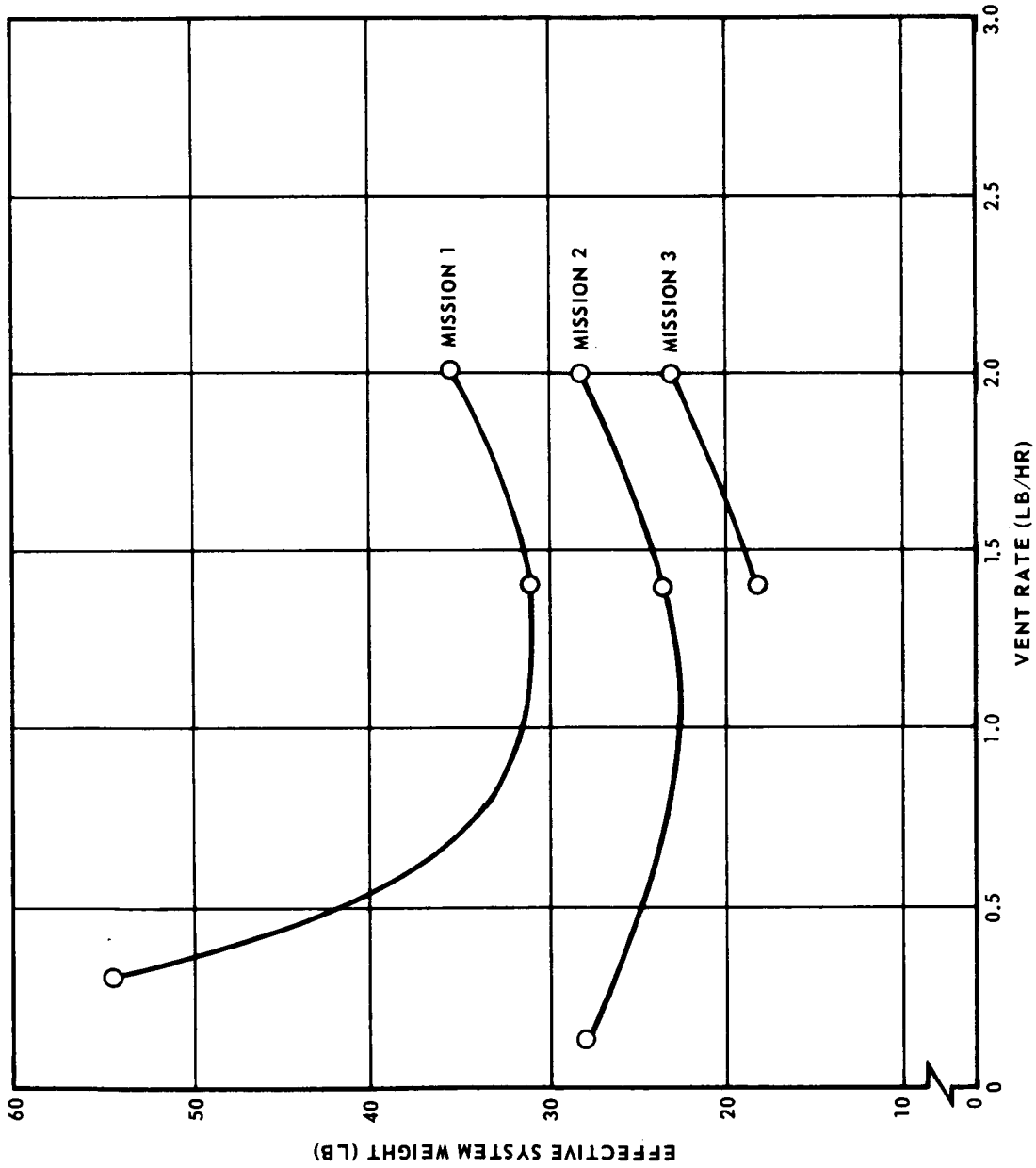

Fig. V-3 Optimum Thermal Conditioning System Vent Flow Rate for Three Missions (Fuel Cell Power Supply)

Table V-5

SYSTEM CHARACTERISTICS (COMPARISON OF FLOW-MATCHED AND MINIMUM-EFFECTIVE-WEIGHT SYSTEMS)

Reference Mission	Flow-Matched Systems						Minimum-Effective-Weight System			
	Mission 1		Mission 2		Mission 3		Mission 2		Mission 3	
Cold-Side Flow Rate (lb/hr)	1.4		0.13		0.3		1.4		1.4	
System Running Time (hr)	89		2940		2400		252		484	
Jet Velocity (ft/sec)	5.0		0.5		1.1		5.0		5.0	
	Helium	LH_2	Helium	LH_2	Helium	LH_2	Helium	LH_2	Helium	LH_2
Warm-Side Flow Rate (lb/hr)	57.4	1320	5.25	121	12.2	280	57.4	1320	57.4	1320
Motor Power Requirements (w)	0.9	2.3	0.6	0.7	0.6	1.4	0.9	2.3	0.9	2.3
System Weight (lb)		z								
Fixed Weight	15.0	15.0	9.0	9.0	10.0	10.0	15.0	15.0	15.0	15.0
Electrical Power System Weight*	2.0	4.9 (0.6)	38.0	44.5 (2.9)	31.1	76.5 (4.8)	5.8	14.1 (1.1)	10.9	27.0 (1.8)
Heat Input Boiloff	0.3	2.5	1.3	15.9	3.0	39.7	0.9	7.3	1.7	14.0
TOTAL	17.3	22.4 (18.1)	48.3	69.4 (27.8)	44.1	126.2 (54.5)	21.7	36.4 (23.4)	27.6	56.0 (30.8)
Weight Saving (lb)								33.0 (4.4)		70.2 (23.7)

* Values in parentheses are based upon the use of a fuel cell; all others are based upon the use of a battery.

Section VI

SELECTED SYSTEM DESIGN AND PERFORMANCE

SYSTEM PERFORMANCE

The design of the hardware package of the selected system for all three reference missions (1.4 lb/hr flow) is shown in Fig. VI-1. The weight of the unit is estimated at 15 lb. The overall envelope dimensions are 11 x 11 x 13-in. The unit can conveniently be attached to the cover plate at the top of the propellant tank as shown in Fig. VI-1.

The regulator, which controls the pressure to 4 psia, is shown schematically in Fig. VI-2. The regulator contains a large integral filter to protect the poppet and seat from particulate contamination. The flow through the valve is modulated by the bellows which is exposed to regulated downstream pressure. The valve is designed to close if a failure occurs (reliability considerations of the system are discussed later in this section).

The heat exchanger is a counterflow plate fin unit (Fig. I-23) with a 3 x 3-in. core frontal area and a 7-in. length. The unit is stainless steel with 20 rectangular fins per inch. The cold-side fins are 0.05-in. high and are offset with an uninterrupted length of 0.1-in. The warm-side fins are 0.075-in. high.

The solenoid valve unit (Fig. VI-3) consists of a solenoid valve with a current limiting assembly located outside the propellant tank. The current limiter is a semiconductor device which permits a high current to pass for 300 to 500 ms to allow the solenoid to pull in. The current then drops to a low value (about 30 ma) to hold the solenoid valve in the open position. With this approach, no coil compensation is necessary to limit current flow. The resultant holding power requirement is maintained below 1 w.

The pressure switch is shown schematically in Fig. VI-4. This switch is mounted outside the tank to improve reliability and to facilitate checkout and replacement. The unit consists of a normally open, hermetically sealed, electrical switch element in contact with a force-transmitting member. The aneroid contracts as the pressure increases; the actuator moves and causes the switch contact to close; and the solenoid and the motor are activated.

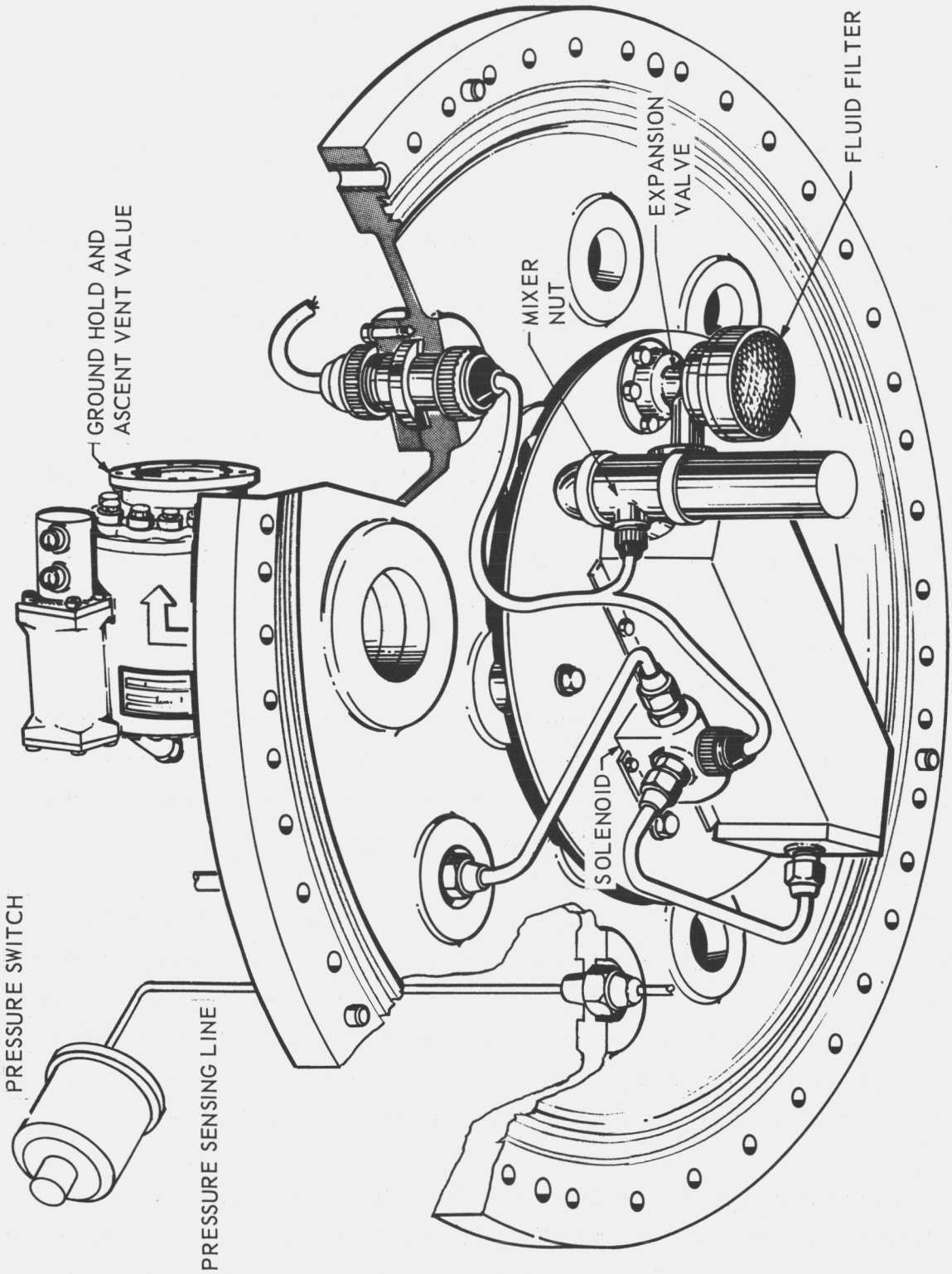

Fig. VI-1 Thermal Conditioning System

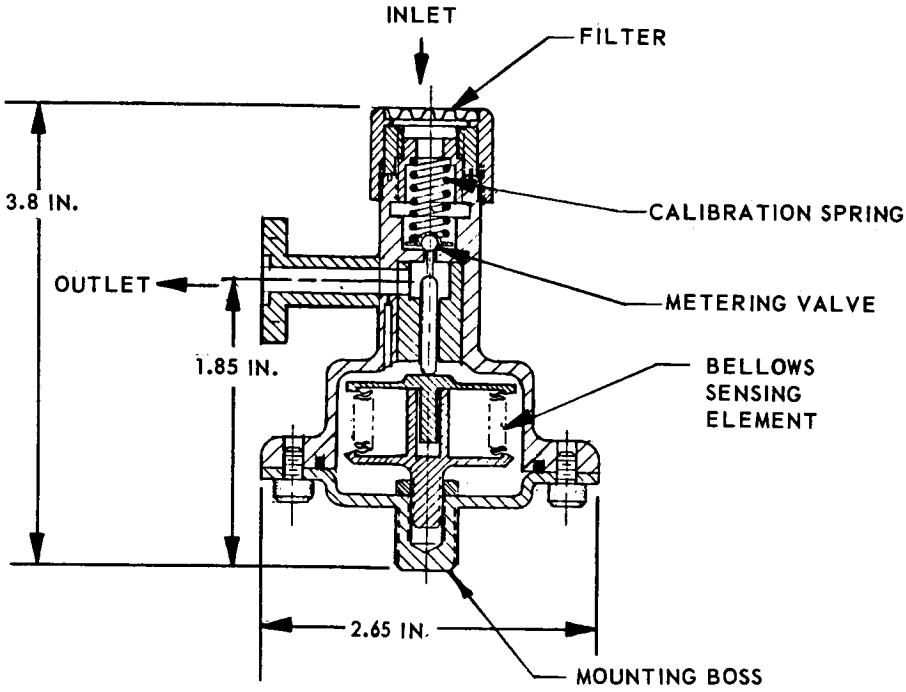

Fig. VI-2 Absolute Pressure Regulating Valve

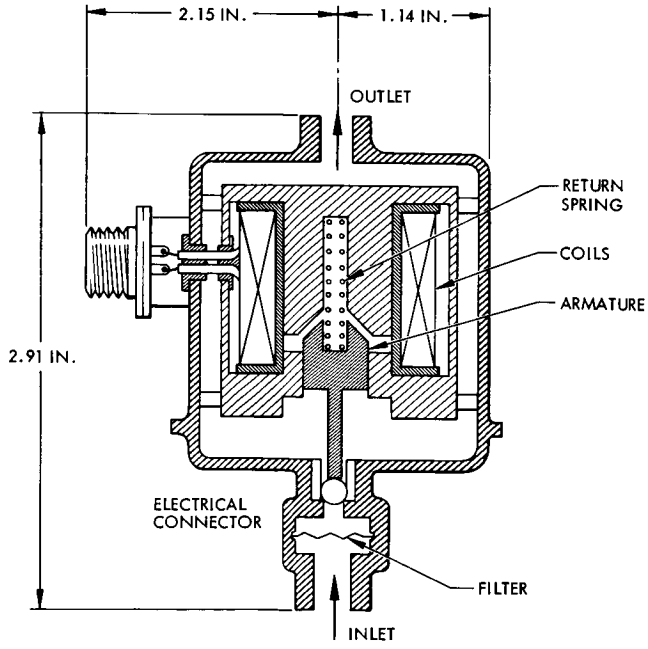

Fig. VI-3 Solenoid Shutoff Valve

The brushless dc motor and fan are shown in Fig. VI-5. The axial flow fan is connected directly to the motor which uses an ironless stator to eliminate iron losses. The permanent magnet rotor provides a strong excitation in a compact size with consequent reduction in windage losses. The rotor position controls the commutation through a small permanent magnet on the rotor with inductive pickups. The actual electronic switching device is located outside the tank.

All of the components described above have been used in liquid hydrogen systems except for the brushless dc motor. The design of a brushless dc motor for liquid hydrogen operation will be based upon experience gained with cryogenic ac motors (bearing design, etc.) and experience with brushless dc motors designed for operation at ambient temperatures.

The heat loads during the prelaunch and ascent environments are typically 100 to 300 times those in the space environment. The thermal conditioning system referred to in the preceding paragraphs is not designed for these high loads. To do so would result in a much larger and heavier system that is oversized for the space flight. This is avoided by direct venting of the ullage through the ground vent and pressure relief valve (Fig. VI-1) during the high heat load periods, at which time the propellant is bottomed in the tank.

PERFORMANCE OF THE SELECTED SYSTEM

A single system design is recommended for use in all three reference missions. The recommended system has a design vent rate of 1.4 lb/hr. The system characteristics are shown in Table V-5. The design point of the heat exchanger is that with helium gas on the hot side and with liquid hydrogen entering the expansion valve. This condition requires the largest heat transfer rate with the lowest overall heat transfer coefficient. The performance of the system for these conditions is shown in Fig. VI-6. The amount of heat removed, i.e., enthalpy change of the vented fluid, is 176 Btu/lb. The temperature profile in the heat exchanger and the heat transfer coefficients are shown in Fig. VI-7. The sharp change in the temperature profile is due to the change in the mode of the flow from annular to mist (see Figs. I-19,20). The area required for heat transfer is much larger in the mist regime; this is due to the low mass flux on the cold side of the heat exchanger.

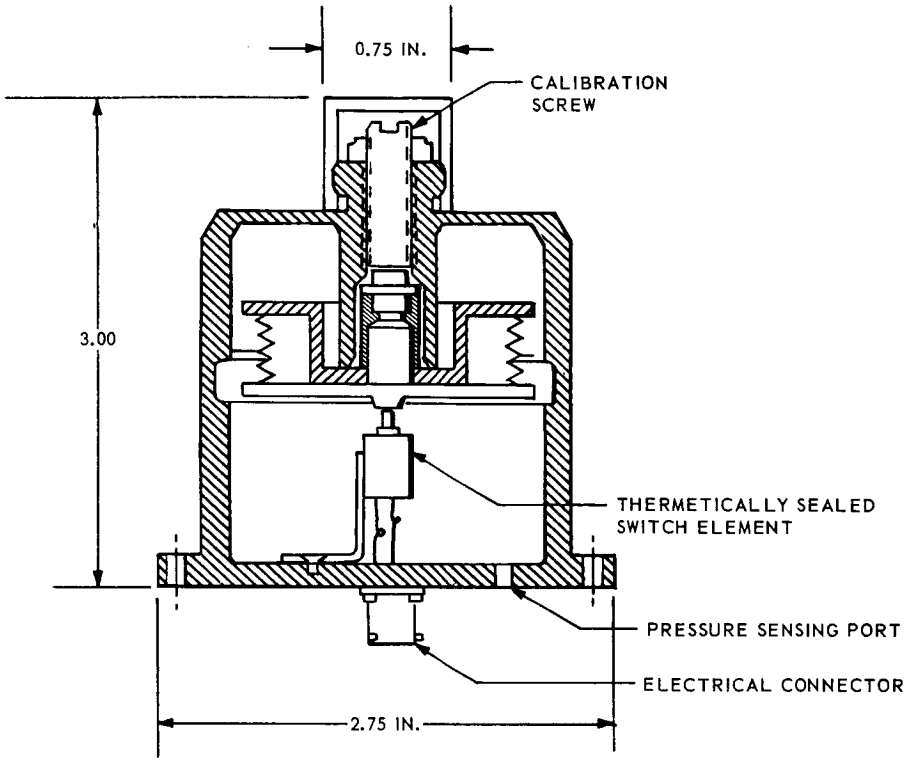

Fig. VI-4 Pressure Switch

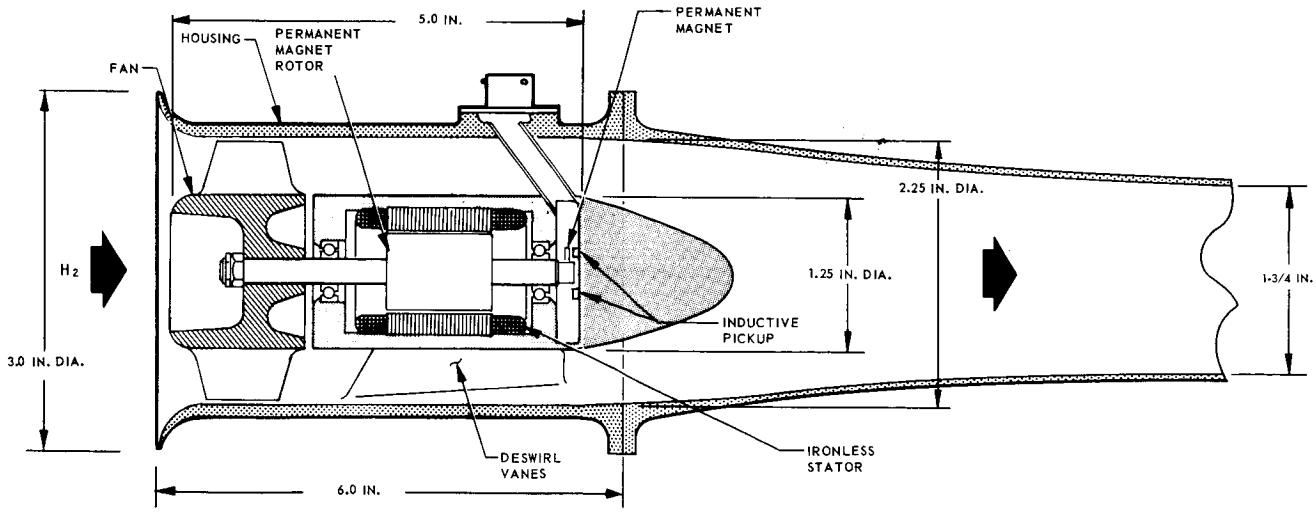

Fig. VI-5 Fan and Motor

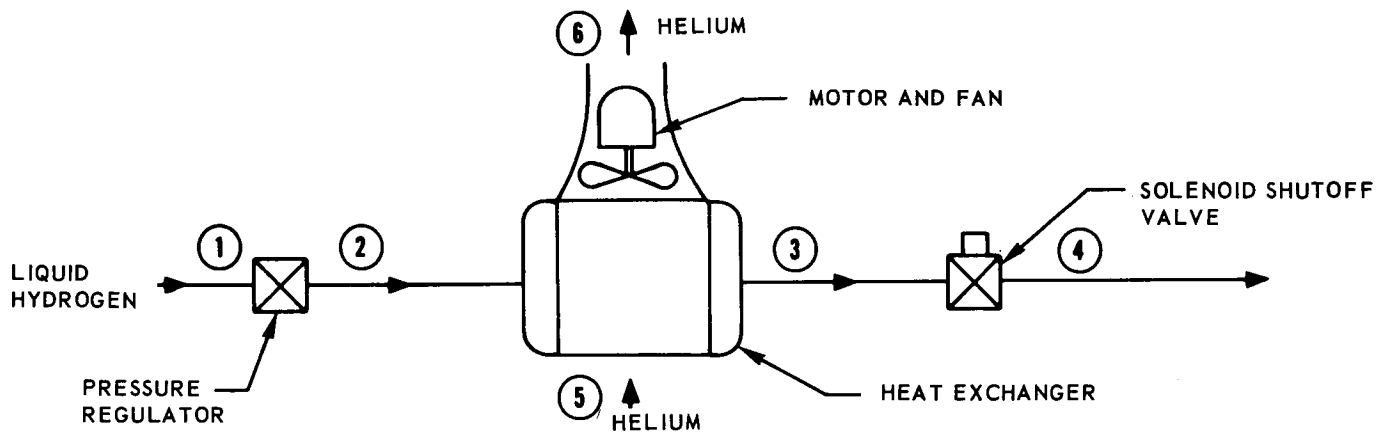

CHARACTERISTIC	LOCATION OF MEASUREMENT					
	1	2	3	4	5	6
FLOW RATE (LB/HR)	1.4	1.4	1.4	1.4	57.4	57.4
PRESSURE (PSIA)	17	4	4	2	17	17
TEMPERATURE (°R)	37.4	29.6	29.6	30.0	37.4	34.1
QUALITY (LB VAPOR/LB FLUID)	0	0.08	1.00	1.00	1.00	1.00

Fig. VI-6 System Performance

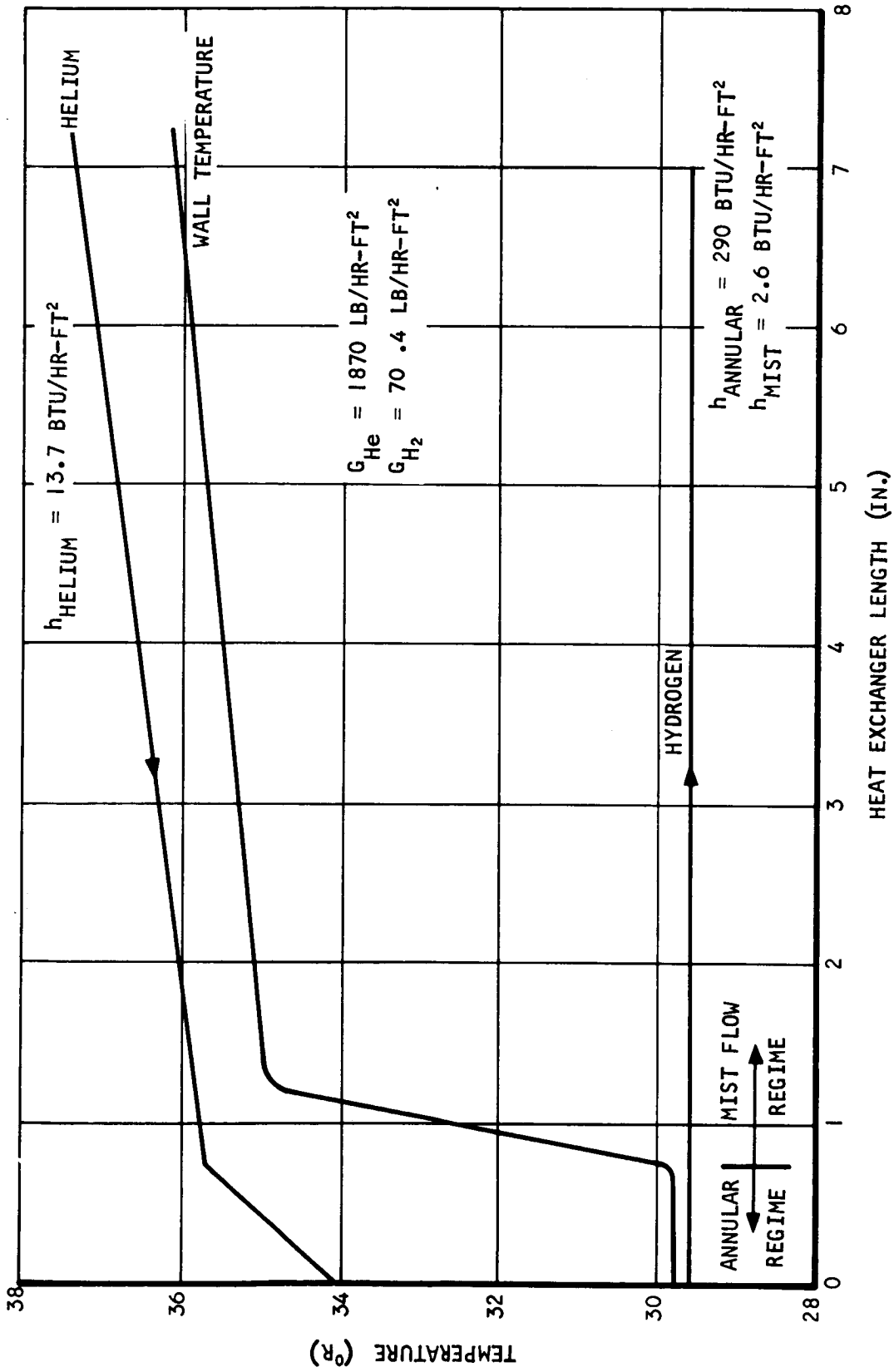

Fig. VI-7 Heat Exchanger Characteristics

The present design has no superheat in the exchanger and has helium flow on the warm side. An additional 21 Btu/lb (maximum) of heat removal is possible if the cold fluid is heated to tank bulk fluid temperature. The present design should provide some superheat even with helium as the hot-side fluid since the design is conservative. For all other conditions of hot- and cold-side flow, some superheat will be obtained. With high quality fluid entering the heat exchanger, the cold-side exit temperature will be very close to bulk temperature. The vent stream from the thermal conditioning system can still absorb a significant amount of heat and could be used to intercept heat from the space environment. The heat capacity of the vent stream is quite large, 1225 Btu/lb if warmed to 400°R.

The mixer duct exit diameter is 1.75 in. with a jet exit velocity of 5 ft/sec with either gas or liquid. This velocity is ten times higher than theoretically required to provide jet continuity and mixing across the full span or diameter of the Mission (2) tank with a liquid hydrogen jet (see Fig. II-23).

RELIABILITY

The reliability requirements of the thermal conditioning system have been reviewed to determine the type and quantity of redundant items needed for the 8-day Lunar mission and the 220-day Mars mission. Two approaches were taken:

a. Method 1 – The relative reliability of systems having various components in redundancy are established assuming that a totally redundant system has an arbitrary target reliability of 0.995.

b. Method 2 – The absolute reliability of systems having various components in redundance are established using actual and accepted failure rates for the various components as determined from similar flight system hardware and Gemini and Dynasoar Programs.

Method 1 – 220-Day Mission (Missions 2 and 3)

The relative reliability requirements of the thermal conditioning system were reviewed to determine the type and quantity of redundant items as may be needed for the 220-day

Mars missions. The approach is parametric in nature; Fig. VI-8 shows the relative reliability as a function of system weight increase.

The data on Fig. VI-8 was determined in the following manner. By definition the system reliability is given by:

$$R = e^{-\lambda t}$$

where

λ = Failure rate, hr^{-1}

t = Mission time = 5280 hr

Substituting

$$e^{-\lambda t} = 0.995$$

$$\lambda t = 0.005$$

Therefore the value of the failure rate, λ, is $0.947 \times 10^{-6}\ hr^{-1}$.

This permits tentative assignment of failure rates and reliabilities as follows:

	λ	R
Heat exchanger	0.1×10^{-6}	0.9995
Pressure regulator	0.247	0.9987
Shutoff valve	0.2	0.999
Motor-fan	0.2	0.999
Pressure switch	0.2	0.999
Total	$0.947 \times 10^{-6}\ hr^{-1}$	

The overall time that the system will be actually operating is a function of average heat leak, withdrawal rate, and motor input power. Whether the heat leak is primarily absorbed by the vapor or by the liquid the setting of the pressure switch determines the frequency of operation. The minimum frequency of operation occurs when

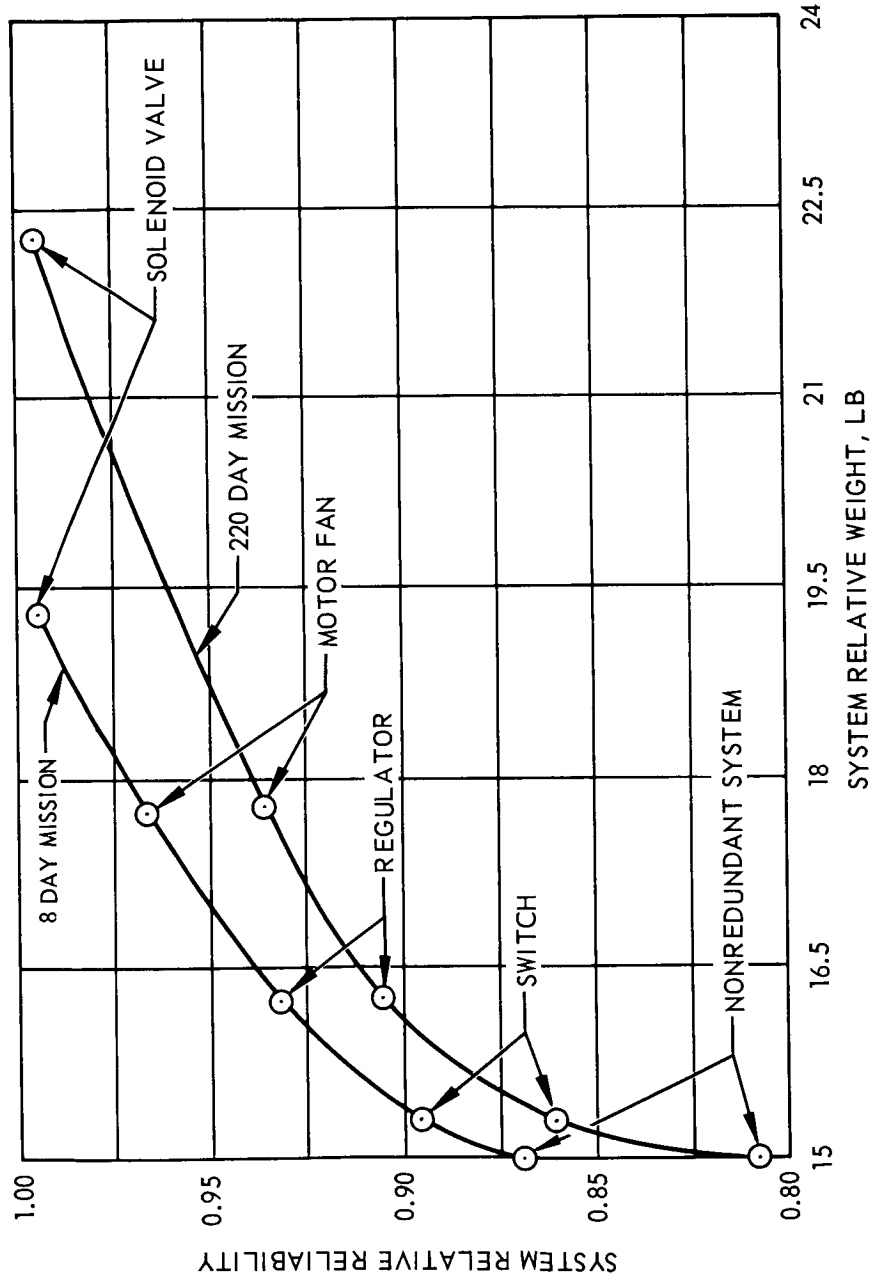

Fig. VI-8 System Reliability Improvement With Redundant Units

the heat is absorbed by the liquid. For Mission (2), with a pressure switch band of 2 psi and with the average value of heat leak, frequency of venting will be once every eight days at the start of the mission and once every five days at the end of the mission. The logarithic mean minimum frequency is, thus, 6.3 days ($\sqrt{8 \times 5}$). The minimum number of actuations during the 220 days is, thus, 35. The maximum rate of pressure increase for Mission (2) is 2.2 psi per hr; this would result in 5808 actuations. A plot of the normal assumed distribution is shown in Fig. VI-9. There is a 50-percent probability that the number of actuations will be between 245 and 820. Thus, there appears to be no excessive cycling since the probable number of cycles is a few hundred, and even the maximum, 5808, is not severe.

The heat exchanger in this system operates at a very low temperature. However, the temperature gradients and pressure differentials are both small. Such a heat exchanger has an inherently high reliability. The counterflow design used is comparatively easy to clean and inspect during the manufacturing process. Improvement relative in reliability is obtained, if necessary, by increasing the gauge of the metal rather than by duplicate units. The target failure rate is 0.1×10^{-6} hr^{-1}. The target Mean Time Between Failure (MTBF) for the heat exchanger is

$$\text{MTBF} = 1/\lambda = 1/0.1 \times 10^{-6}$$

$$\text{MTBF} = 10{,}000{,}000 \text{ hr}$$

There are three design choices, from a reliability standpoint, for the pressure regulator: (1) a single regulator, (2) two regulators operating in parallel, and (3) two regulators with one operating normally and the other on standby.

If a single pressure regulator is used, for a mission time of 5280 hr (220 days), a reliability of 0.9987 will require that the regulator mean time between failures must be 4,060,000 hr.

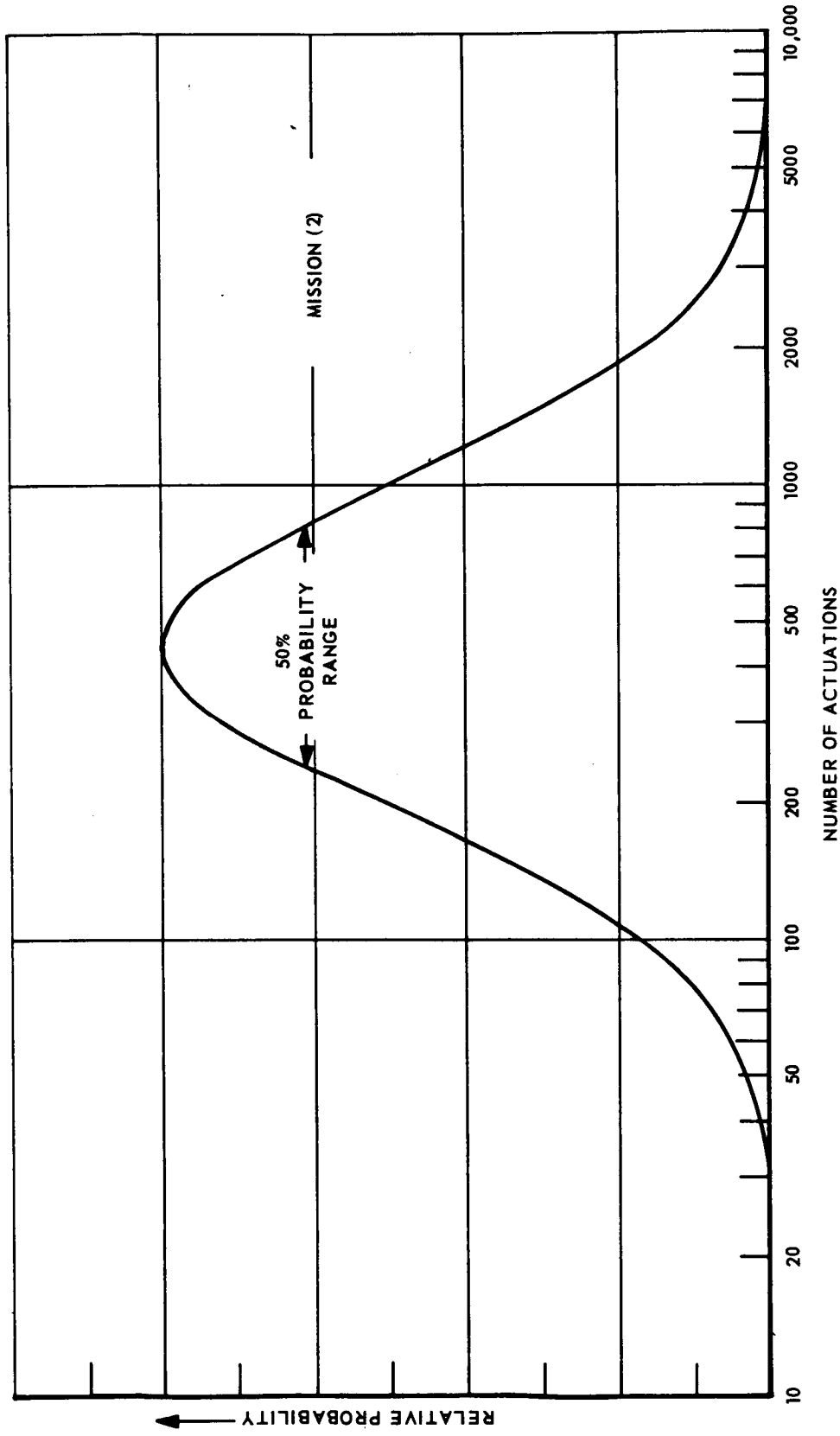

Fig. VI-9 Probable Frequency of Operation

If two pressure regulators are used in parallel and if their opening and closing points (operating bands) are such that both units will normally operate, the mean time between failures for each of the regulators is found as follows:

$$R = 1 - (1 - \ell^{-\lambda t})^2$$

For a reliability of 0.9987, substituting and rearranging,

$$(1 - \ell^{-\lambda t})^2 = 0.0013$$

$$1 - \ell^{-\lambda t} = 0.03606$$

$$\ell^{-\lambda t} = 0.96394$$

$$\lambda t = 0.03674$$

$$\lambda = 6.958 \times 10^{-6}\ \text{hr}^{-1} \text{ per regulator}$$

$$\text{MTBF} = 1/6.958 \times 10^{-6} = 144{,}000 \text{ hr per regulator}$$

Two pressure regulators may be used with one operating normally and the other on standby, that is, operating only if the first regulator fails. If the regulators are designed to close in the event of a failure, the standby arrangement could be obtained by setting the normally operating regulator at 4.0 ±0.3 psia and the standby regulator at 3.0 ±0.3 psia. Since large pressure transients are not expected, the 4-psia regulator, operating correctly, would provide complete control and the 3-psia regulator would be closed and inoperative. The 3-psia regulator would operate only if the 4-psia regulator failed. System operation would degrade slightly with the 3-psia regulator (the heat transfer rate would be lower because there would be a smaller flow of gas through the overboard orifice and, as a result, the motor would be required to operate for a longer period of time per cycle). This would, however, occur toward the end of the mission, if at all, and would be negligible compared to improved reliability.

The applicable equation is:

$$R = \ell^{-\lambda t}(1 + \lambda t)$$

when $R = 0.9987$ and $t = 5280$ the equation is satisfied for

$$\lambda = 9.848 \times 10^{-6}$$

or MTBF = 102,000 hr for each unit.

The standby approach is, therefore, the preferred method; it leads to a reasonable MTBF requirement.

For the solenoid shutoff valve, the use of quadredundancy is indicated to reduce the MTBF requirement below 100,000 hr. Four identical solenoid-operated valves in a series-parallel arrangement would be operated simultaneously as shown in Fig. VI-10.

It is apparent that the failure of one valve in either the open or closed positions does not impair the ability of the system to perform its intended shutoff function. For any two valves, 18 of the 24 modes of failure, including open and closed, can be tolerated; only 6 will cause loss of function. Furthermore, of the 32 modes of failure for three valves, 12 can be tolerated; 20 will cause loss of function.

Defining the probability of failure Q for a single part and the probability of failure Q_s of the quadredundant assembly:

$$Q = 1 - R = 1 - \ell^{-\lambda t}$$

$$Q_s = 1 - R_s = 1 - 0.999 = 0.001 \text{ for a system reliability of } 0.999$$

The appropriate equation for the conditions of the above paragraphs is:

$$0.375\, Q^4 + 0.375\, Q^3 + 0.25\, Q^2 = 0.001$$

solving

$$Q = 0.0604$$

$$R = 1 - 0.0604 = 0.9396 = \ell^{-\lambda t}$$

$$\lambda t = 0.0623$$
$$\lambda = 0.0623/5280 = 11.799 \times 10^{-6}$$
$$\text{MTBF} = 1/11.799 \times 10^{-6} = 84{,}800 \text{ hr}$$

The quadredundant arrangement of valves leads to this reasonable MTBF valve. All the valves can be included in one housing.

A mixer driven by a dc brushless motor is used to circulate the tank fluid through the heat exchanger. The only significant mode of failure is that in which the impeller does not turn when the appropriate electric power input is sent to the control box.

For a redundant system, it is recommended that two complete mixer units be used, each designed to handle 50 to 75 percent of the nominal fluid circulation rate. Normally, both motors would operate; the resulting fluid circulation would be ample. In case of the failure of one motor, the other motor would continue to operate. The warm side effectiveness must increase above the present 0.45 design point; the heat transfer rate would degrade slightly. The system would be less efficient since a larger amount of hydrogen would be vented; however, the system would not become inoperative.

The calculation procedures for this unit are the same as those for cases (1) and (2) of the pressure regulator, as given above. For a single motor fan, the required λ is 0.2×10^{-6} hr^{-1} or a MTBF of 5,280,000 hr. For two parallel units, the required λ per unit is 6.261×10^{-6} hr^{-1} or a MTBF for each unit of 160,000 hr.

The function of the pressure switch is to turn the system on at a specified tank pressure and to turn it off at a lower pressure. It consists of an on-off switch operated by an aneroid which senses tank pressure. For reasons analogous to those for the solenoid shutoff valve, above, one bellows would operate four single-pole switches, connected to provide quadredundancy of the switching function. The switches turn on the two impeller motors and also energize the four solenoids of the quadredundant shutoff valve assembly.

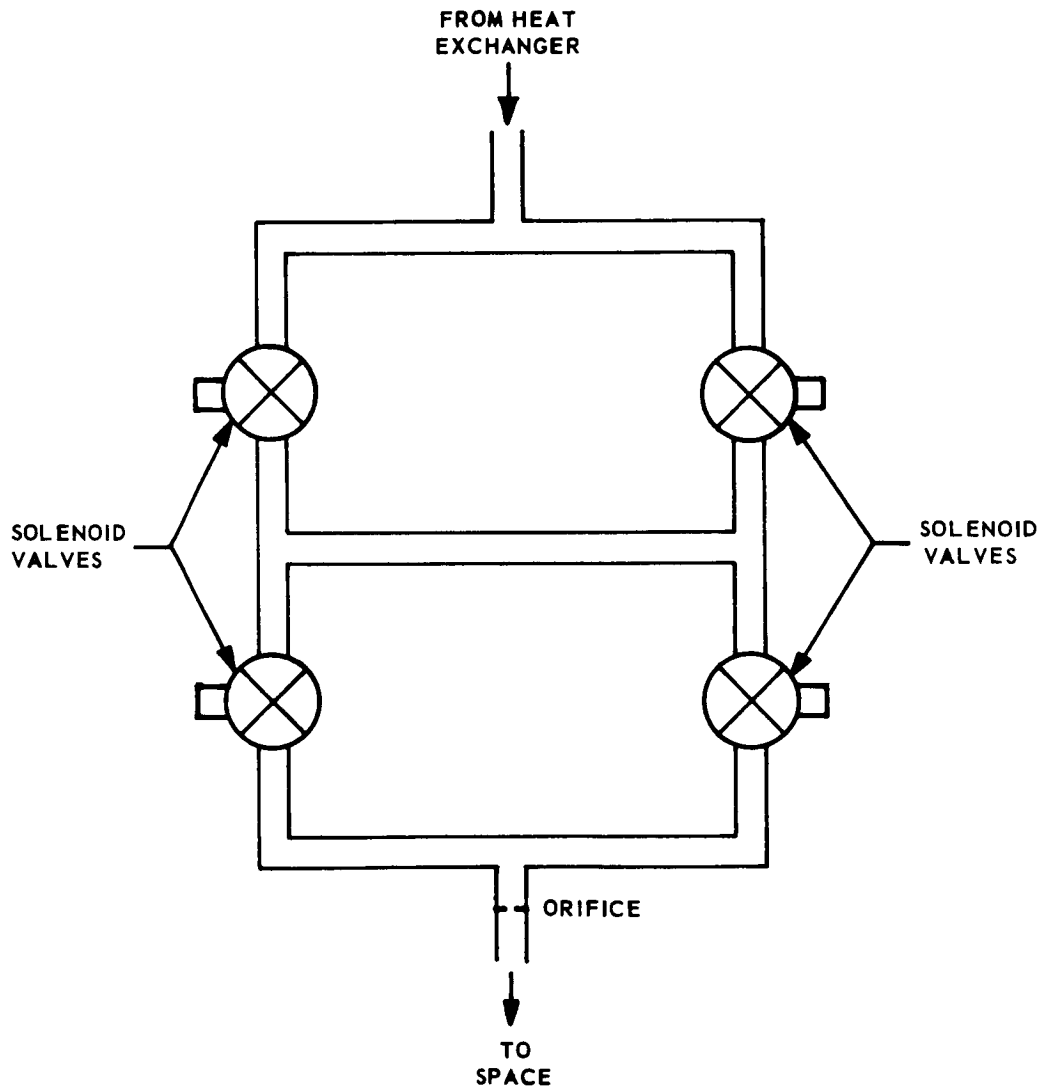

Fig. VI-10 Quadredundant Arrangement of Solenoid Valves

Certain circuit features, not previously mentioned, are essential for high reliability. These include:

a. There should be two micronic filters, one upstream of the pressure regulator assembly and one upstream of the solenoid shutoff valve assembly. In each case, the filter would preferably be part of the assembly that it protects to reduce the number of plumbing connections.

b. The electric switches should be well protected by condensers or diodes from arcing or other surges of current.

c. The design should consider access to the pressure switch, located outside the tank, since this is the element most likely to fail. Provision should be made for checking each of the four switches individually without disassembly.

Method 1 – 8-Day Mission (Mission 1)

The overall reliability of the totally redundant thermal conditioning system is assumed to be 0.995. The mission time, t , is 192 hours. Substituting this into the equation $R = e^{-\lambda t}$, we get

$$e^{-\lambda t} = 0.995$$

$$\lambda^{t} = 0.005$$

$$\lambda = \frac{0.005}{192} = 26.04 \times 10^{-6}/\text{hr}$$

This permits tentative assignment of failure rate and reliabilities as follows:

	λ	Reliability, R
Heat Exchanger	0.1×10^{-6}/hr	0.99998
Pressure Regulator	6.77	0.99870
Solenoid Shutoff Valve	6.39	0.99877
Motor-Impeller	6.39	0.99877
Pressure Switch	6.39	0.99877
Total	26.04×10^{-6}/hr	0.995

The target MTBF for the heat exchanger for this mission is, therefore:

$$\text{MTBF} = \frac{1}{\text{failure rate}} = \frac{1}{0.1 \times 10^{-6}/\text{hr}} = 10^{+7}\ \text{hr}$$

When the previously described analyses are applied to the pressure regulator, for the 8-day Lunar mission, the following values of MTBF are obtained:

a. For a single regulator, MTBF = 147,000 hr

b. For two regulators operating in parallel, MTBF = 5235 hr per regulator

c. For two regulators, one operating normally and the other on standby, MTBF = 4800 hr for each regulator

When the 8-day mission time is substituted into the governing equations for a single motor-impeller, the required λ is 6.39×10^{-6}/hr or a MTBF of 156,100 hr. For two units in active parallel, the required is 181.9×10^{-6}/hr or a MTBF of 5500 hr.

For the 8-day mission, quadredundancy is not required for the solenoid valves. A single valve and two valves operating in parallel are considered. The governing equations are the same as those used for the regulators and the results are as follows:

a. For a single solenoid valve, MTBF = 156,100 hr

b. For two valves operating in parallel, MTBF = 5500 hr per valve

As with the solenoid valve, the 8-day mission requires only biredundance of the pressure switch instead of the quadredundancy required for the 220-day mission. In this case one bellows operates two single pole switches, providing parallel redundance of the switching function, and the MTBF is 5235 hr.

By using the values developed for MTBF for the 220-day mission, the basic nonredundant system reliability is 0.81 as shown below.

Component Name	Failure Rates (λ)
Heat Exchanger	0.1×10^{-6}/hr
Pressure Regulator	9.848
Shutoff Valve	11.799
Motor Fan	6.261
Pressure Switch	11.799
Total	39.807×10^{-6}/hr

For t = 220 days or 5280 hr

$$R = e^{-39.807 \times 10^{-6} \times 5280}$$

$$R = 0.81044$$

Similarly it can be shown that the reliability for the 8-day mission is 0.866:

Component Name	Failure Rate
Heat Exchanger	0.1×10^{-6}/hr
Pressure Regulator	191.2
Shutoff Valve	181.9
Motor Fan	181.9
Pressure Switch	191.2
Total	746.3×10^{-6}/hr

For t = 8 days or 192 hr

$$R = e^{-746.3 \times 10^{-6} \times 192}$$

$$R = 0.86658$$

The increase reliability obtained for redundant units as a function of increase in system weight is shown in Fig. VI-8. The basic system (no redundancy) weight is approximately 15 lb. Thus, increased reliability leads to a very small weight increase. The totally

redundant system for both the 8 day and 220 day missions are shown in Fig. VI-11, respectively. For the 220-day mission, the totally redundant system includes two pressure regulators, four solenoid valves (Fig. VI-11a), two mixer units, four single-pole pressure switches, and one heat exchanger. For the 8-day mission, it includes one heat exchanger and two each of the other four components.

Method 2

Component failure rates are reliability estimates assigned to the particular component. These estimates are based on evaluations of the component design, its operational environment, and its operational function. Previous experience with similar flight-qualified components permits assignment of conservative estimates to the components proposed due to their similarity to existing Gemini ECS and RSS, and Dynasoar. The estimated component failure rates are summarized below.

Component Name	Failure Rate (λ)	Previous Usage
Heat Exchanger	0.02×10^{-6}/hr	Gemini RSS
Pressure Regulator	5.0	New
Shutoff Valve	1.0	Gemini ECS
Motor Fan	5.0	Dynasoar
Pressure Switch	0.16	Gemini ECS
Total	11.18×10^{-6}/hr	

Using the analyses described in Method 1 and the above component failure rates, the nonredundant system reliability, for the 220-day mission is

$$R_s = 0.94270$$

This is increased to 0.9987 with total redundancy as defined for Method 1.

For the 8-day mission, these component failure rates give a nonredundant system reliability of 0.998, and a totally redundant system reliability > 0.9999.

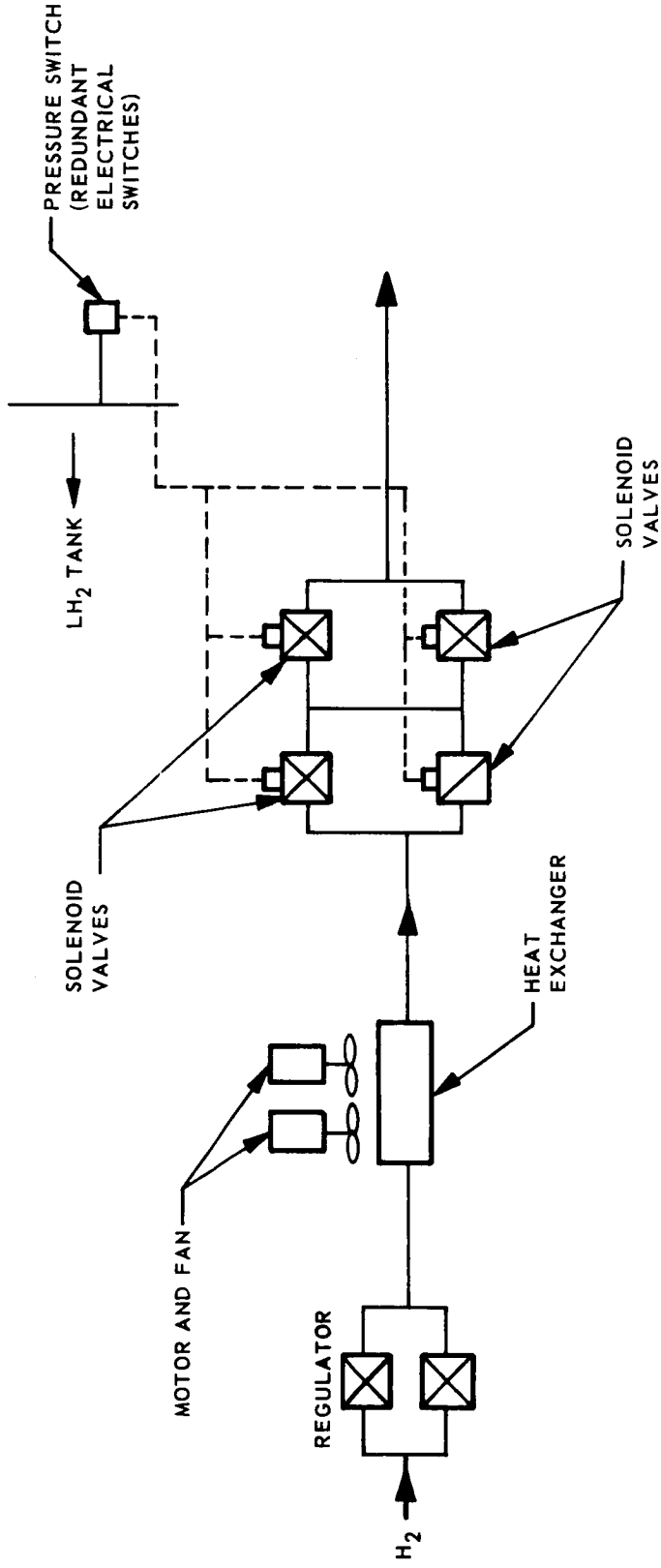

Fig. VI-11 a Recommended Redundant System for Missions (2) and (3)

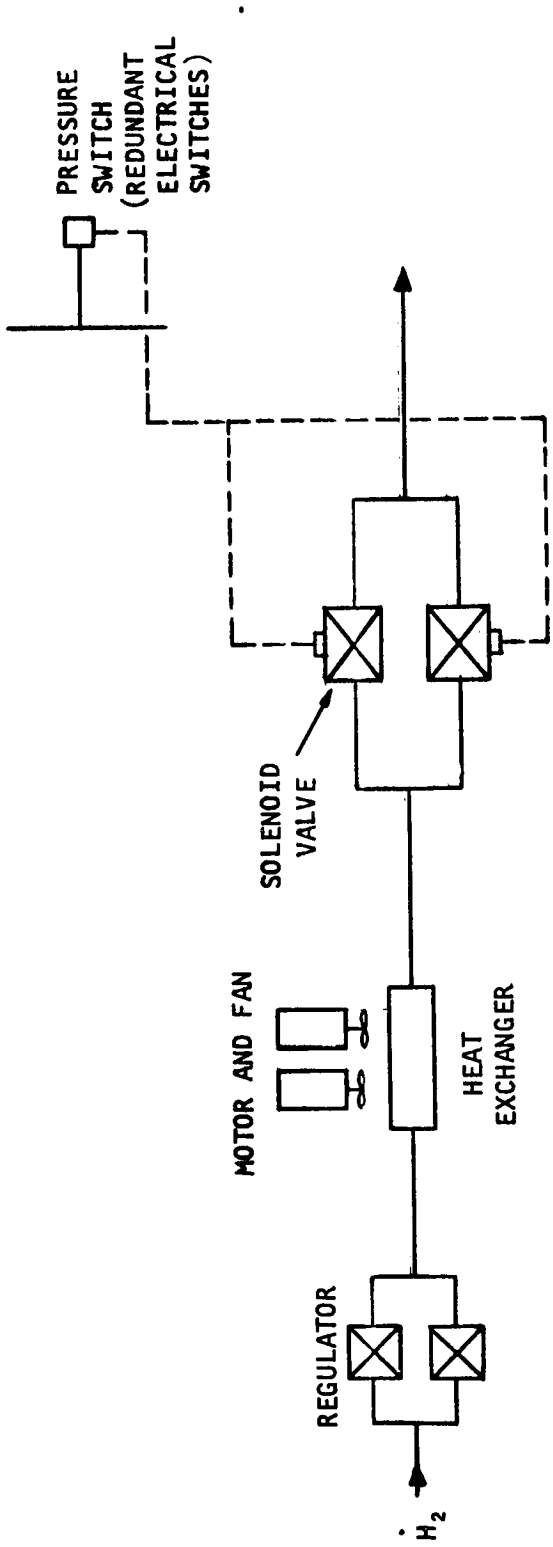

Fig VI-11 b Totally Redundant System (8-Day Lunar Missions)

VEHICLE INTEGRATION

Figure VI-12 shows the recommended liquid propellant thermal conditioning system installed in the hydrogen tank of the Mission (2) vehicle. The mixer discharges axially into the tank approximately 70 in. above the bottom of the tank with an exit velocity of 5 ft/sec. The jet spreads as it spans the tank, being turned into a wall bound jet at the bottom of the tank, and providing a jet velocity at the slosh baffles of approximately 0.1 ft/sec. Referring to Fig. II-8, it is evident that this velocity would produce a minimum pressure decay rate of approximately 1 psi/min, with only 1°R temperature difference between the ullage and the circulating liquid.

The tank pressure history immediately following an engine firing is dependent upon the temperature of the pressurizing gas. During the expulsion cycle, the walls are heated by the warm pressurant. When the flow of pressurant stops, the tank pressure will start to decay due to condensation at the liquid-vapor interface, if the colder liquid does not contact the walls. In this case, the walls are gradually cooled by conduction through the vapor. However, if the liquid runs up the walls after engine cutoff, the walls will be cooled rapidly by boiling the liquid. If condensation of the warm pressurant gas is not rapid enough to offset this heat input from the walls, the tank pressure will increase before starting its decay. It is not possible to analyze the condensation.

The combination of boiling and condensation phenomena is not amenable to simultaneous analysis. However, if the condensation is neglected, the maximum tank pressure following engine cutoff can be determined. Applying the perfect gas law to the ullage and assuming the volume change is insignificant yields

$$(P_2 - P_1) = \frac{R}{V_g}(M_2 T_2 - M_1 T_1)$$

But

$$(M_2 T_2 - M_1 T_1) = \frac{1}{C_{V_g}} \Delta E$$

and

$$\Delta E = \rho_w \delta_w A_w C_{P_w} (\overline{T}_w - T_\ell)$$

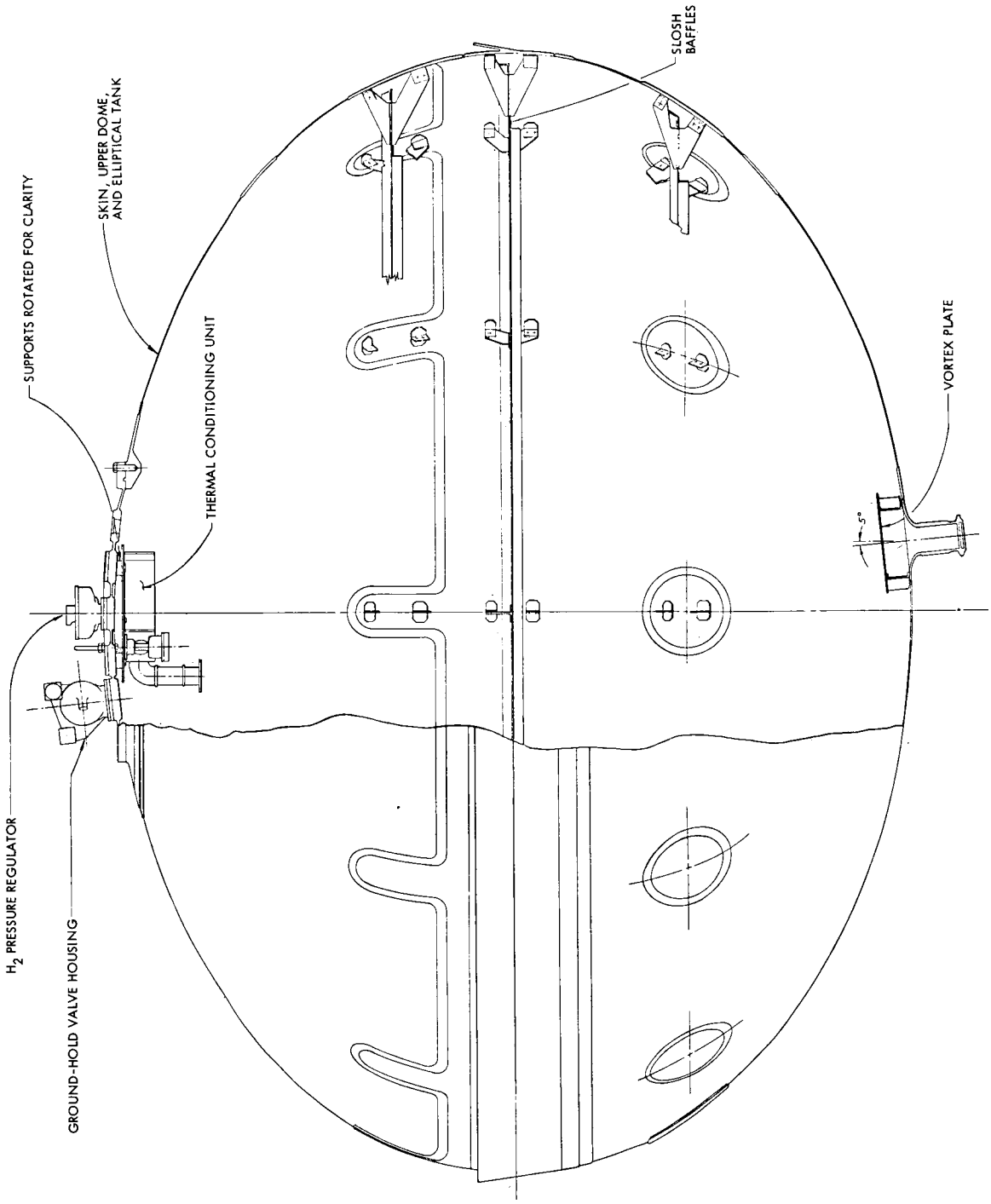

Fig. VI-12 Tank Assembly With Thermal Conditioning System

Therefore, the pressure rise becomes:

$$P_2 - P_1 = \frac{R_g}{V_g C_{V_g}} \left(\rho \delta A C_P\right)_w (\overline{T}_w - T_\ell)$$

During the expulsion cycle, the walls establish a temperature gradient between the liquid and the incoming pressurant. Assuming the average wall temperature corresponds to the average temperature between these two fluids, a maximum pressure spike occurs following engine cutoff (Fig. VI-13).

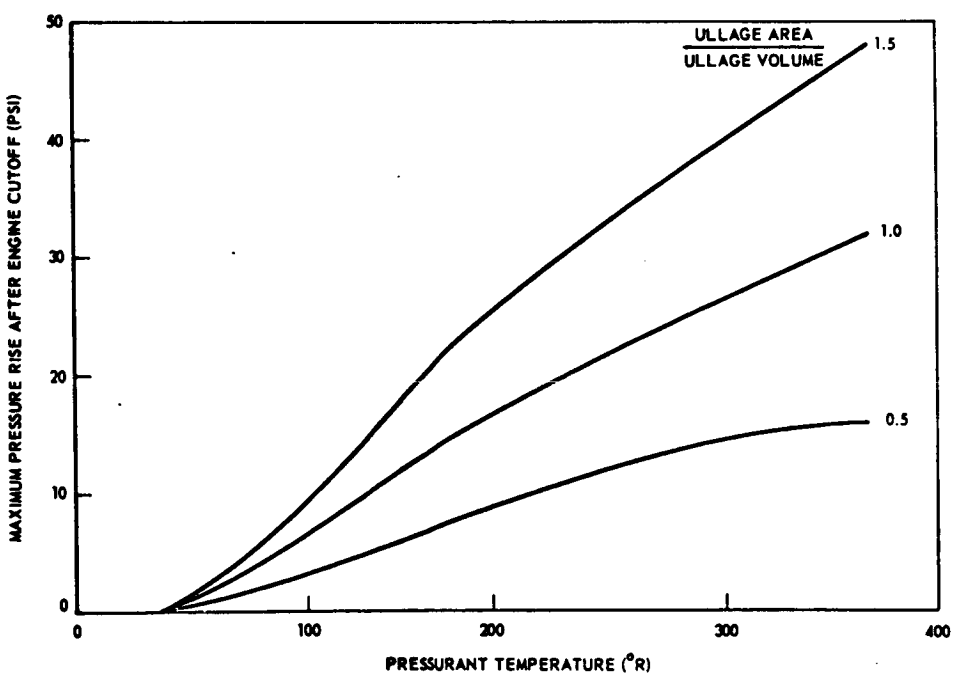

Fig. VI-13 Maximum Pressure Spike at Engine Cutoff

Consider, the model depicted in the sketch below. Upon engine cutoff, the liquid-vapor interface is flat. Then the liquid starts moving up the warm walls with some velocity U_o, and simultaneously cools the warm walls and the hot ullage.

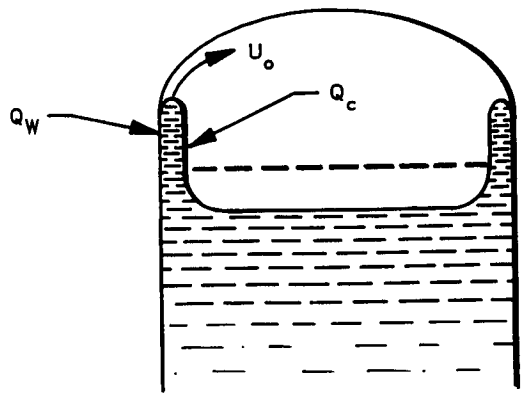

The heat transfer from the walls is given by:

$$\dot{Q}_W = h_B A_W (T_W - T_\ell) = \frac{d}{d\theta}\left[\rho\,\delta\,C_P A_W (\overline{T}_W - T_\ell)\right]$$

If one makes the conservative assumption that each element of the wall is instantaneously cooled as it becomes immersed,

$$Q_W = \left[\rho\,\delta\,C_P (T_W - T_\ell)\right]_W \frac{dA_W}{d\theta} = \left[\rho\,\delta\,C_P (T_W - T_\ell)\right]_W b\,U_o$$

Combining these equations defines an effective boiling coefficient

$$h_B = \frac{\rho\,\delta\,C_P\,b\,U_o}{A_W}$$

Now consider the heat being removed by condensation,

$$Q_c = h_c A_f (\overline{T}_g - T_\ell)$$

The theoretical expression for h_c, developed in the discussion on propellant mixing, is applicable here, since condensation occurs as a result of the film velocity. Therefore,

$$h_c = 1.12 \left[\frac{k_\ell \rho_\ell \lambda U_o}{L \Delta T}\right]^{1/2}$$

The ratio of heat added to the ullage by vaporization and that removed by condensation is given by:

$$\frac{Q_w}{Q_c} = \frac{h_B}{h_c} \frac{A_w (\overline{T}_w - T_\ell)}{A_f (T_g - T_\ell)}$$

This can be reduced conservatively to the ratio of effective coefficients. This ratio becomes

$$\frac{Q_w}{Q_c} = \frac{\left(\rho \delta C_P\right)_w b/A_w U_o}{1.12\left(\frac{k_\ell \rho_\ell \lambda U_o}{L \Delta T}\right)^{1/2}} = \frac{\left(\rho \delta C_P\right)_w}{1.12\left(k_\ell \rho_\ell \lambda\right)^{1/2}} \left(\frac{U_o \Delta T}{L}\right)^{1/2}$$

For the Mission (2) vehicle hydrogen tank, this becomes

$$\frac{Q_w}{Q_c} = 0.0065 \left(\frac{U_o \Delta T}{L}\right)^{1/2}$$

If this ratio is less than unity, condensation will control tank pressure, and there will be no pressure spike following engine cutoff. From this cursory analysis, it does not seem likely that this spike will occur.

The pressure history following first and second burns is shown in Fig. VI-14 for the Mission (2) vehicle. Both uniform heating and stratified heating are shown.

It can be seen that in either case, the vent time is short compared to the nonvent duration. From the stratified heating model, one can determine the highest vent frequency and the maximum number of cycles for which the thermal conditioning system must be designed. For the 220-day Mission (2), a maximum of 2640 cycles should be required, which is not unreasonable for components such as those in the thermal conditioning system.

MISSION ENVIRONMENT CONSIDERATIONS

Proper integration of the liquid propellant thermal conditioning system into a vehicle requires some consideration of each of the environments which the vehicle will encounter. The effects of the ground hold and ascent environments are reviewed in this section.

Ground Hold Environment

The propellant heating rate on the launch pad will be at least 100 times that occurring during space flight. This makes it necessary to provide a separate ground vent system which bypasses the thermal conditioning unit and vents the ullage directly. Thus, the ground environment has no effect on selecting and sizing of components for the liquid propellant thermal conditioning system.

However, the capability for checking out the thermal conditioning system on the launch pad must be provided. This requires that a two-way valve be placed in the line downstream of the thermal conditioning system shutoff valve. This two-way valve may be mounted on the outer load carrying shell of the vehicle.

During system checkout, the two-way valve permits the vented propellant to flow to a vacuum pump which must be provided as part of the thermal conditioning system ground-support equipment.

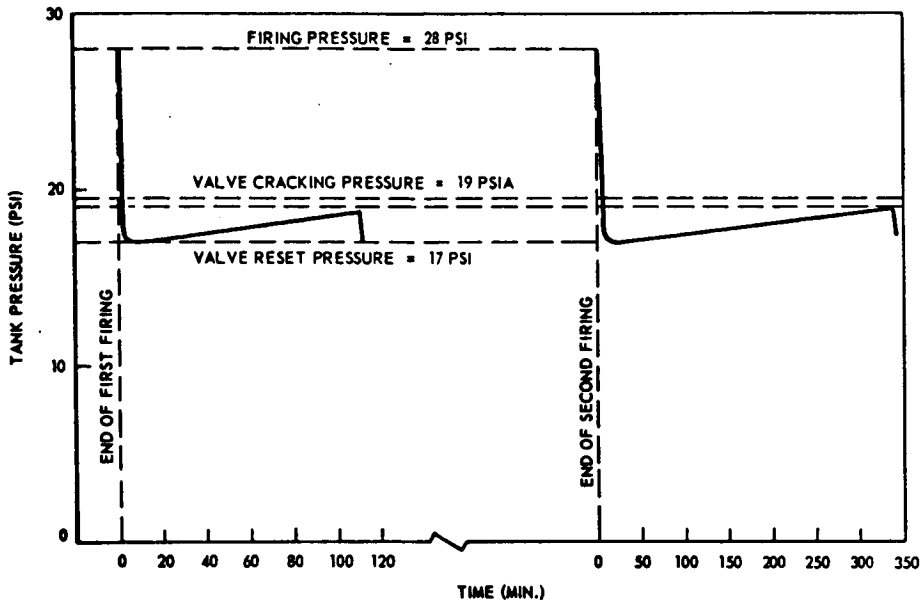

Fig. VI-14a Tank Pressure History for Mission (2) Vehicle (Stratified Model)

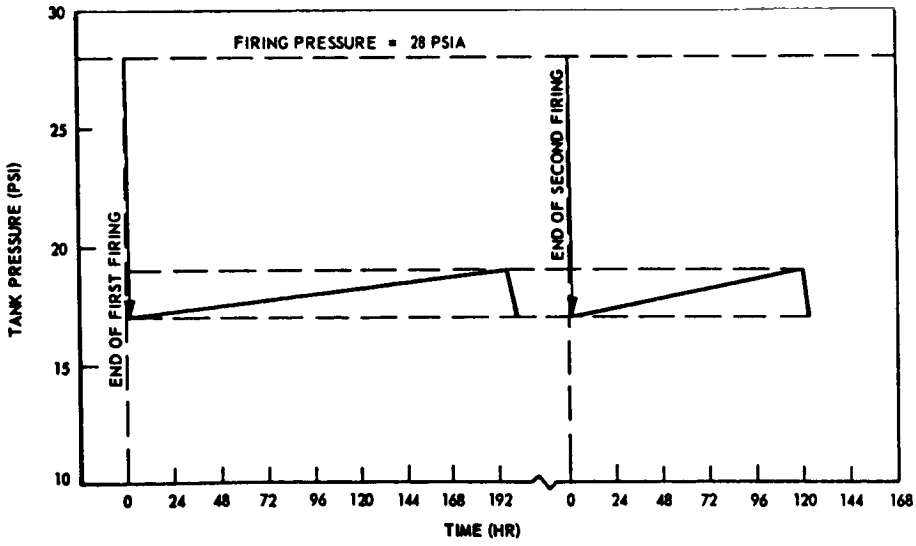

Fig. VI-14b Tank Pressure History for Mission (2) Vehicle (Mixed Model)

The ground hold and ascent pressure relief systems are integrated with the thermal conditioning system to provide the checkout capability and the proper operational sequence. This integration is shown schematically in Fig. VI-15.

The operational sequence is listed below (symbols refer to Figs. VI-15 and VI-16):

- Fill. During the fill procedure the venting function of the ground vent and relief valve (U2) is in operation. The vent function is obtained by supplying ground power to the flight vent control pilot valve (U4) which permits ground GH_e pneumatic control pressure to enter the system. Simultaneously, ground power is supplied to the ground vent pilot valve (U1) which permits ground control pressure to open the vent function of U2. Boiloff is delivered to ground facilities for proper disposal through the tank vent disconnect (QD2).
- Thermal Conditioning System Checkout. The thermal conditioning system can be checked out during ground hold operations after the fill operation by utilizing a vacuum pump from ground facilities and energizing the thermal conditioning system checkout valve (U3). Energizing U3 permits appropriate vacuum conditions to exist at the thermal conditioning system, thereby permitting a functional check of the system components through facility monitoring of the vent flow rate. When satisfactory checkout is obtained, U3 is deenergized, permitting the valve to return to its normal position and permitting bypass of the vent and relief functions of U2 by the thermal conditioning system. This procedure permits use of normal vent and relief manifold.
- Ground Hold. During ground hold operations the vent function of U2 is maintained as previously described during the fill operation.
- Launch. Just prior to launch, ground power is discontinued to the ground vent pilot valve (U1), which permits ground control pressure to close the vent function of U2. Full closure is monitored by the Limit Switch (LS1). When full closure is indicated ground power is discontinued to the flight vent control pilot valve (U4). The deenergized position is monitored by the Limit Switch (LS2). Launch is then initiated.

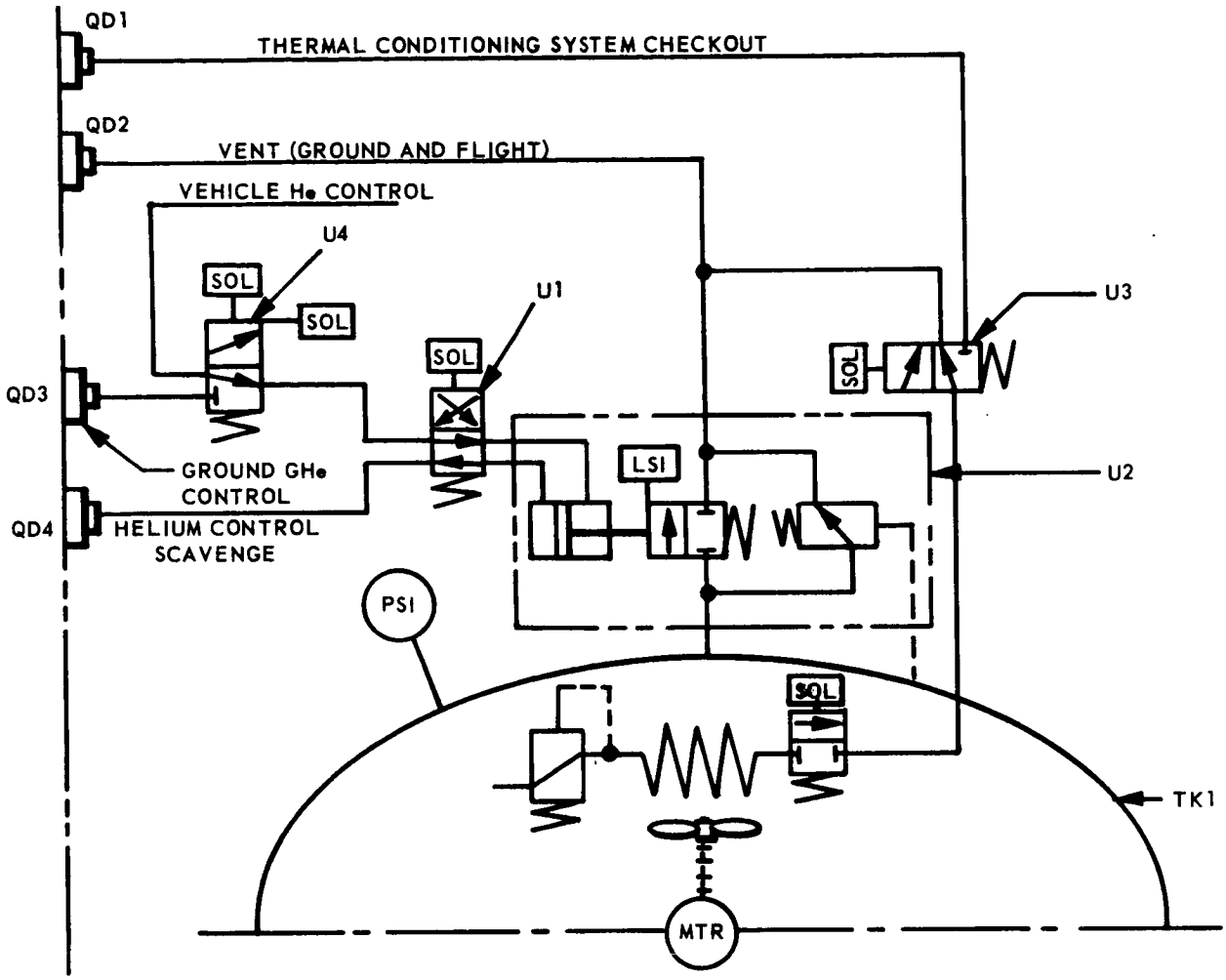

SYMBOL	NOMENCLATURE
U1	VALVE, GROUND VENT PILOT
U2	VALVE, GROUND VENT AND FLIGHT RELIEF
U3	VALVE, THERMAL CONDITIONING SYSTEM CHECKOUT
U4	VALVE, FLIGHT VENT CONTROL PILOT
QD1	DISCONNECT, THERMAL CONDITIONING SYSTEM CHECKOUT
QD2	DISCONNECT, TANK VENT
QD3	DISCONNECT, GROUND GHe PNEUMATIC CONTROL
QD4	DISCONNECT, GHe PNEUMATIC CONTROL SCAVENGE
PS1	SWITCH, FLIGHT VENT SHUTOFF PRESSURE
TK1	TANK, LH_2

Fig. VI-15 Thermal Conditioning System Vent and Checkout Schematic

- Flight Venting. The system is designed so that ascent heating deposited into the LH_2 tankage can be vented through Q2, thereby negating the addition of a flight vent system. The flight vent sequence is initiated by a programmed input just prior to booster engine cutoff (BECO). The sequence of operations for flight vent is best explained by referring to Figs. VI-15 and VI-16. The programmed flight vent command closes the normally open (NO) contact on line 2 (Fig. VI-16), which permits vehicle power to energize the ground vent pilot valve (U1) through the closed contacts of the flight vent shutoff pressure switch (PS1-Line 2). PS1 is set to actuate from its normal position (Fig. VI-16) at 17 psia. The ascent heating has therefore increased the tank pressure above 17 psia. The switch is actuated, permitting vehicle power to energize U1. Vehicle pneumatic control energizes the vent function of U2 open through U1. When the tank pressure decreases to 17 psia the pressure switch returns to its normal position and permits vehicle power to energize the flight vent shutoff latching relay (K1-L-Line 1) which opens the normally closed contacts of K1 on Line 2. Vehicle power is then permanently discontinued to U1. The ground vent pilot valve (U1) returns to its normal position and permits vehicle pneumatic control to close the vent function of U2. All subsequent venting of the tank will be conducted through the thermal conditioning system.

  The relief function of U2 remains in the system as a safety relief.

VENT GAS UTILIZATION

The sensible heat capacity of saturated hydrogen vapor at space ambient temperatures is much higher than its latent heat. If this capacity can be efficiently used, it will effect a significant weight savings for the vehicle. Some potential uses for this vent gas are discussed below.

Cooling Supports

With a well designed thermal protection system for long term hydrogen storage in space, the supports should contribute less than 30 percent of the total propellant heating.

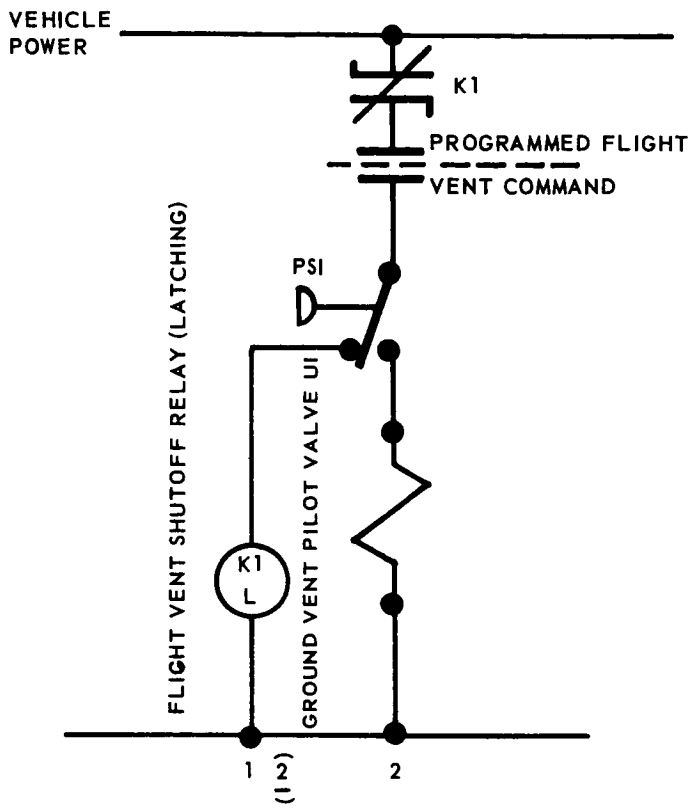

Fig. VI-16 Flight Vent Electrical Schematic

The liquid hydrogen tank of the Mission (2) vehicle might use a fiberglass, minimum point support system for which the heat leak is 1.5 to 3.5 Btu/hr (see Fig. VI-17).

If a heat exchanger is used that intercepts all of this heat coming through the support on a continuous basis, it saves between 20 and 95 lb in hydrogen boiloff for Mission (2). For intermittent operation, this saving is reduced in proportion to the non-operative portion of the mission. In the systems optimization section, it was shown that intermittent operation of the thermal conditioning system with a vent flow rate of 1.4 lb per hour was optimum because of the excessive power requirements for continuous operation of the mixer. The penalty associated with continuous operation was approximately 35 lb. Therefore, the use of a penetration cooler might, theoretically, eliminate the weight advantage for intermittent operation. Analysis must be applied to a specific support system design before a final evaluation of the effectiveness of a penetration cooler can be made.

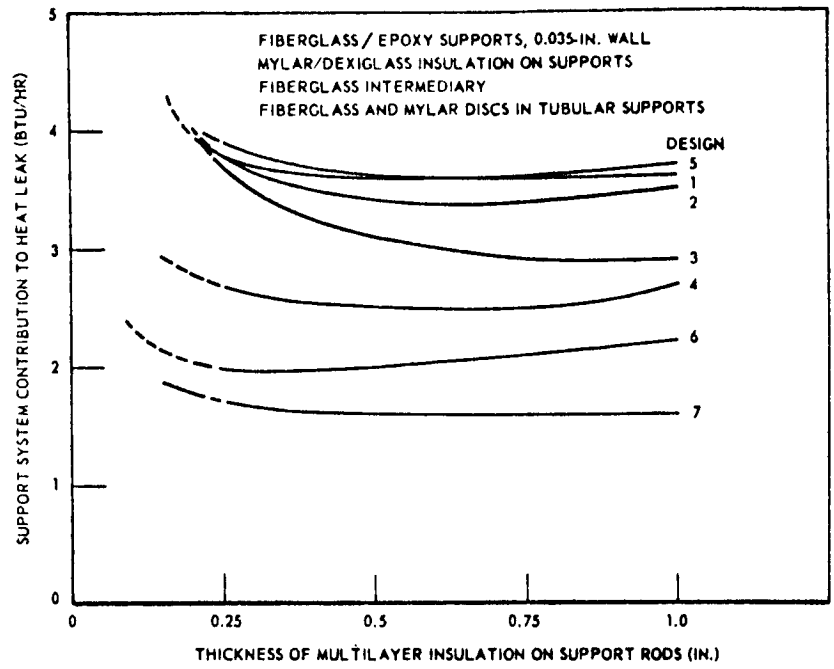

Fig. VI-17 Calculated Heat Leak Through Tank Support System, Mission (2) Vehicle

Insulation Cooling

Another technique for increasing propellant storability would involve the placement of cooling coils within the insulation. Figure VI-18 shows that this technique can reduce the heat input through the thermal protection system by approximately 50 percent. However, as with support cooling, this savings is realized only for continuous operation, and thus it is partially offset by component inefficiences at the low, continuous, vent rates. Perhaps more important is the difficulty in supporting this cooler within the thermal protection system without seriously degrading its performance. Also, if this thermal conditioning superheater is placed within a high performance, multilayer thermal protection system, the insulation performance will be seriously impaired by any leakage from the heat exchanger that is sufficient to increase the interstitial pressure in the multilayers to above 10^{-5} torr.

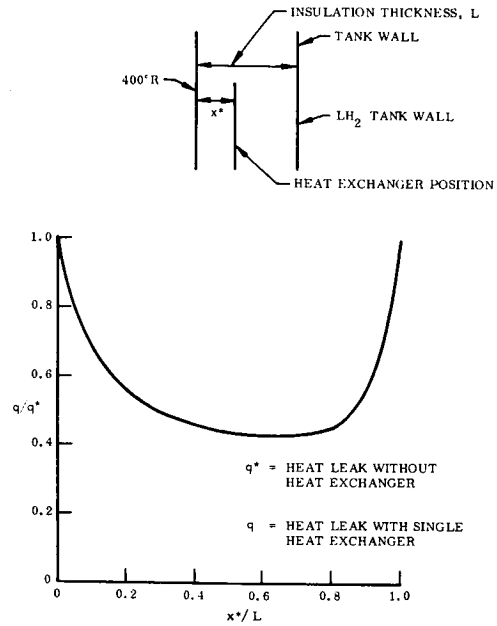

Fig. VI-18 Effect of Heat Exchanger Position Within Insulation

Para-Ortho Conversion

The potential advantage of slush lies in its ability to absorb more energy while in the propellant tank. A catalytic converter can only be advantageously applied to the vented vapor after it has left the tank and been superheated. The catalyst speeds up the process of changing the para-hydrogen to the higher energy equilibrium form. This process is temperature dependent as shown on Fig. VI-19, which shows that the maximum heat of absorption occurs at $100^{\circ}K$.

A system employing para-ortho conversion might consist of a valve, an internal heat exchanger (with fan) to vaporize the vented propellant, followed by tubes running along the tank supports. These tubes would be filled with a catalyst such as hydrous ferric oxide, and the heat of conversion would come from that normally conducted down the support into the tank. This process is illustrated by the dashed line on Fig. VI-20.

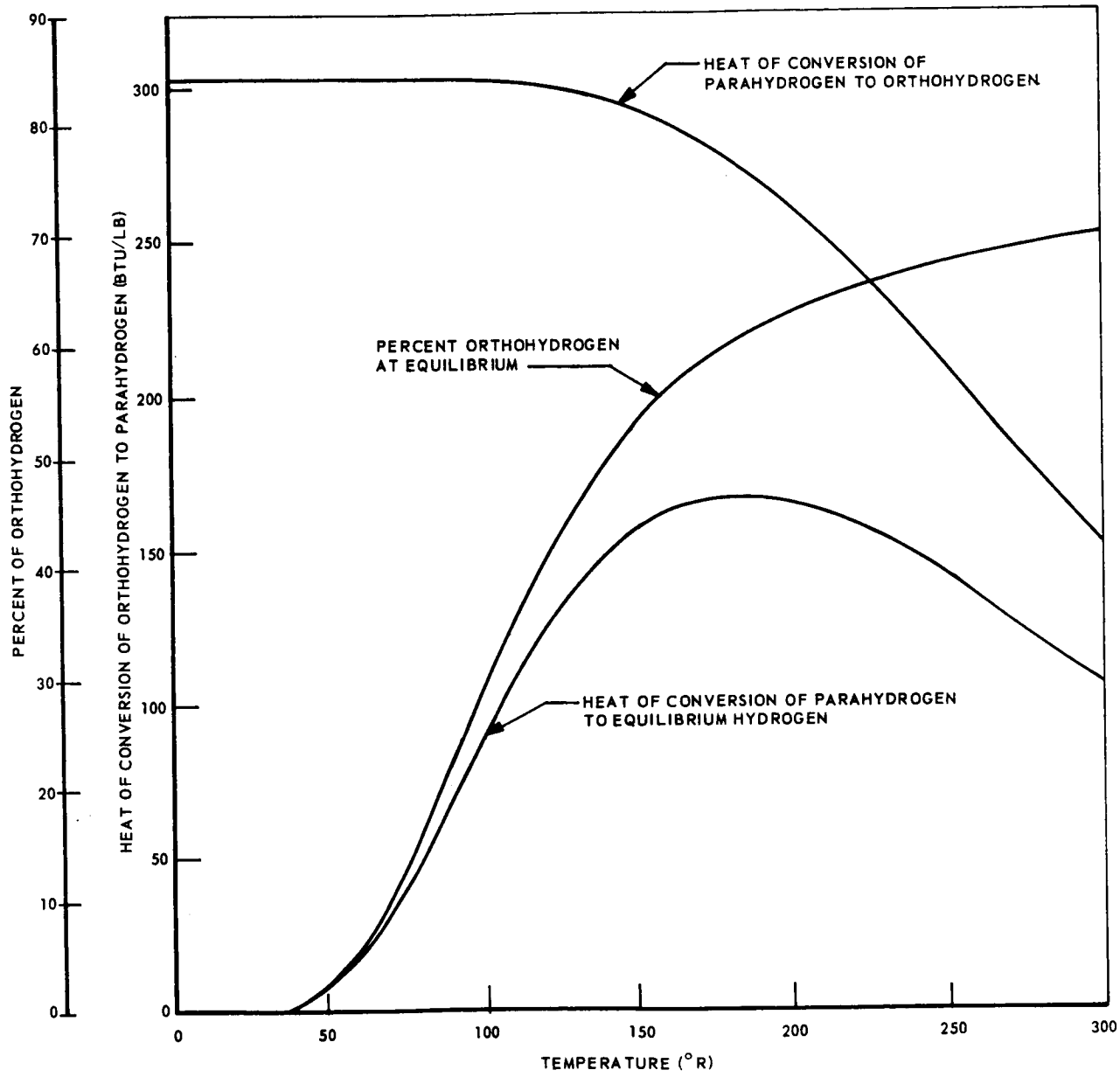

Fig. VI-19 Heat Resulting From Conversion of Parahydrogen to Equilibrium Hydrogen

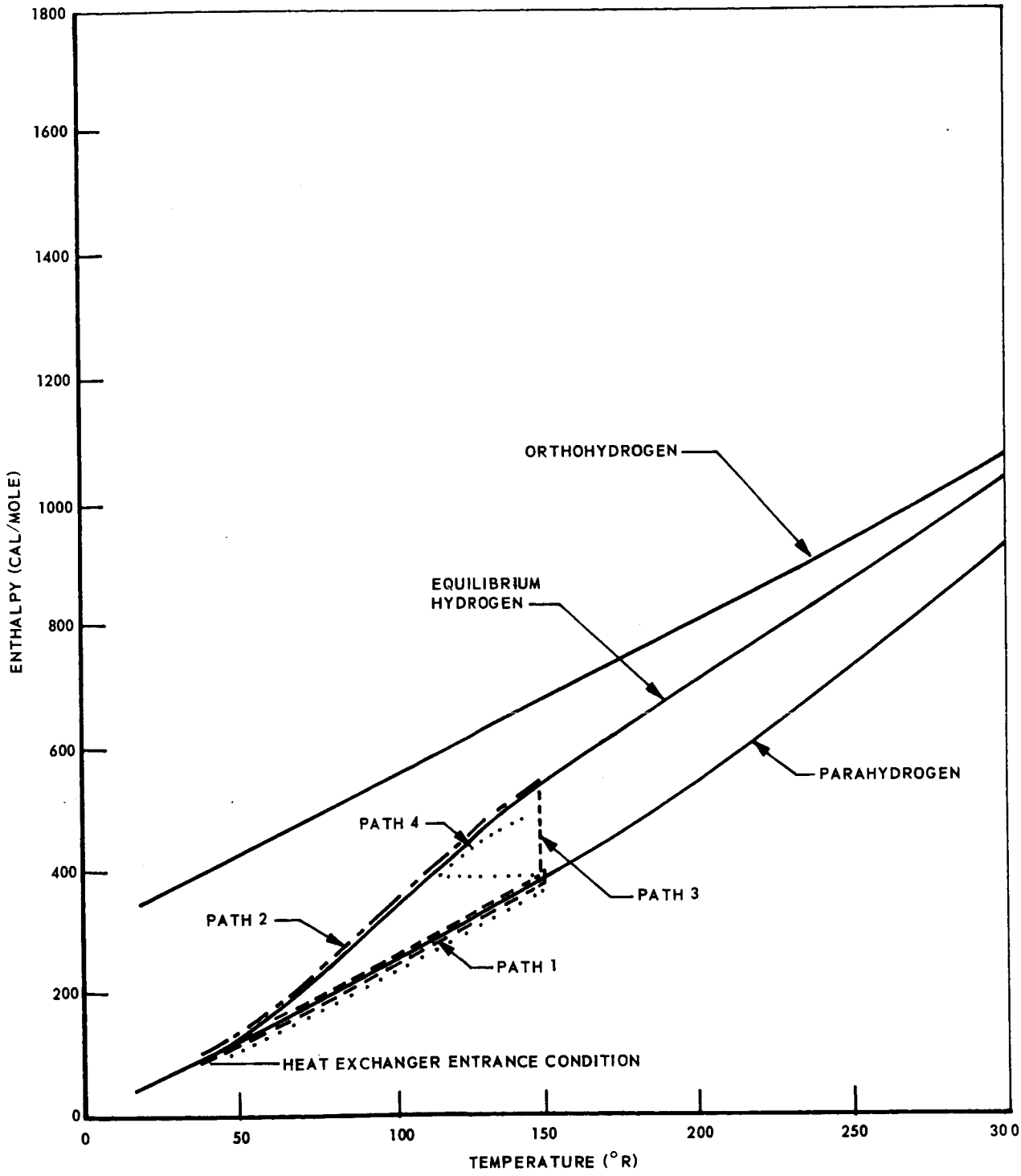

Fig. VI-20 Temperature-Enthalpy Relationship for Hydrogen at 1 Atmosphere

The total refrigeration capacity at 100°K, represented by heat of conversion plus the latent and sensible heats is approximately three times the one atmosphere latent heat; i.e., the boiloff reduction could approach 66 percent. This would be realized only with continuous operation. For intermittent operation, the effectiveness should be reduced in proportion to the nonoperating time. Again, most of the continuous flow rates of interest in this program are so low as to be unrealistic; this reduces the potential usefulness of para-ortho conversion. Also, the development of potential catalysts is still in its infancy and is limited primarily to investigation of the physical and chemical processes involved. Very little information is available on the pressure drop and heat transfer characteristics within a catalyst bed, making a meaningful investigation at this time beyond the scope of this program.

Nonvented Oxidizer Tanks

Each lb of vented hydrogen vapor, when heated from its saturation temperature to that of liquid oxygen, absorbs energy equivalent to the latent heat of 3 lb of oxygen. When the thermal protection systems for a vehicle's hydrogen tanks and oxygen tanks are optimized individually, the optimum oxygen boiloff is approximately half the hydrogen loss. Therefore, the capacity of the vented vapor is more than sufficient to absorb all of the energy input to the oxidizer tank and negate the need for venting. For the Mission (2) vehicle this results in a total weight savings in excess of 200 lb. This appears to be the most profitable vent gas utilization.

Slush Hydrogen

The heat of fusion of the solid plus the sensible heat capacity of the liquid in rising to the boiling temperature results in a significant reduction in the propellant boiloff, compared to a 1 atmosphere liquid loading. The percent usable propellant is shown in Fig. VI-21, assuming that boiling will occur when the tank pressure reaches 28 psi (mixed temperature = 41.2°R). For 60 percent solid, boiloff is eliminated if the total heat input is less than 50 Btu per lb of propellant, providing there is no stratification. For the Mission (2) vehicle this means that venting would not be required for the first 200 days; the Missions (1) and (3) vehicles would not have to be vented at all.

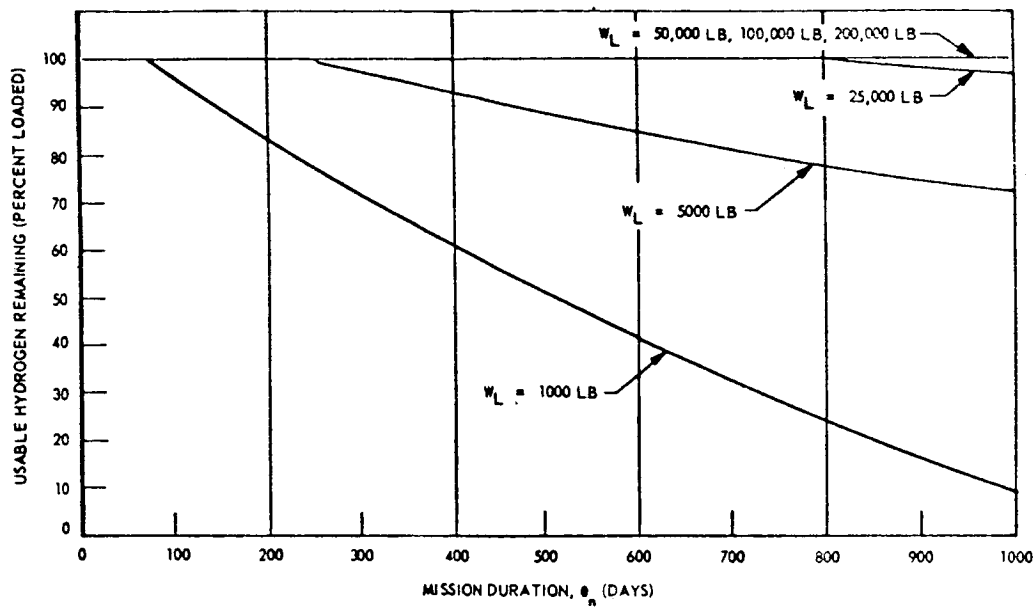

Fig. VI-21 Percent Usable Hydrogen vs Mission Duration (50 Percent Slush)

One cannot, however, depend upon continuous thermodynamic equilibrium with slush hydrogen any more than with all liquid. In either case, the possibility exists of local superheating, with the associated increased rate of pressure rise. Thus, a zero-g propellant thermal conditioning system will likely be required with slush, but the functional requirements will depend upon the vehicle size.

Consider the Missions (1) and (3) vehicles. Since the thermal capacity of the propellant is sufficient to absorb all of the incoming heat, the thermal conditioning system might consist only of a mixer and drive unit which is controlled to operate when the tank pressure reaches 28 psi. Thus, it would operate intermittently for nonuniform heating, each time bringing the tank contents into thermal equilibrium. For uniform energy absorption, the system would not be actuated throughout the entire mission.

Consider, now, the Mission (2) vehicle which must be vented at some point in time.

If one assumes that the incoming heat is uniformly absorbed throughout the propellant until such time as the tank comes up to the desired storage condition, then the thermal conditioning system for maintaining that state will be the same as though the tank was initially loaded with liquid. Only the operating time is different.

The practical thermal conditioning system, however, will consist of the same functional components but will have a separate control on the mixer. This control will actuate the mixer at a pressure slightly lower than the vent pressure. Therefore, in the case of stratified propellant, the mixer will function in the manner described for Missions (1) and (2). When the propellant has absorbed sufficient energy to raise the equilibrium pressure above the mixer actuation pressure, the tank pressure will continue to rise as a mixed propellant until it reaches the vent pressure, at which time the solenoid valve will be actuated and the vent system will operate as a zero-g liquid propellant thermal conditioning system.

SYMBOLS AND ABBREVIATIONS

R – Component or Subsystem Reliability, $e^{-\lambda t}$

λ – Failure rate/hr

t – Mission Time, hr

MTBF – Mean Time Between Failures, $1/\lambda$

Q – Probability of Failure of Single Part

Q_S – Probability of Failure of Quadredundant Assembly

ΔE – Wall Energy Added to Ullage, Btu

R – Universal Gas Constant

M – Weight of Gas in the Ullage, lb

ρ_w – Density of Tank Wall Material, lb/ft^3

δ_w – Thickness of Tank Wall, ft

A_w – Unwetted Tank Surface Area, ft^2

C_{P_w} – Specific Heat of Tank Wall, Btu/lb-^oR

$\overline{T}_w$ – Average Temperature of the Tank Wall, ^oR

T_L – Temperature of the Liquid Propellant, ^oR

Q_w – Heat Transfer From Walls, Btu/hr

U_o – Liquid Velocity up Wall, ft/sec

Q_c – Heat Removed by Condensation, Btu/hr

h_c – Condensation Coefficient, Btu/hr-ft^2-^oR

$\overline{T}_g$ – Average Temperature of the Ullage Gas, ^oR

K_ℓ – Thermal Conductivity of the Liquid Propellant, Btu/hr-ft-^oR

Section VII
REFERENCES

CITED

1. P. Dergarabedian, "The Rate of Growth of Vapor Bubbles in Superheated H_2O, Journal of Applied Mech., Dec, 1963
2. J. H. Keenan, Thermodynamics, Wiley & Sons, New York, 1954
3. J. C. Chen, A Correlation for Boiling Heat Transfer to Saturated Fluids in Convective Flow, ASME Paper No. 63-HT-34, 1963
4. R. C. Hendricks, et. al., Experimental Heat Transfer and Pressure Drop of Liquid Hydrogen Flowing Through a Heated Tube, NASA TN D-765, 1961
5. W. J. O'Reilly and E. F. Busch, Study of Remote Storage Evaporative Oil Cooling Systems for High Performance Aircraft, WADD Tech. Report 60-918, Jan 1961 Jan 1961
6. R. W. Lockhart and R. C. Martinelli, " Proposed Correlation of Data for Isothermal Two-Phase, Two-Component Flow in Pipes," Chem. Eng. Prog., Vol. 45, No. 1, 1949
7. R. C., Martinelli and D. P. Nelson, "Prediction of Pressure Drop During Forced Circulation of Water," Trans. ASME, 70, 695-702, 1948
8. J. C. Seader, W. D. Miller, and L. A. Kaluinskes, Boiling Heat Transfer for Cryogenics, NASA CR-243, Jun 1965
9. E. G. Brentari, P. J. Giarratano, and R. V. Smith, Boiling Heat Transfer for Oxygen, Nitrogen, Hydrogen, and Helium, NBS Tech. Note No. 317, 20 Sep 1965
10. R. J. Richards, W. G. Steward, and R. B. Jacobs, A Survey of the Literature on Heat Transfer from Solid Surfaces to Cryogenic Fluids, NBS Tech. Note No. 122, Oct 1961

11. D. E. Drayer and K. D. Timmerhaus, "An Experimental Investigation of the Individual Boiling and Condensing Heat-Transfer Coefficients for Hydrogen," Advances in Cryogenics, Vol. 7, Plenum Press, 1962, p. 401

12. H. H. Walters, "Single-Tube Heat Transfer Tests with Liquid Hydrogen," Advances in Cryogenic Engineering, Vol. 6, Plenum Press, 1960, pp. 509-516

13. R. J. Richards, R. F. Robbins, R. B. Jacobs, and D. C. Holten, "Heat Transfer to Boiling Liquid Nitrogen and Hydrogen Flowing Axially Through Narrow Annular Passages," Advances in Cryogenic Eng., Vol. 3, Plenum Press, 1957, pp. 375-389

14. S. G. Sydoriak and T. R. Roberts, " A Study of Boiling in Short Narrow Channels and Its Application to Design of Magnets Cooled by Liquid H_2 and N_2," J. Appl. Physics, 28: 143-148, 1957

15. T. C. Core, J. F. Harkee, B. Misra, and K. Sato, Heat Transfer Studies, Aerojet-General Report No. 1671, WADD 60-239, 1959

16. R. C. Mitchell, Study of Zero-Gravity, Vapor/Liquid Separators, General Dynamics Convair Report GDC-DDB-009 (Contract NAS 8-20146), Jan 1966

17. W. H. McAdams, Heat Transmission, McGraw-Hill, New York, 1954

18. G. K. Batchelor, "On Steady Laminar Flow with Closed Streamlines at Large Reynolds Number," J. Fluid Mech., Vol. 1, 1956, p. 177

19. G. E. Myers, J. J. Schauer, and R. H. Eustis, The Plane Turbulent Wall Jet, Part II, Dept. Mech. Eng., Stanford University, NSF G9705

20. M. B. Glauert, "The Wall Jet," J. Fluid Mech., Vol. 1, 1956, p. 625

21. G. E. Myers, J. J. Schauer, and R. H. Eustis, The Plane Turbulent Wall Jet, Part I, Dept. Mech. Eng. Stanford University, NSF G9705

22. -----, Heat Transfer to Plane Turbulent Wall Jets, ASME Paper No. 62-HT-33

23. J. O. Hinze, Turbulence, McGraw-Hill, 1959, p 541

UNCITED

Abramovich, Turbulent Jets and Wakes

S. J. Coloprete, Preliminary Investigation For A Zero-Gravity Water Separator, NA-63-1097, 23 Sep 1963

M. P. Hollister, Propellant Containment Utilizing Screen Mesh and Perforated Plate Materials, LMSC-A665481, 29 Dec 1964

S. F. Horner, Fluid Dynamic Drag, Published by author, 1958

Kruka, and Eskinazi, "The Wall-Jet in a Moving Stream," J. Fluid Mech., Vol. 20, 1964, p. 555

W. H. Schwarz and W. P. Cosart, "The Two-Dimensional Turbulent Wall Jet," J. Fluid Mech., Vol. 10, 1961, p. 481

A. Sigalla, "Experimental Data on Turbulent Wall Jets," Aircr. Eng., Vol. 30, 1958, p 131

APPENDIXES

Appendix A

VAPOR BUBBLE DETACHMENT

A possible use of the mixing unit is to dislodge hydrogen vapor bubbles as they are formed at hot spots in the tank before they can grow to such a size as to seriously influence the tank pressure. The liftoff volume of bubbles from horizontal surfaces as a function of liquid surface tension, density, and the contact angle is well established theoretically and experimentally. The literature contains no information which would enable the calculation of the critical size of a bubble attached to a vertical surface. If such a relation were available, dynamic pressure forces could be substituted for buoyant forces, enabling calculation of the necessary velocity for a given size bubble.

Lacking the necessary relation, the following simple theory developed by Satterlee is presented as a means of obtaining a rough estimate of velocity requirements. Consider the bubbles shown in the two views below. Liquid is blowing onto the bubble from the right with velocity u , bending it toward the left relative to its equilibrium axis.

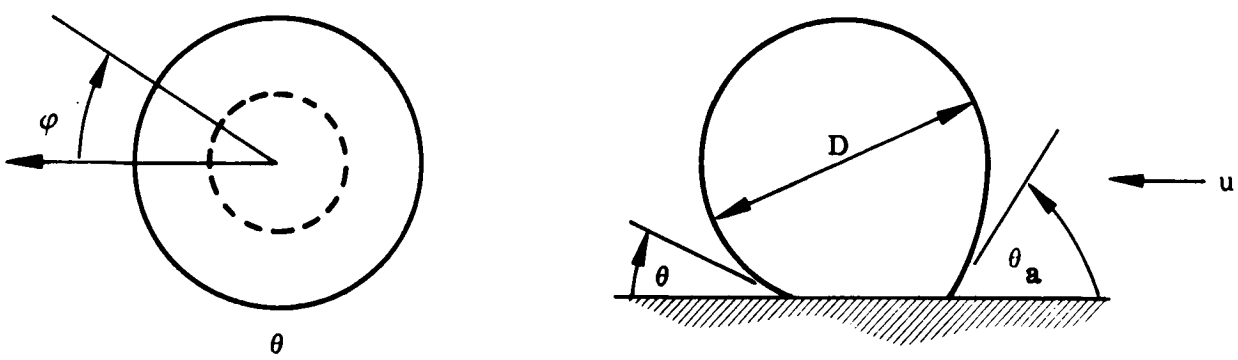

A force balance on the bubble relating dynamic pressure forces to the sum of surface tension forces around the footprint of the bubble results in

$$C_D \frac{\rho u^2}{2g_c} = 2\sigma r \sin \theta_m \int_0^{\pi} \cos \phi \cos \theta \, d\phi \qquad \text{(A .1)}$$

Assuming that θ is given by

$$\theta = \theta_m - \frac{\theta_a - \theta_r}{2} \cos \phi \qquad \text{(A .2)}$$

where $\theta_m = 0.5(\theta_a + \theta_r)$, Eq. (A.1) can be evaluated to obtain

$$\frac{\rho D u^2}{\sigma} = 2 \frac{\sin 2\theta_m}{C_D} J_o \frac{\theta_a - \theta_r}{2} \qquad \text{(A .3)}$$

When the fluid properties appropriate to liquid hydrogen are inserted [$C_D \sim 1$, $\sigma/\rho \sim 30\ cm^3/sec^2$, $\theta_a = 1$ deg, $\theta_r = 0$ deg, $\theta_m = 0.5\ (\theta_a + \theta_r) = 0.5$ deg], the velocity requirement is calculated to be approximately 0.1 ft/sec for a 0.1-in.-diameter bubble. This value of bubble detachment velocity neglects the effects of velocity gradients in the wall boundary layer.

SYMBOLS AND ABBREVIATIONS

θ – Local Contact Angle, deg

θ_m – Average Contact Angle, deg

C_D – Drag Coefficient

g_c – Gravitational Constant

r – Bubble Radius, ft

σ – Surface Tension, lb/ft

ρ_ℓ – Liquid Density, lb/ft^3

K_o – Bessel Function of Zero Order

D – Bubble Diameter, ft

Appendix B

VAPOR BUBBLE CONDENSATION

If only liquid is circulated through the heat exchanger and mixer, then proper tank pressure response will require that this circulating liquid be brought in contact with and condense the vapor in the tank. The classical theories of vapor condensation deal with streamline flow where the condensate is removed by gravitational forces. A theory is developed herein which is applicable in a circulating flow field, in zero-gravity fields.

Consider a cooler fluid, with velocity u_0, passing over a pure vapor in the absence of gravity. Some condensation occurs on the moving stream; a condensate film of thickness y is deposited and flows along with the free stream. In a streamline flow, this condensate film will remain in tact, having a laminar velocity profile.

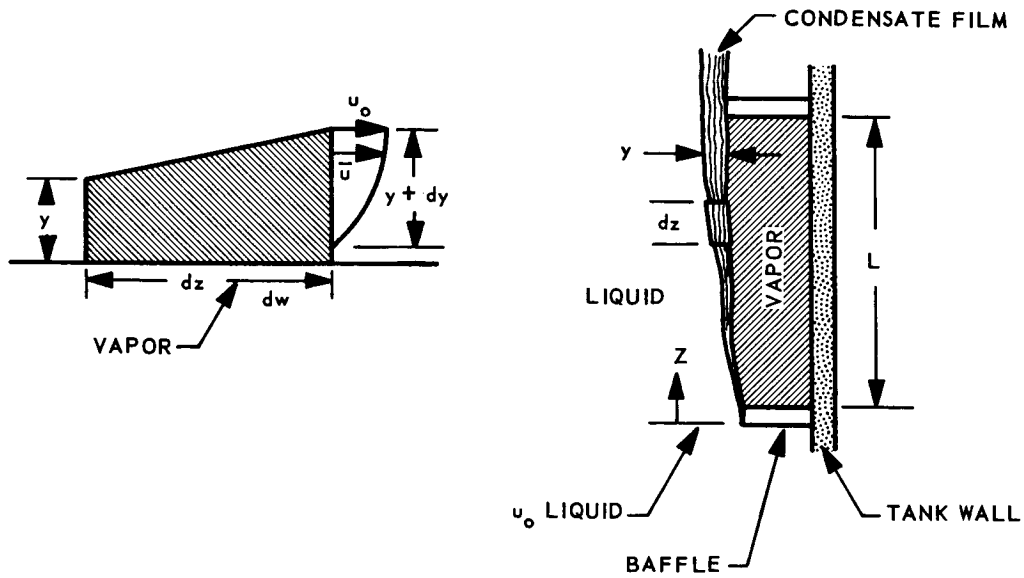

The heat transferred by conduction only across an element of the condensate film having a local thickness of y gives the equation

$$dQ_z = \left(\frac{k_\ell}{y}\right) \Delta T \, dA = \left(\frac{k_\ell}{y}\right) \Delta T \, (b)dz = h_y \, \Delta T \, (b)dz \tag{B.1}$$

This quantity of heat transferred is also equal to the condensation heat of the condensate film. Therefore,

$$\left(\frac{k_\ell}{y}\right) \Delta T \, (b)dz = \lambda \, d\omega_z \tag{B.2}$$

For the entire length L of the vapor pocket, by definition,

$$h_m = \frac{\lambda \omega}{bL \Delta T} \tag{B.3}$$

Combining these three equations, to eliminate ΔT which is assumed constant, gives

$$\frac{k_\ell}{y} = \frac{h_m L \, d\omega_z}{\dot{w} \, dz} \tag{B.4}$$

The local mass flow in the layer is given by

$$\omega_z = \rho_\ell \, \bar{u} \, b \, y \tag{B.5}$$

Eliminating y from Eqs. (B.4) and (B.5), yields

$$\left(\frac{h_m L}{\dot{w}}\right) \omega_z \, d\omega_z = k_\ell \, \rho_\ell \, \bar{u} b \, dz \tag{B.6}$$

Integrating Eq. (B.6) from O to L and O to $\dot{w}$ and assuming that the u_0 and therefore $\bar{u}$ is constant yields

$$k_\ell \rho_\ell \bar{u} b = h_m (\omega/2) \tag{B.7}$$

Eliminating $\dot{\omega}$ from Eqs. (B.3) and (B.7) gives

$$h_m^2 = \frac{2 k_\ell \rho_\ell \lambda \bar{u}}{L \Delta T} \tag{B.8}$$

Equation (B.8) can be rewritten in terms of constant free-stream velocity. Therefore,

$$h_m = \left[\frac{2 k_\ell \rho_\ell \lambda u_0}{L \Delta T} \left(\frac{u}{u_0}\right)\right]^{1/2} \tag{B.9}$$

Consistent with the assumption of streamline flow, the term $\bar{u}/u_0$ will have a fixed value of 0.625. Substituting this value into Eq. (B.9) gives the desired equation for the streamline flow forced convection heat transfer coefficient

$$h_m = 1.12\left(\frac{k_\ell \rho_\ell \lambda u_0}{L \Delta T}\right)^{1/2} \tag{B.10}$$

across a vapor-liquid interface in a zero-gravity field.

SYMBOLS AND ABBREVIATIONS

ω – Vaporization Rate, lb/sec

k_ℓ – Thermal Conductivity of the Liquid, Btu/hr-ft-^{o}R

b – Tank Circumference in the Region of the Baffles, ft

y – Condensate Film Thickness, ft

z – Condensate Film Length, ft

λ – Heat of Vaporization, Btu/lb

h_m – Average Condensation Coefficient, Btu/hr-ft^2-^{o}R

L – Distance Between Baffles, ft

ΔT – Temperature Difference Between Liquid and Vapor, ^{o}R

ρ_ℓ – Liquid Density, lb/ft^3

$\bar{U}$ – Average Velocity in Condensate Layer, ft/sec

Appendix C

TANK PRESSURE DECAY RATE

Having related the induced circulation velocities to vapor condensation rates, the effect on tank pressure response can now be determined. The theoretical model used herein is shown in the sketch below and is the same conservative model used in developing the condensation heat transfer coefficient.

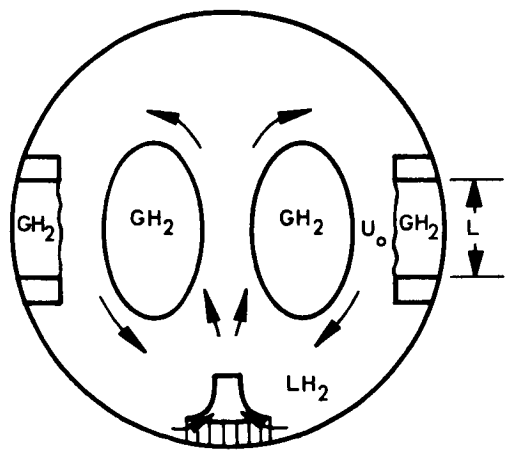

The pressure in the tank is everywhere uniform and described by the perfect gas law

$$P = \frac{M_g}{V_g} RT \tag{C.1}$$

A mass and volume balance on the entire system gives

$$M_g = M_T - M_\ell \tag{C.2}$$

$$V_g = V_T - V_\ell \tag{C.3}$$

Combining these three equations, we get

$$\frac{P\,V_g}{R\,T_g} = M_T - \rho_\ell\,V_\ell + \rho_\ell\,V_g \tag{C.4}$$

Differentiating this equation and simplifying, we get

$$\frac{1}{P}\frac{dP}{d\theta} - \frac{1}{T}\frac{dT}{d\theta} = \left(\frac{\rho_\ell}{\rho_g} - 1\right)\frac{1}{V_g}\frac{dV_g}{d\theta} \tag{C.5}$$

It is assumed that the pressure decay is sufficiently rapid that the vapor expansion or contraction is adiabatic. Therefore,

$$T = T_0\left(\frac{P}{P_0}\right)^{\frac{\gamma - 1}{\gamma}} \tag{C.6}$$

Differentiating this gives

$$\frac{P}{T}\frac{dT}{d\theta} = \frac{\gamma - 1}{\gamma}\frac{dP}{d\theta} \tag{C.7}$$

When this is substituted into the previous differential equation and simplified, we get

$$\frac{dP}{d\theta} = \frac{\gamma P}{V_g}\left(\frac{\rho_\ell}{\rho_g} - 1\right)\frac{dV_g}{d\theta} \tag{C.8}$$

But $\frac{\rho_l}{\rho_g} >>> 1$. Therefore,

$$\frac{dP}{d\theta} = \frac{\gamma P}{V_g}\left(\frac{\rho_\ell}{\rho_g}\right)\frac{dV_g}{d\theta} \tag{C.9}$$

The rate of heat transfer from the vapor to the liquid is given by

$$Q = \lambda \frac{dM_g}{d\theta} \tag{C.10}$$

But, from the mass and volume balances,

$$\frac{dM_g}{d\theta} = \rho_\ell \frac{dV_g}{d\theta} \tag{C.11}$$

Therefore, we get

$$\frac{dV_g}{d\theta} = \frac{Q}{\rho_\ell \lambda} \tag{C.12}$$

When this is substituted into the expression for pressure response, we get

$$\frac{dP}{d\theta} = \frac{\gamma P}{V_g}\left(\frac{\rho_\ell}{\rho_g}\right)\frac{Q}{\rho_\ell \lambda} \tag{C.13}$$

Another expression for the rate of heat transfer is:

$$Q = h_m A \Delta T \tag{C.14}$$

and then we have

$$\frac{dP}{d\theta} = \frac{\gamma P}{V_g}\left(\frac{\rho_\ell}{\rho_g}\right)\left(\frac{\Delta T}{\rho_\ell \lambda}\right) A h_m \tag{C.15}$$

This expression is general and may be applied to various ullage volumes and heat transfer areas.

For the diagram shown, if no heat transfer occurs, we then have the worst situation, where pressure is diminished only by cooling the gas trapped between the slosh baffles. If the wall curvature is neglected (i.e., $R/L >> 1$), the area for heat transfer is

$$A = b\,L \tag{C.16}$$

The condensation coefficient developed previously is

$$h_m = 1.12\left(\frac{k_\ell\ \rho_\ell\ u_0\ \lambda}{L\ \Delta T}\right)^{1/2}$$

Substituting these into Eq. (A.28), we get

$$\frac{dP}{d\theta} = \gamma\ P\left(\frac{\rho_\ell}{\rho_g}\right)\left(\frac{\Delta T}{\rho_\ell\ \lambda}\right)\left(\frac{b\,L}{V_T}\right)\left(\frac{V_T}{V_g}\right)\left(\frac{k_\ell\ \rho_\ell\ u_0\ \lambda}{L\ \Delta T}\right)^{1/2} \tag{C.17}$$

This shows that the pressure response in a hydrogen tank is dependent upon the tank and baffle geometry, the precent ullage, the available temperature difference, and the stream velocity.

SYMBOLS AND ABBREVIATIONS

P – Pressure in Tank, psi

M_g – Mass of Gas, lb

M_L – Mass of Liquid, lb

M_T – Total Mass, lb

R – Gas Constant

T_g – Temperature, ^oR

V_g – Volume of Gas, ft^3

V_T – Total Volume, ft^3

V_L – Volume of Liquid, ft^3

$\frac{dp}{d\theta}$ – Rate of Change of Tank Pressure, psi/sec

γ – Rate of Specific Heats

ρ_g – Density of Ullage Gas, lb/ft^3

Q – Heat Transfer Rate, Btu/hr

h_m – Condensation Heat Transfer Coefficient, $Btu/hr\text{-}ft^2\text{-}^oR$

A – Heat Transfer Area at Liquid Vapor Interface, ft^2

b – Tank Circumference in the Region of the Baffles, ft

L – Distance Between Baffles, ft

Appendix D

TANK PRESSURE RISE IN STRATIFIED PROPELLANT

Consider a propellant tank at time zero, for which the liquid and ullage are in thermodynamic equilibrium, with a single ullage as shown in the sketch below.

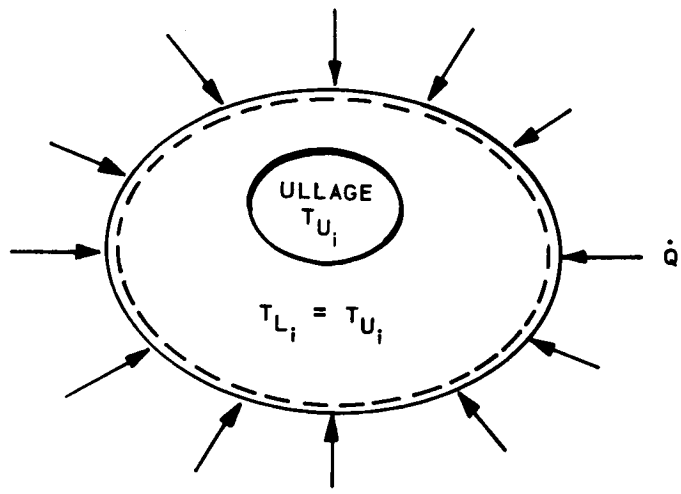

A heating rate Q is entering the tank and creating vapor such that, at some time θ, the conditions indicated by the dotted lines exist. The newly created vapor occupies approximately 40 times the volume it did as liquid. Considering the liquid to be incompressible relative to the vapor, this expansion of liquid upon vaporizing creates a change in pressure by compressing the initial ullage and restricting the growth of the newly created vapor layer. Since pressure is uniform throughout the tank, we can say

$$P_1 = \frac{M_1}{V_1} RT_1 = \frac{M_2}{V_2} RT_2 \qquad \text{(D. 1)}$$

where subscripts [Eq. (D.1)] refer to the mass in the initial ullage bubble and subscripts [Eq. (D.2)] refer to the vapor formed at the tank wall. The former is assumed removed from the tank wall and thus, it is compressed isothermally by the growth of the vapor layer. We can say

$$\frac{\Delta P_1}{\Delta \theta} = - \frac{\left(M_1 R_1 T_1\right)}{V_1^2} \frac{\Delta V_1}{\Delta \theta}$$

$$\frac{\Delta P_2}{\Delta \theta} = \frac{M_2 R}{V_2} \frac{\Delta T_2}{\Delta \theta} + \frac{R T_2}{V_2} \frac{\Delta M_2}{\Delta \theta} - \frac{M_2 R T_2}{V_2^2} \frac{\Delta V_2}{\Delta \theta} \tag{D.2}$$

A total volume balance gives

$$\frac{\Delta V_1}{\Delta \theta} + \frac{\Delta V_2}{\Delta \theta} + \frac{\Delta V_\ell}{\Delta \theta} = 0 \tag{D.3}$$

Considering the liquid to be incompressible a mass balance gives

$$\frac{\Delta V_\ell}{\Delta \theta} = - \left(\frac{\Delta M_2}{\Delta \theta}\right) \frac{1}{\rho_\ell} \tag{D.4}$$

An energy balance on the system gives

$$Q = \frac{\Delta M_2}{\Delta \theta} \lambda + M_2 C_{p_g} \left(\frac{\Delta T_2}{\Delta \theta}\right) \tag{D.5}$$

Combining Eqs. (D.1) through (D.5) results in the following general expression for the rate of pressure rise, which includes both vaporization and vapor superheat

$$\frac{\Delta P}{\Delta \theta} = \frac{1}{V_1 + V_2} \left[\frac{R_g}{C_p} Q - \left(\frac{R_g \lambda}{C_{p_g}} \sim R_g T_2 + \frac{P_1}{\rho_\ell} \right) \frac{\Delta M}{\Delta \theta} \right] \tag{D.6}$$

The first term on the right is the equivalent of putting all the heat into the initial ullage volume. This represents the maximum rate of pressure rise. Vapor generation and bubble superheat will result in lower rates, i.e.,

$$\left(\frac{\Delta P}{\Delta \theta}\right)_{max} = \frac{R}{V_1 C_p} Q$$

This can be rewritten to give

$$\left(\frac{\Delta P}{\Delta \theta}\right)_{max} = \frac{R}{\left(V_1/V_T\right) C_p} \frac{Q}{V_T} \tag{D.7}$$

V_1/V_T is the minimum percent ullage volume (at least 5 percent for cryogenic stages). Q/V_T is the heating rate per unit tank volume. The specific missions of interest in Task II encompass a wide spectrum of values for Q/V_T. The maximum rates of pressure rise for these three missions are:

Mission I : $(\Delta P/\Delta \theta)_{max} = 4.8$ psi/hr

Mission II : $(\Delta P/\Delta \theta)_{max} = 2.2$ psi/hr

Mission III: $(\Delta P/\Delta \theta)_{max} = 0.04$ psi/hr

From these, it would seem vent frequency in the absence of mixing does not impose severe response requirements upon the components.

SYMBOLS AND ABBREVIATIONS

P – Tank Pressure, psi

V_1, V_2 – Vapor Volumes, ft^3

M_1, M_2 – Mass of Vapor in Volumes V_1, V_2, lb

T_1, T_2 – Temperature of M_1, and M_2, ^oR

R – Gas Constant

$\frac{\Delta p}{\Delta \theta}$ – Rate of Change of Pressure, psi/sec

V_ℓ – Liquid Volume, ft^3

ρ_ℓ – Liquid Density, lb/ft^3

Q – Heat Transfer Rate, Btu/hr

λ – Heat of Vaporization, Btu/lb

C_{pg} – Specific Heat of Gas, Btu/lb-^oR

Appendix E

SINGLE WALL-BOUND JET

Since no analytic model of a single wall-bound jet in a spherical tank was found in available literature, the mixing phenomenon in a propellant tank in a zero-g field as predicted from an axisymmetric analysis has been developed. A jet leaving a pump at the bottom of sphere will quickly become a wall jet almost in pure radial outflow. This becomes a two-dimensional wall jet at the equator, then approaches a radial inflow jet as it progresses in the upper half of the sphere. Separation from the wall will occur somewhere in the upper part of the sphere of a full tank, and some of the wall jet fluid returns down the vertical axis of symmetry to the pump. The natural thickening of the wall jet is partially counteracted in the lower half by the axisymmetric thinning effect of increasing circumference; and the thickening is aided by this effect in the upper half. When the jet flow is initiated, the central fluid is at rest; but it gradually arrives at a steady-state motion of a nonisentropic toroidal vortex. At this steady-state condition, the core flow is separated from the wall jet by an axisymmetric stream sheet, shown as a stream line in the cross section cut through the tank in the following schematic. Friction on this dividing stream line near the

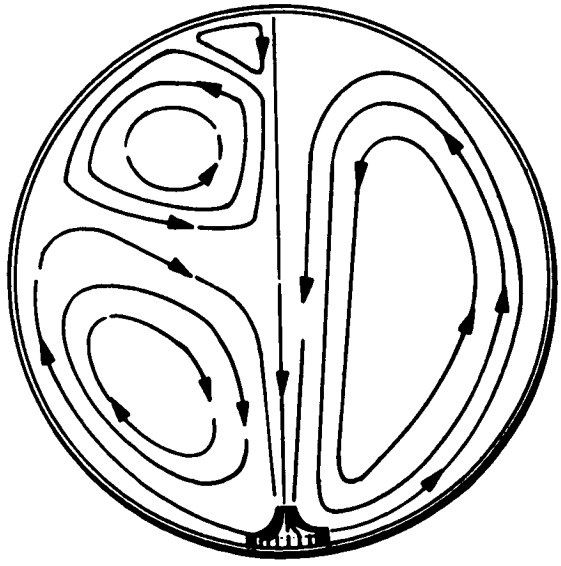

pump exit provides an energy input to the vortex which is partially redeemed elsewhere where the vortex will help drag the wall jet along. For axisymmetric steady flow, an integral condition can be shown (Ref. 18) to the effect that the net diffusion of (radius) x (vorticity) across the dividing streamline is zero. Boundary layer separation may even occur not too far above the equator, and one more or even several more closed vortexes may form as shown in the left half of the above schematic. For a given full tank and starting wall jet, geometry dimensional analysis shows that the fluid motion is solely a function of a characteristic Reynolds number, and the heat transfer, of Reynolds and Prandtl numbers.

To predict the wall heat transfer q_w, certain characteristics of the jet at each point, such as skin friction τ_w, maximum velocity u_m, and/or distance from the wall to the point of the maximum velocity δ_m, are needed, depending on the type of heat transfer equation used. Thus the fluid mechanics problem is considered first.

The effect of the toroidal vortex, while no doubt very important, has necessarily been neglected in this analysis, as only the most sophisticated, costly computer programming could include the vortex at this time. From results of this analysis, an order-of-magnitude estimate can be made of the toroidal vortex strength and its effect on the wall jet.

We apply the moment of momentum equation about the center of a sphere with radius R and use angles θ and ϕ in two mutually perpendicular planes as shown in the following schematics. In steady flow, the moment of momentum equation is: Sum of torques on control volume = net angular momentum flux out of control volume.

Applying this to the control volume of length ds and width $R \sin\theta \, d\phi$ and extending from the wall to some arbitrary distance δ_i from the wall where the shear is τ_i, results in (assuming $\delta << R$):

$$-R\,(\tau_w + \tau_i)\, ds\, R \sin\theta\, d\phi$$

$$= \frac{d}{ds}\left(R^2 \sin\theta\, d\phi \int_0^{\delta_i} \rho\, u^2\, dy\right) ds + m_i\, u_i\, R^2 \sin\theta\, d\phi\, ds \qquad \text{(E.1)}$$

This also assumes constant pressure along the wall.

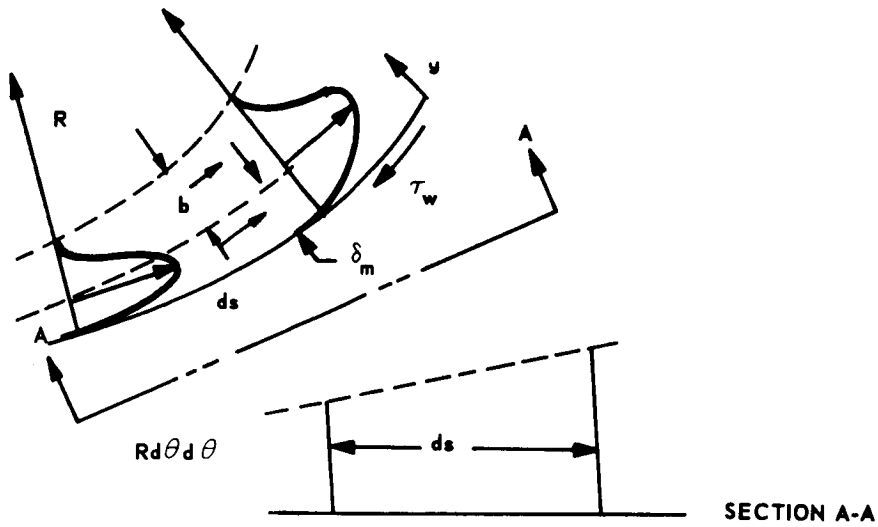

CONTROL VOLUME NOTATION

The continuity equation applied to the same control volume yields

$$\frac{d}{ds}\left(R \sin\theta \; d\phi \; \rho \int_0^{\delta_i} u dy\right) ds + m_i R \sin\theta \, d\phi \; ds = 0 \qquad \text{(E. 2)}$$

Combining these equations to eliminate m_i, and reducing:

$$-R \frac{(\tau_w + \tau_i)}{\rho} = \frac{d}{d\theta}\int_0^{\delta_i} u^2 dy + \frac{1}{\tan\theta}\int_0^{\delta_i} u^2 dy - u_i \frac{d}{d\theta}\int_0^{\delta_i} u dy$$

$$- \frac{u_i}{\tan\theta}\int_0^{\delta_i} u dy \qquad \text{(E. 2a)}$$

If the control volume extends to the edge of the wall jet then τ_i and $u_i = 0$.

We now pick inner and outer velocity profile shapes which are to join at the position δ_m of maximum velocity u_m. For the inner part, a power law fit is used as it is very useful in boundary layer type profiles and has been used in many of the plane wall jet analyses:

$$0 < y < \delta_m \quad ; \quad u/u_m = \left(y/\delta_m\right)^{1/n} \tag{E.3}$$

where n is an unspecified constant. Two useful integrals are

$$\int_0^1 \frac{u}{u_m}\, d\left(\frac{y}{\delta_m}\right) = \frac{n}{n+1} \quad ; \quad \int_0^1 \left(\frac{u}{u_m}\right)^2 d\left(\frac{y}{\delta_m}\right) = \frac{n}{n+2}$$

Abramovich proposes the following form for the outer half of the profile:

$$u/u_m = \left(1 - \xi^{3/2}\right)^2 \quad \text{where} \quad \xi = \frac{y - \delta_m}{b} \tag{E.4}$$

where the quantity b is the width of the outer part of the boundary layer.

The following integral is needed:

$$\int_0^1 \left(1 - \xi^{3/2}\right)^4 d\xi = 0.31$$

Introducing Eqs. (E.3) and (E.4) into Eq. (E.2a) for a control volume that includes the total jet thickness yields

$$-\frac{R}{\rho}\tau_w = \frac{d}{d\theta}\left(\frac{n}{n+2}\, u_m^2\, \delta_m + 0.31\, u_m^2 b\right) + \frac{1}{\tan\theta}\left(\frac{n}{n+2}\, u_m^2\, \delta_m + 0.31\, u_m^2 b\right) \tag{E.5}$$

Here we have five unknown dependent variables: τ_w, u_m, δ_m, b, and n.

Glauert, Meyers, and others have all used Blasius' turbulent skin friction relationship and based it on u_m and δ_m (but the coefficient is here changed from their value as explained later):

$$\frac{\tau_w}{\rho} = 0.0620\, u_m^2 \left(\frac{\nu}{u_m\, \delta_m}\right)^{1/4} \tag{E.6}$$

Combining,

$$-0.0620\, R\, u_m^2 \left(\frac{\nu}{u_m\, \delta_m}\right)^{1/4} = \frac{d}{d\theta}\left(\frac{n}{n+2}\, u_m^2\, \delta_m + 0.31\, u_m^2 b\right) + \frac{1}{\tan\theta}\left(\frac{n}{n+2}\, u_m^2\, \delta_m + 0.31\, u_m^2 b\right) \tag{E.7}$$

This skin friction relationship implies the 1/7-power velocity profile often used. However, we will keep n an unspecified constant and obtain solutions for several values of n to see its effect. Meyers et al. (Ref. 19) found the best fit n to be about 13. We still need two more relationships. Using a control volume which only extends out from the wall to the locus of points where $u = u_m$, momentum and continuity equations can be written which add no new variables. For this case $u_i = u_m$, $\tau_i = 0$, $\delta_i = \delta_m$ and using the above Blasius' relationship,

$$-0.0620\, R \left(\frac{\nu}{u_m\, \delta_m}\right)^{1/4} = -\frac{u_m^2\, \delta_m}{\tan\theta}\, \frac{n}{(n+2)(n+1)} + \frac{n}{(n+2)}\, \frac{d}{d\theta}\left(u_m^2\, \delta_m\right) - \frac{n}{(n+1)}\, u_m\, \frac{d}{d\theta}\left(u_m\, \delta_m\right) \tag{E.8}$$

One more relationship is still needed. The characteristic outer layer thickness b should be related to the inner layer. Glauert (Ref. 20) uses instead the width δ_t, which is the width from the maximum velocity point to the point where the velocity has dropped to half this value. Glauert solved two nonlinear ordinary differential equations, one each for inner and outer regions and matched these solutions together at u_m. His Fig. 3, which shows the solutions for a radial turbulent jet for: dimensionless stream function at u_m, denoted f_{om}; maximum velocity, u_m; inner thickness, δ_m; and outer thickness, δ_t, for various values of his parameter α, is included here as Fig. E-1. In his Table 1, he relates α to Reynolds number by assuming k, the proportionality factor for the eddy mixing in the outer half of the jet, to be $k = 0.012$ (Bakke suggests 0.013 from his experiment). Fortunately, the solutions given in Fig. E-2 also apply to the plane jet, meaning that the transformed velocity profiles are identical. This could be expected, actually, according to Mangler's axisymmetry transformation. Most important, the same transformed (affinely stretched) profiles can be expected to hold for any given α in the sphere. Since we are willing to be satisfied with the ratio of thicknesses δ_t/δ_m the transformation is not needed since at any given position along the wall jet the transformation for each thickness is the same; thus

$$\delta_t/\delta_m = \eta_t/\eta_m$$

This is very fortunate, since the transformation is known only for the radial and plane jet; for the sphere it can be expected to be a function of θ. Using Fig. E-1 and his α vs. Re values, η_t/η_m vs. Re is plotted on log-log paper in Fig. E-2 and found to be nicely fitted by

$$\delta_t/\delta_m = \eta_t/\eta_m = 0.775\ Re_{\delta_t}^{\ 0.192} \quad \text{where} \quad Re_{\delta_t} = \frac{u_m\ \delta_t}{\nu} \qquad (E.9)$$

This relationship is valid for the spherical wall jet if k does not vary significantly. If it does, the right-hand side should be corrected with the ratio of k's to the fourth power.

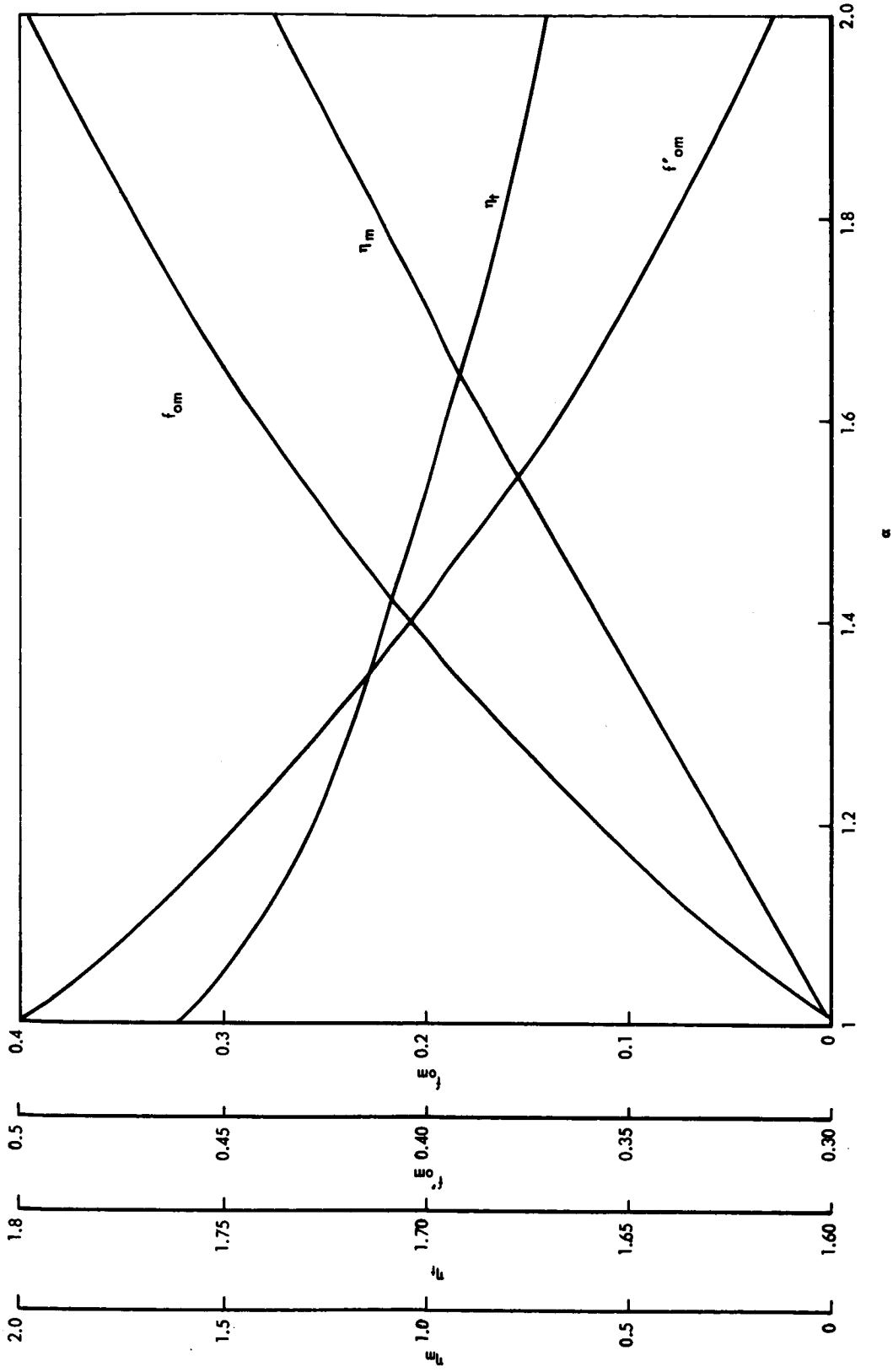

Fig. E-1 Glauert's Figure 3 — Turbulent Wall Jet Parameters

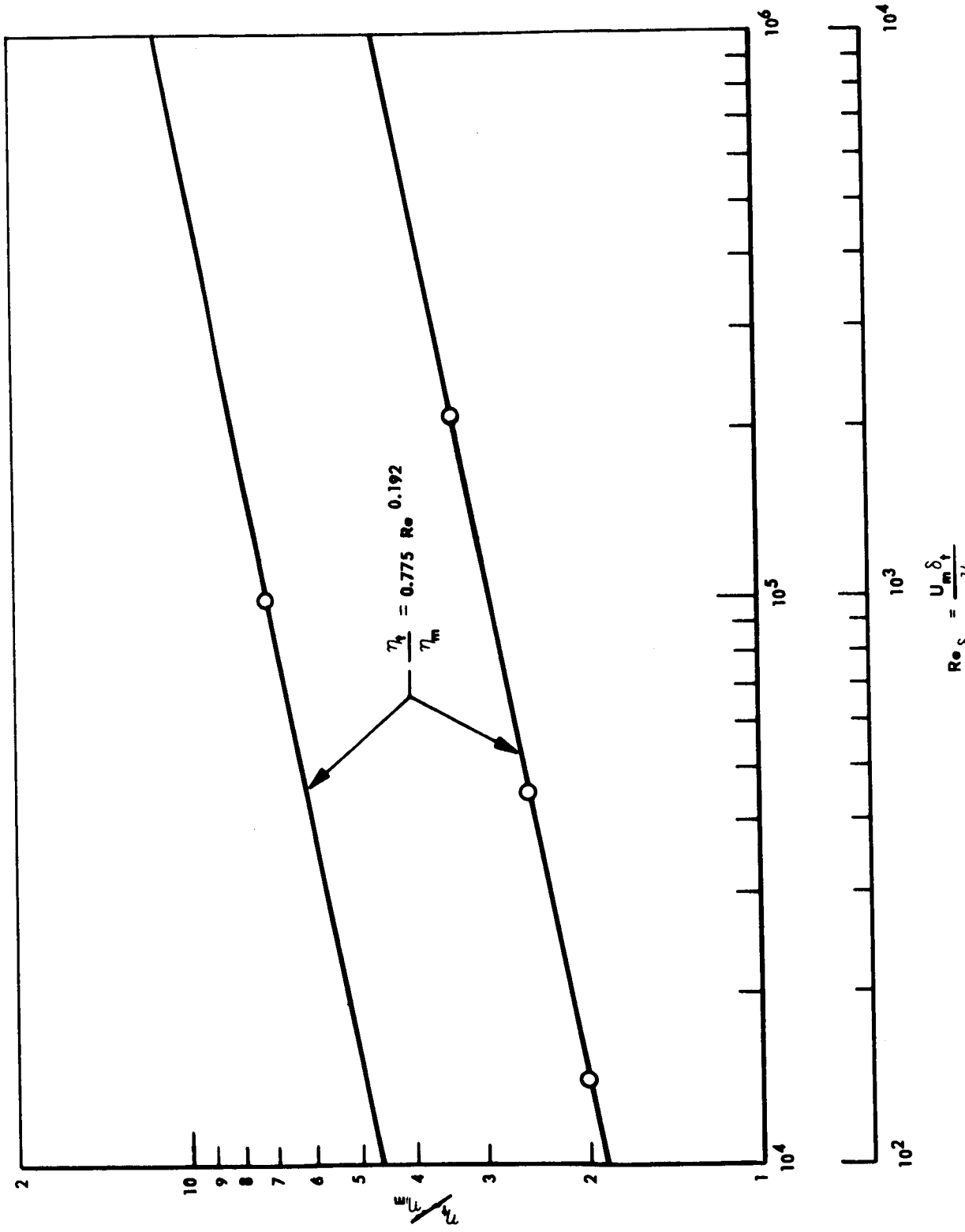

Fig. E-2 Curve Fit to Glauert's Results for Turbulent Wall Jet

It is now only necessary to relate b and δ_t. The quantity b has purposely been left rather undefined so far, but this is now corrected. Rearranging the outer profile shape given in Eq. (E.4),

$$\left(1 - \sqrt{u/u_m}\right)^{2/3} = \xi = \frac{y - \delta_m}{b} = \frac{y - \delta_m}{\delta_t} \cdot \frac{\delta_t}{b}$$

$$\frac{\delta_t}{b} = \left(1 - \sqrt{u/u_m}\right)^{2/3} \left(\frac{y - \delta_m}{\delta_t}\right)^{-1} \tag{E.10}$$

The quantity δ_t/b can be made to agree with any one point on Glauert's outer layer profile, and it is convenient to match up the point: $u/u_m = 0.5$ at $(y - \delta_m)/\delta_t = 1$.

Thus,

$$\delta_t/_b = 0.440 \tag{E.11}$$

Checking the fit at $(y - \delta_m)/\delta_t = 0.5$, Glauert has 0.83 and the momentum integral profile gives 0.805.

For $u/u_m = 0$

$$b/_{\delta_t} = 2.27$$

We now obtain the final dimensional form of the overall momentum equation. Combining Eqs. (E.9) and (E.11):

$$b = 1.76\, \delta_m \left(\frac{u_m\, \delta_t}{\nu}\right)^{0.192} \tag{E.12}$$

Combining this with Eq. (E.7),

$$\frac{dM}{d\theta} + \frac{M}{\tan\theta} = -0.0620\, u_m^2 \left(\frac{\nu}{u_m \delta_m}\right)^{1/4} R \tag{E.13}$$

where

$$M = \frac{n}{n+2} u_m^2 \delta_m + 0.511\, u_m^2 \delta_m \left(\frac{u_m \delta_m}{\nu}\right)^{0.24} \tag{E.14}$$

which is the wall jet momentum when multiplied by $\sin\theta$.

We make Eqs. (E.7) and (E.8) dimensionless by using initial values of inner jet width δ_{m_o} and maximum velocity u_{m_o}. Assuming the original equations to be written with primed quantities and indicating the dimensionless ratios formed by the original symbol (i.e., $u_m'/u_{m_o} = u_m$, $\delta_m'/\delta_{m_o} = \delta_m$, $\frac{M'}{\delta_{m_o} u_{m_o}^2} = M$), plus $\frac{R'}{\delta_{m_o}} = R_o$, and the following set of dimensionless equations is obtained:

$$-\frac{n}{n+2}\frac{1}{u_m^2}\frac{d}{d\theta} u_m^2 \delta_m - \frac{n}{(n+1)(n+2)}\frac{\delta_m}{\tan\theta} - \frac{n}{(n+1)\, u_m}\frac{d}{d\theta} u_m \delta_m = \frac{0.062\, R_o}{\left(u_m \delta_m Re_o\right)^{1/4}} \tag{E.15}$$

$$\frac{dM}{d\theta} + \frac{M}{\tan\theta} = -0.0620\, R_o \left(u_m \delta_m Re_o\right)^{-1/4} u_m^2 \tag{E.16}$$

where

$$M = \frac{n}{n+2} u_m^2 \delta_m + 0.511\, u_m^{2.24} \delta_m^{1.24} Re_o^{0.24} \quad \text{and} \quad Re_o = \frac{u_{m_o} \delta_{m_o}}{\nu} \tag{E.17}$$

With the initial conditions $u_{mo} = 1$, $\delta_{mo} = 1$ plus specified values of R_o, Re_o, and n at the initial value of θ, the fluid dynamics problem statement is complete.

In Myers, et al., (Refs. 19, 21, and 22), the heat transfer to a plane wall jet was measured and a theory developed to predict these measurements. This theory could probably be generalized to the radial jet case, but a far simpler and more satisfactory approach for the present purposes is to examine Reynolds' analogy for this wall jet. In the notation of Myers (Refs. 25 and 26), the wall heat transfer and skin friction are written using the effective eddy diffusivities of heat and momentum, ϵ_H and ϵ_M, respectively:

$$\frac{q_w}{\rho c_p} = -\epsilon_H \left(\frac{\partial T}{\partial y}\right)_{y=o} \; ; \; \frac{\tau_w}{\rho} = -\epsilon_M \left(\frac{\partial u}{\partial y}\right)_{y=o}$$

Taking the ratio of these two equations, where $\lambda = \epsilon_H/\epsilon_M$:

$$\frac{q_w}{\rho c_p \Delta} = \lambda \frac{\tau_w}{\rho} \frac{\Delta T_m}{u_m} \left(\frac{\dfrac{\partial u/u_m}{\partial y/\delta}}{\dfrac{\partial T/\Delta T_m}{dy/\delta}} \right)$$

The standard Reynolds' analogy is to assume the dimensionless velocity and temperature profiles are identical (see Hinze, Ref. 23 for a more general statement of Reynolds' analogy), which is the case for at least laminar flow with $Pr = 1$. Cancelling the bracketed quantity and dividing through by $u_m \Delta T_m$, the left-hand side is the dimensionless Stanton number. With the commonly accepted Prandtl number correction included, Reynolds' analogy becomes

$$St = \lambda \frac{c_f}{2} Pr^m$$

Using the Blasius skin friction relationship, and Reynolds' analogy, we then have the relationship between the local heat transfer coefficient and the local boundary layer velocity and thickness.

A digital computer program has been utilized to integrate numerically these equations for specific cases. For specified initial conditions of tank radius, jet velocity, and jet thickness, the following parameters are computed as a function of position around the tank wall: maximum velocity in jet, distance between tank wall and maximum jet velocity stream line, jet momentum, total jet thickness, heat transfer coefficient between jet and wall.

These results have been obtained for a variety of initial conditions. Examination of output from computer runs has indicated that the thickness of the wall jet grows very rapidly. Therefore, results beyond a meridional angle of approximately 120 deg are not valid,due to the thickness of the jet in relation to the radius of the tank. Computed results will, however, be conservative since with the wall jet model it is assumed that the jet will be in contact with stagnant liquid. This condition would occur only when the mixer unit is first started. In time, a central vortex will develop in the tank, tending to drag the upper portions of the jet along so that a more constant velocity (and heat transfer coefficient) is maintained around the tank.

SYMBOLS AND ABBREVIATIONS

q_w – Wall Heat Transfer Rate, Btu/hr-ft^2

τ_w – Skin Friction at Wall, lb/ft^2

τ_i – Shear at Arbitrary Distance From Wall, lb/ft^2

δ_m – Point of Maximum Velocity, ft

δ_i – Arbitrary Distance From Wall, ft

u_m – Maximum Velocity in Wall Bound Jet, ft/sec

y – Direction Perpendicular to Tank Wall, ft

R – Radius of Sphere, ft

θ, ϕ – Angles in Two Mutually Perpendicular Planes Through Center of Sphere

η – Unspecified Constant

ξ – $(y - \delta_m/b)$

υ – Kinetic Viscosity, ft^2/sec

δ_t – Outer Thickness, $\delta_m - \delta_m/2$, ft

f_{om} – Dimensionless Stream Function at u_m

K – Proportionality Factor for Eddy Mixing in Outer Half of Jet

η_t/η_m – Ratio of Boundary Layer Thicknesses, δ_t/δ_m

ϵ_H – Eddy Diffusivity of Heat, ft^2/hr

ϵ_M – Eddy Diffusivity of Momentum, ft^2/hr

St – Stanton Number

P_r – Prandtl Number

C_f – Skin Friction Coefficient

NOTE: Primed quantities are symbols from original equations; subscript o indicates initial value.

Appendix F

CENTRAL OR AXIAL JET

For this analysis, consider the model shown in the sketch below. A jet of liquid is emitted at one end of the tank, along the axis.

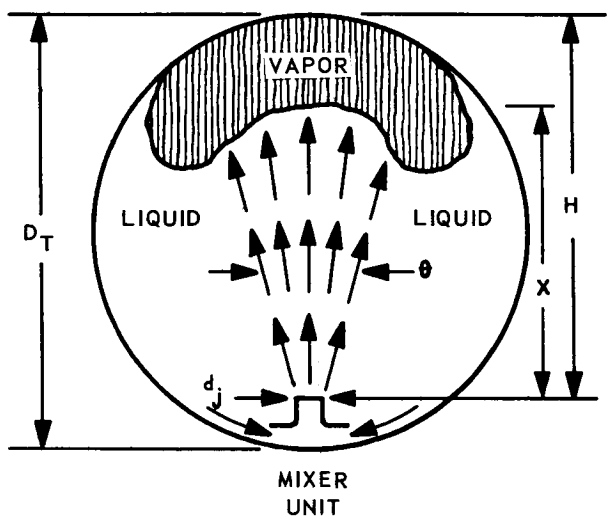

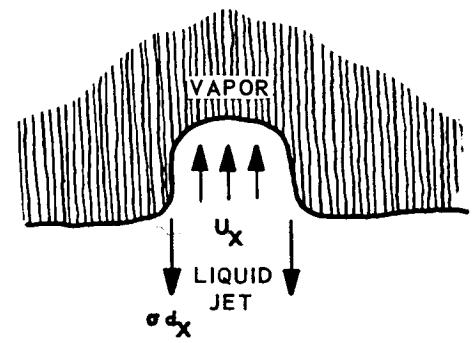

In a zero-g environment, only inertial and viscous forces act on the jet. If a vapor bubble is in the path of the liquid stream, the free surface will be distorted by the dynamic forces which are opposed by the surface tension. If these dynamic forces are large enough, the jet will break through the bubble and then be constrained to flow along the wall. A free-body diagram of the deflected portion of the free surface is also shown in the sketch. The inertial force deflecting the bubble is

$$F_I = \rho A U^2 = \frac{\pi}{4} \rho d^2 U^2 \qquad \text{(F.1)}$$

The opposing surface tension force is

$$F_\sigma = \pi d_x \sigma \tag{F.2}$$

For bubble break-through, the following condition must be satisfied

$$\frac{F_I}{F_\sigma} > \frac{\rho U^2 d_x^2}{4\sigma d_x} \tag{F.3}$$

From this, the critical Weber number is determined to be:

$$W_{e_{cr}} = 4 = \frac{U_x^2 d_x}{\sigma/\rho} \tag{F.4}$$

The critical Weber number is based upon local conditions at the interface. However, for design purposes, these conditions must be related to the jet velocity and size.

Conservation of jet momentum gives

$$P_j A_x + \rho_j A_j U_j^2 = P_x A_x + \rho_x A_x U_x^2 \tag{F.5}$$

In a large axisymmetric tank, in a zero-g environment, the pressure can be assumed to be uniform throughout, i.e., $P_j = P_x$. The momentum equation reduces to

$$A_j U_j^2 = A_x U_x^2 \tag{F.6}$$

Substituting this into the expression for critical Weber number, we get for a critical jet Weber number

$$W_{ej_{cr}} = W_{e_{cr}} \left(\frac{d_x}{d_j} \right) \tag{F.7}$$

If we now assume that the jet spreads at a constant angle θ , and that x = H, then

$$\frac{d}{d_j} = 1 + \frac{H}{d_j} \tan \theta \tag{F.8}$$

Therefore, combining Eqs. (F.4), (F.7), and (F.8)

$$W_{ej_{cr}} = 4 \left(1 + \frac{H}{d_j} \tan \theta \right) \tag{F.9}$$

The theoretical analysis of a submerged circular jet predicts that $\theta = 9$ deg , which results in the following equation for critical jet Weber number:

$$W_{ej_{cr}} = \frac{\rho U_j^2 d_j}{\sigma} = 4 \left(1 + 0.16 \frac{H}{d_j} \right) \tag{F.10}$$

SYMBOLS AND ABBREVIATIONS

A_x – Flow Area of Jet at x, ft^2

U_x – Velocity at x, ft/sec

d_x – Width of Jet at x, ft

σ – Surface Tension, lb/ft

We_{cr} – Critical Weber Number at Liquid Vapor Innerface

P_x – Pressure at x

P_j – Pressure at Nozzle, psi

U_j – Velocity at Nozzle, ft/sec

d_j – Jet Diameter at Nozzle, ft

H – Jet Height, ft

θ – Jet Spreading Angle, deg

Wej_{cr} – Critical Weber Number at Jet Nozzle

Appendix G

TWO-DIMENSIONAL JET

Consider a jet being confined between two closely spaced plates, as shown in the sketch below.

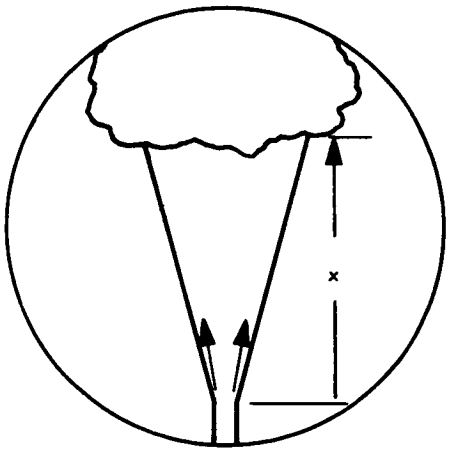

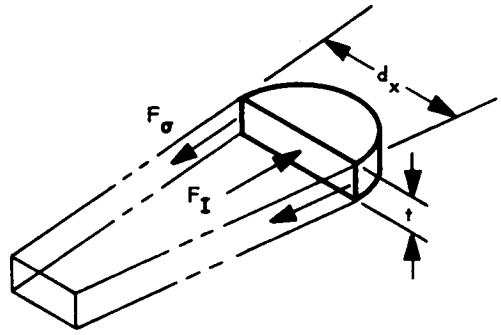

The ratio of forces at the liquid vapor interface is

$$\frac{F_I}{F_\sigma} = \frac{\rho A U_x^2}{2\sigma (t + d_x)} = \frac{\rho U_x^2 \; t d_x}{2\sigma \quad (t + d_x)} \tag{G. 1}$$

From which we define a critical Weber number based upon the plate, spacing is

$$\frac{\rho U_x^2 \; t}{\sigma} = 2 \left(1 + \frac{t}{d_x}\right) \tag{G. 2}$$

Again, conservation of momentum gives

$$P_j A_x + \rho_j A_j U_j^2 = P_x A_x + \rho_x A_x U_x^2 + F_0 \tag{G. 3}$$

where F_0 is the jet drag on the two flat plates.

Because of this drag, $P_j \neq P_x$ and additional relations are needed to relate jet and local quantities.

The continuity equation is

$$\rho_j A_j U_j = \rho_x A_x U_x - \Delta m \tag{G.4}$$

where Δm is the entrained mass. Since the flow is incompressible, $\rho_j = \rho_x$. Continuity of mass then gives

$$U_x = \left(\frac{A_j}{A_x}\right) U_j + \frac{\Delta m}{\rho_j A_x} \tag{G.5}$$

If the thickness of the jet (distance between plates) is small compared to the width, then Δm can be assumed to be negligible. Also,

$$A_x = d_x t$$

$$A_j = d_j t$$

and we get for the velocity

$$U_x = U_j\left(\frac{d_j}{d_x}\right) \tag{G.6}$$

Substituting this into the expression for the critical Weber number expression (G.2) gives,

$$\frac{\rho U_j^2 \left(\frac{d_j}{d_x}\right)^2 t}{\sigma} = 2\left(1 + \frac{t}{d_x}\right) \tag{G.7}$$

or

$$\frac{\rho U_j^2 t}{\sigma} = 2\left(1 + \frac{t}{d_j}\frac{d_j}{d_x}\right)\left(\frac{d_x}{d_j}\right)^2 \tag{G.8}$$

It is assumed that the jet spreads at a constant angle θ , and that $x = H$ and the equation for the critical jet Weber number becomes

$$W_{ej_{cr}} = \frac{\rho U_j^2 t}{\sigma} = 2 \left[1 + \frac{t}{d_j} \left(\frac{1}{1 + H/d_j \tan \theta} \right) \right] \left(1 + \frac{H}{d_j} \tan \theta \right)^2 \qquad (G.9)$$

SYMBOLS AND ABBREVIATIONS

F_I – Inertia Force, lb

$F\sigma$ – Surface Tension Force, lb

ρ – Density of Circulating Fluid

A_x – Jet Flow Area at Distance x From Nozzle, ft^2

U_x – Jet Velocity at Distance x , ft/sec

σ – Surface Tension, lb/ft

t – Distance Between Plates (Thickness of Two-Dimensional Jet), ft

d_x – Width of Jet at Distance x , ft

P_j – Pressure at the Nozzle, psi

A_j – Nozzle Flow Area, ft^2

U_j – Jet Velocity, ft/sec

Δm – Entrained Mass, lb

$We_{j_{cr}}$ – Critical Weber Number at Jet Nozzle

θ – Jet Spreading Angle, deg

Appendix H

SUBSCALE TEST PROGRAM

The experimental program presented herein has provided significant insight into the expected circulation patterns of a propellant tank, employing a mixer in a zero-g environment. Both qualitative and quantitative information were obtained on the effect of jet geometry and internal tank hardware on circulation patterns and mixer requirements.

TEST APPARATUS

Earth-bound simulation of zero-g fluid mechanics is most generally, and perhaps most precisely, accomplished with the use of a drop tower. However, drop-tower tests are extremely limited in the time available for observation of a dynamic flow field. This disadvantage was avoided with the test apparatus shown in Fig. H-1. Basically, the simulated tank is a very thin cylinder, 2 ft in diameter but only 1/8 in. deep. A 2-ft-diameter circle was cut from a 1/8-in. sheet of Plexiglas. This sheet is then sandwiched between two 1/2-in.-thick Plexiglas face plates which form the ends of the shallow cylinder. The lower plate has two holes drilled in it – one for an inlet to the jet and the other for a discharge port which is connected to the reservoir. A pump is connected between this reservoir and the inlet port to form a closed circulation loop. Two different jet plates were provided so that the jet could be directed out along the major axis (i.e., a central jet) or along the wall. The Plexiglas flow tank was supported around the edges with an aluminum box structure. This entire package was then mounted in a support frame through a horizontal axis, which allowed easy reorientation of the flow tank from the horizontal (simulated 0-g) to the vertical (1-g) position.

Fig. H-1 Two-Dimensional Flow Test Apparatus

TEST OPERATION

If one is to simulate the zero-g flow patterns, the body forces must be insignificant compared to the inertial and surface tension forces. This was accomplished by placing the thin two-dimensional apparatus horizontally, with the jet directed in the horizontal plane. The body force is then limited to the equivalent of 1/8 in. of fluid and acts orthogonally to the much larger dynamic forces created by the jet. It was also much smaller than the surface tension forces. This was evidenced by the inability of the fluid to form a free horizontal surface with a partially filled tank in a no-flow condition, i.e., the upper and lower plates were equally wetted by the fluid under all levels of the tank fill.

The test operation was rather simple, once the desired jet configuration was installed. The apparatus was locked in the horizontal position and filled to some arbitrary level. Then the pumps were turned on, with the flow restricted to a value less than sufficient to span the tank. The volumetric flow rate was measured, and a qualitative evaluation of the flow patterns was made from observations on the activity and location of the air bubbles in the tank. Jet velocities were calculated from the measured volumetric flow and the known jet area. The flow rate was increased, in steps, beyond the point where the jet completely spanned the tank, and flow was visually observed everywhere along the walls. In some cases, the patterns were recorded with photographs and movies.

TEST RESULTS

Approximately 60 tests have been run in which data were recorded. These tests are presented in Table H-1, along with a subjective evaluation of the mixing patterns. The various test series are associated with specific modifications to the basic test apparatus described previously in the paragraph entitled Test Apparatus. These modifications are shown schematically in Fig. H-2. The basic apparatus shown in Fig. H-1 and the modified apparatus A and B provide data on the central jet and correspond to the two-dimensional analytical model for establishing critical Weber number. In addition, B provides data on the effect of baffles on the circulation patterns created by the central jet. Apparatus C simulates a tangential mixer discharge.

Table H-1

EXPERIMENTAL CIRCULATION DATA

Fluid	Apparatus	Orientation	Flow Rate (gpm)	Jet Velocity (ft/sec)	Jet Weber Number $\left(\frac{\rho U_j^2 t}{\sigma}\right)$	Visual Observations
Water-Air	Basic	Horizontal	2.7	13.77	758	Blow-by at jet negated data
	A	Horizontal	0.32	1.63	10.6	Less than complete
		Horizontal	0.95	4.84	93.6	Bordering on complete circulation
		Horizontal	1.24	6.32	160.0	Complete; more energetic than 3
		Vertical	1.37	6.99	196.0	Complete; more energetic than 3
		Horizontal	1.09	5.56	124.0	Complete circulation indicated
		Horizontal	1.63	8.30	276.0	Vigorous circulation throughout
		Horizontal	0.85	4.33	75.0	Indicates we are slightly below complete circulating; bubbles do not reach wall. Some pulsation in flow; bubbles located $\approx$ 2.5 in. from top and deflect flow; occasionally break up.
		Horizontal	0.53	2.70	29.2	Bubbles form $\approx$ 3-4 in. below top and deflect flow; circulation hardly visible.
		Horizontal	1.50	7.65	234.0	Complete circulation indicated; bubbles along wall forced down.
Water-Air	A	Horizontal	0.42	2.14	18.3	Incomplete circulation; hardly noticable. Large bubbles form $\approx$ 5 in. from top

Table H-1 (Cont.)

Fluid	Apparatus	Orientation	Flow Rate (gpm)	Jet Velocity (ft/sec)	Jet Weber Number $\left(\frac{\rho U_j^2 t}{\sigma}\right)$	Visual Observations
Water-Air	Basic	Vertical	3.3	16.8	1130	Very definite complete circulation throughout full tank.
		Vertical	1.22	6.21	155	Incomplete
		Vertical	1.78	9.08	330	Incomplete
		Vertical	2.74	14.0	783	Circulation to top but not out to sides; flow just reaches top, but jet pulsates.
		Horizontal	0.53	2.70	29.2	Jet just barely makes the top; no movement of bubbles along the wall; jet hardly visible.
	Basic	Horizontal	2.05	10.45	437	Just critical, i.e., jet is deflected at the top of the tank
	B	Vertical	2.4	12.2	595	Flow deflected 2-3 in. from top; generally flow moves around baffles; very slight movement behind baffles.
		Horizontal	1.09	5.56	124	Slightly supercritical
		Horizontal	1.49	7.60	231	Well above critical
Water-Air	B	Horizontal	0.8	4.07	66.4	Flow very pulsating, with air being alternately sucked into the exhaust. Flow apparently below critical; large bubbles attached to lip of jet: broken off when jet velocity apparently increases due to air entrainment.

Table H-1 (Cont.)

Fluid	Apparatus	Orientation	Flow Rate (gpm)	Jet Velocity (ft/sec)	Jet Weber Number $\left(\frac{\rho U_j^2 t}{\sigma}\right)$	Visual Observations
Water-Air	B	Horizontal	1.63	8.30	276	Flow appears above critical; bubbles behind first baffle eventually move out into stream.
		Horizontal	1.83	9.34	348	Flow well below critical; some movement of bubbles between baffles with gap; large bubbles remain between.
		Horizontal	No Measurement			Below critical; large bubble forms $\approx$ 5 in. from top. Blow-by noted at jet; suction pump removed.
		Horizontal	0.92	4.69	88.1	Flow less than critical; bubbles agglomerate $\approx$ 2 in. from top, but movement noted throughout. Large bubbles trapped behind baffles adjacent to wall; none behind baffles with gaps.
		Inclined 10 Deg				Blow-by at jet negated all attempts
		Vertical				Blow-by at jet negated all attempts.
		Horizontal	1.67	8.51	290	Flow well above critical. Seems to be deflected by both sets of baffles; bubbles in the vicinity of baffles are agitated but don't break away.
Water-Air	B	Horizontal	0.77	3.92	61.5	Flow < critical just barely; fairly low ullage ratio; no large torroidal bubbles such as in No. 1.

Table H-1 (Cont.)

Fluid	Apparatus	Orientation	Flow Rate (gpm)	Jet Velocity (ft/sec)	Jet Weber Number $\left(\frac{\rho U_j^2 t}{\sigma}\right)$	Visual Observations
Water-Air	B	Horizontal	0.62	3.16	40	Flow < critical; slugging. Incoming bubbles never get closer than ≈ 1-1/2 in. from top; large bubbles break up ≈ 2 in. from exit.
		Horizontal	1.3	6.63	176	Flow appears slightly > critical; no bubbles along side with gap and baffles; some attached on opposite side but probably due to film on the plates.
		Inclined 10 Deg	1.2	6.12	150	Flow pattern just reaching top with some oscillation; large ullage.
		Vertical	3.0	15.3	938	Nozzle covered; jet does not reach top oscillation of jet side to side.
		Vertical	2.3	11.7	550	Jet reaches halfway up tank; some oscillation side to side.
	B					Blow-by when tried to go up in flow.
	C	Horizontal	1.33	6.78	184	Flow on one side with gaps reaches past the top of tank.
	C	Horizontal	1.1	5.61	126	Flow still reaches top.
	D	Horizontal	1.39	7.1	201	Flow just large enough to push baffle through last baffle gap.
Water-Air	D	Horizontal	0.38	1.94	15.1	Bubbles in region of first baffle remain fixed, just behind first baffle, i.e., We < Weer @ first baffle; no vortex visible in upper portion of tank.

Table H-1 (Cont.)

Fluid	Apparatus	Orientation	Flow Rate (gpm)	Jet Velocity (ft/sec)	Jet Weber Number $\left(\frac{\rho U_j^2 t}{\sigma}\right)$	Visual Observations
Water-Air	D	Horizontal	0.6	3.06	37.4	Bubbles slowly moved along the wall until reaching second baffle. There they deflect the flow until pump suction pulls them loose.
		Horizontal	0.82	4.18	70.0	Wall lined with bubbles at stream interface up to first baffle; not much bubble growth or agitation between baffles; liquid moving through gaps is visible; small bubbles are moved along the wall until the last baffle.
		Horizontal	1.4	7.14	204	Wall jet contained by large bubble almost to first baffle. Flow moves well behind every baffle along wall. Large bubbles, elongated to stretch between baffles. Flow vortex at lower end of each bubble.
			2.14	10.9	476	Good throughout; bubble agitation behind every baffle; upper vortex between top baffle and top very obvious.
			0.87	4.44	79.0	Jet well lined with bubbles up to first baffle; not much bubble growth or agitation between baffles; large vortex at top not apparent.
Water-Air	D		0.56	2.85	32.6	Very little bubble movement behind baffles; ullage bubble attached to jet and standpipe; no vortex action.

Table H-1 (Cont.)

Fluid	Apparatus	Orientation	Flow Rate (gpm)	Jet Velocity (ft/sec)	Jet Weber Number $\left(\frac{\rho U_j^2 t}{\sigma}\right)$	Visual Observations
Water-Air	D		0.59	3.01	36.2	Bubbles block flow between second baffle and tank wall until pump suction overcomes the capillary. Then new bubble forms.
			0.32	1.63	10.6	Small bubbles lay on tank wall just behind first baffle.
			1.2	6.12	150	Small bubbles lay on tank wall just behind first baffle, except that small bubbles moved more slowly along wall after passing through third baffle.
		Vertical	0.34	1.74	12.1	Jet just spills over the lip, i.e., does not stay attached to the wall. Tank almost empty at this flow.
		Vertical	0.985	5.02	101	Jet remains attached all the way; tank still almost empty; some spill-over at first and third baffles.
	D	Vertical	1.82	9.28	344	Level just below top baffle; vortex action behind each submerged baffle; liquid level continuously dropping.
Water-Air	D*	Horizontal	1.57	8.0	256	Flow slightly below critical; bubbles hang up $\approx$ 4 in. from bottom until they reach a critical size; then they start to move again.

D* is the same apparatus as D, with baffles removed.

Table H-1 (Cont.)

Fluid	Apparatus	Orientation	Flow Rate (gpm)	Jet Velocity (ft/sec)	Jet Weber Number $\left(\frac{\rho U_j^2 t}{\sigma}\right)$	Visual Observations
Water-Air	D*	Horizontal	0.9	4.6	84	Small bubbles remain attached to the wall along the lower half of the tank
	D*	Horizontal	0.5	2.55	26	Elongated gas bubbles remain attached to the wall in the lower portion of the tank.
Water-Air	D*	Horizontal	2.0	17.7	1260	Bubbles completely swept off the wall.
Alcohol-Air	A	Horizontal	0.42	2.1	59	Jet does not reach the top. Air bubbles in the stream get approximately 3 in. from top and then peel off; all bubble diameters appear to be less than 1 in.
		Horizontal	0.8	4.1	213	Air bubbles in the stream reach to within 1/2 in. of the top, but liquid reaches top and flows along the wall. Flow appears to be slightly above critical. Again, bubble diameters < 1 in. All bubbles in motion, but none located out along the wall.
		Horizontal	0.72	3.7	171	Same general observations as in previous run; smallest bubbles reached top of tank and deflected.
Alcohol-Air	A	Horizontal	1.28	6.5	547	Very good circulation throughout the tank; larger bubbles caught in a vortex; continuously broken up and entrained in the jet.

D* is the same apparatus as D, with baffles removed.

Table H-1 (Cont.)

Fluid	Apparatus	Orientation	Flow Rate (gpm)	Jet Velocity (ft/sec)	Jet Weber Number $\left(\frac{\rho\ U_j^2\ t}{\sigma}\right)$	Visual Observations
Alcohol-Air	A	Horizontal	1.28	6.5	547	Same as above.
			1.07	5.5	382	Flow appears well above critical; small bubbles being deflected at top of the tank.
			0.72	3.7	171	Small bubbles reaching top; larger bubbles entrained by the jet and broken up into smaller bubbles $\approx$ 2 in. from top of the tank.
			0.65	3.3	141	Small bubbles pushed within 1 in. of top of the tank. All bubbles in motion throughout the tank.
Alcohol-Air	A	Horizontal	0.55	2.8	101	Large bubbles that span the jet appear to deflect the jet $\approx$ 3 in. from top.

LOCKHEED MISSILES & SPACE COMPANY

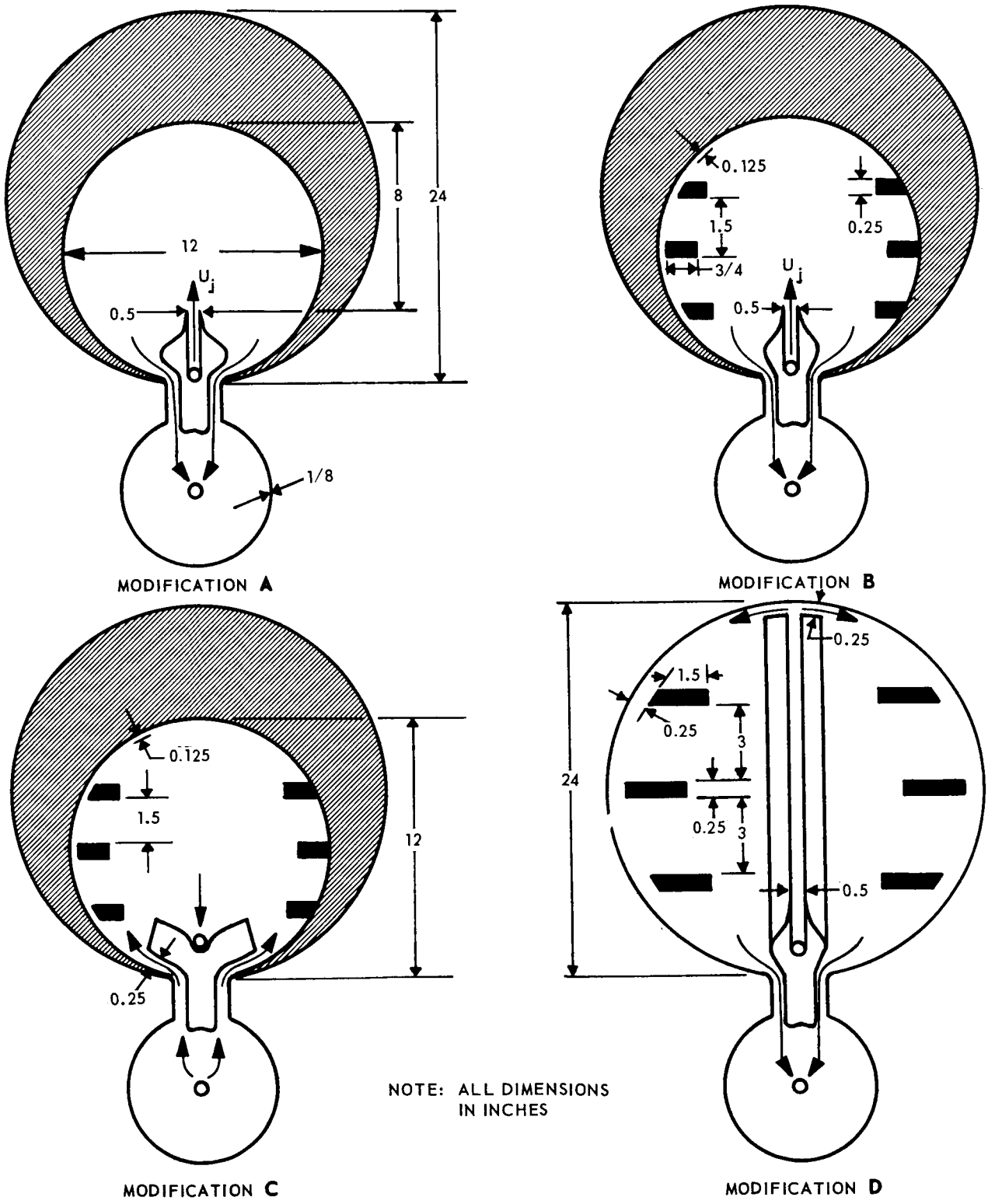

Fig. H-2 Modified 2-D Flow Test Apparatus

In D, a simulated pipe is provided to duct the circulating propellant to the opposite end of the tank so that the mixer intake and discharge are on opposite ends of the tank. This guarantees circulation throughout the tank.

There were six tests conducted with the basic apparatus, of which only two were in the simulated 0-g position. The higher of the two flow rates agreed very well with the critical Weber number theory developed previously. The other four tests were with the apparatus in the upright position. No quantitative conclusions were obtained from these tests.

Apparatus A was identical to the basic apparatus, except for size. A 1-ft-diameter circle was cut from a sheet of gasket material. This sheet was then contoured to fill in the 2-ft circle and sealed in place so that the effective tank diameter was reduced to 12 in. Twenty tests were conducted with this modification, of which 10 were with alcohol and air and the rest with water and air. These simulated 0-g tests also tended to confirm critical Weber number theory. Figure H-3 is a series of photographs showing circulation with various flow rates which progressively increase to a value well above that for the critical Weber number for this series of tests. When the Weber number exceeded critical, the gas bubbles were removed from the walls. Eighteen tests were conducted with B. This apparatus is identical to A except for scaled baffles that were placed on each side of the tank. On one side, they were adjacent to the wall; on the other, they were displaced. It was generally noted that the circulating fluid would flow through the gap and wash the bubbles from between the baffles when the flow rate was approximately 30 percent greater than the critical flow rate in the clean tank (i.e., the flow rate for which $We = W_{e_{cr}}$). However, even for much lower velocities, there is obvious agitation of the trapped gas bubbles.

Apparatus D was used for approximately 15 tests. With this arrangement, all gas bubbles were washed away from the walls, and the circulating fluid flowed behind all three baffles when the flow rate was approximately the same as the critical flow for the central jet in the 2-ft tank. A photo array showing the circulation patterns for progressively higher flow rates is shown in Fig. H-4.

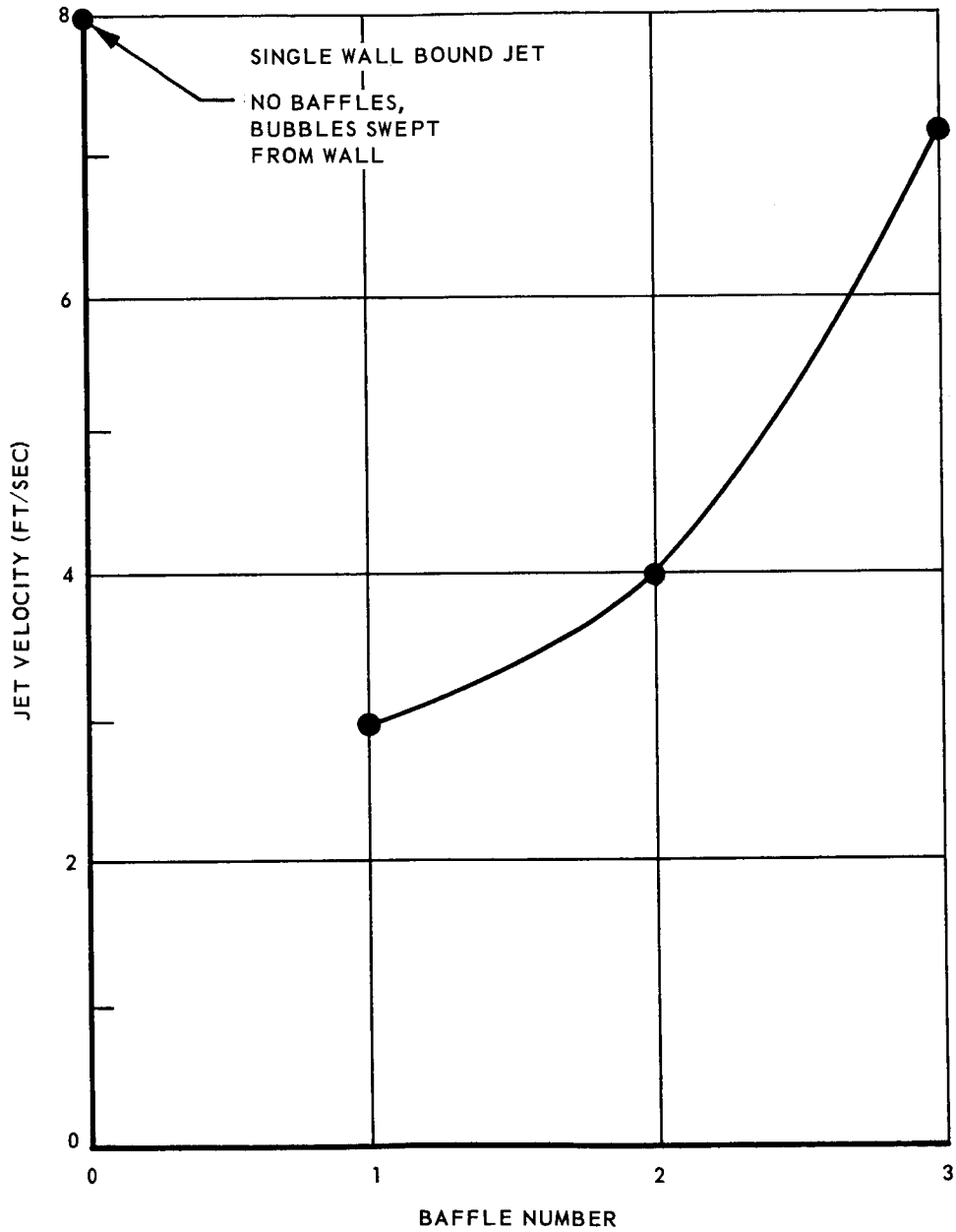

Fig. H-3 Jet Velocities Required to Break Through a Gas Bubble Located Behind a Given Baffle in the Two-Dimensional Test Apparatus

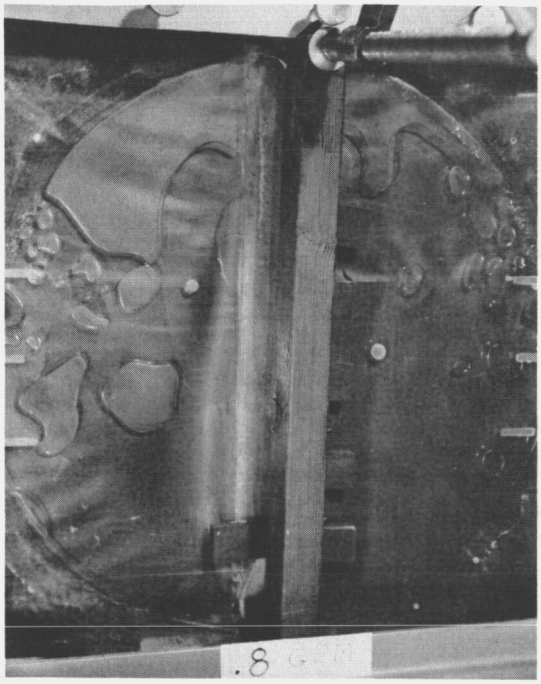

JET VELOCITY = 1.7 FT/SEC

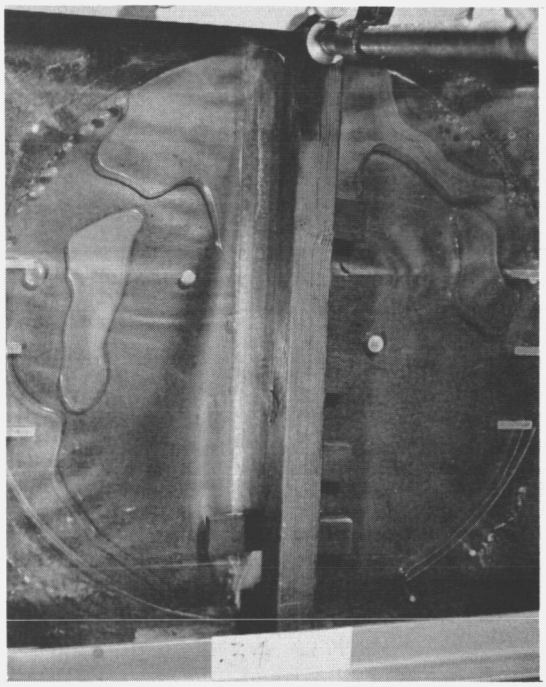

JET VELOCITY = 4.1 FT/SEC

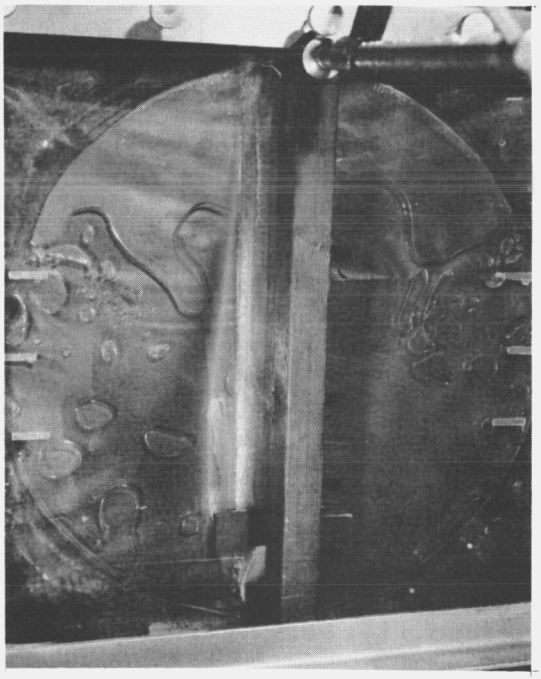

JET VELOCITY = 7.1 FT/SEC

Fig. H-4 Typical Liquid-Ullage Patterns With a Single Wall-Bound Jet

DISTRIBUTION LIST FOR INTERIM REPORT NASA CR-72113

"LIQUID PROPELLANT THERMAL CONDITIONING SYSTEM"

NAS3-7942

LOCKHEED AIRCRAFT CORPORATION
MISSILES & SPACE DIVISION

	Copies
National Aeronautics and Space Administration Lewis Research Center 21000 Brookpark Road Cleveland, Ohio 44135	
Attention: Contracting Officer, MS 500-210	1
Liquid Rocket Technology Branch, MS 500-209	8
R. Knoll, MS 501-2	1
Technical Report Control Office, MS 5-5	1
W. Masica, MS 54-1	1
Technology Utilization Office, MS 3-16	1
R. DeWitt, MS 86-1	1
AFSC Liaison Office, MS 4-1	2
J. Sivo, MS 501-2	1
Library	2
D. Petrash, MS 54-1	1
Office of Reliability & Quality Assurance, MS 500-203	1
K. Abdalla, MS 54-1	1
E. W. Conrad, MS 100-1	1
National Aeronautics and Space Administration Washington, D. C. 20546	
Attention: Code MT	1
RPX	2
RPL	2
SV	1
Scientific and Technical Information Facility P.O. Box 33 College Park, Maryland 20740	
Attention: NASA Representative Code CRT	6

	Copies
National Aeronautics and Space Administration Ames Research Center Moffett Field, California 94035	
Attention: Library	1
C. A. Syvertson	1
National Aeronautics and Space Administration Flight Research Center P.O. Box 273 Edwards, California 93523	
Attention: Library	1
National Aeronautics and Space Administration Goddard Space Flight Center Greenbelt, Maryland 20771	
Attention: Library	1
National Aeronautics and Space Administration John F. Kennedy Space Center Cocoa Beach, Florida 32931	
Attention: Library	1
National Aeronautics and Space Administration Langley Research Center Langley Station Hampton, Virgina 23365	
Attention: Library	1
National Aeronautics and Space Administration Manned Spacecraft Center Houston, Texas 77001	
Attention: Library	1
National Aeronautics and Space Administration George C. Marshall Space Flight Center Huntsville, Alabama 35812	
Attention: Library	1
Keith Chandler, R-P&VE-PA	1
Clyde Nevins, R-P&VE-SAA	1
R. Wegrich, R-P&VE-PTP	1
Dave Arnett, R-P&VE-PTF	1
National Aeronautics and Space Administration Western Operations Office 150 Pico Boulevard Santa Monica, California 90406	
Attention: Library	1

	Copies
Jet Propulsion Laboratory 4800 Oak Grove Drive Pasadena, California 91103 Attention: Library	1
Office of the Director of Defense Research & Engineering Washington, D.C. 20301 Attention: Dr. H. W. Schulz, Office of Asst. Dir. (Chem. Technology)	1
Defense Documentation Center Cameron Station Alexandria, Virginia 22314	1
RTD (RTNP) Bolling Air Force Base Washington, D. C. 20332	1
Arnold Engineering Development Center Air Force Systems Command Tullahoma, Tennessee 37389 Attention: AEOIM	1
Advanced Research Projects Agency Washington, D. C. 20525 Attention: D. E. Mock	1
Aeronautical Systems Division Air Force Systems Command Wright-Patterson Air Force Base, Dayton, Ohio Attention: D. L. Schmidt, Code ASRCNC-2	1
Air Force Systems Command (SCLT/Capt. S. W. Bowen)	1
Andrews Air Force Base Washington, D. C. 20332	1
Air Force Rocket Propulsion Laboratory (RPR) Edwards, California 93523	1
Air Force Rocket Propulsion Laboratory (RPM) Edwards, California 93523	1
Air Force Office of Scientific Research Washington, D. C. 20333 Attention: SREP, Dr. J. F. Masi	1

	Copies
Air Force Aero Propulsion Laboratory Research & Technology Division Air Force Systems Command United States Air Force Wright-Patterson AFB, Ohio 45433 Attention: APRP (C. M. Donaldson)	1
Aerojet-General Corporation P.O. Box 296 Azusa, California 91703 Attention: Librarian	1
A. Weinstein	1
Aerojet-General Corporation 11711 South Woodruff Avenue Downey, California 90241 Attention: F. M. West, Chief Librarian	1
Aerojet-General Corporation P. O. Box 1947 Sacramento, California 95809 Attention: Technical Library 2484-2015A	1
Dr. C. M. Beighley	1
D. T. Bedsole	1
Aerospace Corporation P.O. Box 95085 Los Angeles, California 90045 Attention: J. G. Wilder, MS-2293	1
Library-Documents	1
Arthur D. Little, Inc. Acorn Park Cambridge 40, Massachusetts Attention: A. C. Tobey	1
Astropower, Incorporated Subs. of Douglas Aircraft Company 2968 Randolph Avenue Costa Mesa, California Attention: Dr. George Moc Director, Research	1
ARO, Incorporated Arnold Engineering Development Center Arnold AF Station, Tennessee 37389 Attention: Dr. B. H. Goethert Chief Scientist	1

	Copies
Battelle Memorial Institute 505 King Avenue Columbus, Ohio 43201 Attention: Report Library, Room 6A	1
Beech Aircraft Corporation Boulder Facility Box 631 Boulder, Colorado Attention: J. H. Rodgers	1
John A. Pike	1
Bell Aerosystems, Inc. Box 1 Buffalo, New York 14205 Attention: T. Reinhardt	1
W. M. Smith	1
Kert Berman	1
The Boeing Company Aero Space Division P.O. Box 3707 Seattle, Washington 98124 Attention: Ruth E. Peerenboom (1190)	1
J. D. Alexander	1
C. Tiffany	1
R. Sjack	1
Chemical Propulsion Information Agency Applied Physics Laboratory 8621 Georgia Avenue Silver Spring, Maryland 20910	1
Chrysler Corporation Space Division New Orleans, Louisiana Attention: Librarian	1
Curtiss-Wright Corporation Wright Aeronautical Division Woodridge, New Jersey Attention: G. Kelley	1
University of Denver Denver Research Institute P.O. Box 10127 Denver, Colorado 80210 Attention: Security Office	1

	Copies
Douglas Aircraft Company, Inc. Santa Monica Division 3000 Ocean Park Blvd., Santa Monica, California 90405	
Attention: J. L. Waisman	1
R. W. Hallet	1
G. W. Burge	1
S. H. Schwartz	1
E. Marion	1
General Dynamics/Convair P. O. Box 1128 San Diego, California 92112	
Attention: Mr. W. Fenning	
Centaur Resident Project Office	1
Library & Information Services (128-00)	1
Karl Leonhard	1
Paul Stevens	1
R. Tatro	1
General Electric Valley Forge Space Technology Center P.O. Box 8555 Philadelphia, Pennsylvania 19001	
Attention: M. W. Mitchell	1
A. D. Cohen	1
Grumman Aircraft Engineering Corporation Bethpage, Long Island, New York	
Attention: Joseph Gavin	1
IIT Research Institute Technology Center Chicago, Illinois 60616	
Attention: C. K. Hersh, Chemistry Division	1
Office of Research Analyses (OAR) Holloman Air Force Base, New Mexico 88330	
Attention: RRRT	1
Maj. R. E. Brocken, Code MDGRT	1
U. S. Air Force Washington, D. C., Zone 25	
Attention: Col. C. K. Stambaugh, Code AFRST	1

	Copies
U. S. Army Missile Command Redstone Scientific Information Center Redstone Arsenal, Alabama 35808 Attention: Chief, Document Section	1
Dr. W. Wharton	1
Commander U. S. Naval Missile Center Point Mugu, California 93041 Attention: Technical Library	1
Space-General Corporation 777 Flower Street Glendale, California Attention: C. E. Roth	1
Stanford Research Institute 333 Ravenswood Avenue Menlo Park, California 94025 Attention: Thor Smith	1
P. R. Gillette	1
Thiokol Chemical Corporation Alpha Division, Huntsville Plant Huntsville, Alabama 35800 Attention: Technical Director	1
Marquardt Corporation 16555 Saticoy Street Box 2013 - South Annex Van Nuys, California 91404 Attention: Librarian	1
W. D. Boardman, Jr.	1
McDonnell Aircraft Corporation P.O. Box 6101 Lambert Field, Missouri Attention: R. A. Herzmark	1
North American Aviation, Inc. Space & Information Systems Division 12214 Lakewood Boulevard Downey, California 90242 Attention: Technical Information Center, D/096-722 (AJ01)	1
H. Storms	1

	Copies
Northrop Space Laboratories 1001 East Broadway Hawthorne, California Attention: Dr. William Howard	1
Rocket Propulsion Laboratory DGRPP Edwards, California 93523 Attention: 2/Lt. E. Dahl	1
Wright-Patterson AFB, Ohio 45433 Attention: AFML (MAAE)	1
Wright-Patterson AFB, Ohio 45433 Attention: AFML (MAAM)	1
Air Products and Chemicals, Inc. Allentown, Pennsylvania Attention: Abraham Lopin	1
Air Products and Chemicals, Inc. West Broad Street Emmaus, Pennsylvania Attention: Andrew Hospider	1
University of California Los Alamos Scientific Laboratory P.O. Box 1663 Los Alamos, New Mexico	1
Cryonetics Corporation Northwest Industrial Park Burlington, Massachusetts Attention: James F. Howlett	1
The Garrett Corporation 1625 Eye Street, NW Washington, D.C. Attention: G. R. Shepard	1
General Electric Company Apollo Support Department P.O. Box 2500 Daytona Beach, Florida 32015 Attention: C. Day	1

	Copies
Goodyear Aerospace Corporation 1210 Massillon Road Akron, Ohio Attention: Clem Shriver, Dept. 481	1
Ling-Temco-Vought Box 5907 Dallas, Texas Attention: Library	1
Linde Company Tonawanda, New York Attention: R. Lindquist	1
L. Niendorf	1
Arthur D. Little, Inc. Division 500 Acorn Park Cambridge, Massachusetts 02140 Attention: Mr. R. B. Hinckley	1
Lockheed Aircraft Corporation Marietta, Georgia Attention: Library	1
The Martin Company Baltimore, Maryland Attention: Science-Technology Library	1
R. Crawford	1
National Research Corporation 70 Memorial Drive Cambridge, Massachusetts	1
New York University University Heights New York, New York Attention: Paul F. Winternitz	1
Space General Corporation 9200 East Flair Drive El Monte, California Attention: John Kortenhoeven, Dept. 5131	1
Space Technology Laboratory, Inc. 1 Space Park Redondo Beach, California 90200 Attention: STL Tech. Lib. Doc. Acquisitions	1
Pravin Bhuta	1

	Copies
General Dynamics/Forth Worth P.O. Box 748 Fort Worth, Texas Attention: P. R. Tonnancour	1
The Martin Company Denver, Colorado Attention: D. W. Murphy	1
Library	1
Dynatech Corporation 17 Tudor Street Cambridge, Massachusetts 02139 Attention: J. M. Bonneville	1